

ERRATA

- p.3 Line 2 add "method" after "analytical"
- p. 5 Line 5 replace "into" with "in"
- p. 6 Line 12 replace "into" with "in"
- p. 7 Line 1 replace "NFLEA" with "NLFEA"
- p. 7 Line 6 Line 6 omit "was"
- p. 10 Line replace "crack" with "cracked"
- p. 13 Line 10 replace "affect" with "effect"
-
- p. 74 Equation 4.4.1 should read $F = \sqrt{J_2} - \alpha_f I_1 - \zeta c = 0$
- p. 81 para 3 add the following statement to after point 2.
"Condition 2 applied to all analyses presented in this thesis. In addition to this, inspection of the state of stress and strain in all cases revealed phenomena such as yielding of stirrups and plasticised concrete in the compression region and cracking of concrete that were consistent with the failure mechanisms that were displayed by the experimental specimens. A detailed discussion of the relevant characteristics of the models at the failure load is discussed in Chapter 8."

H 24/3441

MONASH UNIVERSITY
THESIS ACCEPTED IN SATISFACTION OF THE
REQUIREMENTS FOR THE DEGREE OF
DOCTOR OF PHILOSOPHY

ON..... 12 August 2003

.....
Sec. Research Graduate School Committee

Under the Copyright Act 1968, this thesis must be used only under the normal conditions of scholarly fair dealing for the purposes of research, criticism or review. In particular no results or conclusions should be extracted from it, nor should it be copied or closely paraphrased in whole or in part without the written consent of the author. Proper written acknowledgement should be made for any assistance obtained from this thesis.

Flange Effectiveness in the Resistance of Shear on RC T-Beams Subjected to Point Loads

by

Craig Giaccio
BE (Hons) *Adel.*

A thesis submitted in conformity with the requirements
for the degree of **Doctor of Philosophy**
Department of Civil Engineering
Monash University
January 2003

ABSTRACT

This thesis presents an examination into the effectiveness of the flange of a web reinforced RC T-beam subjected to a concentrated point load in the resistance of shear forces. The research implemented three methods of investigation of this effect. Two stages of experimental work were implemented, and an investigation into the capability of nonlinear finite element analysis to predict the results of experimental work was also implemented.

The first of the two stages of experimental work presented is an investigation into the effect of the variation of flange proportions on the shear strength of three series' of point loaded web reinforced RC T-beams. The second of the two stages presented in this thesis outlines the development, verification, and implementation of an experimental method and accompanying analytical technique capable of calculating the magnitude of the shear force that is resisted by the flange of web reinforced RC T-beam.

The implementation of nonlinear finite element analysis (NLFEA) presented in this thesis firstly determines the optimum combination of material models as well as displacement increments in the application of this solution scheme. This scheme was then used to determine the capability of NLFEA to predict the peak loads, measured strains, crack patterns and failure mechanisms of the experimental specimens, and was further implemented to a series of specimens with constant material properties.

The results showed that increasing the flange proportions of a web reinforced RC T-beam subjected to a point load produces an accompanying increase in the shear strength of that specimen. Increases in the flange width were found to have more effect in increasing shear capacity than increases in flange depth. It was observed that two failure mechanisms were exhibited by experimental specimens; one corresponding to the

classical mechanism of shear failure (termed the beam shear failure mechanism), and a failure mechanism associated with the method of application of the load (termed the punching shear failure mechanism). The increases in shear strength with increases in flange width prevailed while the beam shear mechanism formed. When the flange width was wide enough for the punching shear mechanism to form, this trend of increasing shear strength with increasing flange width ceased. This research suggests that the formation of the punching shear mechanism in a web reinforced T-beam provides the upper bound to the trend of increasing shear strength with increasing flange width.

The propagation of shear forces into the flange of a T-beam specimen was found to be a major contributor to the increase in shear strength associated with increases in the flange width. Shear stresses were forced into the flanges as a result of the redistribution of longitudinal strains in the flange that prevailed to accommodate the formation of the failure mechanism. Flange contributions of greater than 20% were calculated during the experimental work. This flange contribution to the resistance of shear was found to significantly increase on formations of stages of the failure mechanism.

NLFEA was found to be capable of predicting ultimate strengths and failure mechanisms of the majority of the specimens used in comparison with experimental work. The shortcoming found with this solution scheme is the inability to predict these parameters in specimens with wide and thin flanges.

STATEMENT

This thesis contains only original material none of which has been previously submitted for any other degree or diploma at any other University. To the best of my knowledge all material in this thesis is original unless due reference has been made to the relevant authors in the text.



CRAIG GIACCIO

28/1/03.

ACKNOWLEDGEMENTS

I would like to gratefully acknowledge the contributions of my project supervisors, Dr Riadh Al-Mahaidi, and Dr. Geoff Taplin. Riadh has consistently provided excellent technical advice throughout the project, and has provided much useful advice regarding project direction. Geoff has consistently provided quality assistance and critiques of the techniques and results that are presented in this thesis as well as sound guidance on the presentation of these to the scientific community both through this thesis, and through the publications that have arisen from this work. My colleague Tuan Kuan Lee has also provided me with good assistance throughout the project in the form of technical discussions and debates and assistance in the laboratory. For this I am grateful.

I wish also to acknowledge the support of VicRoads Australia. As the industry partner to this project, they provided some financial support, and also valuable input to the relevance of the results to the engineering community.

I would like also to like to thank my partner Donna Hazelman and my family for their help along the way especially when it was required to put in the extra hours required to complete this project.

TABLE OF CONTENTS

ABSTRACT	I
STATEMENT	III
ACKNOWLEDGEMENTS.....	IV
TABLE OF CONTENTS.....	V
LIST OF FIGURES.....	IX
LIST OF TABLES.....	XV
LIST OF SYMBOLS.....	XVI
CHAPTER 1 INTRODUCTION	1
1.1 Introduction	1
1.2 Aims of the Research.....	3
1.3 Outline of the Thesis.....	4
1.3.1 Experimental Work.....	5
1.3.2 Finite Elements Analysis.....	6
CHAPTER 2 LITERATURE REVIEW.....	9
2.1 Introduction	9
2.2 The Mechanisms of Shear Resistance.....	9
2.3 Investigations Relating to the Shear Strength of T-Beams	11
2.3.1 Experimental Investigations into the Shear Strength of T-beams.....	12
2.3.2 Experimental Investigations Including the Effect of Flange Proportions on the Shear Strength of RC T-beams	14
2.3.3 Analytical Investigations Including the Effect of Flange Proportions on the Shear Strength of RC T-beams.....	20
2.4 State of the Art Research Methods for Calculation of Shear Capacity	24
2.4.1 The Disturbed Stress Field Model.....	24
2.4.2 Compressive Force Path Theory	27
2.4.3 Softened Truss Models.....	28
2.4.4 Other Methods of Predicting Shear Capacity	29
2.5 How effective is the Flange of an RC T-beam in the Resistance of Shear?	30
2.6 Objectives of This Research	32

CHAPTER 3 EXPERIMENTAL PROGRAM	34
3.1 Introduction	34
3.2 Procedure for Stage 1 Experimental Work	35
3.2.1 The Reference Rectangular Beam.....	35
3.2.2 Flange Proportions Investigated.....	36
3.2.3 Flange Reinforcing Arrangements	38
3.2.4 Loading	40
3.2.5 Material Properties.....	41
3.2.6 Measurement.....	42
3.3 Procedure for Stage 2 Experimental Work	43
3.3.1 Application of Equilibrium Principles to Determine the Shear Force in the Flange of a T-Beam.....	44
3.3.2 Specimen Outline.....	56
3.3.3 Details of the Instrumentation	58
CHAPTER 4 NUMERICAL MODELLING USING NON LINEAR FINITE ELEMENT ANALYSIS ..	65
4.1 Introduction	65
4.2 Objectives of the Implementation of Non-Linear Finite Element Analysis	66
4.3 The Physical Model.....	67
4.3.1 Model Geometry and Boundary Conditions.....	67
4.3.2 Element Selection	69
4.4 Material Models.....	73
4.4.1 Concrete Model.....	73
4.4.2 Steel Model	79
4.5 The Iteration Scheme and Convergence	80
4.5.1 The Iteration Scheme	80
4.5.2 Numerical Convergence Criteria.....	81
4.5.3 Definition of Failure.....	81
4.6 The Parametric Study	82
4.6.1 The Material Model Parametric Study	82
4.6.2 The Displacement Step Size Parametric Study	84
4.7 Modelling Plan	85
CHAPTER 5 FLANGE PROPORTIONS, ULTIMATE STRENGTH AND FAILURE MECHANISMS ..	89
5.1 Introduction	89
5.2 Normalisation of Ultimate Strength Results	90
5.2.1 An Assumption Regarding Stirrup Contribution.....	92
5.2.2 Normalisation With Respect to Concrete Strength.....	94
5.3 Failure Mechanisms Exhibited by Stage 1 Specimens.....	95
5.3.1 The Beam Shear Mechanism.....	95
5.3.2 The Punching Shear Mechanism.....	97
5.4 Effect of the Flange Proportions on the Concrete Contribution of Stage 1 Specimens	99
5.4.1 Variation of Normalised Concrete Contribution With the Width Ratio for Series 1 Specimens ($d_r=0.33$).....	99
5.4.2 Variation of Normalised Concrete Contribution With the Width Ratio for Series 2 Specimens ($d_r=0.25$).....	100

5.4.3	Variation of Normalised Concrete Contribution With the Width Ratio for Series 3 Specimens ($d_r=0.17$).....	101
5.4.4	Variation of the Normalised Concrete Contribution With the Depth Ratio	104
5.5	The Effect of Lateral Reinforcing Bars on the Ultimate Shear Strength.....	105
5.5.1	Effect of Lateral Reinforcing on Series 3 Ultimate Strength Results.....	105
5.5.2	Anomalies in Series 1 and Series 2 Results.....	105
5.6	Conclusions from Stage 1 Experimental Work.....	106
CHAPTER 6 VALIDATION OF THE EXPERIMENTAL ANALYSIS METHOD.....		108
6.1	Introduction.....	108
6.2	Outline of Validation Procedure.....	109
6.3	Specimen Details.....	110
6.3.1	Specimen Geometry and Loading.....	110
6.3.2	Specimen Instrumentation.....	111
6.4	Analytical Considerations for Data Analysis.....	113
6.4.1	Extrapolation of Strains.....	113
6.4.2	Calculation of Concrete Stresses From Strains.....	113
6.4.3	Calculation of Resultant Forces From Stress Distribution.....	114
6.4.4	Calculation of Sectional Actions.....	116
6.5	Results From the Experiments.....	117
6.5.1	Ultimate Load.....	118
6.5.2	Results From Strain Gauges.....	118
6.6	Results of Calculations Using Prescribed Analytical Procedure.....	119
6.6.1	Results From the Calculation of Axial Forces.....	121
6.6.2	Results From the Calculation of Sectional Bending Moments.....	124
6.6.3	Results From the Calculation of Shear Force.....	125
6.7	Discussion of Experimental Results.....	127
6.8	Conclusions From Validation Experiments.....	128
CHAPTER 7 THE CONTRIBUTION OF THE FLANGE TO THE ULTIMATE SHEAR STRENGTH OF A POINT LOADED RC T-BEAM.....		130
7.1	Introduction.....	130
7.2	Specimen B16 Analysis.....	131
7.2.1	Ultimate Strength and Failure Mechanism.....	132
7.2.2	Range of Calculation of Shear Forces.....	134
7.2.3	Results of the Calculation of Shear Lag Forces.....	134
7.2.4	Results of the Calculation of Interface Shear Forces.....	136
7.2.5	Flange Effectiveness of Specimen B16.....	139
7.3	Specimen B17 Analysis.....	143
7.3.1	Ultimate Strength and Failure Mechanism.....	143
7.3.2	Range of Calculation of Shear Forces.....	145
7.3.3	Results of the Calculation of Shear Lag Forces.....	146
7.3.4	Results of the Calculation of Interface Shear Forces.....	148
7.3.5	Results of the Calculation of Sectional Shear Forces.....	149
7.3.6	Flange Effectiveness of Specimen B17.....	152
7.4	A Further Examination of Stage 1 Failure Mechanisms.....	154
7.5	Conclusions.....	157

CHAPTER 8 RESULTS OF THE FINITE ELEMENT STUDY	159
8.1 Introduction	159
8.2 Stage I – The Parametric Study	160
8.2.1 Material Model Study	160
8.2.2 Load Step Size Study	169
8.3 Stage II – The Specimen Study.....	170
8.3.1 Ultimate Strength	170
8.3.2 Load Deflection Response	171
8.3.3 Crack Patterns	173
8.3.4 Reinforcing Strains	179
8.3.5 Specimens B12 and B13	180
8.3.6 Failure Mechanisms as Predicted by NLFEA	181
8.3.7 Prediction of Longitudinal Flange Strains.....	184
8.3.8 Estimation of the Flange Contribution to Shear Resistance	194
8.3.9 Discussion of the Results of Stage II NLFEA.....	195
8.4 Stage III - Flange Geometry Study	196
8.4.1 Ultimate Strength	197
8.4.2 Load Deflection Response	198
8.4.3 Discussion of Results	202
8.5 Conclusions From the Finite Element Study	202
CHAPTER 9 CONCLUSIONS AND RECOMMENDATIONS	205
9.1 Overview of the Research Undertaken	205
9.2 Conclusions From This Research	206
9.3 Suggestions for Future Work	208
REFERENCES	210
APPENDIX A COMPRESSION SOFTENING DUE TO PERPENDICULAR STRAINS IN SPECIMEN B16 AND B17	A-1
APPENDIX B LONGITUDINAL FLANGE STRAINS, REDISTRIBUTIONS AND THE FAILURE OF SPECIMEN B16.....	B-1
APPENDIX C LONGITUDINAL FLANGE STRAINS, REDISTRIBUTIONS AND THE FAILURE OF SPECIMEN B17.....	C-1
APPENDIX D RESULTS OF CHECKS ON THE CALCULATION OF INDIVIDUAL BLOCK SHEARS	D-1
APPENDIX E LOAD VS. DEFLECTION PREDICTIONS FROM NLFEA FOR THE EXPERIMENTAL SPECIMENS.....	E-1
APPENDIX F EXAMPLE CALCULATION OF THE FLANGE CONTRIBUTION.....	F-1
APPENDIX G PUBLICATIONS ARISING FROM THIS RESEARCH.....	G-1

LIST OF FIGURES

Figure 1.3-1 Schematic of experimental set up to examine overall affect of variation of flange area on ultimate shear strength of a T-beam	5
Figure 1.3-2 Instrumentation for the calculation of the magnitude of shear force in the flange of a T-beam	6
Figure 1.3-3 Output of crack distribution obtained from NLFEA.....	8
Figure 2.2-1 Four contributions to shear resistance	10
Figure 2.3-1 Variation of shear strength with flange width from Placas and Regan (1971)	15
Figure 2.3-2 Illustration of loading ledge used by Fok (1972).....	16
Figure 2.3-3 Results from Chong (1980) for RC T-beams without shear reinforcing	18
Figure 2.3-4 Variation of shear strength with flange width in Taplin & Al-Mahaidi (2000)	19
Figure 2.3-5 Inclined plane considered in formulation of theory of Placas and Regan (1972)	21
Figure 2.3-6 T-beam failure mechanism assumed by Hoang (1997)	22
Figure 2.3-7 Hoang (1997) assumptions of compressive strain distribution throughout width of flange.....	23
Figure 2.4-1 Plane stress state by tests for constitutive relations in the MCFT.....	26
Figure 2.4-2 Illustration of the concept of the compressive force path	27
Figure 3.2-1 Elevation of reference rectangular beam.....	36
Figure 3.2-2 Cross section of reference rectangular beam	36
Figure 3.2-3 Cross section of specimen B8 showing flange reinforcement details for Series 2 beams	39

Figure 3.2-4 Plan of specimen B12 showing typical arrangement of flange reinforcing for Series 3 beams.....	39
Figure 3.2-5 Load and support arrangement for specimens	40
Figure 3.2-6 Schematic of second end test.....	41
Figure 3.2-7 Strain gauging arrangement for Series 1 and 2 beams.....	43
Figure 3.3-1 A shear critical T-beam	45
Figure 3.3-2 Shear critical region of T-beam showing approximate size of disturbed region and region considered for calculations.....	45
Figure 3.3-3 Region under consideration.....	46
Figure 3.3-4 Discretisation of block of T-beam showing forces acting along the length of the span on component regions.....	46
Figure 3.3-5 Stresses on an arbitrary body in the cartesian coordinate system	47
Figure 3.3-6 Stress distribution on arbitrary flange block after application of assumptions	48
Figure 3.3-7 Detail of flange block α_2 showing all forces that cause moment about the z-axis.....	49
Figure 3.3-8 Elevation of flange block α_2	49
Figure 3.3-9 Arbitrary stress strain and force distribution on a flange block	53
Figure 3.3-10 Discretisation of flange throughout the width only	56
Figure 3.3-11 Cross section of specimens used in Stage 2 of the experimental work	57
Figure 3.3-12 Schematic layout of longitudinal gauges.....	60
Figure 3.3-13 Schematic of lateral gauging system used for stage 2 experimental work.	62
Figure 3.3-14 Location of embedded instrumentation with reference to load and support	63
Figure 3.3-15 Photo of embedded gauge system showing longitudinal and lateral gauges	63
Figure 3.3-16 Photo of specimen B19 showing top surface gauges.....	64
Figure 3.3-17 Close up photo of top surface strain gauging system on specimen B19 ..	64

Figure 4.3-1	Elevation of dimensions used in the FE model.....	68
Figure 4.3-2	Modelling of the T-beam cross-section	68
Figure 4.3-3	Details of the finite element mesh	72
Figure 4.4-1	Linear tension softening response	78
Figure 4.4-2	Illustration of the nonlinear tension softening curve	79
Figure 4.6-1	Schematic of the levels used in the parametric study	83
Figure 5.2-1	Mechanisms of resistance of shear by an RC beam with shear reinforcing	92
Figure 5.2-2	Typical stirrup strain vs. applied load for a stirrup which was intersected by a crack.....	93
Figure 5.3-1	Typical beam shear crack patterns exhibited by Specimen B4.....	96
Figure 5.3-2	Beam shear failure mechanism cracks exhibited by Specimen B11	96
Figure 5.3-3	Typical punching shear cracks on the underside of the flange of specimen B15	97
Figure 5.3-4	Typical crack pattern for punching shear mechanism on the top of the flange of specimen B12	98
Figure 5.4-1	Normalised concrete contribution vs. width ratio for series 1 specimens	100
Figure 5.4-2	Normalised concrete contribution vs. width ratio for series 2 specimens	101
Figure 5.4-3	Normalised concrete contribution vs. width ratio for series 3 specimens	102
Figure 5.4-4	Comparison of average concrete contribution for series 3 with 1 and 2 stirrups considered effective for Specimens B12 and B14.....	102
Figure 5.4-5	Ultimate strength vs. width ratio for series 3 specimens	103
Figure 5.4-6	Average normalised concrete contribution comparison.....	104
Figure 6.3-1	Plan of specimens S1 and S2.....	111
Figure 6.3-2	Elevation of specimen geometry and loading.....	111
Figure 6.3-3	Plan of surface gauging arrangement	112
Figure 6.3-4	Elevation of strain gauging arrangement.....	112
Figure 6.4-1	Profiles assumed for calculation of sectional forces.....	115

Figure 6.4-2	Free body of region enclosed by strain gauges.....	117
Figure 6.5-1	Average concrete strains produced at the three layers of gauging on section 1 of Slab S1.....	119
Figure 6.6-1	Variation of strain distribution of section 1 on Slab S1 throughout loading history.....	120
Figure 6.6-2	Slab 1 axial forces on section 1.....	123
Figure 6.6-3	Slab 1 axial forces on section 2.....	123
Figure 6.6-4	Slab 2 axial forces on section 1.....	123
Figure 6.6-5	Slab 2 axial forces on section 2.....	123
Figure 6.6-6	Slab 1 bending moments on section 1.....	126
Figure 6.6-7	Slab 1 bending moments on section 2.....	126
Figure 6.6-8	Slab 2 bending moments on section 1.....	126
Figure 6.6-9	Slab 2 bending moments on section 2.....	126
Figure 6.6-10	Shear force on slab 1 from equilibrium and sectional analysis.....	127
Figure 6.6-11	Shear force on slab 2 from equilibrium and sectional analysis.....	127
Figure 7.1-1	Identification of Section A and Section B.....	131
Figure 7.1-2	Notation used for location of flange blocks.....	131
Figure 7.2-1	Photo of B16 failure mechanism.....	132
Figure 7.2-2	Specimen B16 Load Deflection Curve.....	133
Figure 7.2-3	Shear lag distribution at 20kN load increments for specimen B16.....	135
Figure 7.2-4	Variation of Shear Lag with Applied Load calculated for Specimen B16.....	136
Figure 7.2-5	Distribution of interface shear throughout the width of the flange at 20kN intervals for specimen B16.....	137
Figure 7.2-6	Variation in interface shear with applied load as calculated for specimen B16.....	138
Figure 7.2-7	Distribution of sectional shear throughout the width of the flange as calculated for specimen B16.....	139

Figure 7.2-8	Variation of percentage of total sectional shear in flanges for specimen B16	140
Figure 7.2-9	Variation of shear in each layer at 20kN intervals for specimen B16.....	140
Figure 7.3-1	Specimen B17 failure mechanism	144
Figure 7.3-2	Specimen B17 load deflection curve.....	144
Figure 7.3-3	Shear lag distribution at 20kN increments for specimen B17.....	147
Figure 7.3-4	Variations of shear lag with applied load for specimen B17	147
Figure 7.3-5	Distribution of interface shear throughout the width of the flange at 20kN intervals for specimen B17	150
Figure 7.3-6	Variation of interface shear with applied load at rows	150
Figure 7.3-7	Distribution of sectional shear throughout the width of the flange as calculated for specimen B17.....	151
Figure 7.3-8	Variation of percentage of total sectional shear in flanges for specimen B16	152
Figure 7.3-9	Variation of shear in each layer at 20kN intervals for specimen B17.....	152
Figure 7.4-1	Cracks on specimens B1 (punching shear failure mechanism) at failure.	155
Figure 7.4-2	Cracks on specimen B5 at failure (beam shear mechanism).....	155
Figure 7.4-3	Cracks on specimen B3 at failure (beam shear failure)	156
Figure 8.2-1	Comparison of load deflection plot for varying values of β and varying constitutive model combinations for Specimen B2.....	162
Figure 8.2-2	Comparison of load deflection plot for varying values of β and varying constitutive model combinations for Specimen B5.....	163
Figure 8.2-3	Crack pattern obtained for B2 using $\beta=0.1$: TSM-L.....	168
Figure 8.2-4	Crack pattern obtained for B5 using $\beta=0.1$: TSM-L.....	168
Figure 8.2-5	Comparison of load displacement plots for different increments of displacement	169
Figure 8.3-1	Comparison of two load-deflection curves for series 2 specimens.....	171
Figure 8.3-2	Comparison of two load-deflection curves for series 3 specimens.....	172

Figure 8.3-3 Comparison of load-deflection behaviour obtained from NLFEA for series 1 specimen.....	173
Figure 8.3-4 Comparison of predicted crack strains and exhibited on specimen B2 during experiment.....	176
Figure 8.3-5 Comparison of predicted crack strains and exhibited on specimen B5 during experiment.....	177
Figure 8.3-6 Comparison of predicted crack strains and exhibited on specimen B12 during experiment	178
Figure 8.3-7 Notation used for comparison of strain gauge results.....	179
Figure 8.3-8 Load - deflection curves for specimens B12 and B13	181
Figure 8.3-9 Failure mechanism predicted for specimen B13.....	183
Figure 8.3-10 Notation used for description of gauge location.....	185
Figure 8.3-11 Comparison of longitudinal strains in specimen B16 section A	186
Figure 8.3-12 Comparison of longitudinal strains in specimen B16 section.....	188
Figure 8.3-13 Comparison of longitudinal strains at section A in specimen B17 at locations in the flange	190
Figure 8.3-14 Comparison of longitudinal strains at section B in specimen B17 at locations in the flange	192
Figure 8.4-1 Variations in the ultimate strength with width ratio predicted by NLFEA for Stage III NLFEA	199
Figure 8.4-2 Load deflection curves for all specimens in series 1 of the Flange Geometry Study	199
Figure 8.4-3 Load deflection curves for all specimens in series 2 of the Flange Geometry Study.....	200
Figure 8.4-4 Load deflection curves for all specimens in series 3 of the Flange Geometry Study	201

LIST OF TABLES

Table 3.2-1	Series 1-3 Beam Tags and Flange Proportions.....	37
Table 3.2-2	Material properties for each series	42
Table 4.7-1	Specimen numbers and material properties for stage 2 numerical modelling	87
Table 4.7-2	Specimen numbers and material properties for stage 3 numerical modelling	88
Table 5.2-1	Ultimate shear strengths recorded for Stage 1 experimental work.....	91
Table 5.2-2	Total force carried by stirrups in each specimen series for stage 1 experiments.	94
Table 6.5-1.	Ultimate loads and failure mechanisms of specimens.....	118
Table 8.2-1	B2 peak load comparison ($P_E= 181.0\text{kN}$).....	165
Table 8.2-2	B5 peak load comparison ($P_E= 159\text{kN}$).....	166
Table 8.3-1	Comparison of peak loads obtained from experimental work and NFLEA.....	172
Table 8.3-2	Comparison of stirrups strains at the peak load (Positive strains are tension)...	180
Table 8.3-3	Comparison of flexural reinforcing strains at the peak load.....	182
Table 8.3-4	Comparison of failure mechanisms from experimental and NLFEA work	184
Table 8.4-1	Comparison of peak loads produced from the flange geometry study	198

LIST OF SYMBOLS

a_v	Shear span
b_f	Width of flange of T-beam
b_r	Ratio of flange width to web width ($= b_f / b_w$)
b_w	Width of web of T-beam
$C_{A\alpha j}$	Compression force acting on section A of block j in layer α
D	Total beam depth ($= d_f + b_f$)
d_f	Total depth of flange of T-beam
d_o	Effective depth of a beam for shear. Distance from top of beam to centroid of bottom layer of reinforcement (depth of shear resistance region in web)
d_r	Ratio of flange depth to total beam depth ($= d_f / d_o$)
d_w	Total depth of web of T-beam
E_c	Youngs modulus for concrete
f_c	Ultimate cylinder strength of concrete
f_{cr}	Cracking stress
f_{c1}	Principal tensile stress
f_{c2}	Principal compressive stress
$f_{u,l}$	Ultimate strength of longitudinal reinforcing
$f_{u,v}$	Ultimate strength of shear reinforcing
$f_{y,l}$	Yield strength of longitudinal reinforcing
$f_{y,v}$	Yield strength of shear reinforcing
G	Shear modulus
G_f	Fracture energy
h	Crack bandwidth
I_1	First invariant of stress
J_2	Second invariant of the deviatoric stress
J_3	Third invariant of the deviatoric stress
$L_{C\alpha j}$	Lever arm of compression force acting on section A of block j in layer α

P_u	Peak load carried by a specimen
P_{NLFEA}	Peak load estimated by NLFEA
P_E	Peak load carried by a specimen during experiment
V_a	Contribution from aggregate interlock across a crack in a beam toward the ultimate shear strength
V_c	Contribution from the concrete in the compression region of a beam toward the ultimate shear strength
V_d	Contribution from resistance of a flexural reinforcing bar in a beam toward the ultimate shear strength
V_s	Contribution from the stirrups of a beam toward the ultimate shear strength
V_u	Shear acting on the critical section at the peak load of a shear critical beam
$V_{s\alpha j}$	Shear lag on flange block j in layer α
V_{ij}	Interface Shear lag on flange block j
$V_{\alpha j}$	Sectional shear on block j in layer α
β	Shear retention factor
ϵ_1	Principal tensile strain
ϵ_2	Principal compressive strain
ϵ_{cr}	Cracking strain
ϵ_o	Strain at peak compressive stress
ϵ_u	Ultimate strain
γ	Equivalent stress block factor
ϕ	Friction angle
ψ	Dilatancy angle
χ	Cohesion
ϵ^p	Plastic strain
ϵ^c	Crack strain
ϵ_{lat}	Lateral or perpendicular tensile strain
σ^c	Crack stress
σ_c	Compression stress
σ_x	Normal stress in the x -direction
τ_{xy}	Shearing stress on the xy plane
κ	Hardening parameter
ν	Poissons ratio

Chapter 1 INTRODUCTION

1.1 Introduction

Reinforced concrete has had a rapid elevation over the past 140 Years. Hsu (1998) outlines that this material was first patented in 1867 by Joseph Monier. Since this date, the practical simplicity of construction using this material, and the low cost in production has lead to this material being rivalled by only structural steel in its prevalence in construction in Australia, and the world.

The challenge that has faced researchers and engineers since its discovery has been to try and quantify its behaviour in a sufficient manner to facilitate its use in construction. This has historically followed along the lines of adapting the well understood fundamentals of solid mechanics, and to some extent, linear elastic models. It has been only recently that the mathematical fundamentals of solid mechanics developed by Navier have been able to be investigated with the development of computer hardware, and accompanying algorithms capable of solution of these indeterminate relations. Even though these algorithms are capable of solving these equations for some materials, it is the challenges associated with material nonlinearities, heterogeneous materials and fracture that are now posing a challenge to researchers in the determination of suitable methods of modelling the behaviour of a reinforced concrete solid.

Regardless of the lack of a unified method of predicting strength of reinforced concrete solids and structures, engineers have nonetheless been able to produce some remarkable structures with this material. These structures range from the tallest buildings in the world, The Petronas Twin Towers in Kuala Lumpur, to the newly constructed Bolte Bridge in Melbourne. These structures have been possible through the tireless efforts of researchers and

engineers over the past 100 years to develop relations based on the phenomenological observations of overall behaviour of structural elements formed with reinforced concrete. The relations that are developed have improved over time with the development of more precise experimental equipment, data acquisition systems that increase in capacity, and the general improvement in the understanding of the material that is developed over time.

What is becoming a great concern with the existing, old reinforced concrete structures can be summarised with the following questions; How safe is a reinforced concrete structure that was constructed nearly a century ago, when the understanding of the behaviour of reinforced concrete was very basic? Furthermore, what happens to this structure if it is subjected to loads that increase over time?

There are many instances that exist where this is a significant issue, this discussion will focus only on one particular type of structure. Al-Mahaidi and Taplin (1998) have identified a large number of reinforced concrete bridge structures that comprise of girders with a T-shaped cross section (T-beams) on the rural roads in Victoria, Australia, that were built prior to 1950, one of these was built in 1905. Their research demonstrated that within this period, the allowable loading on these roads increased from 15.24 tonne, to a truck of weight 160 tonnes as required by the Australia Bridge Design Code (Austroads (1999)). Rudimentary analysis of the deck of these structures in accordance with the Australian Concrete Code of practice (AS3600 (2001)) quite often yields that these structures are deficient. These structures are deficient in both shear and flexure.

Assessment of the shear strength of a bridge deck as prescribed in this code of practice (and by all others concrete codes of practice) is undertaken by estimation of the shear force that acts on one girder on the span, and then calculation of the shear capacity of this girder by assuming a rectangular cross section. This approach is a great simplification in behaviour of the deck of the structure in shear, as it does not allow for the contribution of the deck to be considered. Darwish et al. (2000) recently acknowledged this and commented that many concrete structures comprise of beams that are cast monolithically with a slab element, therefore forming a T-shaped cross section for the purpose of analysis.

Theoretical evaluation of the shear strength of a rectangular RC beam that forms this type of structure using any of the codes around the world is predicted using an analytical developed by Ritter (1899) and Morsch (1906). The research using this model over the last century has been mostly focussed on the determination of empirical relations that describe the effect of the variables of material properties and geometry on the shear strength. Since the application of finite element analysis to reinforced concrete structures was first undertaken in 1969, a huge research effort has been applied to this field, in particular the determination of constitutive relations that will allow the accurate implementation of this solutions scheme.

It is apparent that there is insufficient understanding of the influence of the flange of an RC T-beam on the shear strength of an RC T-beam. The research presented in this thesis examines the effect of the flange dimensions on the shear strength of a web reinforced RC T-beam, and the contribution of the flange to the resistance of shear by experimental determination of the shear force that is resisted by the flange. In addition to this, the ability of NLFEA to predict the shear strength, and flange contribution is also examined.

1.2 Aims of the Research

The primary aim of this investigation is to determine the effect of changing the dimensions of the flange (in the compression zone) of a reinforced concrete T-beam on the shear strength of the specimen. To achieve this overall aim, the research was broken into two components; an experimental component, and a component of numerical analysis.

The experimental component had the following aims,

1. Determine experimentally if the change in flange proportions of a series of specimens with identical web and reinforcing arrangement produces a corresponding change in the shear strength.
2. Develop and implement an experimental technique capable of calculating the amount of shear force that is present in the flange of a T-beam. This allowed

quantification of the contribution of the flange to the resistance of an applied shear to an RC T-beam specimen.

The numerical analysis component had the following aims.

1. Determine the performance of common concrete constitutive models in the prediction of shear strength. This allowed selection of the most suitable model to perform numerical simulations on series of T-beams.
2. Determine the capability of the selected combination of constitutive models to capture the significant results of the experimental work. These were deemed to be prediction of peak load, load-deflection behaviour, crack patterns, and strains (both concrete and reinforcing).
3. Apply the solution scheme to a series of specimens that did not have any variations in material properties. The material property variations in the above series of analysis were introduced as a result of the requirement to break the specimens into four series for the purpose of testing.

1.3 Outline of the Thesis

The general structure of this thesis is as follows.

- A survey of previous experimental and analytical work that is related to this research.
- The methods adopted in this thesis
 - Methods of experimental work
 - Methods of finite element (numerical) analysis.
- The results of the work presented in this thesis
 - Results from the experimental work
 - Results from finite element analysis

- A series of conclusions and recommendations that have arisen from this work.

The experimental work was divided into two stages, and the numerical analysis was divided into three stages. These are summarised below.

1.3.1 *Experimental Work*

The methods and results of the experimental work are presented into two sections. An outline of these two stages is presented below.

1.3.1.1 Stage 1 Experimental Work

Stage one of the experimental work examined the variation on the shear strength of three individual series of specimens of RC T-beams produced by varying the dimensions of the flange. Within each series, the flange depth remained constant, and the flange width varied. There was also a variation in the flange depth between each series to investigate this aspect of changing the area of concrete above the neutral axis. Figure 1.3-1 below shows schematically the test setup used in this work.

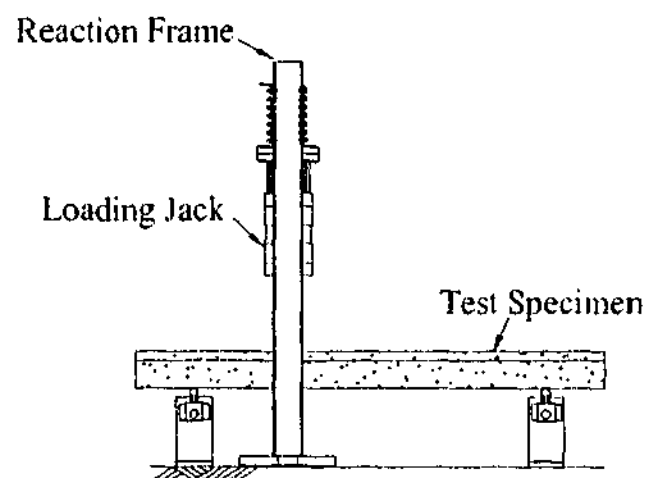


Figure 1.3-1 Schematic of experimental set up to examine overall affect of variation of flange area on ultimate shear strength of a T-beam

The method used in implementing stage one is outlined in Chapter 3, and the results that were obtained for the variation in the shear strength are discussed in Chapter 5.

1.3.1.2 Stage 2 Experimental Work

The second stage of the experimental work developed and implemented an instrumentation technique capable of calculating the magnitude of shear force that was carried in the flange of a T-beam. The implementation was limited to two specimens owing to the large cost of instrumentation. A photograph illustrating the instrumentation used in the technique is shown below in Figure 1.3-2. The experimental method in the implementation of this method, including a summary of the analytical component is outlined in Chapter 3, and the results of the implementation are outlined in Chapter 7. In an effort to determine the suitability of this method to calculate sectional shearing forces, trial experiments were undertaken. These are discussed in Chapter 6, as well as the validity of the technique.

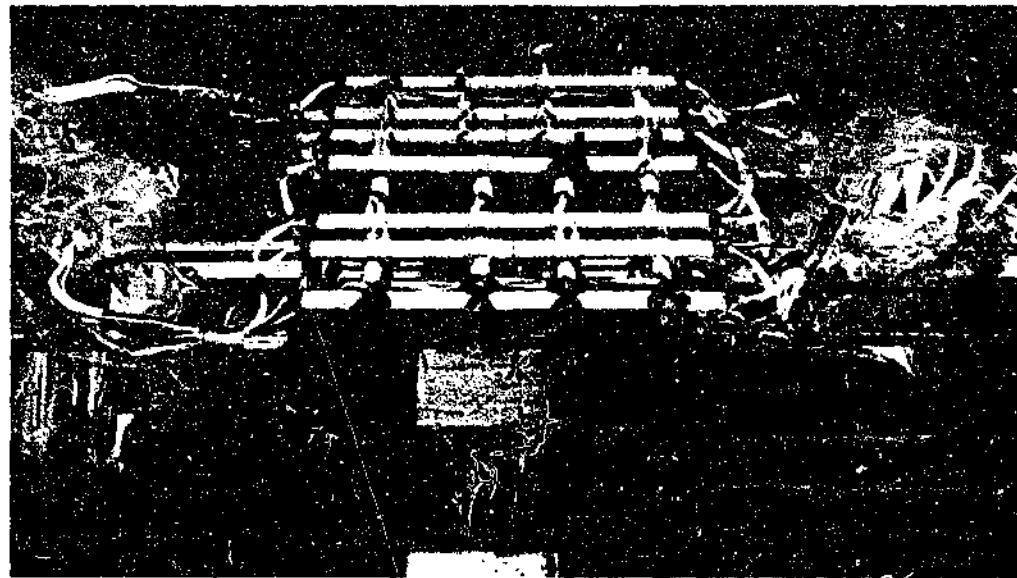


Figure 1.3-2 Instrumentation for the calculation of the magnitude of shear force in the flange of a T-beam

1.3.2 *Finite Elements Analysis*

The finite element analysis work is presented into two sections in this thesis. An outline of these two stages is presented below.

1.3.2.1 Stage 1 Numerical Analysis

The capability of NFLEA to reproduce results of the experimental work was examined in this work and is presented as stage 1 numerical analysis.

Finite element analysis of reinforced concrete structures is sensitive to many parameters, most of all constitutive models selected, displacement increment applied to the solution scheme and the mesh density. The work presented below uses results of previous analysis reported in literature to select a fixed mesh density and uses this to examine the effect of constitutive models of the concrete and displacement increment. The optimal combination of constitutive models and displacement increments are used consistently throughout the following two stages of work.

1.3.2.2 Stage 2 Numerical Analysis

Having selected the optimal combination of constitutive models to describe the behaviour of the concrete, the most time efficient displacement increment, based on the fixed mesh density, the procedure was applied to experimental specimens to determine the capability of the procedure to replicate the peak load recorded in the experiments.

Several parameters were used for comparison, these included peak loads, load deflection response, reinforcing strains, and crack patterns (an example of the finite element output of crack patterns can be seen in Figure 1.3-3), and consequently failure mechanisms.

1.3.2.3 Stage 3 Numerical Analysis

The limitation of laboratory space required four separate castings of specimens, which resulted in some significant variations in material properties throughout the work. This final stage of the finite element analysis presented in this thesis is a numerical investigation into the effect on the ultimate strength and failure mechanisms of this type of specimen with all other variables (including material properties) being constant.

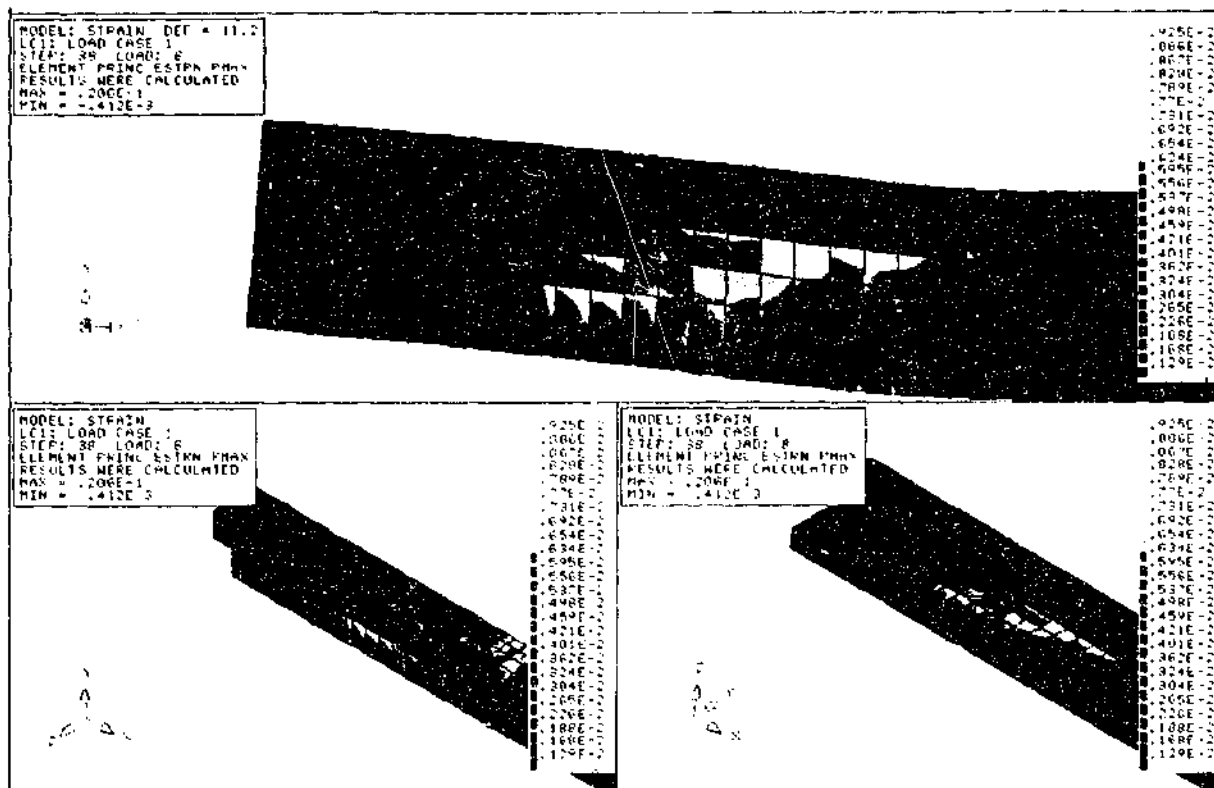


Figure 1.3-3 Output of crack distribution obtained from NLFEA

Chapter 2 LITERATURE REVIEW

2.1 Introduction

This chapter is intended to give the reader a description of the previous research into the shear strength of RC T-beams. As outlined in Chapter 1, the particular focus of this research is the contribution of the flanges to the shear strength of an RC T-beam; therefore significant attention is given to previous investigations that have included this effect. Experimental investigations that have been undertaken as well as formulation of strength prediction equations are discussed.

There are some general theories of the prediction of shear capacity that have been formulated that are capable of predicting some influence on the shear strength that arise with variations in the flange geometry. The basis of these methods is discussed in this section, and the ability that these methods have for the prediction of shear strength of this type of structural element is discussed. These theories are seen as indicative of the general approach that is being followed in shear theory in the current state of the art methods of analysis. This approach is examined to determine the validity of extrapolating beam theory concepts to this type of structural element that no longer has the general cross section upon which much of the shear theory has been established.

2.2 The Mechanisms of Shear Resistance

This discussion defines the four components of shear resistance that are commonly accepted amongst researchers of reinforced concrete. This brief discussion is by no means intended to completely summarise the current knowledge of the shear resistance mechanism

but to define these individual contributions and the way they will be referred to for the remainder of this thesis.

Figure 2.2-1 illustrates the internal mechanisms of reinforced concrete outlined in Warner et al. (1993) that resist an applied shear. It is noted that this figure illustrates the mechanisms as they are after the formation of the diagonal tension crack in the web of an RC beam.

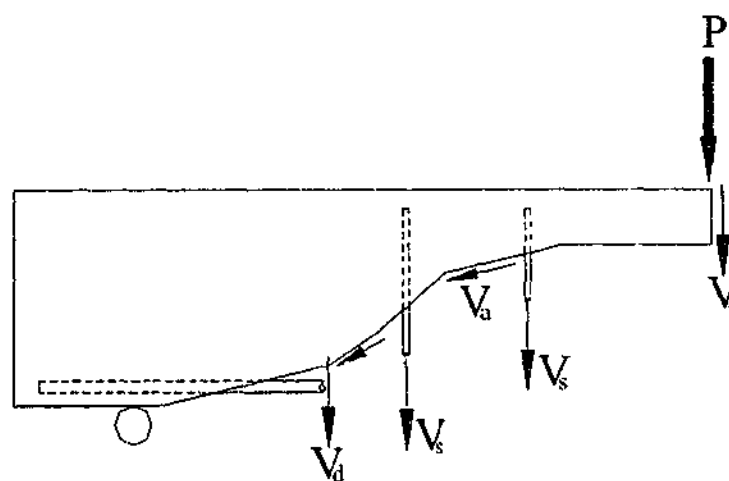


Figure 2.2-1 Four contributions to shear resistance

Idealisation of an RC beam subjected to shear is most generally approached by assuming that crack reinforced concrete behaves in a similar fashion to a truss. This has been the basis for all code methods of describing this behaviour, and also forms the basis for two of the most prominent theories for prediction of the shear strength that are in development. This idealisation was developed over 100 years ago by Ritter (1899) and Morsch (1906).

The concrete in compression has a capacity to resist shear and is considered to be part of the mechanism at failure of an RC beam. The contribution will be referred to as the concrete contribution and is denoted here as V_c . Tension forces that arise in the shear reinforcing assist in the resistance of shear. This contribution will be referred to as the stirrup contribution, and will be denoted V_s . It has been shown that there is relative movement of the two bodies of concrete that are bounded by the diagonal crack. With the interpenetration of

the aggregates between these two bodies, these relative movements will initiate frictional resistance on the surface of the crack. This contribution is known as the aggregate interlock contribution, and will be denoted here as V_a . As this relative movement becomes significant, a downward force is induced on the flexural reinforcing. A resistive force is induced through the dowel like action of the flexural reinforcing group. This will be referred to as dowel action, and will be denoted V_d .

Agreement is yet to be reached on the relative contributions of each of the above components of the resistance of an RC beam to shear, and has been the subject of much ongoing debate in literature. For example, Pang and Hsu (1996) present a mathematical proof based on a series of assumptions which precludes the concrete contribution from the shear resistance mechanism, whereas Kotsovos (1988) presented experimental evidence to suggest that aggregate interlock does not form part of the mechanism, and that the mechanism is simply the sum of the concrete and stirrup contributions. The Modified Compression Field Theory (MCFT) of calculating shear capacity (discussed in Section 2.4) neglects dowel action, and implicitly includes in its formulation the remaining three components.

2.3 Investigations Relating to the Shear Strength of T-Beams

Presented below is a discussion of the previous research that is relevant to this investigation. Some comparison is required between investigations, and to keep the results analysis consistent, the following is implemented: all ultimate strengths that are reported below are normalised with respect to the square root of the concrete strength, as well as the web area, i.e. $V_u/(bd\sqrt{f_c})$ is presented. The relative proportions of the web and flange affect the strength, so dimensionless parameters, $br (=b_f/b_w)$ and $dr (=d_f/d_o)$ will be used for discussion. The quantity d_o is the effective depth for shear taken by the Australia Standard AS3600 (2001); it is the distance from the compression surface of a beam to the centroid of the outermost layer of reinforcing.

2.3.1 *Experimental Investigations into the Shear Strength of T-beams*

Shear strength of T-beams has been the subject of some investigations in the past. Much of the early research such as that undertaken by Swamy (1969), Swamy and Qureshi (1971), and Al-Alusi (1957) has focussed on the behaviour of T-beams subject to variations in variables similar to those examined in rectangular beams. Other aspects of the behaviour of T-beams have been examined in literature, and a summary of the major variables, and the results that are relevant to this investigation are discussed below.

Swamy and Qureshi (1971) investigated the cracking and deformation behaviour that is exhibited by specimens with a T-shaped cross section as well as the ultimate load of this type of specimen. The variables of the investigation were the percentage of shear reinforcing, as well as aggregate size, and scaling. The authors made several conclusions from their experimental investigation, and many significant aspects of the scaling and the effect of scaling aggregates were made. Swamy (1969) discussed experimental work by Adepegba (1966). The focus of the discussion was the difference in post cracking behaviour of RC beam with and without shear reinforcing. T-beams were included in this discussion, but only for the purpose of validating the above comments. Al-Alusi (1957) tested 25 T-beams to determine the effect of varying the shear span on the shear strength of RC T-beams. Some were inverted and tested in negative bending, and some varied the percentage of compression reinforcing in the flange. None of these specimens that were tested in this investigation had shear reinforcing.

An investigation by Kotsovos et al. (1987) into the shear strength of RC T-beams without web reinforcing indicated that for a given a_v/d ratio for a beam subject to four point loading, a significant increase in ultimate shear strength (up to 200%) can be attained with the addition of a flange. It is noted that the loading on the flange surface is applied over the entire width of the flange, further discussion of this will be provided later. Kotsovos et al. (1987a) concluded that the shear resistance of a T-beam is at least in part provided by the flange of a T-beam and not simply the web. These authors noted that a common assumption in the consideration of shear resistance is that only the web provides the shearing capacity of a T-beam. In this paper it is noted that the shear strength of a T-beam is significantly higher than

that of a rectangular beam with similar web geometry. The considerable increase in shear strength is attributed to the triaxial stress state in the area adjacent to the load point. This triaxial stress is made up by the presence of the load, the longitudinal compressive forces induced by bending and the hypothesised confining action of the flange. The confining action may have resulted from the influence of the load point, as this was a line load over the entire width of the flange.

Seraj et al. (1992) carried out detailed three-dimensional nonlinear finite element analysis (NLFEA) of T-beams. The purpose of this research was to provide a finite element model capable of predicting the ultimate strength of T-beams constructed with both high and low strength concrete. Unfortunately, no comment on the affect of the triaxial stresses in the region of failure on the load capacity of a T-beam was made. This paper mainly focuses on the economical three-dimensional modelling of this type of structural element.

The response of T-beams in shear subjected to negative bending was the subject of an investigation undertaken by Rodrigues and Darwin (1987). The purpose of this investigation was to determine the contribution from both stirrups and concrete to shear resistance provided in negative moment by a T-beam. The results essentially illustrated that ACI 318 (1999) values for shear design in these regions were conservative, and that the stirrup contribution is in fact higher than that allowed for in this concrete code.

A more unique investigation was conducted by El-Niema (1988). This investigation was aimed at determining the effect of a haunch at a support on the shear strength of a beam. No specific attention was paid to the effect of the flange in the development of the theoretical model proposed in this paper. The main focus was to decipher the effect of additional depth at the support when considering a web crushing type shear failure.

The above examples of the investigations that have been carried out are not intended to summarise all experimental work on shear that has included T-beams. It shows that in most cases, the flange is not considered in the investigations, and the study of variables that affect the shear strength of T-beams is usually kept to those that are routinely studied for rectangular beams. In the above examples of previous research only that of Kotsovos et al. (1987a) shows

consideration of the contribution of the flange to the shear strength of an RC T-beam specimen. This investigation only gives a comment to the fact that the flange had made a significant contribution in the experiment that was reported, no detailed study of the effect of the dimensions was undertaken. In fact, only four significant investigations that isolate the variation of the geometric proportions of the flange as the sole variable in a series of experiments have been performed. These are discussed in the following section.

2.3.2 Experimental Investigations Including the Effect of Flange Proportions on the Shear Strength of RC T-beams

Placas and Regan (1971) undertook an analytical and experimental investigation into the shear strength of T-, I-, and rectangular shaped beams. This study formed a very exhaustive experimental study, and covered many variables including material properties, reinforcing percentages, and loading arrangements. While some specimens did not include shear reinforcing, the focus of the discussion in this paper, as well as this discussion, will be on T-beams with shear reinforcing. Within this study, ultimate strengths for four specimens can be used to investigate the effect of the variations of the flange dimensions on the shear strength of a series of specimens. These four specimens included a rectangular beam, and three T-shaped cross sections, each with an equal amount of reinforcing, shear span to effective depth ratio (a_v/d) of 5.4 (which corresponded to a central load), equal web width of 152 mm, and equal effective depth of 254mm. The three T-shaped cross sections varied in flange width, and included flange widths of $b_f=305\text{mm}$, 610mm , and 1067mm corresponding to $b_r=2.0$, 4.0 , and 7.0 . The flange depth remained constant for these T-shaped cross sections at 76mm. Small variations in the concrete strength were present in the results presented, but the aforementioned normalization procedure eliminates the effect of this variation on the ultimate strength. The loading arrangement was noted to be a point load; no reference was made to the size of the loading point. Apart from the small material variations, the only variable in the above specimens is the width of the flange.

Figure 2.3-1 presents the results of the normalized ultimate strength results against the width ratio obtained from this study. Klein and Popovic (1985) were the first to identify this trend from the results of the experimental work of Placas and Regan (1971). The specimen

with the largest width ratio of $br=7.0$ does not display a normalized shear strength higher substantially than that of the beam with a width ratio of $br=2.01$. The intermediate point, with $br=4.0$, has a higher ultimate shear strength than either of these. These results show a maximum increase in the normalized shear strength resulting from the variation in the width ratio of 26%; however, the trend of this increase is not clear in these results.

Fok (1972) also presents a study, which included an experimental study that was focused on the effect of all major variables on the shear strength of concrete beams. Like the study of Placas and Regan (1971), the effect of the flange proportions on the ultimate shear strength was isolated for only one portion of the study. These specimens had a constant total depth (240mm), effective depth (200mm), as well as a constant web width (100mm) and percentage of flexural reinforcing. Within this series of tests, there was a sub-series of tests that had a constant shear span to effective depth ratio. Each specimen was point loaded with a line across the width of the flange at the location of the point load. At the location on the flange where the load was applied, the web was widened locally; the width of this widening was almost equal to the width of the flange. This formed a "ledge" that was provided to each specimen in an effort to ensure a uniform distribution of load across the width of the flange. This is illustrated in Figure 2.3-2.

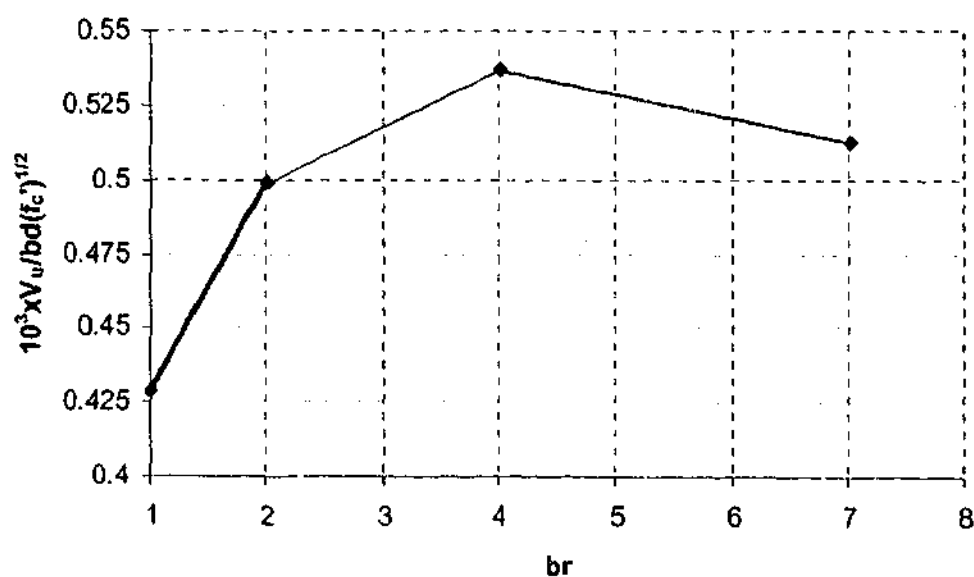


Figure 2.3-1 Variation of shear strength with flange width from Placas and Regan (1971)

For each constant shear span to effective depth ratio, information regarding the effect of the flange proportions on the shear strength was examined. For each shear span to depth ratio, three different flange depths of 40mm, 60mm, and 80mm were investigated, and for each different flange depth, a variation in flange widths was studied (the flange width was 300mm, 400mm, or 500mm, a rectangular beam was also studied for each shear span to depth ratio). Tests of each end of the specimens were undertaken to ensure that both shear spans failed. One end of each of these specimens was provided with shear reinforcing. The percentage of longitudinal tensile steel remained the same throughout the duration of this series of tests.

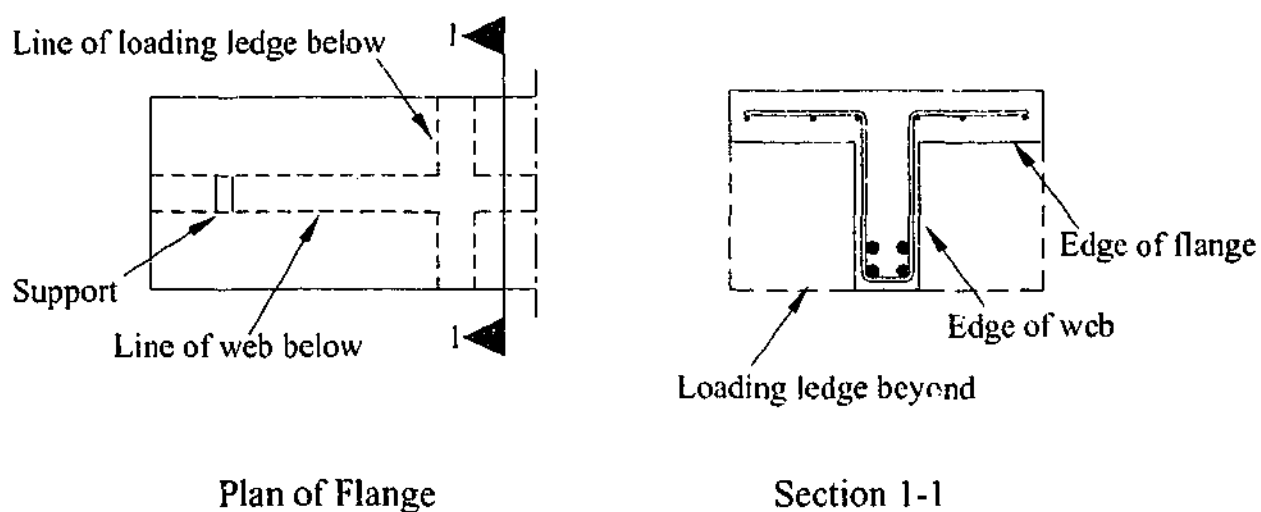


Figure 2.3-2 Illustration of loading ledge used by Fok (1972)

Based on the results of the above series of specimens, and other correlation of some results from other series, the author concluded that the variation of flange width did not affect the shear strength, but variations of the flange depth did have some affect. Close examination of the results of ultimate strength and failure mechanisms indicate that in most cases, the ends to which shear reinforcing were provided failed in flexure, and those without this reinforcing failed in shear. The former of the two points from this research regarding cross section geometry is in direct conflict with the results of Placas and Regan (1971).

Placas and Regan (1971) include in their formulation the fact that the failure of the compression region signifies the failure of a specimen in shear. In the study of Fok (1972),

the loading ledge illustrated in Figure 2.3-2 is positioned directly underneath the load point. This is a significant change to the cross section in this region. The alteration of the critical cross section to this extent is thought to render these results unrepresentative of the trends that may occur in a specimen that is not subject to such an extreme geometry change. It is noted that the above statement regarding to the effect of the flange width on the ultimate shear strength is only valid for the specimens tested without shear reinforcing as those with shear reinforcing generally failed in flexure, and therefore no true trend for the specimens with shear reinforcing could be deduced from these results.

Chong (1980) undertook an experimental investigation similar to that of Fok (1972) above. This study differed in that the applied loading to all specimens was a line load along the centreline of each specimen. As part of this series of beams, 10 beams were tested to investigate the variables of flange width and flange depth and their effect on the shear strength of reinforced concrete T-beams without shear reinforcing.

Three different flange depths ($d_f=40\text{mm}$, 60mm , and 80mm) were examined, and for each of these separate flange depths, three flange widths ($b_f=300\text{mm}$, 400mm , and 500mm) were tested. A rectangular beam with identical web properties to the T-beams was also tested.

All specimens tested in this investigation were reported to fail in shear. To determine the effect that the flange was having on the ultimate shear strength, the author normalized the results of ultimate shear stress (over the web area) with the cracking shear stress (again, over the web area). The results produced from this process indicate that any variation in flange proportions in a reinforced concrete T-beam without shear reinforcing produced no variation on the ultimate strength of that specimen.

To provide a consistent set of data for the varying arrangements of load that have been tested by Chong (1980), the process of normalizing the ultimate shear value with concrete strength and web dimensions (as described in Section 2.3) was applied to the results obtained in this study. This is shown in Figure 2.3-3. This normalization procedure shows that as a series of specimens is given an increasing flange width, the trend is upwards in the normalized

shear strength. Similarly, this process shows that for a series of specimens with an increasing flange depth, there is an increasing trend in the result of the normalized shear strength.

The above results directly contradict the statement made by Chong (1980) regarding the effect of the variations in flange proportions of the ultimate shear strength of a reinforced concrete T-beam without shear reinforcing. The analysis performed by the author normalizes the ultimate shear strength with the cracking shear strength, but not with the cylinder strength. The cracking shear strength has been shown to be highly variable in many publications including Vecchio and Collins (1986). It is suggested that variability in the results that is introduced by normalisation with respect to the cracking shear strength has hidden the trend of the increasing shear strength with flange proportions.

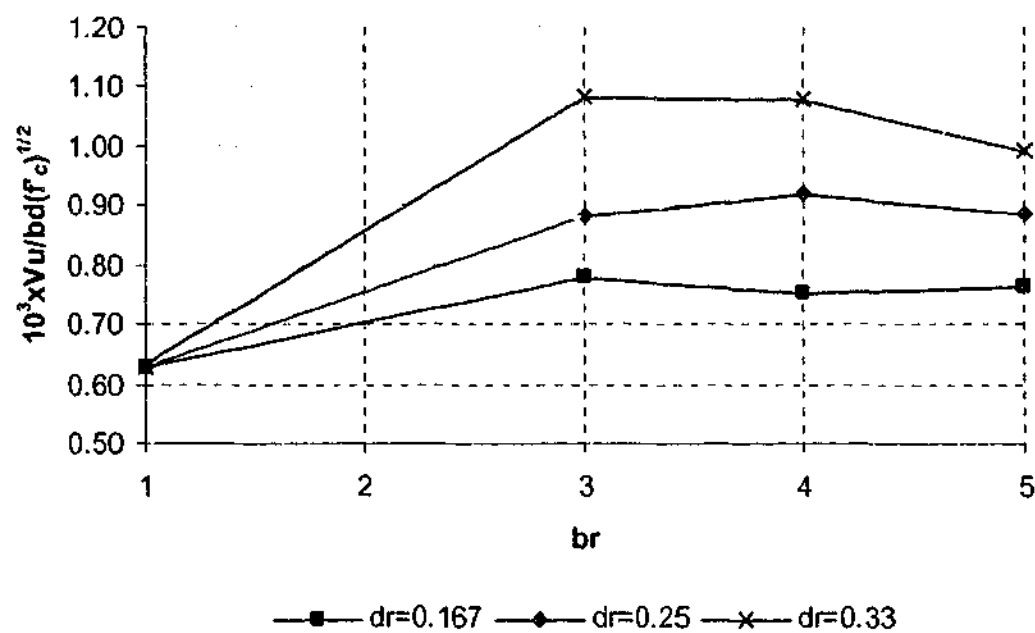


Figure 2.3-3 Results from Chong (1980) for RC T-beams without shear reinforcing

Taplin and Al-Mahaidi (2000) reported on an experimental investigation into the ultimate shear strength of T-beams. Five of the 21 beams tested as part of the investigation were tested solely to determine the variation in shear strength that arises from varying the flange width. No variation in the flange depth was used throughout this experimental investigation. These beams contained shear reinforcing, with a percentage equal to the minimum that is required by the Australian Standard AS3600 (2001). The web width of these

specimens was 140mm. The flange dimensions were scaled from typical dimensions of existing T-beam bridges in Victoria, Australia. The flange depth remained constant at 75mm (corresponding to $d_r=0.25$), the flange width varied from a rectangular beam to a flange width of 600mm. The value of the width ratio that this encompassed was $br=1.0, 1.61, 2.64, 3.46,$ and 4.29. Loading was applied to these specimens as a line load across the width of the flange at a constant shear span to depth ratio of 3.0. The effective depth of these specimens was 260mm; all reinforcing ratios were constant at 3.3% percent for flexural reinforcing, and 0.13% for shear reinforcing.

Figure 2.3-4 shows the variation in the normalized concrete strength with the variation in the width ratio br . Similar to the results presented for Placas and Regan (1971) and Chong (1980), the results shown in this figure indicate that the normalized shear strength increases with the flange width of a T-beam with all other material and geometric properties constant.

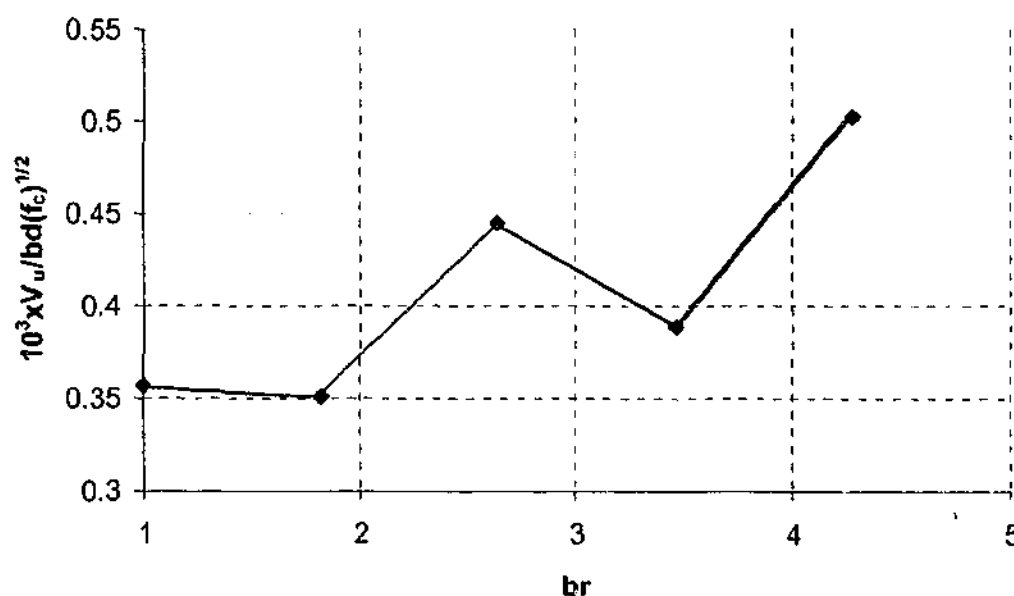


Figure 2.3-4 Variation of shear strength with flange width in Taplin & Ai-Mahaidi (2000)

This figure illustrates that the shear strength does increase with the width of the flange. The experimental point at a flange width of 485mm ($br=3.46$) does not appear to fit a trend as it produces a shear strength lower than that of the 310mm flange beam ($br=2.64$). The shear strengths for specimens with a 225mm wide flange ($br=1.61$) and the rectangular beam are the

same. It is noted at this stage that these results correspond only to one test point; repeatability was not tested as part of these experiments. Given the scatter in these results, the trend cannot be assumed to be definitive.

2.3.3 Analytical Investigations Including the Effect of Flange Proportions on the Shear Strength of RC T-beams

Given the scarcity of experimental data that isolates the effect of the flange width on the shear strength of an RC T-beam, it is no surprise that only two analytical investigations acknowledge this effect in their formulation.

Placas and Regan (1972) developed relationships to calculate shear capacity of RC beams based on failure mechanisms. To do this equilibrium conditions were established on the inclined surface of the shear crack as shown in Figure 2.3-5. Dowel action is neglected in this formulation based on results of a study undertaken by Baumann (1968), and aggregate interlock is ignored in this formulation based on crack inclinations from the experimental work showing flat cracks (hence little aggregate interlock) for T-beams. It was assumed for the purpose of the formulation that the concrete contribution was complete over the width of the flange, and that at failure, a 'shearing' failure of the compression concrete would occur. This assumption renders this formulation only applicable to specimens that exhibit this type of failure mechanism.

As the authors removed the dowel action and aggregate interlock component from consideration, the shear strength was taken as the sum of the stirrup and compression concrete contributions. The assumption that the failure of the compression concrete is shear facilitated the use of Coulomb relations for describing the failure surface of the concrete. The authors noted that the area of concrete available is a product of the depth to the neutral axis, and the effective width of the flange resisting the shear. In their application of the relations that were developed in this work, Placas and Regan (1972) had to determine an effective width of flange for the application of these relations to a given set of specimens. This was taken as 150mm greater than the width of the web (and is noted only to be relevant to the specimens which they considered). The detail of the formulation will not be given in this summary of the

formulation of the relationships, but the result of the above can be seen in Equation 2.3.1. This equation is in SI units.

$$V_c = 1.038 \left(\frac{100 A_s}{bd} \frac{Vd}{M} f'_c \right)^{1/2} bd \quad 2.3.1$$

These authors also considered the case of a T-beam where the neutral axis is located outside the flange. This results in a modification to the term describing the area of the compressive concrete.

A simplification of Equation 2.3.1 was introduced by the authors. They suggested that since cracks do not appear on the underside of the flange until near the failure load, then the longitudinal strain on the underside of the flange was small, so that the maximum shearing stress on the underside of the flange can be considered to be approximately equal to the tensile stresses on the soffit of the flange. Equation 2.3.2 introduces both this and the effective flange width in to the formulation for the concrete contribution term. This equation is written in SI units.

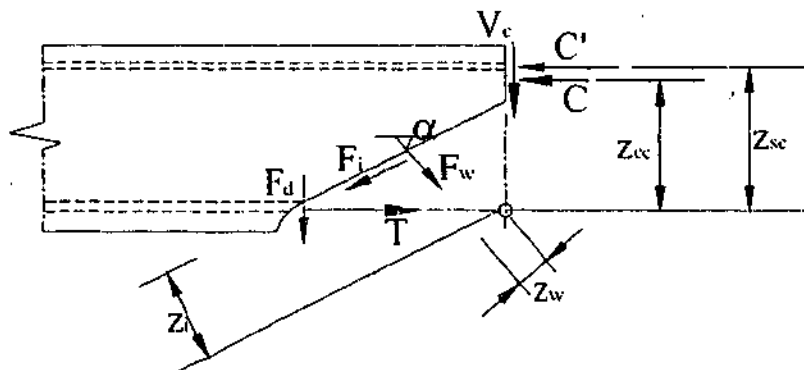


Figure 2.3-5 Inclined plane considered in formulation of theory of Placas and Regan (1972)

$$V_c = 0.906 (f'_c)^{1/3} d_f (b + 6) \quad 2.3.2$$

To calculate the shear capacity of a beam, these authors simply summed this concrete contribution to the stirrup contribution.

Hoang (1997) developed relationships for calculation of the shear strength of an RC T-beam without shear reinforcing based on plasticity relationships. The failure mechanism assumed to formulate the relations is illustrated in Figure 2.3-6 below. The failure mechanism considers points a and b are points of rotation. Then, if part III of this figure does not move, part II is assumed to rotate about b, and part I rotates about a at an angle which is equal and opposite to that at which part II rotates about b. The net movement is then vertical movement of part I relative to part III.

To include the contribution of 'Part II' from Figure 2.3-6 into the calculation of shear resistance, Hoang (1997) had to assume a width of flange that is effective in the resistance of shear. The formulation considered only point loaded T-beams, and the calculation of the effective flange width considered two cases of point loading the surface of a T-beam. These are line loading across the full width of the flange, and a point load that covers only the web region.

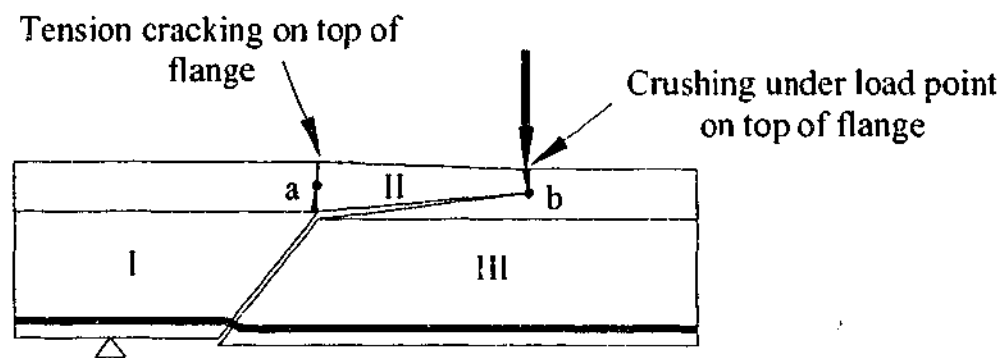


Figure 2.3-6 T-beam failure mechanism assumed by Hoang (1997)

Figure 2.3-7 shows part of a T-beam as seen on top of the flange, and demonstrates the assumptions used by Hoang (1997) in the calculation of the effective flange width for shear. Two load cases on the top surface of the flange are considered, namely, a point load across the width of the web, and a line load across the entire width of the flange. This shows the linear distribution of compressive stress throughout the top surface of the flange used in Hoang (1997) assumption. The author assumed that the compressive stresses propagate laterally

across the width of the flange at an angle corresponding to $\tan\alpha=1/2$. In the formulation, it was considered that the compressive stress distribution must be the width of the web at the intersection of the web crack and the flange crack direction below point a in Figure 2.3-6. These two conditions were used to produce the equivalent linear compressive stress distribution stress distribution as shown in Figure 2.3-7.

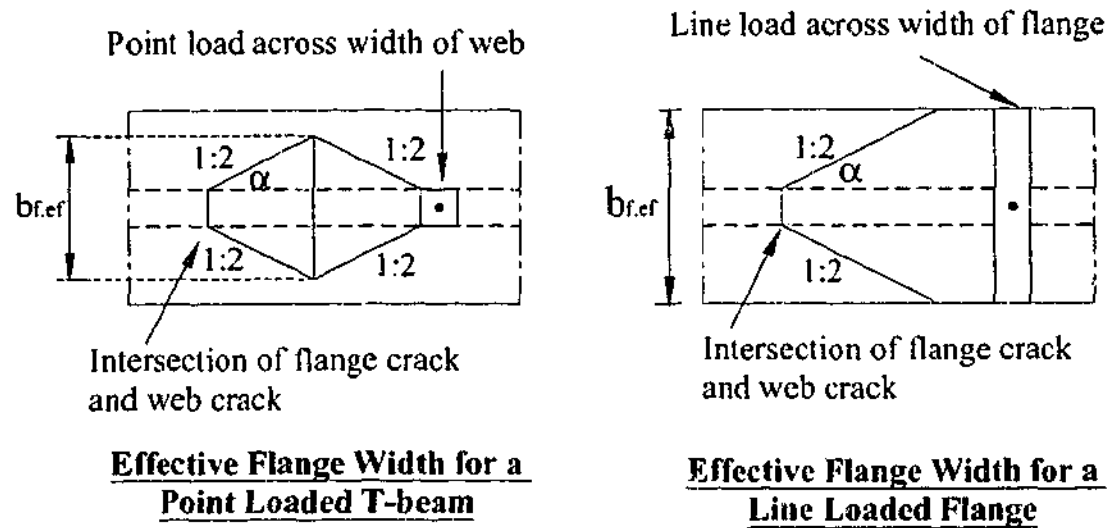


Figure 2.3-7 Hoang (1997) assumptions of compressive strain distribution throughout width of flange

Hoang (1997) was able to incorporate this assumed effective width of flange in the resistance of shear to complete a plasticity based formulation to be used for the calculation of the shear strength of RC T-beams without shear reinforcing. The author presents results of implementation of the theory and uses it to predict the influence of variation in the depth ratio (d_r) as well as with the effective flange width to web width (effective width ratio, $b_{e,r}$). The conclusions are that a linear variation in the shear resistance with the depth ratio prevails, and that differing variations in the shear resistance effective width ratio prevail depending on the loading conditions. Direct comparison with a series of tests that has only the flange proportions as a variable was not performed for the case of a line load across the width of the flange, and was not possible in the case of a point load equal to the width of the web owing to a lack of experimental results of this type.

2.4 State of the Art Research Methods for Calculation of Shear Capacity

Research into shear strength of reinforced and unreinforced concrete beams has been prevalent in literature since the early 1900's. A recent publication of the Journal of Structural Engineering (ACI-ASCE Committee 445 (1998)) was devoted to research on shear capacity. Ramirez (1998) attributed recent interest in the behaviour of reinforced concrete elements subjected to shear to the failure of a warehouse roof at Wilkinson Airforce in 1955. The failure was deemed to be instigated by a deficiency of shear capacity in one location in the roof. It was found that throughout the roof structure, inadequate shear resistance was provided by the concrete frame even though it was designed in accordance with the current concrete standard of the time. This failure has led to the fundamental question of the shear resistance mechanism being questioned, and hence much research in this area that is still ongoing.

The purpose of this section is to give a brief overview of the current state of the art methods of determining shear capacity available in literature. The methods that are considered in this section are those that are capable of accounting for variations of part of the geometry of a cross section (such as the flange width and depth of a T-beam). No consideration is given to those methods that have been developed for and applicable only to rectangular beams. A discussion in ASCE-ACI Committee 445 (1998) outlines many deterministic methods that are capable of calculating shear strength of RC rectangular beams.

2.4.1 *The Disturbed Stress Field Model*

Collins (1978) and Collins and Mitchell (1980) proposed the Diagonal Compression Field Theory in an attempt to adapt fundamental elements of Wagners Diagonal Tension Field Theory (1929) for steel to concrete. The similarity in these two theories comes about from the post local failure shear resistance mechanism. In Wagner's theory, it is assumed that shearing forces are carried by a field of diagonal tension after the web of a steel beam has buckled. Collins (1978) assumed that after cracking has occurred in concrete, the resistance to shear is provided by a field of diagonal compression. The formulation of this theory assumes that a truss type mechanism carries the applied shear to the supports.

Mechanisms such as aggregate interlock and steel stresses across cracks did not appear in the original formulation. It was Vecchio and Collins (1986) that furthered the original theory to incorporate these effects and called it the Modified Compression Field Theory. A thorough outline of the evolution of the MCFT and its applications can be found in Vecchio and Collins (1988), Vecchio (1989), Vecchio (1990), Vecchio and Selby (1991), Stevens et al. (1991), Vecchio and Collins (1993), Selby (1993), Selby and Vecchio (1996), Collins (1998a), and Collins (1998b).

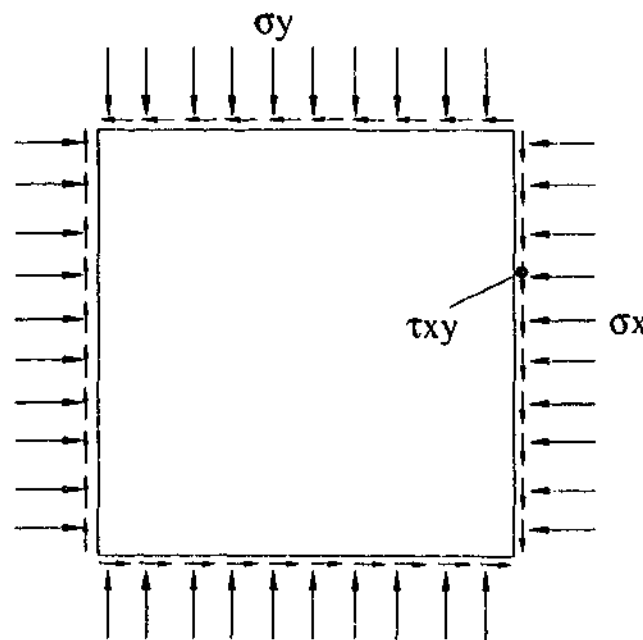
The experimental work to enable formulation of the constitutive relations for the theory was developed using a purpose built rig, Collins et al. (1985), which enabled the interaction between axial forces and shear on a two-dimensional plane stress type element to be observed and modelled. A schematic of the plane stress element used in the experimental formulation is shown in Figure 2.4-1. This enabled many important facets of the behaviour of reinforced concrete to be modelled, such as the softening in compression arising from a coexistent perpendicular tensile force. The unique approach given by this theory is that constitutive relations used in conjunction with the computational technique were derived for reinforced concrete. This enables reinforced concrete to be treated as a unique material with its own stress-strain characteristics.

Calculation of the strength of a specimen requires assumption of a strain distribution throughout the depth of a specimen, and a calculation of the corresponding stresses and internal actions. Discretisation throughout the depth of a specimen makes the application of this theory capable of estimating the effect of dimensional changes such as those of flange proportions.

Selby (1993) extended the MCFT into three dimensions by observing that a confining force existing in a third dimension will enhance the concrete strength. This was predicted by incorporating a failure surface that originated from work undertaken by Hseih (1979). Effects of transverse tension are also accounted for by using this failure surface. The results of merging of the MCFT with this failure surface proved successful in terms of replication of

ultimate strength of structures, although the prediction of lateral stresses were noted by the author to require further work.

The most recent development in the theory has come about following comments by Hsu (1998) and Lee and Hsu (2000). The comments suggested that the imposition of certain conditions relating to the amount of shearing stress transmitted across a crack put errors in the theory. They also suggested that the method of decomposing the local and average stress conditions was in error. Vecchio (2000), Vecchio (2001), and Vecchio et al. (2001) developed the Disturbed Stress Field Model (DSFM) which utilises constitutive relations of the MCFT but considers rigid body movements in the vicinity of crack locations so that a continuum strain can be used in the calculation of stresses and strains, and rigid body movements can be used in the calculation of shearing stresses across a crack. Some examples of the implementation of this theory into NLFEA have shown promise for the theory, but as yet a testing of the theory is not complete enough for a conclusive judgment to be made with regard to the validity of the theory.



Note : All forces provided by the use of jacks orientated at an angle to the relevant axis.

Figure 2.4-1 Plane stress state by tests for constitutive relations in the MCFT

2.4.2 Compressive Force Path Theory

Kotsovos (1987b) suggests that at the ultimate load of a reinforced concrete beam, the compressive force in a beam is transmitted to the supports from the application of load along a bilinear path. A schematic of this is shown in Figure 2.4-2. This bilinear path is the flow of compressive stresses from an applied load point back to the supports. This is conceived as the mechanism of load resistance in an RC beam, tensile stresses exist to keep the element in equilibrium.

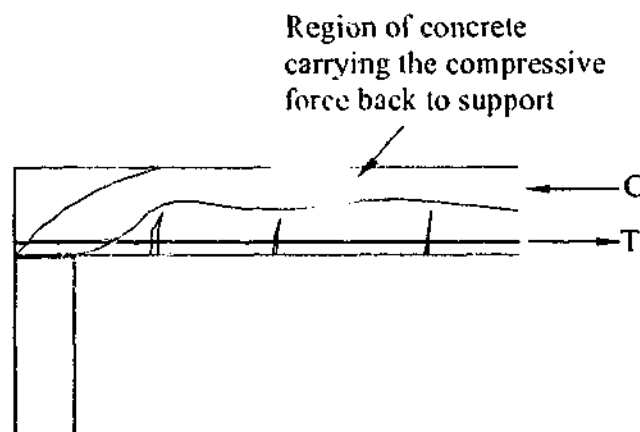


Figure 2.4-2 Illustration of the concept of the compressive force path

In this theory, Kotsovos (1988) hypothesizes that the failure of a beam in shear is caused by the propagation of tensile stresses into the region carrying the compressive force through the length of the beam. The theory incorporates four reasons for which tensile stresses may enter the region in which compressive force are being transferred. These include change in direction of compressive force path, variations in compressive stress intensity, the presence of inclined cracks, and bond failure.

Kotsovos and Bobrowski (1993) describe the application of the theory of the compressive force path. This procedure is quite simple. The design actions on a beam are calculated, and nominal triaxial considerations are given to the compression zone so that the enhancement of strength from this stress state can be incorporated. Transverse (or vertical) tensile forces are calculated and reinforcing is proportioned given this force.

Kotsovos et al. (1987a) and Kotsovos and Lefas (1990) show that application of this theory can lead to safe and efficient designs for RC T-beams. Unfortunately, their test specimens are not representative of specimens that would be found in service, so some degree of reservation in the theory should be exercised until further comparison with specimens of real size is undertaken.

2.4.3 Softened Truss Models

A similar idealisation of reinforced concrete to the MCFT is considered in the formulation of this theory. The development of the softened truss model was intended to eliminate some assumptions that lie in the MCFT by adopting a slightly different theoretical approach. There are two approaches that have been developed in the formulation of softened truss models, both of these are attributable to work carried out at the University of Houston. The Fixed Angle Softened Truss Model, Pang and Hsu (1996), allows for a difference in the principal angle of stress and the principal angle of strain while keeping the crack angle constant, while the Rotating-Angle Softened Truss Model, Hsu (1988), considers the crack angle changing with the principal angles of stress. Each of these is discussed below.

2.4.3.1 Rotating-Angle Softened Truss Model (RA STM)

The Rotating Angle Softened Truss Model outlined by Hsu (1988) bears much resemblance to the MCFT. Constitutive relations relating to the behaviour of reinforced concrete subjected to normal and shearing plane stresses are similar to those from the work of Vecchio and Collins (1986) and are incorporated into this theory. The difference between the RA STM and the MCFT is the treatment of local conditions at cracks, and the calculation of reinforcement stresses at these crack locations.

While the MCFT considers equilibrium between the cracked section and a section of uncracked concrete that can be considered to represent an average condition, the RA STM considers only the average stresses. As described in Pang and Hsu (1995), the RA STM introduces a method of calculating the steel stresses, hence local conditions at a crack based on

the average stress. This does not require assumption of an equilibrium state to determine the local stresses in reinforcing at the location of a crack as is required in the DSFM.

Hsu et al (1987) and Hsu (1988) implemented algorithms to solve the equations, which arise from the above theory to analyse small concrete specimens. The comparisons to experimental results given are to push off tests. Results from this collaboration show that the theory can produce good results for the simple type of test undertaken. Pang and Hsu (1995) compare this theory with 13 full-size RC panels, again this theory compares well.

2.4.3.2 Fixed-Angle Softened Truss Model (FA STM)

Pang and Hsu (1995) noted that the RA STM could not accurately predict the concrete contribution as it allows for rotation of a crack throughout the loading history. The extension of this theory, the Fixed-Angle Softened Truss Model FA STM, attempted to incorporate this.

This method was developed to include the concrete contribution that was outlined by the author to arise solely from the aggregate interlock contribution, the crack angle is assumed to remain constant after cracking. This angle is assumed to be the initial angle of the crack (i.e. perpendicular to the principal tensile stress). A constitutive law is introduced into the formulation relating the shearing stress to the shearing strain. This allows the concrete contribution to be introduced into the formulation as well as eliminating the assumption that the principal angle of stress and principal angle of strain are coincident.

Pang and Hsu (1996) developed an efficient algorithm capable of solving the set of equations that are produced from the above considerations. This study reported a reasonable correlation with experimental results, and was able to provide an estimate of the concrete contribution term that this theory attributes solely to aggregate interlock.

2.4.4 Other Methods of Predicting Shear Capacity

Plasticity theory has been applied recently to shear design, for example Ibell et al. (1997) has undertaken a very ambitious program to determine the mechanisms that could be

found on T-beam bridge decks. At the current stage of development, the theory requires determination of a failure mechanism that requires the least energy of all possible failure mechanisms. The task of finding these mechanisms is quite tedious, and mostly suited to computational application. It is noted that all possible failure mechanisms must be investigated for a true prediction of failure load to be found. Averbuch and Buhan (1999) implemented a linear programming function to calculate shear capacity using an upper bound and a lower bound approach.

Nonlinear Finite Element Analysis has been applied on many occasions to the prediction of shear capacity of structures (e.g. Seraj et al. (1992), Giacico et. al. (2000)). The main draw back in the application of this approach to the structures is the uncertainty in many aspects of the procedure. No one unified constitutive relation for concrete has been found; in fact many of the current constitutive models are simple extensions of linear elastic theory or plasticity theory, neither of which truly depict the behaviour of concrete. Size of load step, and the effect of stress distribution following cracking are aspects of the modelling that effect the stability, as well as the final result output from the scheme. The latter is attributable to the path dependent nature of concrete and the solution scheme.

Loov (2000) proposed a theory for prediction of shear strength in which elements of plate tectonics were used. This approach assumes that the weakest plane through which shear must be transferred is a cracked plane, and that the resistance across this plane is provided by shear friction. Reibez (1999) used the numerical techniques of multiple regression, dimensional analysis and interpolation in an attempt to fit equations of shear strength to a large pool of shear strength data.

2.5 How effective is the Flange of an RC T-beam in the Resistance of Shear?

The above discussion in Section 2.3 outlines that a very limited number of experimental investigations have isolated the effect of the proportions the flange of a T-beam on the strength of RC specimens that fail by exhibiting a mechanism of shear. It is interesting

to note that an investigation by Dei Poli et al. (1990) noted that the effect of the compression flanges had to be ignored in the formulation of an aggregate interlock model owing to the 'uncertainties of the effective flange width'.

In the investigations that have been performed, the loading arrangement is not identical between each of these investigations. Taplin and Al-Mahaidi (2000) and Fok (1972) loaded the surface of the flange with a line load that spanned the width of the flange, Chong (1980) subjected specimens to a line load along the length of the span, and no indication of the loading arrangement in the investigation by Placas & Regan (1971) could be found in literature.

It is thought that the application of a point load to an RC T-beam specimen across the width of the flange results in a greater flange effectiveness than might be the case if the same load were applied as a concentrated point load. In some cases, a T-beam that is representative of an element from a real structure may be subjected to this type of concentrated point load. An example of this is a girder from a T-beam bridge deck. The load from the wheels of a truck will be applied as a concentrated point load. In the experimental investigations undertaken to date that investigate the effect of flange geometry on the shear strength of an RC T-beam, this loading arrangement has not been investigated. Specimens that are loaded with a concentrated point load may not exhibit the failure mechanism that is assumed for specimens that are loaded over the entire width of the flange or the same trend in the increase in the shear strength with the flange proportions.

The prediction of the shear capacity of T-beams using analytical procedures is currently possible through two types of formulation. The first form is the use of formulations that are specific for RC T-beams (those by Placas and Regan (1971) and Hoang (1997)). These both assume that the failure mechanism of such a specimen is essentially an extension of that of a point loaded rectangular beam. The second category are those by those that are iterative procedures (DSFM and STM). Although they are fundamentally sound in the formulation and can predict the distributions of strain vertically at a section including the effect of cracking, the distribution in the lateral direction is inherently assumed as constant as a function of the discretisation procedure that these formulations require. This may not be the

case in the consideration of an RC T-beam subjected to a concentrated point load. In addition to the above, there is the CFP method; this again neglects to include the failure mechanism that is exhibited by this type of specimen.

The investigations that do exhibit a trend of increase in the shear strength with the flange proportions do not comment on the source of the increased shear strength. The variation of flange proportions could affect any component of the shear resistance mechanism. The lack of agreement in the individual contribution, of each component make this impossible to estimate using theoretical approaches. It is thought in this research that the majority of the contribution arises from the propagation of shearing stresses into the flange. This is suggested to be a necessary result of the compatibility of the flange and the web. It is unknown what proportion of the shear forces are resisted by the flange.

The investigation by Seraj et al. (1992) appears to be the only significant investigation into the capability of NLFEA to model the behaviour of a shear critical RC T-beam. This study only examined the degree of mesh refinement that was required to predict the crack pattern, stiffness and peak load of this type of structural element. No consideration was given to the state of stress in the flange, and the contribution that it made to the failure mechanism and to the peak load. In addition to this, no study to date has examined the capability of NLFEA to predict the effect of the flange proportions on the shear strength of an RC T-beam.

2.6 Objectives of This Research

In light of the above comments relating to existing studies that have directly included the effect of flange proportions on the shear strength of an RC T-beam, as well as current state of the art analytical methods that have the capacity to predict such an effect, several outstanding issues are to be addressed in this research.

1. Produce experimental results that specifically isolate the effect on the ultimate strength of variations in the flange width and flange depth of an RC T-beam with

shear reinforcing that is loaded with concentrated point load that has a width equal to the width of the web.

2. Examine the failure mechanisms associated with this type of load arrangement, and determine if the assumptions used in the formulation of the failure mechanisms of T-beams are representative for specimens with the considered type of loading arrangement.
3. Investigate the existence of an upper bound to the effect that the flange width has on the shear strength of an RC T-beam for the given type of specimen to be studied.
4. Formulate an experimental method capable of determining the magnitude, and distribution of shear forces in the flange of an RC T-beam.
5. Use the above results to quantify the effectiveness of the flange in relation to the actual shear force that it carries in relation to that in the web.
6. Determine suitable FE modelling procedures that allow extrapolation of experimental results to determine the effect of subtle changes in flange geometry on the ultimate strength of an RC T-beam.
7. Determine the capability of NLFEA to predict the flange contribution by comparison with the value obtained from the experimental work.

Chapter 3 EXPERIMENTAL PROGRAM

3.1 Introduction

Achieving the objectives of this research that are outlined in Section 2.6 required two stages of experimental work. The first stage of the experimental work was dedicated to the determination of the effect of the variation of flange proportions on the shear strength of a series of RC T-beams with shear reinforcing subjected to a point load applied over the width of the web. The determination of the existence of an upper bound to the effectiveness of the flange on the ultimate strength can also be explored with this set of experiments. The second stage of the experimental work required detailed instrumentation of specimens to determine the shearing stresses in the flange both throughout the width and the depth.

This chapter describes the experimental procedure that was implemented for both of the above stages. Selection of the variable flange proportions, and fixed values of reinforcing percentages, material properties, loading arrangements, as well as instrumentation are considered in this section for the first stage of experimental work. This stage of experimental work will be referred to from hereon as stage 1 experimental work. These parameters are discussed in light of isolating flange proportions as the only variation in effecting the ultimate strength throughout specimens cast in this stage. The discussion of the second stage of experiments requires detailing the analysis procedure used to determine shearing stresses in the flange from measured strains. This stage will be referred to from hereon as stage 2 experimental work. This section outlines this, as well as detailing the specimens, and the instrumentation required for implementation of this analytical procedure.

3.2 Procedure for Stage 1 Experimental Work

To examine the effect of the variations of flange proportions on the shear strength of an RC T-beam, a rectangular beam was chosen as a control specimen. The methodology chosen for determining the effect of variations in the flange proportions was similar to that of Chong (1980) whereby three flange depths were tested. For each flange depth, five different flange widths were tested. The ultimate strength results of T-beam specimens were compared to that of the rectangular beam, thereby allowing the effect of flange width and depth to be observed.

This section firstly outlines the reference rectangular beam, then proceeds to detail the flange geometries that were used in this part of the experimental program. A discussion of material properties, and loading arrangements follows.

3.2.1 *The Reference Rectangular Beam*

The reference rectangular beam was designed as a shear critical specimen. The MCFT was used to predict the shear capacity, and an algorithm suggested in Darvall (1987) was adopted to calculate flexural capacity. The difference in load calculated to cause flexural failure compared to that estimated to cause shear failure gave confidence that the specimen would fail by exhibiting a shear mechanism. The details of this beam are given in Figure 3.2-1 and Figure 3.2-2. Cover to the bottom longitudinal bars was 16mm, giving an effective depth to the centroid of the reinforcing group ($d=$) 261mm, and a depth to the centroid of outer most layer of tensile reinforcing ($d_o=$) 279mm.

This specimen was cast as part of series 1 specimens. Identification of series and specimen numbers are presented below in Section 3.2.2. The 28 day cylinder strength for this series of specimens was 36MPa, the yield strength of the flexural reinforcing was 300MPa, and the yield strength of the 6.5mm diameter bars (stirrups and longitudinal compression reinforcing) was 398MPa.

The overall dimensions, reinforcing percentages and the width of this specimen were chosen after considering Taplin and Al-Mahaidi (2000). This research suggested dimensions

as representative of those used in typical T-beam bridge decks on Victorian roads in Australia. These are half scale of those dimensions.

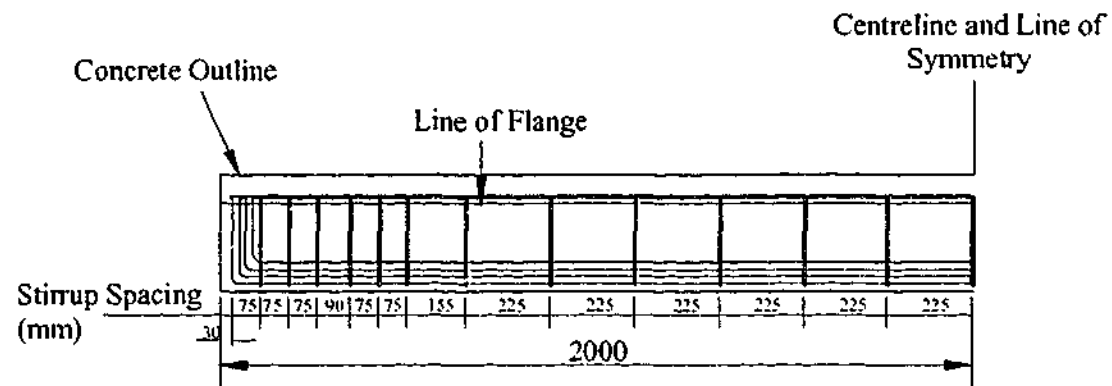


Figure 3.2-1 Elevation of reference rectangular beam

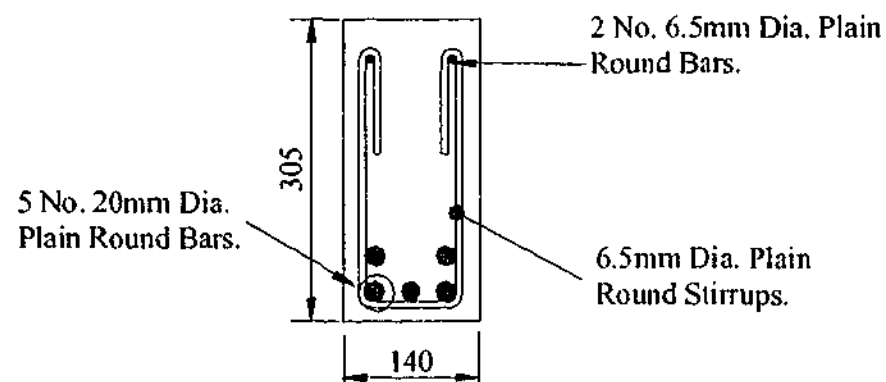


Figure 3.2-2 Cross section of reference rectangular beam

3.2.2 Flange Proportions Investigated

The publication of Taplin and Al-Mahaidi (2000) suggested that at this scale, a typical flange width in use on T-beam bridge decks in Victoria is 620mm. This drove the selection of the flange widths. It was considered to study width variations on flange widths proportioned on these dimensions as a base for scaling.

Limitations of laboratory space required no more than six beams could be cast at a time. It was decided that each series of six specimens should have a different flange depth, and within each series of beams, the flange width would be varied. For the purpose of this

investigation, three flange depths were used. A summary of beam identifications is given in Table 3.2-1.

Table 3.2-1 shows that series 1 and 2 beams included a specimen with flange width of 930mm. After series 1 testing was complete; it became clear that a specimen with a flange width of 930mm and a flange depth of 50mm would have provided a redundant ultimate strength result; therefore, a specimen with a flange of this width was precluded from series 3. A detailed discussion of failure mechanisms exhibited by specimens that drove this decision is presented in Chapter 5.

Table 3.2-1 Series 1-3 Beam Tags and Flange Proportions

Series Number	Beam Tag	b_f (mm)	d_f (mm)	b_r	d_r
1	B1	930	100	6.64	0.35
	B2	620	100	4.43	
	B3	465	100	3.32	
	B4	310	100	2.21	
	B5	225	100	1.61	
	B6	Reference rectangular specimen detailed in Section 3.2.1			
2	B7	930	75	6.64	0.26
	B8	620	75	4.43	
	B9	465	75	3.32	
	B10	310	75	2.21	
	B11	225	75	1.61	
3	B12	620	50	4.43	0.17
	B13	465	50	3.32	
	B14	310	50	2.21	
	B15	225	50	1.61	

As stated earlier, the intent of this stage of experimental work was to examine the ultimate strength of specimens with identical web geometry and reinforcing arrangement, but with varying flange dimensions. Therefore, the arrangement of flexural, shear, and top

longitudinal web reinforcing in these specimens was identical to that of the rectangular beam discussed above in Section 3.2.1. Figure 3.2-3 shows a cross section that was typical for T-beam specimens cast throughout this stage of testing.

3.2.3 Flange Reinforcing Arrangements

In an attempt to scale typical bridge beams, it was required that both lateral and longitudinal reinforcing be provided in the flange of the specimens. The lateral reinforcing across the width of the flange is representative of flexural steel in a bridge deck slab to allow the deck to span laterally across the width of a bridge between beams. Figure 3.2-3 shows a cross section of specimen B8. This cross section outlines the arrangement of flange reinforcing that was provided. It is noted that the lateral reinforcing across the width of the flange was provided only for series 2 beams, and part of series 3 beams.

Figure 3.2-4 shows an elevation of specimen B12 from series 3 of this stage of experimental work. This illustration shows the arrangement of lateral flange reinforcing that was typical to all series 3 specimens. The lateral flange reinforcing was positioned in such a way that the test with the longer total span had a shear span that contained the lateral flange reinforcing. The test of the second end with the shorter total span had no lateral flange reinforcing within the shear span. The purpose of this was to determine the influence of the lateral flange reinforcing on the ultimate strength and failure mechanisms displayed within a series of beams.

It was the intention of the experimental work to keep the area of longitudinal flange reinforcing relative to flange area constant throughout each series of specimens. However, consistent spacing of these flange bars (as shown in Figure 3.2-3) was difficult to achieve in specimens of narrower flange widths (particularly 255mm and 310mm wide flange). Spacing of the bars in the specimens with 225mm wide flange was approximately 40mm (governed by the width of the flange overhang), the spacing of these bars in the 310mm was selected to be the same as this.

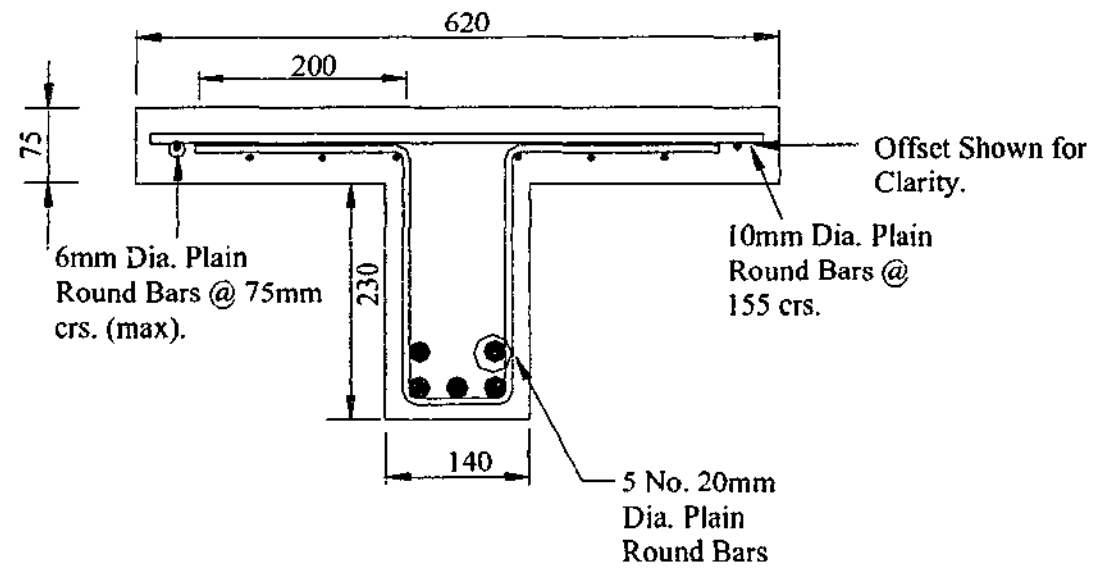


Figure 3.2-3 Cross section of specimen B8 showing flange reinforcement details for Series 2 beams

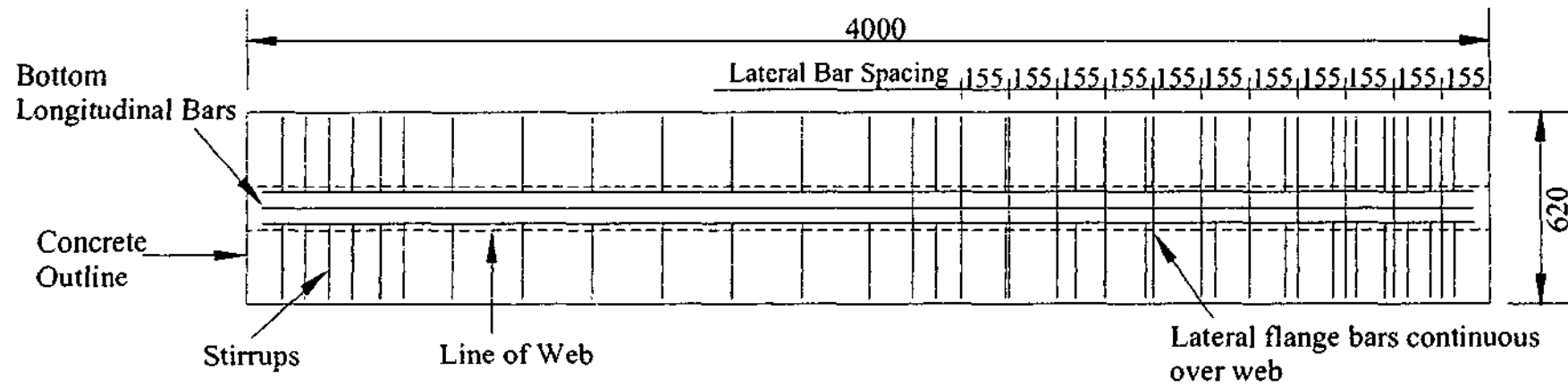


Figure 3.2-4 Plan of specimen B12 showing typical arrangement of flange reinforcing for Series 3 beams

3.2.4 Loading

As discussed in Section 2.6, the application of load in this series of experiments was a point load applied to the top of the flange in such a way that the width of the flange is equal to the width of the web (145mm was used to ensure that the load would still cover the width of the flange in the case of a specimen that was positioned slightly off centre). The location of the load was established by trying to ensure that specimens would not fail in flexure. Using design tools such as the MCFT (computer code implemented by Al-Mahaidi et al. (2000)), the Australia Standard AS3600 (2001), and with information from existing research (Taplin and Al-Mahaidi (2000), Kotsovos et al. (1987)), a shear span to effective depth (a_v/d) of 3.0 coupled with the high flexural reinforcing percentage was deemed likely to ensure that flexural failure would not occur.

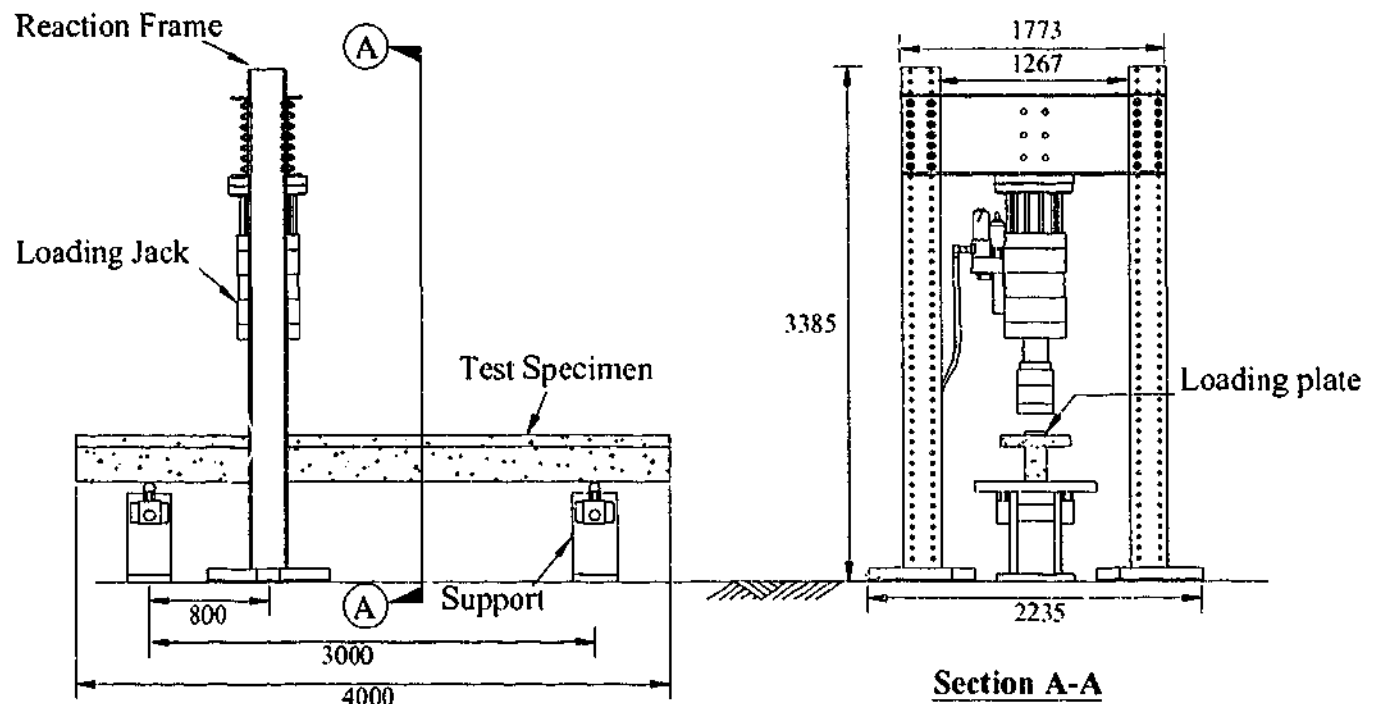


Figure 3.2-5 Load and support arrangement for specimens

Figure 3.2-5 above shows the loading and reaction system used to test the specimens. The specimen length was chosen to be 4.0m, and the span used for testing was 3.0m (these dimensions made the specimens representative of elements from real structures scaled at approximately 50%). The shear span to effective depth ratio of 3.0 produced a shear span of

800mm. The longer of the two shear spans was proportioned in an attempt to ensure that it was not damaged from the test of the shorter shear span. In all but one case this occurred, no cracks were formed in the longer shear span. It was therefore decided that testing of this second end of the beam should be undertaken to examine repeatability of ultimate strength results. The span for the second end test was shortened so that the damaged shear span from testing of the first end was completely precluded from the test. The magnitude of the second test shear span was 800mm as for the first end test. A schematic of the testing of the second end can be seen below in Figure 3.2-6.

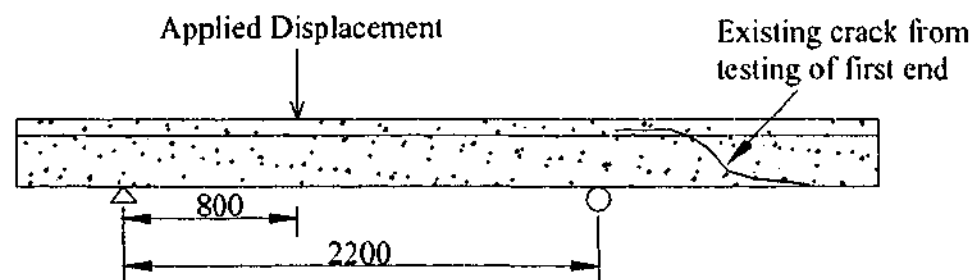


Figure 3.2-6 Schematic of second end test

Application of the point load was via a controlled displacement. The rate of displacement was 0.009mm/sec. The load at the applied displacement was measured using a load cell at the load point (and could be cross checked with the reactions). The application of load using displacement control allowed observation of the formation of the failure mechanism as well as an examination of post peak response.

3.2.5 *Material Properties*

Material properties were not an intended variable in this stage of the experimental work, but the requirement of breaking this stage of the experiments into three series of specimens led to variation in the properties of both the concrete and the reinforcing steel that were supplied by the respective manufacturers.

Testing of three samples of every bar type used in each of the three specimens gave the yield and ultimate strengths of the reinforcing bars. Concrete properties were determined by

cylinder tests after the concrete was placed. The material properties for each series cast for this part of the testing program are shown below in Table 3.2-2.

Table 3.2-2 Material properties for each series

Series Number	Shear Reinforcing		Flexural Reinforcing		$f'_{c,28}$ (MPa)
	$f_{y,v}$ (MPa)	$f_{u,v}$ (MPa)	$f_{y,l}$ (MPa)	$f_{u,l}$ (MPa)	
1	398	455	340	500	36.0
2	308*	405*	340	500	30.8
3	440	510	340	500	33.4

* Denotes that 10mm diameter lateral flange reinforcing in series 2 had identical properties to the 6mm diameter bar.

It is clear from this table that there were indeed some considerable variations in material properties. This is particularly noticeable with the yield stress of series 3 shear reinforcing being 42% higher than that of series 2. There was a maximum 19% variation in the concrete cylinder strength throughout the three series.

3.2.6 Measurement

At the point of application of the measured controlled displacement, a load cell was positioned so that the applied load could also be measured at this point. In addition to this, the reactions were measured from load cells at the support points. Stringpots were attached to the soffit of the beam directly underneath the load point, and at the position of mid span of the specimen. The stringpot attached directly underneath the load point was a consequence of the measured displacement of the loading actuator included the extension of the reaction frame. The displacement obtained from the stringpot was used for the load displacement curves.

In addition to the applied load, reactions, and displacements, strain gauging was provided on specimens in series 1 and 2 to determine the strain in the stirrups, and the flexural reinforcing. Figure 3.2-7 shows a schematic of the placement of strain gauges for these series of beams. It should be noted that the gauges on the shear reinforcing shown in this figure are applied to both legs of the shear stirrups (on the outside of the leg). Two gauges were

provided to the flexural reinforcing in the position shown below, these were attached to the outer two bars in the lowest layer of reinforcing (see Figure 3.2-3).

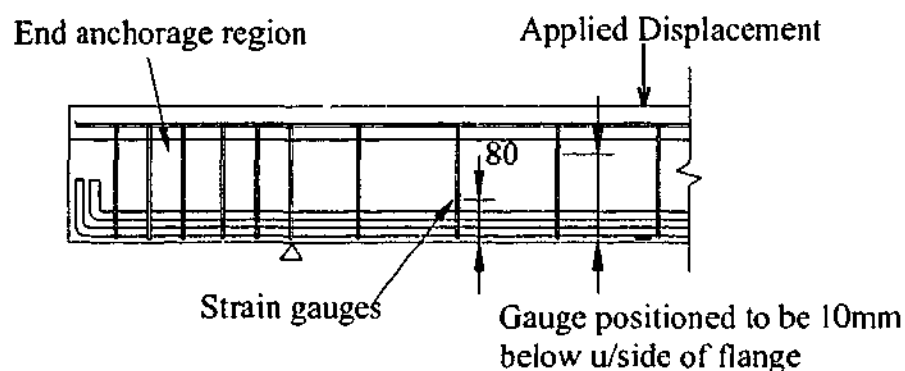


Figure 3.2-7 Strain gauging arrangement for Series 1 and 2 beams

The gauges on the shear reinforcing were located by examination of specimens tested by Taplin and Al-Mahaidi (2000). These were a similar series of tests, so it was possible to estimate the orientation of web cracks for this stage of experimental work from these specimens, which had already been tested. The location of the web crack from these beams was determined, and this was used to estimate the distance from the soffit of the beam at which the crack would be when it intersected the shear reinforcing. The gauges on the flexural steel underneath the point load correspond to the location of the maximum bending moment, hence the maximum tensile strain in flexural reinforcing.

3.3 Procedure for Stage 2 Experimental Work

As aforementioned in Section 3.1, the aim of this stage of experimental work is to provide an experimentally determined value of the magnitude of the shearing force in the flange of a T-beam. This was achieved in these experiments by providing a system of instrumentation to two specimens.

Selection of strain gauges to directly determine the shearing strain proved to be impossible given the required gauge length. Therefore, a method of calculating the stress or force at various locations in the flange was required. This section outlines the equilibrium considerations and constitutive relations used for the determination of shearing forces in the

flange of a T-beam. A discussion is also provided on the cross section used for the application of the instrumentation for implementation of the method. Some additional gauging was provided to these specimens in order to determine lateral strains across the width of the flange. This instrumentation system will also be discussed in this section.

3.3.1 Application of Equilibrium Principles to Determine the Shear Force in the Flange of a T-Beam

To apply equilibrium to calculate the shearing force distribution throughout the width and depth of the flange of a T-beam, the flange overhang needs to be considered as a series of component volumes. Each of these component volumes will be examined to determine the stress state so that the equilibrium of each of these component volumes can be considered.

3.3.1.1 Discretisation of Flange

It is an implicit and logical assumption of this research that the majority of the flange contribution arises from an increase in the concrete contribution term as outlined in Chapter 2. Based on the mechanism given in Figure 2.2-1, the required location for calculation of this concrete contribution term is next to the load point. Close to the load point and close to the support, strain profiles will be disturbed as a result of localisations from the applied external forces. The following application of equilibrium conditions must be applied outside of these regions where the strain profiles are not disturbed by these external forces.

Consider a shear critical point loaded T-beam as illustrated in Figure 3.3-1, with the region where failure will be instigated shown as clouded. The strain distribution in this shear critical region near the load point, but outside of the disturbed region is the region to which instrumentation in the flange will be provided to determine the magnitude of shear force in the flange. This region is illustrated in Figure 3.3-2. Consider now the short portion of this beam that is the instrumented region; Figure 3.3-3 shows this region with the predominant sectional forces that act on it. This illustration also shows a series of dashed lines that are outlines of the discretised component volumes of the flange, referred to here as 'flange blocks', used for

dual sectional analysis. In Figure 3.3-3, a positive moment is in the direction that causes the beam in Figure 3.3-2 to sag. The direction of the positive shear force corresponds to this.

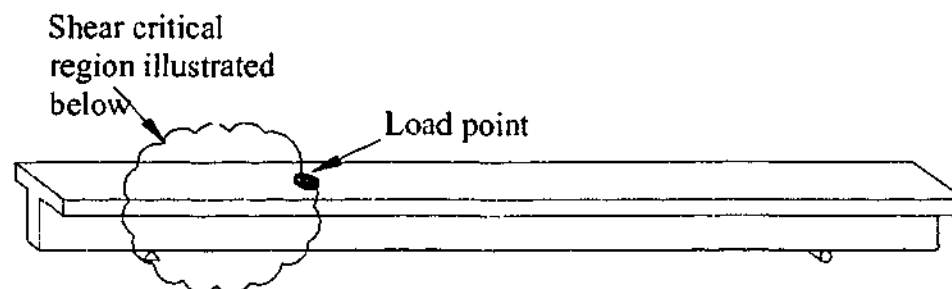


Figure 3.3-1 A shear critical T-beam

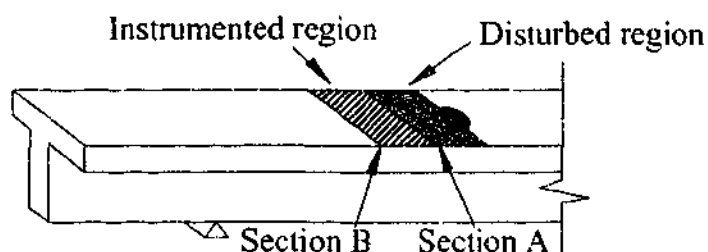


Figure 3.3-2 Shear critical region of T-beam showing approximate size of disturbed region and region considered for calculations

An illustration of the separation of the flange into these flange blocks is shown in Figure 3.3-4. Along with the flange blocks, Figure 3.3-4 also shows some forces that act on each surface. For the sake of clarity, the forces considered in this illustration are only those forces that act along the length of the span. Consideration of forces in the other directions will be considered shortly. Assuming that all of the flange is in compression, and that the web is in tension (which is the convention that will be used for discussion), the forces acting on each block (along the length of the span) are a normal compression force, a shear lag force (the shear force acting on the surface separating rows), and the interface shear force (the shear force on the surface that separates the layers) produced from the discretisation procedure

throughout the depth. In the discretisation shown in Figure 3.3-3 and Figure 3.3-4, the flange blocks in the flange overhang are considered to have equal volume and surface area (the surface area is measured on a cross section of the specimen). In Figure 3.3-4, a positive normal force is considered to be in the direction that causes compression; a shear force on a plane is considered positive if the outward normal to the plane is in the negative direction of the coordinate axis, and the shear acts in a positive direction of the coordinate axes (the converse to this also applies). This is illustrated in Figure 3.3-5.

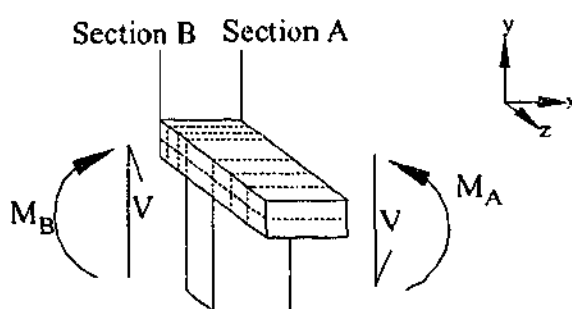


Figure 3.3-3 Region under consideration

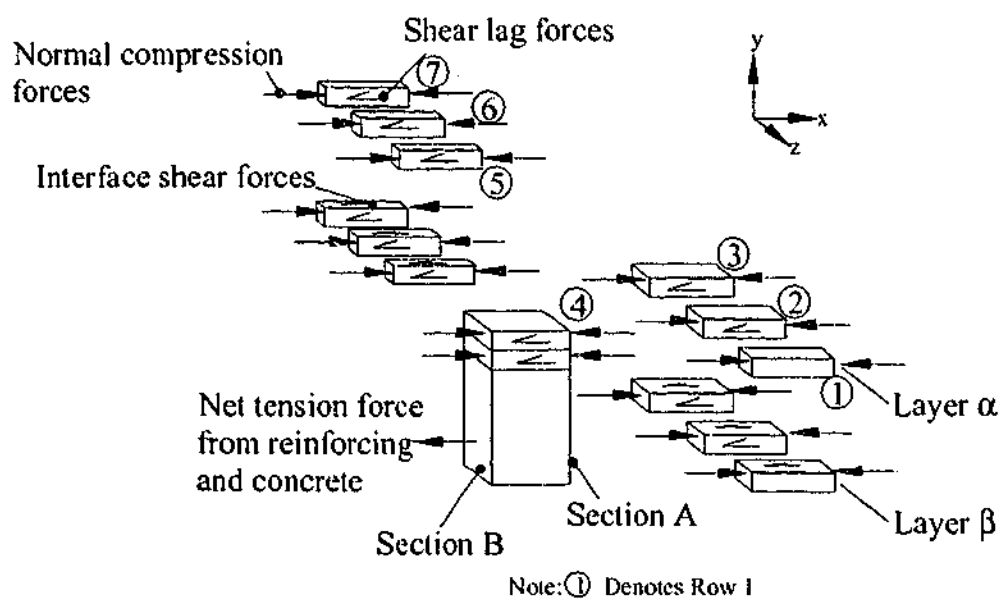


Figure 3.3-4 Discretisation of block of T-beam showing forces acting along the length of the span on component regions

These figures also show the notation that applies to each individual block that will be used for the remainder of this discussion. Section A is the section closest to the load point, and Section B is a short distance away from this closer to the support. The flange overhangs

are discretised into six rows across the width, three in each overhang, therefore there are seven rows in total across the width of the whole flange including the web region, which are numbered 1-7 (row numbers are indicated in Figure 3.3-4 below). There are two layers throughout the depth, layer α is the top half of the flange, and layer β is the bottom half of the flange. Layer α and β are of equal depths corresponding to half of the flange depth.

3.3.1.2 Stresses Acting on an Arbitrary Flange Block

Figure 3.3-5 shows the stresses acting on an arbitrary body in the cartesian coordinate system. Consideration of individual blocks of flange for application of equilibrium conditions requires consideration of the action of all of these stresses. The orientation of the coordinate axis system in this discussion aligns with that given above for the discussion of forces acting on flange blocks.

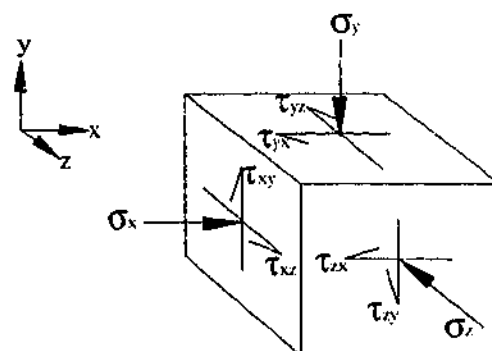


Figure 3.3-5 Stresses on an arbitrary body in the cartesian coordinate system

Consider firstly that the discretisation of Figure 3.3-4 divides the flange into two layers throughout the depth. This eliminates normal stresses in the y-direction on the top of layer α and the bottom of layer β , and the shear stresses τ_{yx} and τ_{yz} on these surfaces of the flange, as they are free surfaces. Since the equilibrium equations will only be applied to Bernoulli regions (outside of the disturbed region in Figure 3.3-2), the normal stress in the vertical direction (σ_y) is assumed to be zero throughout the specimen. Therefore the stress in this direction will be zero at the interface between the two layers of flange blocks.

The shear forces acting at Section A and Section B in Figure 3.3-3 are considered to be equal as self weight of the beam in the region under consideration produces negligible effect on the shear force between these two sections. To simplify equilibrium considerations, assume that the vertical shearing stresses (τ_{xy} in Figure 3.3-5) in the flange blocks are equal at Section A and Section B.

Consider a block at the edge of the flange that does not have any stress acting on the free surface (such as the far surface on the flange block shown in Figure 3.3-5). This corresponds to elimination of τ_{zx} and τ_{zy} in Figure 3.3-5 (which are on the free surface which is hidden by the orientation of the block, this surface is on the yz -plane). Considering the above assumptions that the force produced by σ_y is zero, and that the forces corresponding to τ_{xy} shearing stresses are equal and opposite, then the summation of forces in the vertical direction requires that the shear stress, τ_{zy} , is equal to zero. Repeated application of the summation of forces in the vertical direction leaves this stress equal to zero for all flange blocks. This leaves the stress distribution as shown below in Figure 3.3-6.

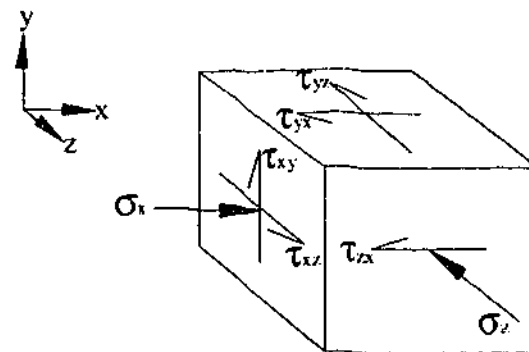


Figure 3.3-6 Stress distribution on arbitrary flange block after application of assumptions

3.3.1.3 Equilibrium Relations to Determine Shear Force on an Isolated Block of the Flange

Figure 3.3-7 shows the above stress distribution applied to flange block $\alpha 2$. The location of the section A and B are shown on this figure, and can be seen to be the same as that in Figure 3.3-3. Note that the only forces shown are those, which will cause a moment about

the z-axis. The shear lag forces are noted as $V_{s\alpha j}$ where the subscript s denotes a shear lag force, the subscript α denotes that it acts on layer α , and the subscript j denotes which rows it acts between. For the flange block $\alpha 2$ $j=2$ (or row 2) shown in Figure 3.3-7, $V_{s\alpha 2}$ represents a shear lag force that acts between rows 2 and 3. Note that the shear lag for $V_{s\alpha 1}$ shown on this figure is equal and opposite to the shear lag force produced on flange block $\alpha 1$.

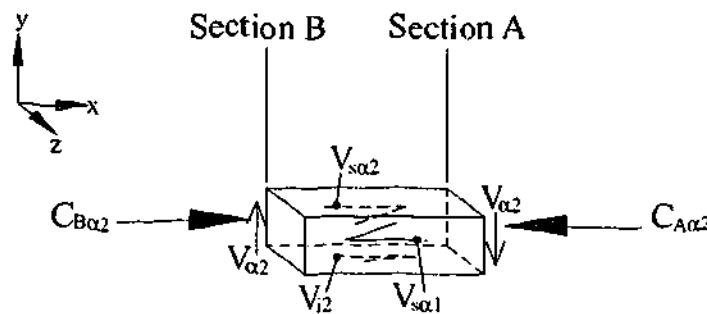


Figure 3.3-7 Detail of flange block $\alpha 2$ showing all forces that cause moment about the z-axis

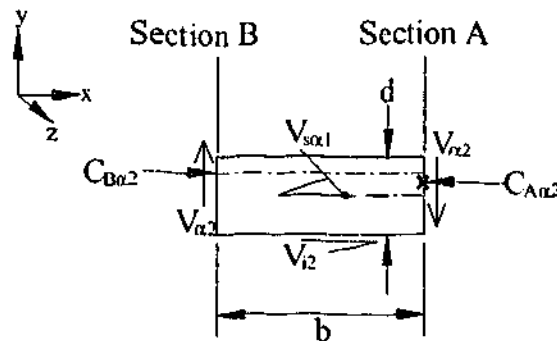


Figure 3.3-8 Elevation of flange block $\alpha 2$

Figure 3.3-8 shows an elevation of the flange block shown in Figure 3.3-7, again with only external forces that cause rotation about the z-axis being shown on the illustration. Note that $V_{\alpha 2}$ is the vertical shear force acting on row 2 in layer α . The convention shown on this figure as a positive vertical shear force corresponds to a shear force that is positive in the dual section shown in Figure 3.3-3. Assuming that no reinforcement is placed in this block, the only surface forces acting (that cause moment about the z-axis) are the compression forces on either side of the block, the interface shear, shear lag, and the vertical shear. Assume that the shear lag force that is shown in this elevation is evenly distributed throughout the depth so that

the line of action from the force is at the centre of depth of the layer. Equation 3.3.2 shows the result of summation of moments about point X, where X is at the line of action of the force $C_{A\alpha 2}$ in Figure 3.3-8. In this figure the line of action of the shear lag forces, and the compression force at section B are shown as centrelines so that the locations relative to the line of action of the compression force at section A are shown. It should be noted that inclusion of reinforcement in this formulation produces another compression force on both section A and B that can easily be included in the summation of moments shown in this equation.

$$V_{\alpha 2} = \frac{-(0.5d - L_{CA\alpha 2})V_{S\alpha 1} + (0.5d - L_{CA\alpha 2})V_{S\alpha 2} - (L_{CA\alpha 2} - L_{CB\alpha 2})C_{B\alpha 2} + (d - L_{CA\alpha 2})V_{i2}}{b} \quad 3.3.1$$

The subscripts on the lever arm terms (L) in the above equation indicate which force they refer to with reference to the top of the layer (eg $L_{CA\alpha 2}$ is the lever arm of force $C_{A\alpha 2}$ measured from the top of block $\alpha 2$). Equation 3.3.2 shows that if all of the forces acting horizontally on this block can be calculated, then the shear force on this block can be calculated.

Application of the above procedure to all flange blocks within the flange overhang produces similar relationships to those shown above for flange block $\alpha 2$. These relationships are shown below in Equation 3.3.2 in general terms for any block 'j' throughout the width of the flange in layer α .

$$V_{\alpha j} = \frac{-(0.5d - L_{CA\alpha j})V_{S\alpha j-1} + (0.5d - L_{CA\alpha j})V_{S\alpha j} - (L_{CB\alpha j} - L_{CA\alpha j})C_{B\alpha j} + (d - L_{CA\alpha j})V_{ij}}{b} \quad 3.3.2$$

3.3.1.4 Calculation Of Normal Forces and Lever Arms From Experimental Data

To calculate the shearing force throughout the flange using Equation 3.3.2, the normal, shear lag force, and interface shear force are required. This section describes the calculation of stresses and forces from measured strains using available constitutive relations. For the purpose of this discussion, the reader should note that specimens that this technique was

applied to were provided with adequate instrumentation to determine the strain at a number of locations throughout the width and depth of the flange.

Calculation of the stresses from strains requires the implementation of constitutive relations. Given the stress state that was produced from the experiments described below, the relations of the MCFT (Vecchio and Collins (1986)) were considered appropriate to calculate compressive stresses. It is acknowledged that these relations have been updated since the formulation of the MCFT (by Vecchio and Collins (1993)) which was implemented into this procedure, however an examination of the old and new relations showed that, in general, there was little change in the calculated values of compressive stress for low to intermediate values of strain, such as those that were obtained from the experiments discussed in Sections 1.3.2 and 1.3.3. In addition to this, the relations of the MCFT are based on the Hognestead (1951) formulation for uniaxial concrete. This formulation is generally accepted in the description of the uniaxial response of concrete as was approximately obtained from these experiments. Another difference between the 1986 and 1993 formulations is the calculation of the softening of the compression response of concrete that arises from co-existing perpendicular tensile stresses. The 1993 formulation is based on more experimental data, and is more accurate in the prediction of this effect. It is this approach that is implemented for consideration of the value of perpendicular strain to produce softening in the compression concrete. An analysis of the compression softening parameter and its effect on the calculation of the stresses from strains in these specimens in light of the differences in these formulations is presented in Appendix A.

The formulations that were used for the calculation of compressive stress from compressive strain in the principal directions are given in Equations 3.3.3 - 3.3.4. Underpinning the implementation of these equations is that fact that the principal compressive direction is along the length of the specimen, and the perpendicular tensile direction is across the width of the flange (when tensile stresses arise in this direction). Given that the predominant actions produced by the applied load are bending and shear, this is easily justified.

$$f_{c2} = f_p \left[2 \left(\frac{\epsilon_2}{\epsilon_o} \right) - \left(\frac{\epsilon_2}{\epsilon_o} \right)^2 \right] \quad 3.3.3$$

where

$$f_p = \frac{f'_c}{\beta}; \quad \beta_d = \frac{1}{1 + C_s C_d} \leq 1.0 \quad 3.3.4$$

$$C_d = 0.35(-\epsilon_{c1} / \epsilon_{c2} - 0.28)^{0.8}$$

Calculation of tensile stresses from tensile strains is given below in Equations 3.3.5 - 3.3.6.

$$f_{c1} = \begin{cases} E_c \epsilon_1 & \epsilon_1 \leq \epsilon_{cr} \\ \frac{f_{cr}}{1 + \sqrt{200\epsilon_1}} & \epsilon_1 > \epsilon_{cr} \end{cases} \quad 3.3.5$$

where the cracking stress is taken as from the relationship in AS3600 (2001) as:

$$f_{cr} = 0.4\sqrt{f'_c} \quad 3.3.6$$

Application of these relations to strains obtained from experimental work produces point stresses. Consider now that the strain gauging was located at six points across the width of the flange and at the centre of the web in such a manner that three point strains throughout the depth (at the same lateral location) were obtained during the experimental program. The above relations can be used to determine compressive forces throughout the width and depth of the flange. The details of location of the gauges throughout the width and depth of the flange can be found in Section 3.3.3.

It is required that the strain measurements are located so that equal sized blocks can be used for implementation of the calculation procedure, and so that the strain measured inside the concrete is at the centre of the depth of the flange. The location of flange reinforcing made it impossible to locate internal gauges in the positions corresponding to flange blocks used for

the calculation procedure. Linear interpolation was used to determine strains at exact locations required. These locations were, laterally, the centre of width of the each flange block (refer Figure 3.3-4), and vertically, the top, centre of depth and bottom of the flange. This linear interpolation procedure was considered acceptable for the low level of strain that was produced during the experiments (Appendices B & C outline these results). Note that the stress in the tension zone is higher at the strain of ϵ_{cr} than at the soffit of the slab as tension softening effects increase throughout the depth of the slab. These are accounted for analytically in Equation 3.3.5.

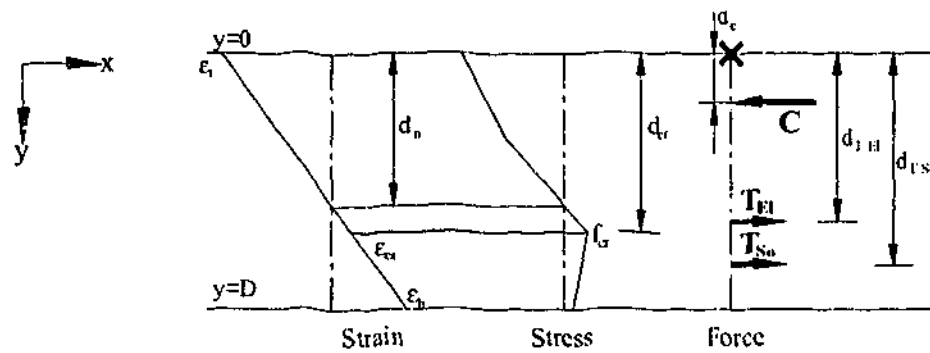


Figure 3.3-9 Arbitrary stress strain and force distribution on a flange block

Consider an arbitrary flange block with known strain profile from experiments, and stress profile calculated from the method prescribed above. Figure 3.3-9 above shows the strain, stress and force distributions for this arbitrary block. To implement the procedure outlined in Section 3.3.1.3, calculation of the forces and lever arms on each flange block are required. In this figure, it is assumed the tensile strain on the bottom face of the arbitrary block is greater than the cracking strain, hence tension softening will have occurred as is shown in the stress distribution.

Implementation of the MCFT to the experimental results produced required consideration of three stress states as shown in the above relations; compression stress, elastic tension stress, and the tension stress associated with the post cracking strength of concrete (termed 'softened' tension stress). Equations 3.3.4 - 3.3.6 summarise the calculation of the three components of force from stresses that are considered in the above formulation of the constitutive relations.

The calculation of the force requires calculation of the area of the stress distribution in each of the regions. These regions are the compression region (which gives calculation of the force C in Figure 3.3-9), the region with linear elastic tension response (which gives rise to force T_{EI} in Figure 3.3-9), and the tension softening zone (which gives rise to force T_{S_0} in Figure 3.3-9). The fact that the peak strains were small (peak compressive strain of approximately $700\mu\epsilon$) was again used in this calculation. The values of strain that were produced were in the regions of response where the assumption of a linear distribution of stress was valid. This was true for the tension region as well as the compression region (peak tensile strain of approximately $120\mu\epsilon$). The area of the tension softening region was calculated based on the value of stress at the cracking strain given by Equation 3.3.5. The values of the lever arms were also calculated by finding the centre of area of the distributions by assuming this linear distribution of stress.

3.3.1.5 Calculation Of Shear Lag and Interface Shear Forces

The normal forces, and lever arms of these forces for implementation of the equilibrium procedure outlined in Equation 3.3.1 have now been developed. Implementation of the relationship in this equation for the determination of the shear force in a flange block now requires calculation of the shear lag force, the interface shear force and the lever arms of these two forces.

Assuming that the shear lag force in the two layers in each row is equal, that is $V_{s2} = V_{s\alpha 2} + V_{s\beta 2}$ (for layer 2), the notation V_{sj} is now used to represent the shear lag force that acts on row j of the flange calculated throughout the entire depth of the flange. Consider the discretisation of the flange of a T-beam into rows that extend for the full depth of the flange. This is shown in Figure 3.3-10. In this figure, the notation C_{A1} represents the compression force acting on row 1 of section A. This is simply the sum of $C_{A1} = C_{A\alpha 1} + C_{A\beta 1}$. This is easily calculated from the results of strain gauging. Summation of forces in the X-direction at row 1 yields Equation 3.3.7.

$$C_{B1} - C_{A1} + V_{s1} = 0 \quad 3.3.7$$

Since C_{A1} and C_{B1} are known, it is then routine to calculate the shear lag force V_{s1} . Similar applications of equilibrium on each row throughout the width of the flange yield all longitudinal shearing stresses required.

If it is assumed that the shear lag stress is uniform throughout the entire depth of the flange, the magnitude of the shear lag force in Figure 3.3-8 is half of the value calculated above from Equation 3.3.7. Summation of forces in the X-direction on the flange block shown in Figure 3.3-8 yields Equation 3.3.8.

$$C_{B\alpha 2} - C_{A\alpha 2} - V_{s\alpha 1} + V_{s\alpha 2} + V_{i2} = 0 \quad 3.3.8$$

$V_{s\alpha 1}$ and $V_{s\alpha 2}$ are calculated using the above procedure, so the only unknown in the above equation is V_{i2} . This again is routinely calculated for each block throughout the width of the flange.

The location of application of the interface shear is known to be either at the top or bottom of the flange block (depending on whether a block in layer α or β is being considered for application of equilibrium conditions). Given the assumption of the uniform distribution of the shear lag stresses, the location of the lever arm of the shear lag force on each individual flange block is the centre of depth of the flange block. With the interface shears and the shear lag forces and lever arms known, application of Equation 3.3.2 allows for simple calculation of the vertical shearing force on any flange block, V_{aj} (where a is the layer number, either α or β , and j is the row number).

In the above free body diagrams, the longitudinal flange reinforcement was not considered for clarity of the illustrations. Inclusion of the longitudinal reinforcing into the above formulation requires only knowledge of the strain at the location of the reinforcing; this can be converted into a force, and simply included in the equilibrium considerations. Strain in the longitudinal flange bars for the series of experiments discussed below was calculated by linearly interpolating strain values measured on the concrete.

3.3.2 Specimen Outline

Selection of the number of specimens was governed by the cost of the instrumentation required for the measurement of the number of strains needed for the implementation of the above equilibrium procedure. Given this cost, two specimens of equal flange width and varying flange depth were chosen.

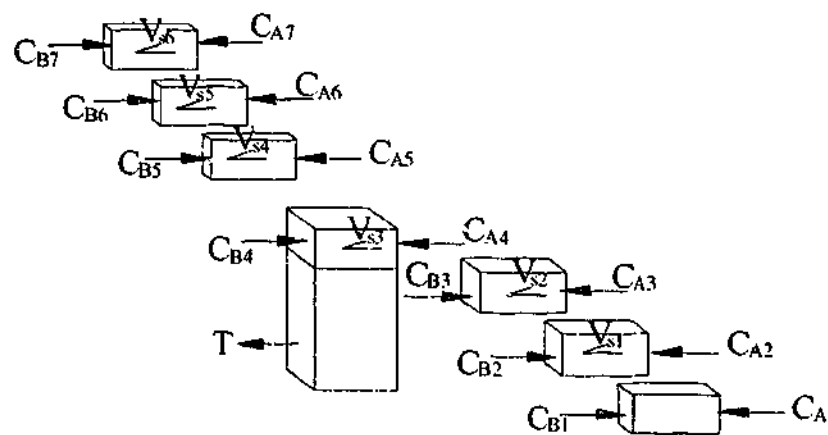


Figure 3.3-10 Discretisation of flange throughout the width only

The flange proportions used in this stage of experimental work were selected after the completion of stage 1 experiments. To investigate the distribution of shearing forces in the flange, specimens from stage 1 work that exhibited significant results in the trend of shear strength versus flange proportions variation were used for experimentation. The discussion in Chapter 5 describes the significance of the specimens with flange width 465mm and flange depths 75mm and 100mm in terms of the failure mechanisms that were obtained throughout stage one of the experimental work. This fact led to selection of these specimens for implementation of the instrumentation and equilibrium procedures for determination of the flange contribution. The reader will gain a greater understanding of this choice once the above section describing the failure mechanisms for the experiments in stage one is examined. A cross section of the specimens used in stage 2 can be seen below in Figure 3.3-11.

Material properties were intended to be similar to those used for the experimental work in stage 1; however, variations in materials supplied were again prevalent. The yield strength of the flexural bars used in this stage was, $f_{y,l}=340\text{MPa}$, the yield strength of the stirrups was $f_{y,v}=300\text{MPa}$, and the concrete cylinder strength was $f'_c=50\text{MPa}$. These specimens were cast together, therefore only a small volume of concrete was required. This proved difficult for the supplier of the concrete to measure exact quantities for the small quantity required using the measurement system available to them; therefore, the concrete strength was higher than anticipated.

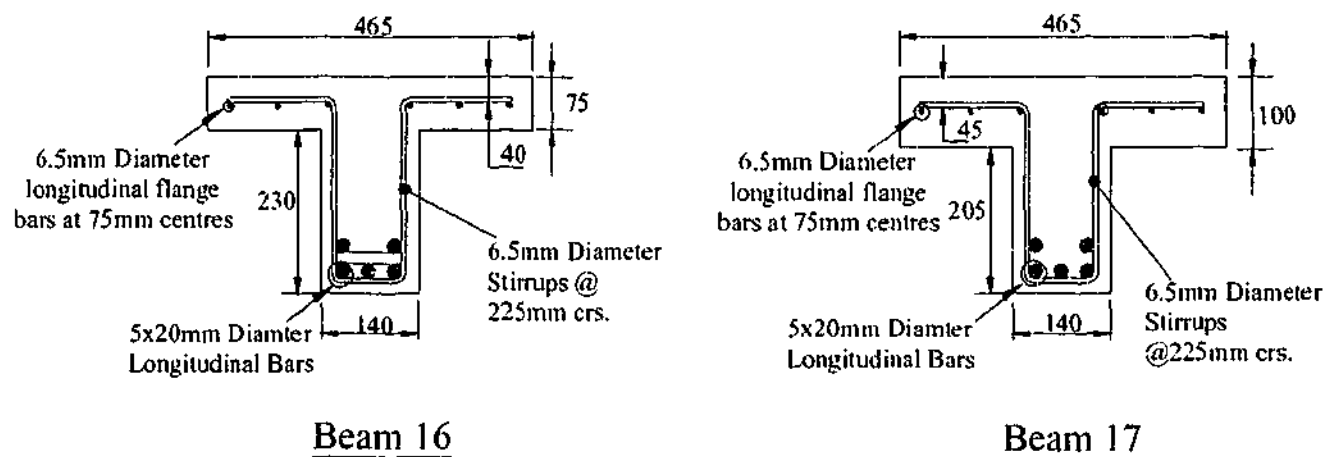


Figure 3.3-11 Cross section of specimens used in Stage 2 of the experimental work

The loading and geometry of these two specimens was identical to the arrangements used for these variables in stage 1 of the experimental work. The shear span to depth ratio was again 3.0, and the total span was again 3.0m. Figure 3.2-1 and Figure 3.2-5 shows these facets of the specimens.

Measurements that were taken throughout this stage of tests were primarily focussed on the strain measurements required to implement the above equilibrium procedure. The strain measurements taken for this are described below in Section 3.3.3. In addition to this the load, midspan deflection, and deflection under the load point, and the support reactions were measured. These were measured using the methods used for stage 1 experimental work described in Section 3.2.6.

3.3.3 *Details of the Instrumentation*

For the implementation of the equilibrium procedure detailed in Section 3.3.1, it was required that this stage of experimental work produce the longitudinal strain profiles throughout the depth at seven points across the width of the flange (including the centreline of the web). For practical reasons, measurement of the strain at three points throughout the depth of the flange (top surface, mid depth, and bottom surface) was considered appropriate. In addition to this, implementation of the constitutive relations of the MCFT and DSFM require that the strain laterally across the width need to be calculated. The latter also requires a distribution throughout the depth.

This section outlines the type of gauges used, estimation of the length of the disturbed region outlined in Section 3.3.1.1, as well as the location of the longitudinal and lateral gauges throughout the width and depth of the flange. The positioning of the gauges longitudinally and laterally throughout the flange is discussed separately for clarity. It should be noted that these were positioned at the same depth at each location throughout the depth, photographs at the end of the section in Figure 3.3-14 -Figure 3.3-17 show the method of location used to achieved this.

3.3.3.1 *Details of The Strain Gauges*

The instrumentation that is described below combines concrete surface gauges, embedded concrete gauges, as well as steel gauges to measure the strain profile at three points across the depth of the flange at 12 separate locations. The 'mixing' of these gauges introduces a potential source of error in the use of different length gauges.

Several authors (eg. Kotsovos (1995)) suggest that an 'average' homogeneous response of concrete is attained when strains are measured over a length of at least three times the maximum aggregate diameter. The concrete mix used in these experiments contained a nominal maximum aggregate diameter of 14mm, so the minimum length of concrete gauge that could be used was 42mm. The concrete gauges used had a length of 60mm, the embedded gauges had a gauge length of 100mm, and the steel gauges had a length of 10mm.

The use of steel gauges to determine strains in the concrete arose from the limited space available for instrumentation within the depth of the flange. If perfect bond between the steel and the concrete is achieved, the strain in the steel is equal to the strain in the concrete; therefore the gauge accurately records the concrete strain. These gauges were shown to measure only small strain, so an assumption of perfect bond between the concrete and the reinforcing is valid.

To determine the accuracy of the results obtained from mixing gauges of different lengths, the longitudinal gauging system outlined in Section 3.3.3.3 was implemented into two trial slabs. Internal bending moment and shear forces were calculated using dual sectional analysis and equilibrium. A detailed description of this is outlined in Chapter 6, and can also be found in Giaccio et al. (2000).

3.3.3.2 Calculation of the Length of the Disturbed Region

With reference to Figure 3.3-2, it was required to estimate the distance from the load point at which the strain profile was to be linear throughout the depth (i.e. not influenced by the load point). The method selected to achieve this was to perform three dimensional linear finite element analysis using solid elements and examine the strain profile produced. The region considered appropriate for instrumentation was the region at which the longitudinal strain profile was linear throughout the depth of the beam.

Observation from stage 1 experimental work indicated that specimens failing in shear did not exhibit any crushing of concrete in the compression zone, and that ultimate load of the specimen was reached in a brittle fashion so that no significant amount of plastic deformation occurred in the specimen. Using this observation, it was assumed that the curvature of the specimen remained constant throughout the duration of the test. Based on this assumption, it is valid to calculate the distance of the strain gauges from the loading point using results from the linear finite element analysis.

This procedure of analysing the strain profile indicated that at a distance of 150mm away from the centre of the load point, the strain profiles were undisturbed by the application

of loading. This distance of 150mm from the centre of the load point requires that the nearest strain gauge be at least 77.5mm from the edge of the load point (the loading plate diameter used was 145mm). This distance of 150mm is close to half the total depth of the specimen. A schematic illustration showing the distance of the gauges from the edge of the load point is shown in Figure 3.3-12.

3.3.3.3 Flange Gauging in the Longitudinal Direction

The strain profile required for implementation of the calculation procedure outlined in Section 3.3.1 required determination of the longitudinal strains in the flange of the specimen. Strain gauging was also provided in the lateral direction along the width of the flange with the purpose of determining the effect of tensile strains across the width of the flange on the compression response of the concrete in the longitudinal direction. The arrangement of this lateral flange gauging will be discussed in Section 3.3.3.4.

The procedure to calculate shearing forces in the flange required gauges at two sections along the length of the specimen as shown in Figure 3.3-12. Each of the locations that were instrumented across the width of the flange was also provided with three gauges throughout the depth, which aligned vertically. This can also be seen schematically in Figure 3.3-12.

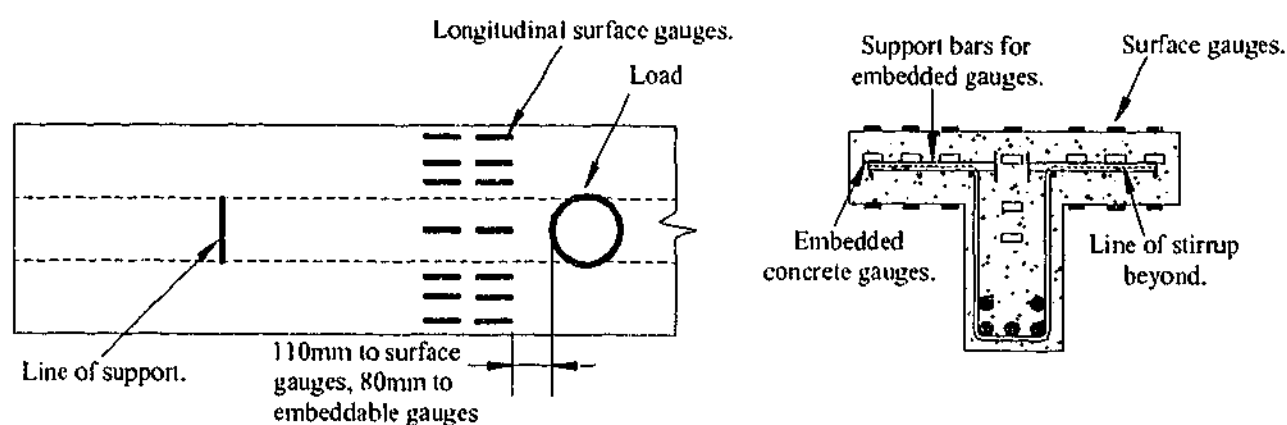


Figure 3.3-12 Schematic layout of longitudinal gauges

In addition to this, the centreline of the web was instrumented. Although results of this instrumentation were not used in the implementation of the equilibrium procedure, they completed the distribution of strains across the width of the flange of the specimens. It can be seen in Figure 3.3-12 that an additional gauge was provided in the web below the bottom of the flange. This was provided to ensure that the location of the neutral axis in the flange could be established throughout the duration of the experiment at all load levels. Photos of the instrumentation used can be seen in Figure 3.3-14 - Figure 3.3-17.

The position of these longitudinal gauges was dictated by the location of the embedded gauges. These gauges were bulky because of the protective coating, and ensuring that these gauges were all clear of reinforcing bars, and at the same depth limited the positioning of the gauges. The depth of the gauges within the flange was dictated by the penetration of the stirrup into the flange, and the location across the width was determined by the position of the longitudinal flange reinforcing bars.

The gauge pattern shown above in Figure 3.3-12 was identical on the top and bottom surfaces, as well as within the flange. The centrelines of the embedded gauges were approximately 25mm from the top surface of the concrete for specimen B16, and 35mm from the top for specimen B17.

3.3.3.4 Flange Gauging in the Lateral Direction

In Equation 3.3.4 in Section 3.3.1.4, the term β depends on the principal tensile strain ϵ_1 . The physical significance of this term is to soften the compression response of concrete with significant perpendicular tensile strains. The strain gauges discussed below which are aligned across the width of the flange measure this perpendicular tensile strain.

To determine the distribution of these lateral strains across the width of the flange, instrumentation was provided at as many points as practically possible at locations as near as could be achieved to the longitudinal gauges. A schematic of the gauging system showing only the lateral gauges is shown in Figure 3.3-13.

The decision to locate strain gauges at three points across the width and depth of the flange was based on the physical limitation of the internal gauges. The use of any more rows of gauging would have made it very difficult to fit all gauges and leadwires internally to the specimens. To ensure that the three gauges provided aligned vertically throughout the depth, it was required that some longitudinal and lateral gauges were in contact. The use of a low voltage excitation unit ensured that strain readings were not influenced by heat transfer between gauges, and advice from the strain gauge manufacturer suggested that providing the gauge had not yielded during installation, the slight physical deformation arising from this contact was insignificant in the output of the gauge.

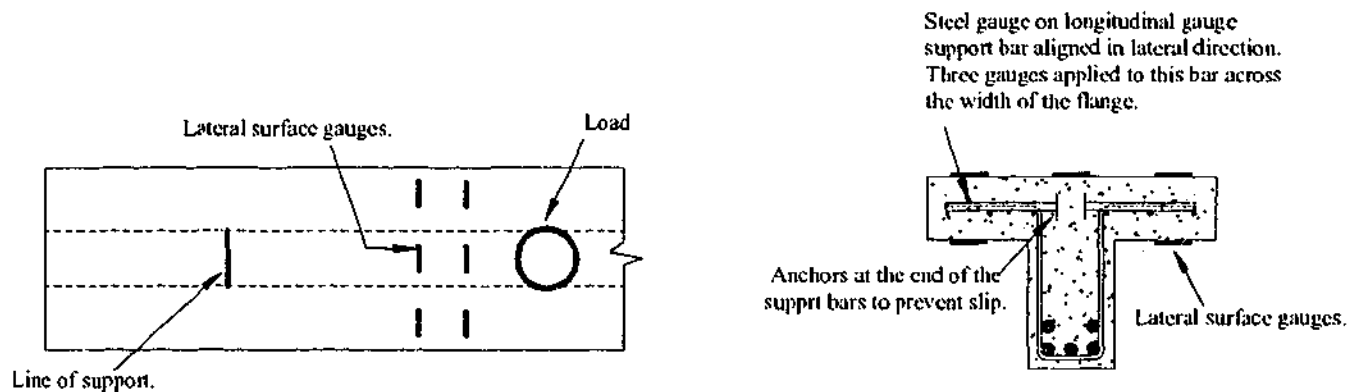


Figure 3.3-13 Schematic of lateral gauging system used for stage 2 experimental work.

To allow sufficient space for all instrumentation to be located within the same region, the lateral strains within the depth of the flange were measured using gauges on the reinforcing bars used to support the embedded longitudinal gauges. The location of this system with reference to the load and support is shown in Figure 3.3-14. To ensure no slip between these reinforcing bars and the concrete, these were anchored at a position near the centre of the web. These support bars did not align vertically with the surface gauges, therefore four bars were instrumented and linear interpolation was used to calculate the strain in the required location. This set up can be seen in Figure 3.3-15.

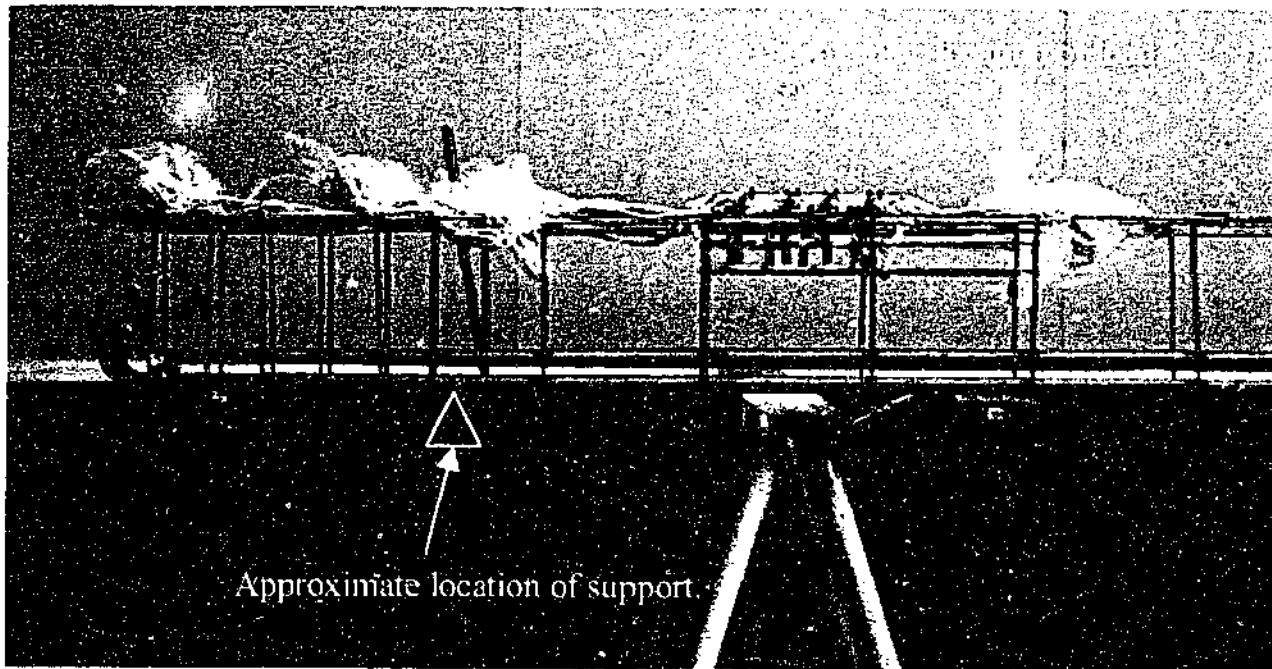


Figure 3.3-14 Location of embedded instrumentation with reference to load and support

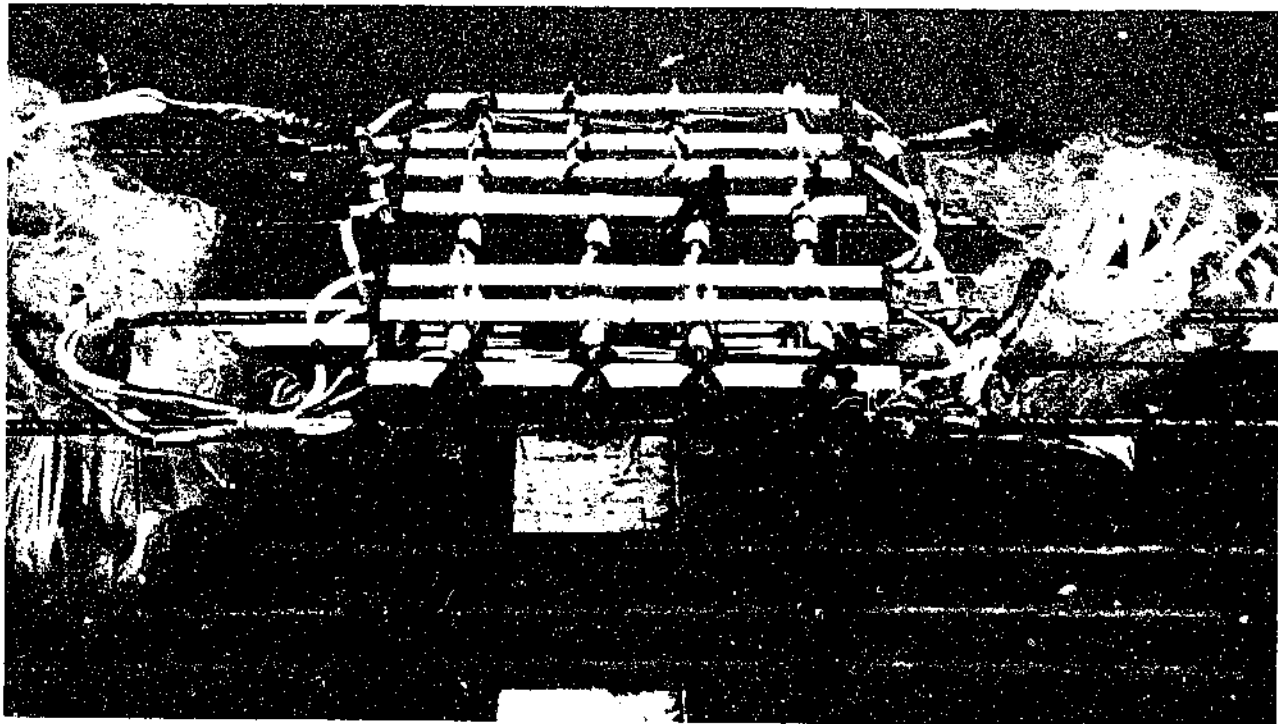


Figure 3.3-15 Photo of embedded gauge system showing longitudinal and lateral gauges

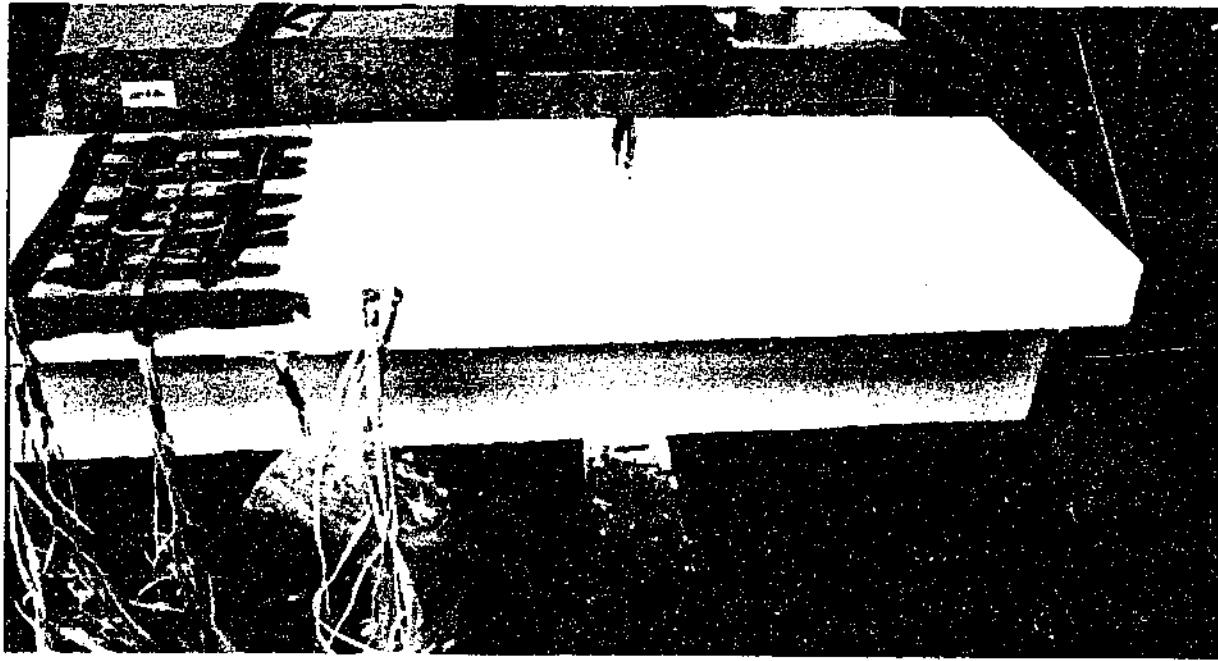


Figure 3.3-16 Photo of specimen B19 showing top surface gauges

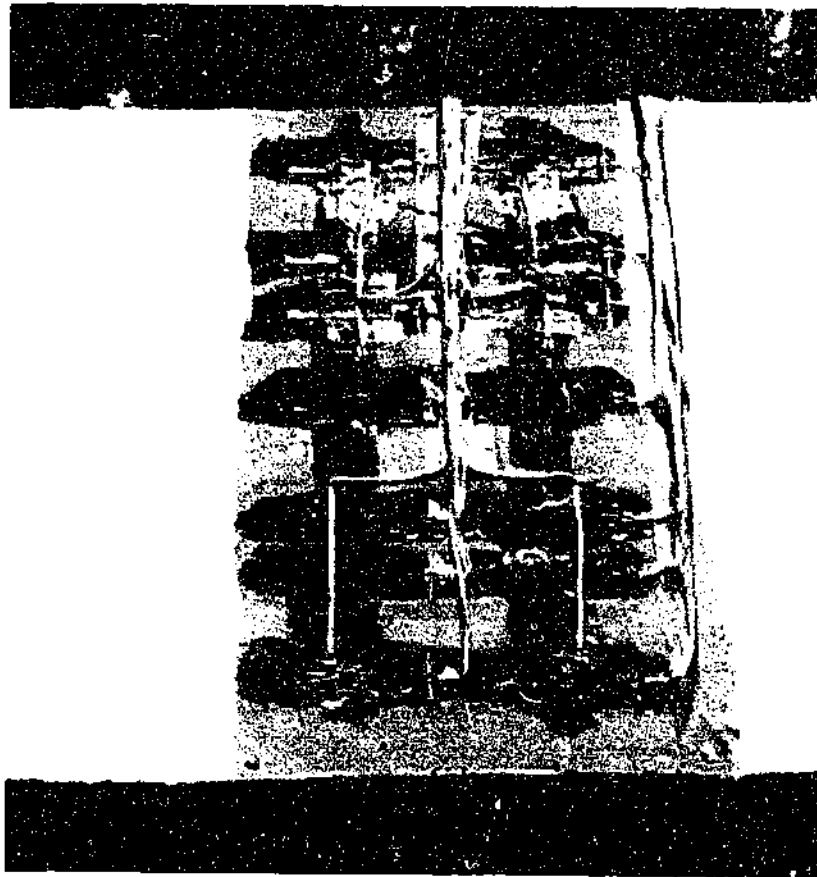


Figure 3.3-17 Close up photo of top surface strain gauging system on specimen B19

Chapter 4 NUMERICAL MODELLING USING NON LINEAR FINITE ELEMENT ANALYSIS

4.1 Introduction

Numerical modelling using NLFEA was adopted in this investigation as it has proven to be very powerful in the prediction of overall behaviour and peak load of reinforced concrete structural elements since the first application by Ngo and Scordelis (1967).

This chapter describes the implementation of NLFEA to the specimens of stage 1 and stage 2 experimental work, and the extrapolation of this method to predict the shear strength of a series of specimens without variations in material properties. The aim is to replicate the experimental results therefore allowing determination of the trend of the variation in shear strength with flange proportions. This aim includes the application of the procedure to a series of specimens (of identical geometric proportions to those in stage 1 experimental work) without the material property variations. Successful modelling using this technique allows for prediction of the stiffness, ultimate load, reinforcement behaviour, and concrete stresses and would produce much more detailed results than those that can be obtained from experimental specimens. The software package DIANA (1998) was used for this analysis.

This chapter presents firstly the objectives of the implementation of NLFEA. Secondly, the development of the physical model, its geometry and simplifications is described. Following this, various relationships to describe the behaviour of the materials are described. A parametric study using these relationships was performed and the details of this

are given in this section. A discussion of the iteration scheme, and the mechanisms used to detect failure is given. Finally, the modelling procedure is described.

4.2 Objectives of the Implementation of Non-Linear Finite Element Analysis

Numerical modelling (NLFEA) was employed in this investigation to predict the effect of variations in the flange geometry on the strength of a shear critical point loaded RC T-beam. This includes the effect of the variation of the stirrup effectiveness, crack patterns, load-deflection response, and the peak loads that arise from changes in the geometry of the flange.

To ensure that the procedure produced satisfactory results, the specimens used in experimental work were modelled with this procedure. The following additional objectives were set to ensure that NLFEA performed satisfactorily in predicting the response of point loaded shear critical RC T-beams:

1. Determining the capability of NLFEA to predict the peak load of the experimental specimens.
2. Determining the capability of NLFEA to predict the stiffness of the specimens as measured from the gradient of the load deflection response.
3. Determining the capability of NLFEA to predict the effectiveness of the stirrups in the resistance of an applied shear.
4. Determining the capability of NLFEA to predict the pattern of cracking at the peak load.
5. Determining the capability of NLFEA to capture the redistributions of stress that occur throughout loading of the specimens.

6. Determine the capability of NLFEA to predict the level of shear force that is carried by the flange.

4.3 The Physical Model

The physical modelling required selection of an adequate representation of the structure, selection of a satisfactory representative loading and support scheme (boundary conditions), and selection of element sizes that were appropriate for the model. This section discusses these aspects of the modelling procedure. It should be noted that these parameters were fixed throughout the modelling procedure and were not investigated as part of the parametric study outlined in Section 4.6.

4.3.1 *Model Geometry and Boundary Conditions*

Figure 4.3-1 and Figure 4.3-2 show the simplifications used in the modelling of the specimen to allow for efficient solution. Figure 4.3-1 shows the reduction in overall length of the specimen that was used in the modelling procedure. The full length of the specimen overhangs at the supports were not critical in the analysis, hence were not modelled. Some overhang was kept as this was found to be required for numerical stability of the solution with the boundary conditions employed. This resulted in a reduction in overall length from 4000mm to 3500mm. The dimensions of both of the shear spans and the reinforcing quantities used in the analysis remained the same as that in the experimental work. The total span that is shown in this figure is 3000mm, this is the same as the span used in the tests of the first end of the stage 1 experiments, and comparison will be made only to the experimental results of this end. Figure 4.3-2 shows half of width of the cross section of the specimen was used in modelling using the symmetry of the cross section about the centre of width.

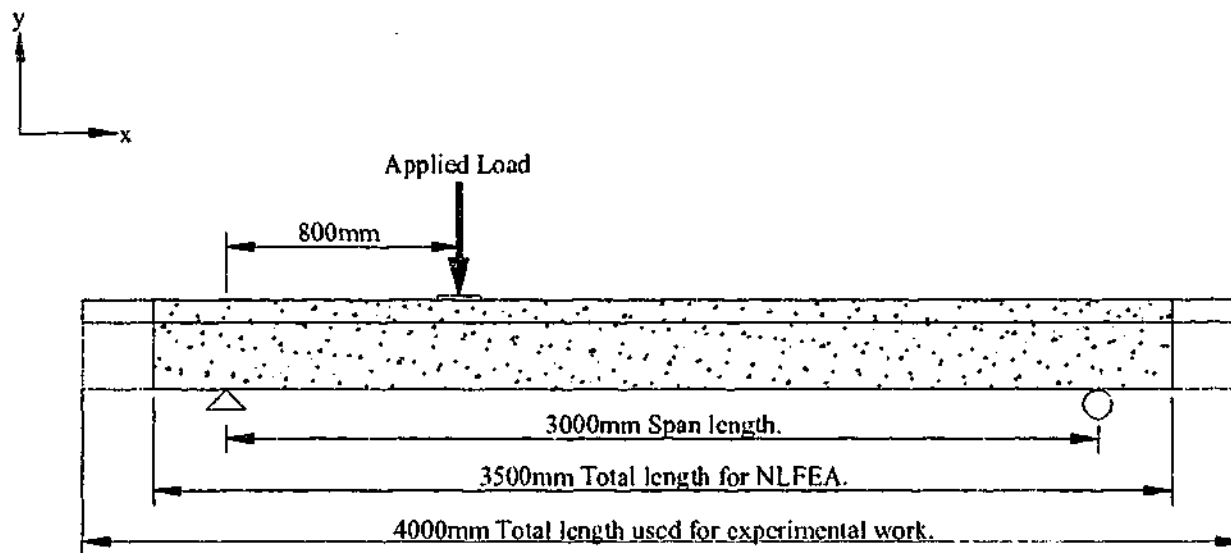


Figure 4.3-1 Elevation of dimensions used in the FE model

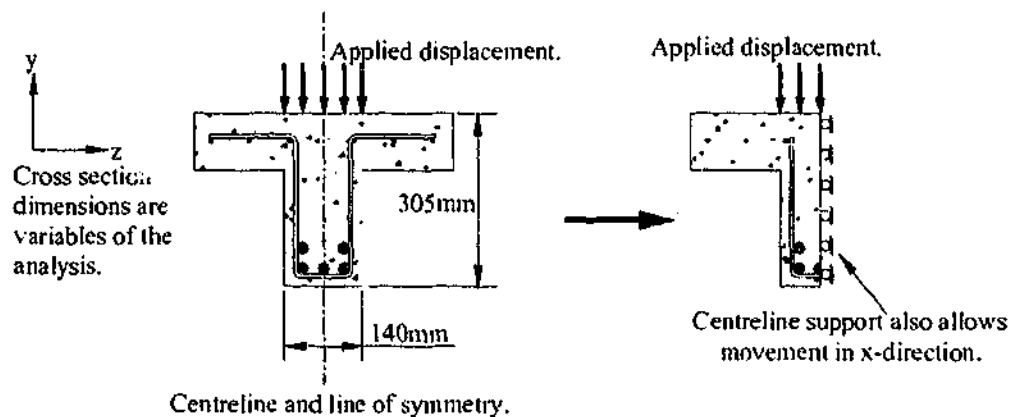


Figure 4.3-2 Modelling of the T-beam cross-section

The boundary conditions that were applied to each model were the applied loading, and the support conditions (including the support required by the symmetric condition that was used). The pin support shown in Figure 4.3-1 was applied as a point support at a node to prevent translation in the x , y , and z (out of the page) direction. The roller support in this figure is also a point support at a node that prevented translation in the y direction. The elements that were used in this model had only translational degrees of freedom; therefore, the nodes at the centre of width of the web were only restrained in the z direction (the roller supports shown in Figure 4.3-2).

The loading was applied to experimental specimens via controlled displacement. The controlled displacement that was applied in the experimental work was distributed over a 145mm diameter plate. This was simulated in the numerical modelling by application of a controlled displacement of nodes that were situated over the width of the web region. This was only applied to one row of elements in the direction of the span as it was found that forcing the displacement of elements along the length of the span to have equal displacement resulted in localisations of stress during the solution that brought about divergence of the numerical scheme. Figure 4.3-2 shows a schematic of the application of the load to a cross section. This load was not applied to midside nodes of the elements (these were 20 noded solid elements as will be discussed later).

4.3.2 Element Selection

To predict the behaviour and effectiveness of the flange of an RC T-beam, the models that were developed required distributions of stresses and strains to be produced in each of the orthogonal directions in the flange. Preliminary studies using plane stress, and shell elements revealed that the simplification of a 3D with these 2D elements produced results that were not consistent with the experimental work. 20 noded solid brick elements were adopted to avoid these problems. The details of these elements, and the reinforcing elements that were provided are discussed in this section.

4.3.2.1 Concrete Elements

The concrete was represented with 20 noded solid brick elements. These elements have a node at each corner, as well as a midside node that is located at half of the length of each side of the element. A 2x2x2 integration scheme was employed. This has been shown DIANA (1998) to be efficient in the calculation of stress profiles within a group of these elements.

This element is embedded within the DIANA software, and has shape functions of the following characteristics.

- (1) The strain ϵ_{xx} varies linearly in the x-direction, and quadratically in the y and z direction.
- (2) The strain ϵ_{yy} varies linearly in the y-direction, and quadratically in the x and z direction.
- (3) The strain ϵ_{zz} varies linearly in the z-direction, and quadratically in the x and y direction.

Seraj (1992) conducted an investigation into the variation in ultimate strength and stiffness (as measured by the slope of the load deflection curve) that was produced with varying element sizes. The results from this study indicated that element sizes up to 260mm produced satisfactory stiffness and ultimate load results for shear spans and total specimen dimensions comparable to the ones that were implemented in this study (note that these were 20 noded brick elements, therefore midside nodes were provided on each edge). Although this was the case from this study, for determination of the stress distribution throughout the depth of the flange, an adequate number of nodes throughout the depth of the flange were required. This was coupled with the fact that the aspect ratio of the element (ratio of two sides of the element) was limited to 2.5. The resulting mesh that was used had 192 elements in the web region in the critical shear span, and the following criteria for the flange overhangs (an illustration of a typical mesh is shown below in Figure 4.3-3).

- (1) Two elements throughout the depth of the flange for all specimens.
- (2) Distance between nodes of as close as possible to 25mm. A closer spacing was used when this was not achievable.
- (3) Alignment in the longitudinal direction with the web elements.

The study by Seraj (1992) does show some variation in the results of the ultimate strength with variation of the mesh size. The variations were mostly with the ultimate strength value, the stiffness remained essentially constant with these variations. These variations in

ultimate load with mesh size decreased as the mesh density increased, and the lower of the two values peak load for the analyses considered in this paper with the greatest mesh density were close. The latter was used to retain a reasonably constant mesh density between all specimens analysed and examine the ability of NLFEA to determine the peak loads, crack patterns, reinforcing response, failure mechanisms, and concrete strains in comparison to experimental work.

4.3.2.2 Steel Elements

The element called 'embedded reinforcement' in DIANA (1998) was used to simulate the reinforcement. This reinforcing element is produced in DIANA by specifying the start and end point of the reinforcing bar. The software package then considers the elements that this line crosses are 'mother' elements to the reinforcing elements. The reinforcing elements themselves do not have any degrees of freedom, and the strains at the integration points of these elements are calculated from interpolation of the strains at the integration points of the mother element. The interpolation of concrete strains in the mother element to the reinforcing element implies that a perfect bond exists in these models between the concrete and the embedded reinforcing steel. The only geometry required by DIANA (apart from the location) was the cross section area.

The location of the reinforcing throughout the length of the span of each specimen analysed was identical to that used in the experimental work (outlined in Chapter 3). Figure 4.3-2 shows the location within a cross section of the model. The stirrups were located at the nominated cover distance (15mm) from the edge of the concrete surface, and the longitudinal reinforcing was located throughout the depth of the model identically to that in the experiment. The cross sectional areas associated to the longitudinal reinforcing elements reflected the arrangement shown in Figure 4.3-2, i.e. the bar at the centre of the width was assigned only half of the area of the other longitudinal bars.

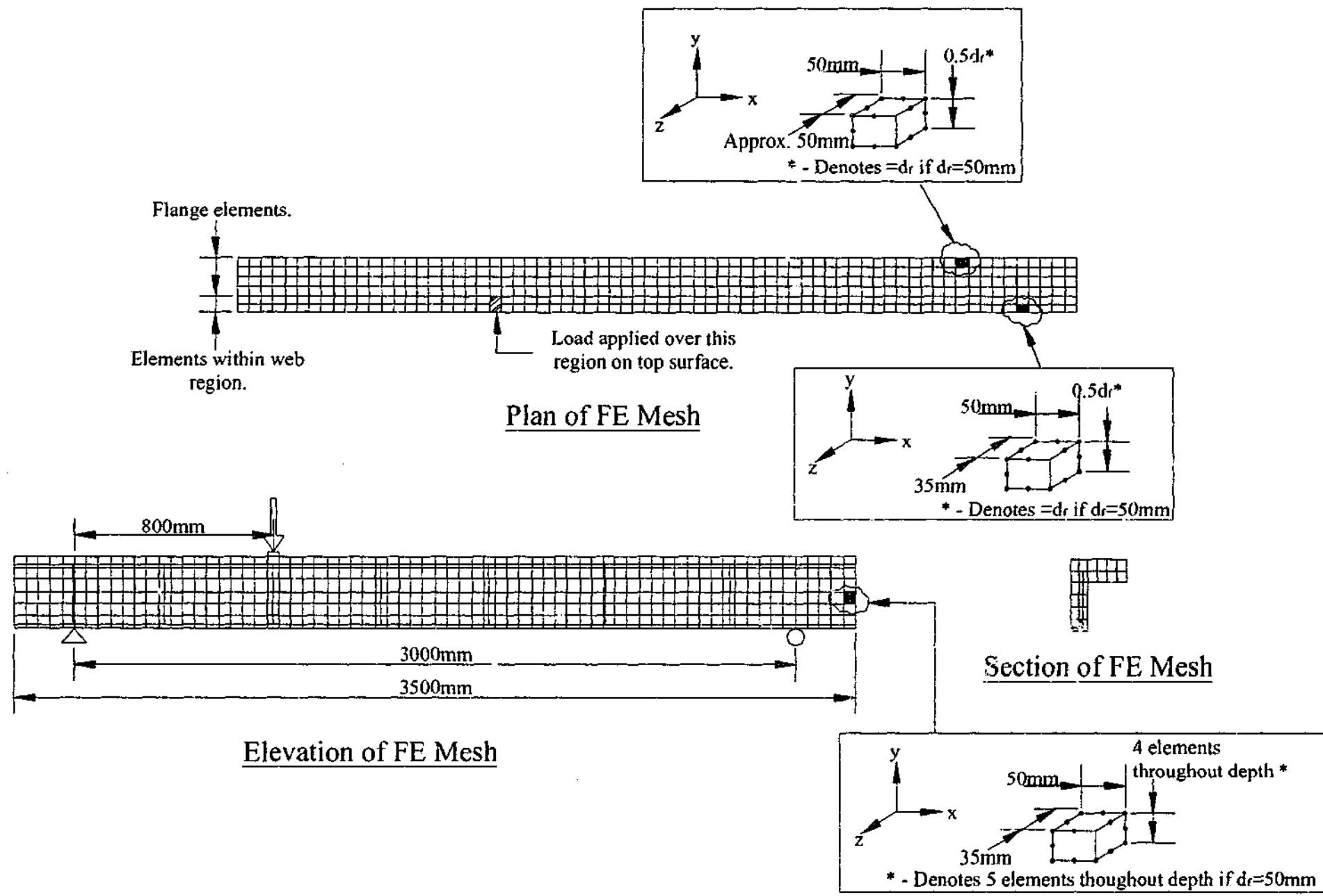


Figure 4.3-3 Details of the finite element mesh

4.4 Material Models

Aspects of the material behaviour were obtained from the tensile tests on steel samples and the concrete cylinders. Instrumentation of beam specimens provided information regarding the stirrup strains, and the strain state in the flange of the specimen, therefore, providing information into criteria required for a suitable constitutive model. This section summarises the material models that were used in the solution scheme based on these results.

4.4.1 Concrete Model

DIANA provides several constitutive models that are appropriate in modelling the compressive response of concrete. These are divided into two categories, the plasticity based formulations, and the total strain formulations. It assumes that the tensile response of concrete is elastic prior to cracking, but offers a variety of constitutive modelling approaches to the postcracking response of tension concrete. These models can also be divided into two categories, linear tension softening models, and nonlinear tension softening models.

The postcracking shear stiffness of an element in DIANA is given by a reduction factor, β that is applied to the shear modulus, G . Kotsovos (1995) implemented a similar method of reducing the postcracking shear stiffness. The study suggested that the value of β should never be zero, as numerical instabilities result, and recommended a minimum value of postcracking shear modulus of 5% of the initial value. The value that is selected for this term implies the amount of shear transfer that can be achieved across a cracked element; this is analogous to aggregate interlock.

Owing to the lack of agreement of the constitutive relations in literature that exist describing the compressive and tensile response of concrete, and also the lack of agreement on the contribution of aggregate interlock to the resistance of shear, a parametric study of the above variables was performed as part of this research. The variables of the parametric study are outlined below.

1. The value of β is assigned values of 5%, 10%, 15%, and 20%.
2. One of the plasticity formulations, and one of the total strain (representative of nonlinear compressive concrete constitutive model) formulations is used for the compressive concrete response.
3. One of the linear softening and one of the nonlinear relations is used for the tension softening response.

Further details of the implementation of the parametric study are outlined in Section 4.6. The remainder of this section describes theoretical aspects of the constitutive models that were implemented.

It should be noted that in both tension softening models, the smeared crack approach developed by Litton (1974) was used to model the cracking that developed at the tensile strength of the concrete.

4.4.1.1 The Drucker – Prager Model

The Drucker – Prager model was chosen as a representative model for the capability of the plasticity models to predict the response of the compression concrete. This model describes the yield surface for plain concrete in terms of the first normal invariant of stress (I_1), the second deviatoric invariant of stress (J_2), and the hardening parameter (κ). The general form of the failure surface is given in Equation 4.4.1. The condition $F=0$ represents failure of concrete. It is noted that associative plasticity was considered in this implementation of the modelling so that the internal angle of friction (ϕ) is equal to the dilatancy angle (ψ).

$$F = \sqrt{J_2} - \alpha_f I_1 - \beta c = 0 \quad 4.4.1$$

The coefficient α_f is a scalar quantity that is dependent on the internal angle of friction (this angle is dependent on the hardening parameter, i.e. $\phi(\kappa)$) and is given in Equation 4.4.2. The coefficient ζ is also a scalar quantity that is dependent on the initial angle of internal friction (ϕ_0), it is shown in Equation 4.4.2. The parameter c is the cohesion and is defined in Equation 4.4.3.

$$\alpha_f = \frac{2 \sin \phi(\kappa)}{3 - \sin \phi(\kappa)} \quad ; \quad \zeta = \frac{6 \cos \phi_0}{3 - \sin \phi_0} \quad 4.4.2$$

Strain hardening is included in the model by the relation of the cohesion to the equivalent plastic strain, κ . DIANA makes this relation within the software. This requires relation of the effective cohesion, and the equivalent plastic strain to a level of applied strain. The implementation of this requires an assumption regarding the stress strain response of the concrete. For the purpose of this analysis, it is assumed that the Thorenfeldt (1987) uniaxial curve describes the compressive response of all elements within a specimen. Application of this assumption yields the relation given in Equation 4.4.3 between the cohesion and the uniaxial compressive concrete stress (σ_c).

$$c = \sigma_c \frac{1 - \alpha_f}{\zeta} \quad 4.4.3$$

Assuming that the friction angle (ϕ) and the dilatancy angle (ψ) remain constant for all states of stress, and equal to the initial values (ϕ_0 and ψ_0), a relation of the equivalent plastic strain to the uniaxial plastic stress can be made. This is shown in Equation 4.4.4.

$$\kappa = - \frac{\sqrt{1 + 2\alpha_x^2}}{1 - \alpha_x} \epsilon_3^p \quad 4.4.4$$

In this equation, α_g is equal to the scalar quantity α_f (this is since associative plasticity is assumed), and the strain ϵ_3^p is the plastic component of the principal compressive strain.

4.4.1.2 Crack Model Based on Total Strain

DIANA uses a model called the Crack Model Based on Total Strain to calculate the compressive response of concrete. This is a hypo-elastic model that is modified to include secant unloading rather than nonlinear elastic unloading. It is this constitutive model that was used as the nonlinear elastic model in this investigation.

The model was based on the modelling approach implemented by Selby (1993). The implementation into DIANA uses a base compressive response curve that is given by Thorenfeldt (1987) and modified using relations by Vecchio and Collins (1993) that account for softening of the compressive response as a result of perpendicular tensile stresses. These relations are shown in Equation 4.4.5.

In this equation, σ_{comp} is the compressive stress, ϵ_{comp} is the compressive strain, f_p is the peak stress, f'_c is the cylinder strength, ϵ_o is the strain at f'_c , ϵ_{lat} is the perpendicular principal strain, β_σ is a factor that reduces the peak compressive stress in the presence of perpendicular tensile strain, and n and k are as shown.

The above equation accounts for softening of the compressive response of the compression concrete in the principal direction. To account for favourable compressive stresses in the perpendicular directions, the failure surface of Hseih et al. (1979) is implemented. This failure surface is shown in Equation 4.4.6.

In this equation, J_2 is the second deviatoric invariant of stress, I_1 is the first hydrostatic invariant of stress, and f_{c1} is the maximum of the three normal stress acting at an arbitrary point. The condition $F=0$ represents failure of the concrete. The Crack Model Based on Total Strain determines the stresses acting at a point, then iterates the principal compressive stress until the condition $F=0$ is true (or, the concrete fails). This results in a factor (identical to the

β_σ in Equation 4.4.5 that is applied to f'_c to produce a peak stress f_p that is the maximum stress that the concrete can sustain under the given triaxial stress condition.

$$\sigma_{comp} = -f_p \frac{\epsilon_{comp}}{\epsilon_o} \left(\frac{n}{n-1 + \left(\frac{\epsilon_{comp}}{\epsilon_o} \right)^{nk}} \right) \quad 4.4.5$$

where

$$n = 0.80 + \frac{f'_c}{17}; \quad k = \begin{cases} 1 & \text{if } 0 > \epsilon > \epsilon_o \\ 0.67 + \frac{f'_c}{62} & \text{if } \epsilon \leq \epsilon_o \end{cases}$$

$$f_p = \beta_\sigma f'_c \quad ; \quad \beta_\sigma = \frac{1}{1 + 0.27 \left(-\frac{\epsilon_{lat}}{\epsilon_o} - 0.37 \right)} \leq 1.0$$

$$F = 2.0108 \frac{J_2}{f_c^2} + 0.9714 \frac{\sqrt{J_2}}{f'_c} + 9.1412 \frac{f_{cl}}{f'_c} + 0.2312 \frac{I_1}{f'_c} - 1 = 0 \quad 4.4.6$$

4.4.1.3 Linear Tension Softening

The linear tension softening of concrete that was implemented into this modelling scheme was a simple formulation that relies only on knowledge of the cracking stress (f_{cr}), and ultimate strain (ϵ_u). The total tensile response of concrete using this model is shown below in Figure 4.4-1. By highlighting previous research Stevens et al. (1991) demonstrated that cracked reinforced concrete can sustain tension forces beyond the yield stress of the steel, for the purpose of this model, the ultimate concrete tensile strain is calculated as the yield strain of the steel.

4.4.1.4 Non - Linear Tension Softening

The nonlinear tension softening model that was implemented into this modelling strategy was that of Reinhardt (1984). This is shown diagrammatically in Figure 4.4-1. In this figure, the horizontal axis is labelled with the strain present after cracking (ϵ^c). This is the difference between the total strain and the cracking strain ($\epsilon - \epsilon_{cr}$). The vertical axis is labelled

with the stress present after cracking (σ^c); this is the value of stress associated with ϵ^c . The relations are described in Equation 4.4.7.

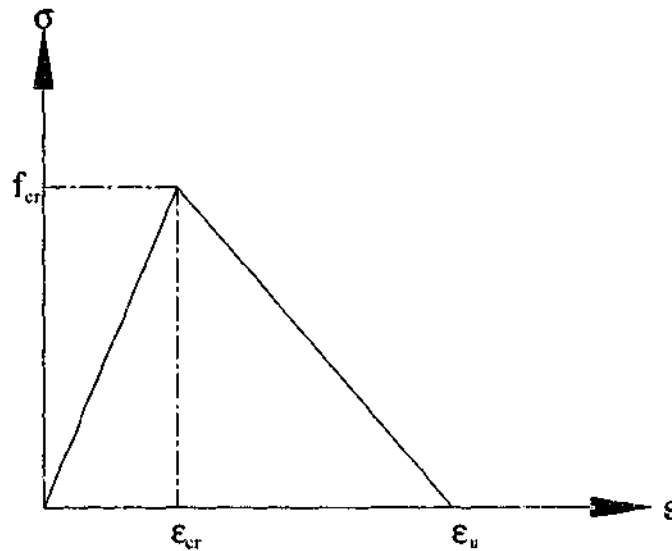


Figure 4.4-1 Linear tension softening response

$$\frac{\sigma^c}{f_{cr}} = \begin{cases} 1 - \left(\frac{\epsilon^c}{\epsilon_u - \epsilon_{cr}} \right)^{0.31} & \text{if } 0 < \epsilon^c < (\epsilon_u - \epsilon_{cr}) \\ 0 & \text{if } \epsilon^c \geq (\epsilon_u - \epsilon_{cr}) \end{cases} \quad 4.4.7$$

DIANA calculates the ultimate strain (ϵ_u) more exactly than that given above for the linear tension softening, the relation in Equation 4.4.8 is used.

$$\epsilon_u = 4.226 \frac{G_f}{h f_{cr}} \quad 4.4.8$$

in this method of calculating the ultimate strain, G_f is the fracture energy, h is the crack bandwidth, and f_{cr} is the cracking strength of concrete. The crack bandwidth is assumed for the purpose of this analysis to be equal to the average dimensions of the side of the elements. This is approximately 42mm. The method of calculating G_f is given in the following section.

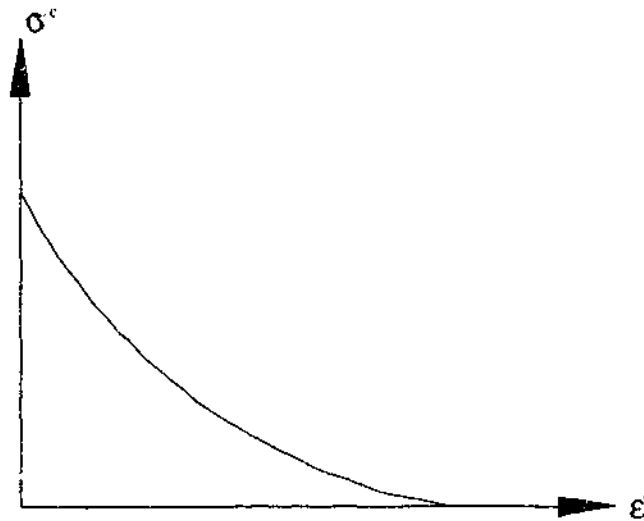


Figure 4.4-2 Illustration of the nonlinear tension softening curve

4.4.1.5 Material Properties

The 28 day cylinder strength for each concrete batch was obtained as part of the testing program. From this value, the Youngs Modulus (E_c), and the fracture energy (G_f), was calculated using the CEB-FIP (1990) Model Code for concrete. The tensile strength of concrete (f_{cr}) was calculated using Equation 4.4.9 which is the method given in the Australian concrete code of practice, AS3600 (3600). Poissons ratio was assumed to remain constant at $\nu=0.2$. These values of material properties were considered constant throughout the analysis procedure.

$$f_{cr} = 0.4\sqrt{f'_c} \quad 4.4.9$$

4.4.2 Steel Model

Results from instrumentation on the stirrups throughout the experimental work, as well as results of tensile tests on samples of the reinforcing batches indicated that if any reinforcing element had yielded, the strain on it was not enough to produce significant hardening. This allowed the use of an elastic perfectly plastic constitutive model to be used that simulates a bilinear stress-strain curve. The Von Mises relation was considered appropriate to model these reinforcing elements. Since this constitutive model is very accurate in the prediction of

the bilinear stress strain curve, any variations in this model were not considered in the parametric study. The Poissons ratio for steel was assumed to remain constant throughout the analysis at a value of $\nu=0.3$.

4.5 The Iteration Scheme and Convergence

To account for the nonlinear response of the specimens to load, the NLFEA solution procedure uses an incremental scheme. This scheme requires applying incremental displacements to the specimen, and within each increment of displacement, iterating to ensure that the internal and external forces balance. Section 4.6.2 outlines the method used to determine the magnitude of the increment of displacement, this section outlines the iterations within each displacement increment.

4.5.1 The Iteration Scheme

Section 4.6.2 outlines the displacement increments that were investigated during the implementation of this numerical model. Within each increment of displacement, the solution was iterated until satisfactory convergence was achieved.

Through preliminary analysis, it was found that the Constant Stiffness Iteration procedure was the most stable prior to the peak load for this implementation. At each increment of displacement, the increment of external load is calculated using a value of stiffness equal to the initial stiffness (the matrix $[K]$) of the previous load step. This stiffness is used to calculate the increment of applied external force (ΔF_{ext}) corresponding to the applied displacement increment (Δu). Application of the shape functions leads to values of strain at the Gauss points which can be used to calculate the increment of stress, hence the increment of internal force (ΔF_{int}). The relative energy calculated from these quantities (described in Section 4.5.2 below) is used to determine if a correct estimate of the internal forces, hence stress field has been achieved.

4.5.2 Numerical Convergence Criteria

DIANA has three choices of criteria for checking convergence. These are the force norm method, the displacement norm method, and the energy norm method. The former of these two criteria check only the force convergence, and displacement convergence respectively. The latter of the options checks a combination of the both (as energy is the product of force and displacement), and was considered to be a stricter, hence more accurate means of checking convergence; therefore, the latter was adopted.

DIANA calculates the value of the energy norm ratio using Equation 4.5.1. In this equation, the numerator of the ratio is the average relative energy variation between the current and previous iterates, and the denominator is the average relative energy of the previous two load steps. In the analysis, the required value of the energy norm ratio was set at 1×10^{-4} , but values less than 1×10^{-3} were considered acceptable in the analysis of the results.

$$\text{Energy Norm Ratio} = \frac{\left| \delta \mathbf{u}^T \begin{pmatrix} f_{-int,i+1} & + f_{-int,i} \end{pmatrix} \right|}{\left| \Delta \mathbf{u}^T \begin{pmatrix} f_{-int,1} & + f_{-int,0} \end{pmatrix} \right|} \quad 4.5.1$$

4.5.3 Definition of Failure

Failure of the numerical scheme, and hence the specimen was deemed to have occurred at the first of the following two items.

1. Divergence of the convergence criteria, i.e. excessive values of the energy norm.
2. The appearance of a large difference between the loads recorded at the point of applied displacement, and the sum of the reactions.

4.6 The Parametric Study

The variables of the parametric study are of two types. Firstly the concrete material properties variables as outlined in Section 4.4.1, and the size of the load step. This division broke up the parametric study on these variables into two parts. Firstly, the material model variations were examined, and secondly, the size of the load step was examined. This section discusses methodology of these two studies.

It was considered that the experimental specimens that were chosen for the purpose of comparison with the results of this parametric study should have the failure mechanisms that were obtained throughout the experimental work. For the purpose of determining the effect of the flange geometry on the shear strength of an RC T-beam specimen, there were in general two failure mechanisms that were exhibited in varying the flange width throughout a series. These are discussed in detail in Chapter 5, but for the purpose of this discussion, it is noted that specimens B2 and B5 failed by displaying mechanisms that were illustrative of this.

4.6.1 The Material Model Parametric Study

The material model variations outlined in Section 4.4.1 are outlined below.

1. The value of β is assigned values of 5%, 10%, 15%, and 20%.
2. The Drucker – Prager (denoted DP) material model, and the Crack Model Based on Total Strain (denoted TSM) were used for the compressive concrete response.
3. The linear tension softening (denoted as LS) and the nonlinear tension softening (denoted as NLS) relations by Reinhardt (1984) were used for the tension softening response.

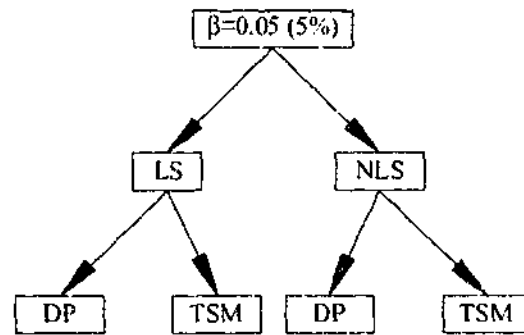


Figure 4.6-1 Schematic of the levels used in the parametric study

Figure 4.6-1 shows a schematic of the method used in implementing the parametric study on material models. The implementation considered firstly the value of β , secondly, the type of concrete tension softening was considered, and finally, the concrete compressive material model was considered. The lowest level in this figure includes all of the variables that were included in the analysis and was the level at which the analysis was run. For example, in the figure below, the analysis run for the left hand block on the bottom row uses Drucker – Prager material model, combined with the linear tension softening response with a value of $\beta=5\%$. The third block from the left also implements the Drucker – Prager material model, this time combined with the nonlinear tension softening response with a value of $\beta=5\%$.

The following notation will be introduced for the purpose of results analysis in Chapter 8. The left hand block on the bottom row which uses Drucker – Prager material model, combined with the linear tension softening response with a value of $\beta=5\%$ will be denoted $\beta=0.05:DP-LS$. This shorthand notation summarises all of the material property variations in this part of the parametric study.

Each value of β was associated with an analysis scheme as illustrated in Figure 4.6-1. This resulted in 16 analyses performed on the variables for each of the two experimental specimens used for comparative purposes (B2 & B5).

4.6.2 *The Displacement Step Size Parametric Study*

It was found during the parametric study that the analysis with material properties $\beta=0.15$:TSM-LS produced a load deflection response that was close to that in the experiment, as well as predicting a value of peak load close to that in the experiment. This combination of material models was used to determine the effect of the step size on the stiffness and ultimate load predictions.

The initial condition in determining the step size was to ensure that cracking did not occur in the first step of the analysis. Displacement steps of 0.2, 0.4, 0.5 and 1.0mm did not cause this to occur. The size of the subsequent steps was governed by two issues; firstly, the size had to be reduced as cracking influenced the results, and if this was not done solutions schemes were found to be unstable; secondly, the ratio between the initial step size when the specimen is uncracked, and that when the specimen is cracked could not be too large. Trial and error in preliminary analysis indicated that halving the displacement increment at a displacement before the cracking load resulted in a stable solution scheme. This was implemented into this parametric study.

In summary, for each specimen, B2 and B5, there were four displacement steps investigated for this parametric study. These are as follows:

1. Initial increment of displacement (D_i)=0.2mm, and subsequent increment (D_s)=0.1 mm (after two load steps).
2. D_i =0.4mm, and D_s =0.2mm.
3. D_i =0.5mm, and D_s =0.25mm.
4. D_i =1.0mm, and D_s =0.5mm.

The following notation will be introduced for the purpose of results analysis in Chapter 8. For material models $\beta=0.05$:DP-LS, a code for the initial applied displacement will be

appended to this. An analysis with initial displacement increment of 0.2mm, and subsequent displacement increment of 0.1mm, this code will be $D_i=0.2$, resulting in a description of $\beta=0.05:DP-LS; D_i=0.2$ for this model.

4.7 Modelling Plan

As stated in the objectives in Section 4.2, this research used NLFEA to examine the results of ultimate strength of specimens with variable flange proportions without the unintended material property variations that arose in the experimental work using a constant mesh density for all models. To do this, three stages of modelling were implemented as described below.

The first stage of the modelling was the application of the solution scheme using the material models and incremental scheme found to be best suited using the parametric study outlined in Section 4.6 to representative specimens of the experimental work to determine the best combination of material models as well as the best increment of displacement.

In the second stage of the modelling, the optimum combination of the above model characteristics was applied to the experimental specimens to determine the capability of NLFEA to predict the results. In this thesis, stage 1 experimental specimens are to compare the peak load, load-deflection response, crack patterns, and reinforcing strains. Stage 2 experimental specimens are used to compare the concrete strains, and the ability of NLFEA to predict the contribution of the flange to the resistance of shear as measured by a percentage contribution at the peak load.

The third and final stage of modelling implemented the optimum modelling scheme determined in stage 2 specimens of the same geometry used in the experiments but with concrete material properties of series 1 of stage 1, and steel material properties of series 2 of stage 1 experimental work.

The specimens in the stage two of the analysis (the experimental specimens) will be labelled with the same identifying mark that was used in the experimental work; e.g. Specimen B1 is the specimen of flange proportions 930x100 with $f_c=36.0\text{MPa}$, $f_{y,l}=340\text{MPa}$, and $f_{y,v}=398\text{MPa}$. The specimen in the stage three of the analysis (those modelled without the unintended variations in the material properties) will be given the same tags, but these will be preceded with the letters CMP to designate that they have constant material properties throughout the analysis procedure. For Example, Specimen CMP-B10 is the specimen with flange proportions 310x75 and has the material properties of $f_c=36.0\text{MPa}$, $f_{y,l}=340\text{MPa}$, and $f_{y,v}=300\text{MPa}$. Results of the second stage of the analysis will be presented for flange geometries identical to those in the experimental work. This is summarised below in table format for both of these stages in Table 4.7-1 & Table 4.7-2.

Table 4.7-1 Specimen numbers and material properties for stage 2 numerical modelling

Specimen Number	Flange Proportions (b _f x d _f (mm))	f _c (MPa)	f _{v,l} (MPa)	f _{v,y} (MPa)
B1	930x100	36.0	340	398
B2	620x100			
B3	465x100			
B4	310x100			
B5	225x100			
B6	Rectangular			
B7	930x75	30.8	340	308
B8	620x75			
B9	465x75			
B10	310x75			
B11	225x75			
B12	620x50			
B13	465x50	33.4	340	440
B14	310x50			
B15	225x50			
B16	465x50			
B16	465x75	50	340	300
B17	465x100			

Table 4.7-2 Specimen numbers and material properties for stage 3 numerical modelling

Specimen Number	Flange Proportions (b _f x d _f (mm))	f _c (MPa)	f _{v,l} (MPa)	f _{v,y} (MPa)
CMP-B1	930x100	36.0	340	398
CMP-B2	620x100			
CMP-B3	465x100			
CMP-B4	310x100			
CMP-B5	225x100			
CMP-B6	Rectangular			
CMP-B7	930x75	36.0	340	398
CMP-B8	620x75			
CMP-B9	465x75			
CMP-B10	310x75			
CMP-B11	225x75			
CMP-B12	620x50	36.0	340	398
CMP-B13	465x50			
CMP-B14	310x50			
CMP-B15	225x50			

Chapter 5 FLANGE PROPORTIONS, ULTIMATE STRENGTH AND FAILURE MECHANISMS

5.1 Introduction

This chapter presents the results of stage 1 experimental work, and subsequent analysis of these results. The primary focus of this discussion is to isolate the effect of the flange proportions on the ultimate strength and failure mechanisms of the specimens tested in this stage.

To ensure an accurate summary of the effect of varying the flange proportions of a T-beam on the shear strength of the considered specimens, the analysis of experimental results is broken up into two parts. Firstly, the ultimate strength results are normalised with respect to material properties so that results between specimen series can be compared. This allows the effect of variation of the depth ratio ($d_r=d_f/d_o$) on the ultimate shear strength to be examined. Secondly, failure mechanisms that were exhibited by the specimens throughout the testing regime are examined. All specimens failed exhibiting a shear mechanism, there were two distinct types of shear failure exhibited. A comparison of these failure mechanisms with the ultimate shear strength results enables determination of an upper bound for the effectiveness of the flange in the resistance of shear. Finally, the trend in the variation of the ultimate shear strength (V_u) with width ratio ($b_r=b_f/b_w$) is discussed.

Consideration is also given to the variations in the flange reinforcing that was placed continuously across the width of the flange. The variations in the ultimate shear strength in the specimens that were provided with this reinforcing are discussed.

5.2 Normalisation of Ultimate Strength Results

To ascertain the effect that the flange proportions have on the shear strength, it is necessary that any affect on specimen strength from the presence of variations in material properties be eliminated. Since web geometry, and reinforcing percentage are equal for all specimens (except where noted otherwise), a group of results can be produced that has only variable flange proportions. This is achieved by normalising the ultimate strength results as outlined below. The ultimate strength results are shown in Table 5.2-1.

As discussed in Section 2.2, the mechanism of shear resistance in a beam is widely accepted as being the sum of four contributions. These can be seen in Figure 5.2-1. These are the axial forces in the stirrups (V_s), the shear resistance of the compression concrete (V_c), the frictional resistance arising from aggregate interlock on the rough surface of a shear crack (V_a), and the shear resistance perpendicular to the span of the longitudinal bars resulting from the tendency for them to behave in a dowel like manner (V_d). Each of these components interacts to provide the ultimate shear strength (V_u) as shown in Equation 5.2.1.

$$V_u = V_c + V_s + V_a + V_d \quad 5.2.1$$

Consider now the approach implied in many codes of practice such as the American concrete code of practice (ACI 318-99 (1999)) and the Australian Standard, AS3600 (2001) whereby the total concrete contribution (denoted here as V_c) is a summation of the dowel action, aggregate interlock, and concrete contributions. This leads to Equation 5.2.2.

$$V_u = V_c + V_s \quad 5.2.2$$

Table 5.2-1 Ultimate shear strengths recorded for Stage I experimental work

	Flange Proportions	End 1 Shear Strength (kN)	End 2 Shear Strength (kN)
Series 1	930x100	132.5	*
	620x100	132.5	134.9
	465x100	122.5	124.7
	310x100	116.0	124.6
	225x100	115.2	116.1
	Rectangular	80.8	98.0
Series 2	930x75	123.4	129.8
	620x75	145.1	115.4
	465x75	98.76	107.5
	310x75	105.8	102.4
	225x75	83.3	92.75
Series 3	620x50	105.6	91.6
	465x50	112.2	110.9
	310x50	90.8	86.8
	225x50	101.4	101.1

* Denotes that the peak load for this specimen was influenced by the first end test and therefore was disregarded

This equation simply considers the ultimate strength of an RC beam as the sum of the steel and concrete contributions. Given the semi-empirical nature of the code formulations, the concrete contribution term within this equation implicitly includes all components of the concrete contribution (aggregate interlock, compression concrete contribution, and dowel action). Therefore, this equation is exhaustive in the consideration of the mechanisms of shear resistance and is appropriate for use in the examination of the shear strength by considering individual components of resistance. For the purpose of this work, Equation 5.2.2 gives a simple relationship by which variations in material properties can be separated and eliminated. The following sections outline the assumptions and process that are used to develop a term that eliminates material variations in the consideration of the strength of the specimens tested.

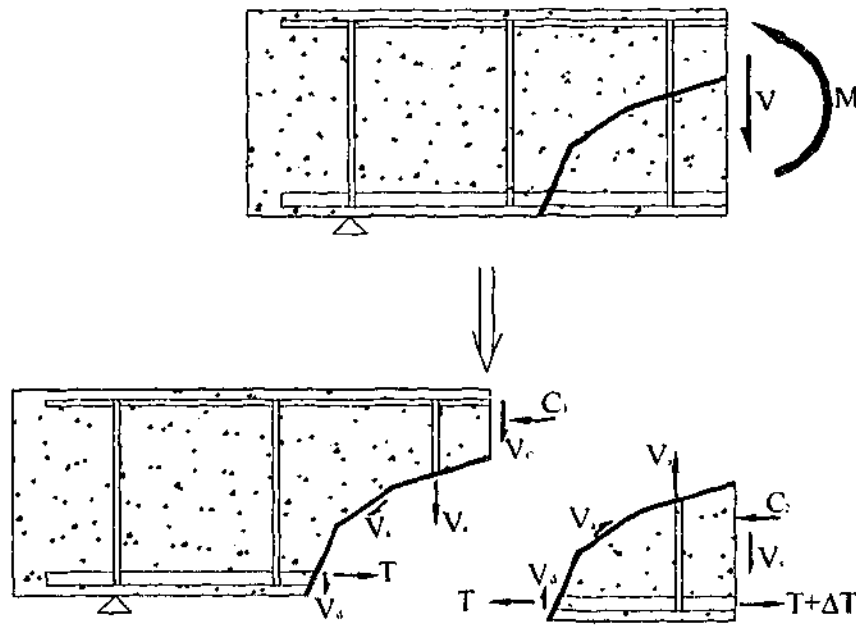


Figure 5.2-1 Mechanisms of resistance of shear by an RC beam with shear reinforcing

5.2.1 An Assumption Regarding Stirrup Contribution

The location of the strain gauges on the stirrups did not always correspond to the position of the shear crack. The results of this instrumentation did however indicate that if the critical shear crack did pass through a stirrup, then this stirrup either yielded, or was so close to yielding that the force in that stirrup was very close to the force attained by yielding that stirrup. It is noted that the critical diagonal web crack was well developed at the peak load in all specimens. The typical strain response of a stirrup that was intersected by a crack throughout the duration of an experiment can be seen in Figure 5.2-2.

Figure 5.2-2 shows an important feature of the stirrup behaviour. The appearance of the shear crack on the surface of the web was at approximately the same level of load that a stirrup that intersected the crack began to become effective. It is assumed that stirrups become effective at the appearance of a critical web crack by which they are intersected.

In addition to the above assumption, it will also be assumed that a stirrup is fully effective (reaches yield) if it is intersected by a crack in the web region of the beam. A stirrup was not considered effective if the crack passed below the level of the top most flexural

reinforcing bar. By superimposing the stirrup locations on the failed specimen, and using the above assumptions, it was found that in general two stirrups were intersected by a crack. This was not true for specimens B12 and B14. The crack came close to these stirrups but did not intersect them. Section 5.4.3 provides further discussion of this.

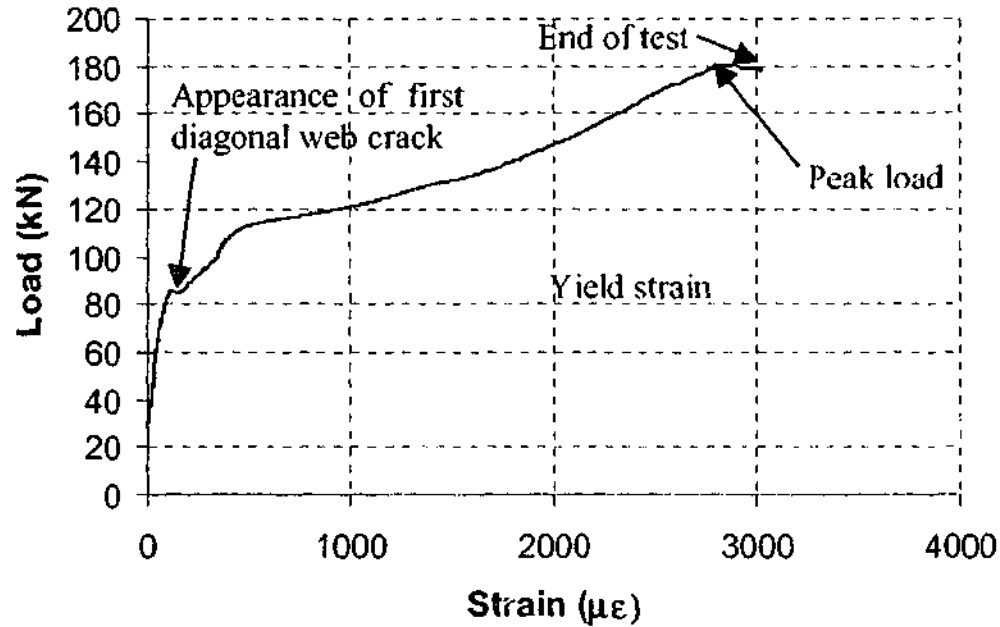


Figure 5.2-2 Typical stirrup strain vs. applied load for a stirrup which was intersected by a crack.

Comparison of the maximum strain recorded during the beam tests with the stress-strain results produced from tensile tests on the batch samples of the stirrup reinforcing indicate that negligible force additional to the yield force in the stirrup is produced by strain hardening in the bars.

From the above statements, it is assumed that the critical shear crack passes through two stirrups for each beam test. At failure these two stirrups give rise to a resistive force equal to the force produced at yield. Therefore, using the yield strength shown in Table 3.3-2 in Chapter 3, the average bar diameter determined from batch samples of 6.39mm, and the fact that each stirrup that is intersected by the crack has two legs in cross section, the stirrup contribution is calculated to be those values shown in Table 5.2-2.

Table 5.2-2 Total force carried by stirrups in each specimen series for stage I experiments

Series Number	Stirrup Contribution (V_s) (kN)
1	25.6
2	19.8
3	28.3

5.2.2 Normalisation With Respect to Concrete Strength

Knowing the stirrup contribution from Table 5.2-2, Equation 5.2.2 now provides a means of determining the total concrete contribution, V_c , for each specimen, as shown in Equation 5.2.3.

$$V_c = V_u - V_s \quad 5.2.3$$

Table 3.3-2 in Chapter 3 shows that there is still a variation in concrete strength between series of specimens that needs to be accounted for so that the results between each of these series can be compared. Many concrete codes of practice such as the Canadian Code, CSA A23.3-94 (1994) and the Australian Standard, AS3600 (2001) suggest that the total concrete contribution is a product of the web area and the square root of the concrete cylinder strength as shown in Equation 5.2.4.

$$V_c = cb_w d_o \sqrt{f_c} \quad 5.2.4$$

In Equation 5.2.4, b_w is the effective web width, d_o is the effective depth of the beam for shear, and quantity c is a constant (magnitude 1) having units of $\sqrt{\text{MPa}}$. Substituting this equation into Equation 5.2.3 results in Equation 5.2.5. The result of this equation is a term that is the concrete contribution that has been normalized with respect to the cylinder strength of the concrete. This term will be used for the examination of ultimate strength results as it

eliminates the effect of variations in concrete from the ultimate strength. This term will be referred to as the normalized concrete contribution of the specimen.

$$\frac{V_c}{b_w d_o \sqrt{f_c'}} = \frac{V_u - V_s}{b_w d_o \sqrt{f_c'}} \quad 5.2.5$$

Since an equal stirrup contribution is assumed for all specimens within each series, any change in the normalised concrete contribution directly follows from a change in the shear strength of the specimen under consideration. The results of experimental work shown below present this normalised concrete contribution against the width ratio (b_f/b_w) for each depth ratio (d_f/d_o). Any change in the normalised concrete contribution with the width ratio for a given depth ratio shows that the shear strength of that specimen is varying with the width of the flange only. Conversely, any change in the normalised concrete contribution for a given width ratio corresponding to a change in depth ratio shows that the shear strength of that specimen is varying with the change in the flange depth only.

5.3 Failure Mechanisms Exhibited by Stage 1 Specimens

The majority of specimens that are described in Chapter 3 failed exhibiting a mechanism of shear. Of the specimens that failed in shear, two distinct mechanisms were displayed. This section discusses these mechanisms, and the range of conditions under which they were produced.

5.3.1 *The Beam Shear Mechanism*

The beam shear mechanism displayed by specimens was identical to the typical failure mechanism used for shear analysis of RC rectangular beams. The diagonal tension crack that formed in the web extended to the longitudinal bars where it began running along the length of these bars instigating dowel action. The other tip of the crack extended to the flange-web interface. At failure, these specimens exhibited a crack on the edge of the flange. This crack appeared to correspond to a diagonal tension splitting of the flange. This type of mechanism

is shown in Figure 5.3-1. The crack on the edge of the flange continued on the underside of the flange to meet with the diagonal tension crack at the flange-web interface as one continuous crack.

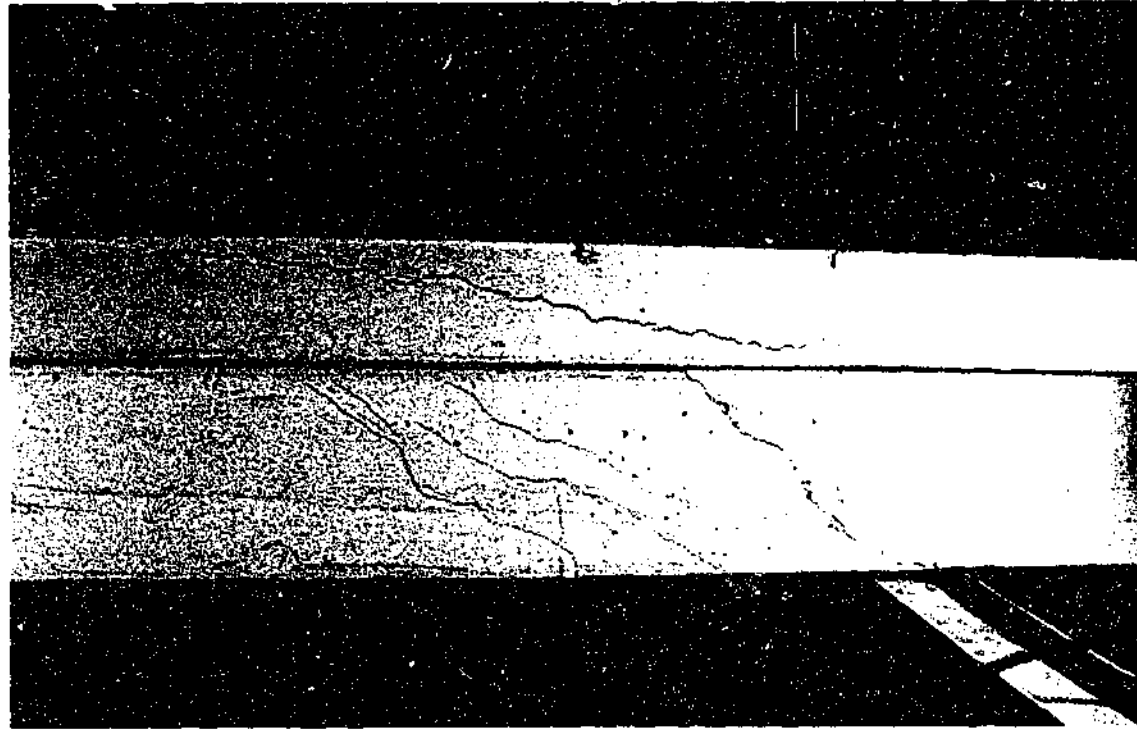


Figure 5.3-1 Typical beam shear crack patterns exhibited by Specimen B4

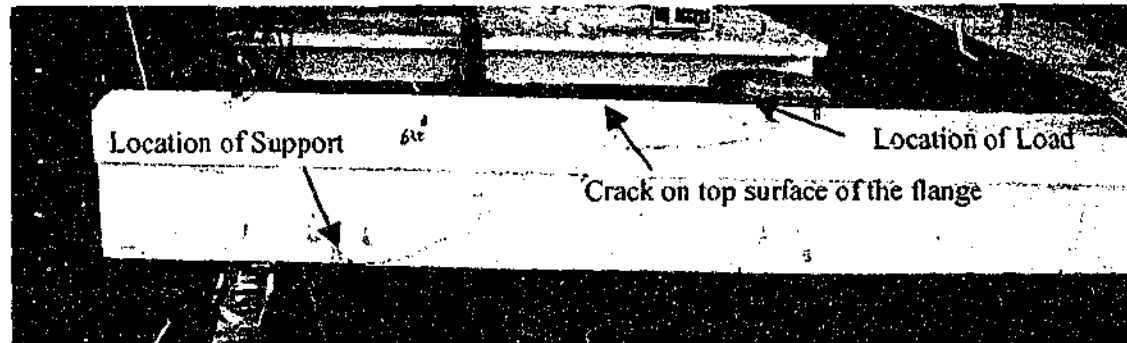


Figure 5.3-2 Beam shear failure mechanism cracks exhibited by Specimen B11

In addition to the above cracking pattern, specimens exhibited cracking laterally across the top surface of the flange similar to that shown in Figure 5.3-2. This photo of specimen B5 shows that at failure, the crack on the top surface of the flange penetrated the entire width of the flange. Not all specimens exhibited a crack that was continuous over the top surface as shown in this picture, but all specimens did display cracking in the lateral direction on the top

surface of the flange. This suggests that the beam shear mechanism that is described above is similar to the mechanism proposed by Hoang (1997) discussed in Section 2.2.3

5.3.2 *The Punching Shear Mechanism*

Formation of the punching shear mechanism began in a similar fashion to the aforementioned beam shear mechanism. The lower tip of the diagonal tension crack in the web continued through to the longitudinal reinforcing where it propagated as a dowel crack. The other tip met with the flange-web interface. As the load approached the ultimate load, the crack at the flange-web interface started to propagate into the underside of the flange at an angle that was inclined to the transverse directions of the beam. At the failure load, this crack on the underside of the flange continued along the length of the span. In addition to this, cracking appeared on the top surface of the flange. These crack patterns are shown in Figure 5.3-3-. It can be clearly seen from these photos that the cracking corresponds to the tendency of the load point to punch through the flange.

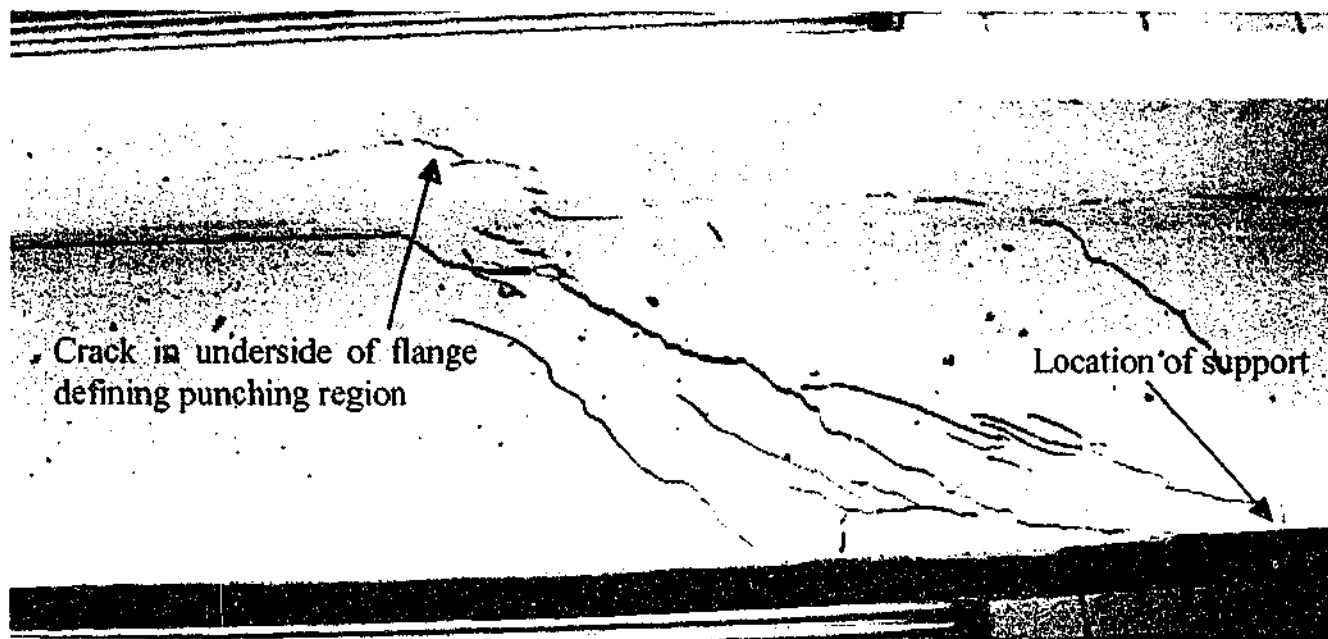


Figure 5.3-3 Typical punching shear cracks on the underside of the flange of specimen B15

Series 1 and series 2 specimens exhibited the beam shear mechanism for specimens with width ratio $b_f/b_w \leq 3.32$. Other specimens in each of these series ($b_f/b_w = 4.43, 6.64$) exhibited punching shear failure mechanisms. Although series 3 displayed the same bounds as

series 1 and 2 beams, it is noted that the specimen with width ratio $b_f/b_w=3.32$ began to display cracking on the underside of the flange consistent with the aforementioned punching shear cracks. However, the beam shear cracks were predominant on this specimen at failure.

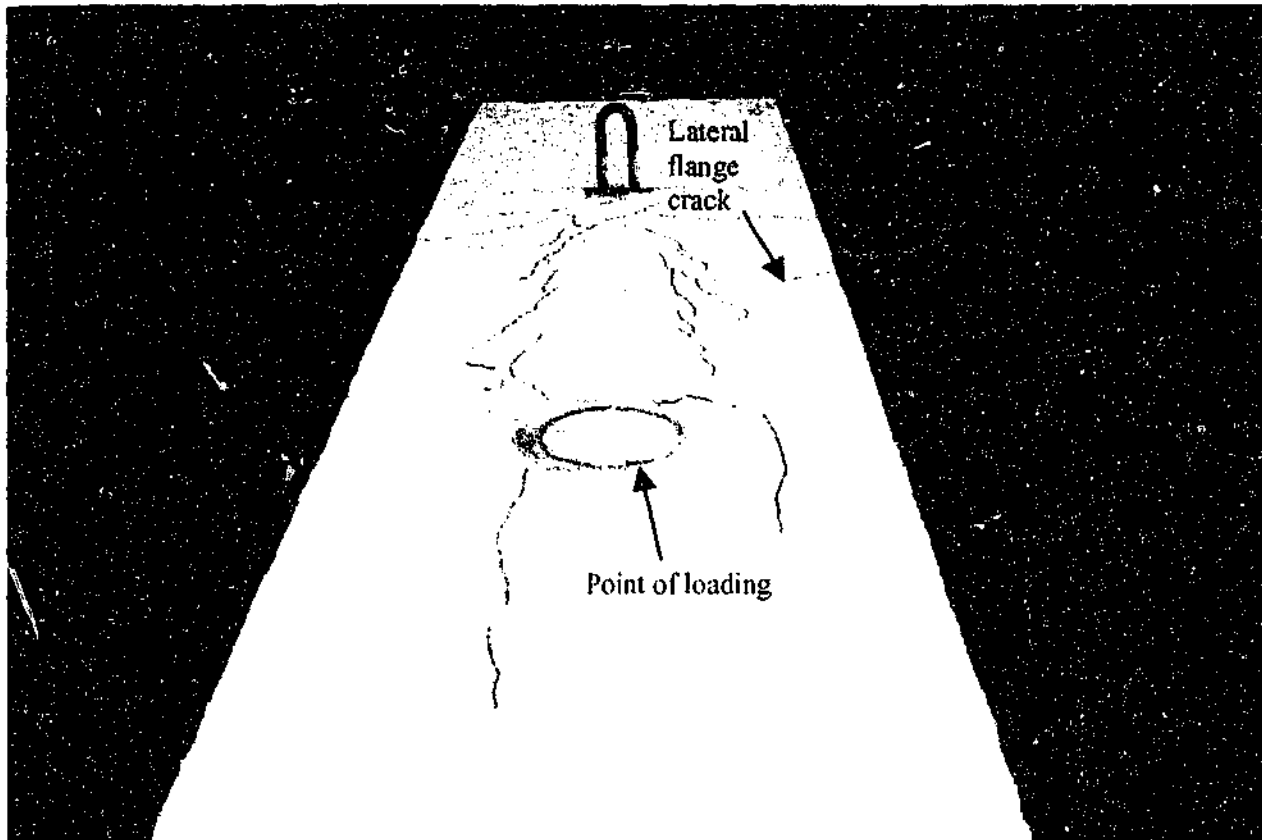


Figure 5.3-4 Typical crack pattern for punching shear mechanism on the top of the flange of specimen B12

It can be seen in that there were cracks that propagated laterally across the width of the flange in this mechanism. In the above photo, the crack is not continuous over the entire width, but is present over almost half the width of the flange. These cracks did not form part of the failure mechanism, but it is noted for later discussion that they were present on all specimens that displayed the punching shear mechanism.

5.4 Effect of the Flange Proportions on the Concrete Contribution of Stage 1 Specimens

The effect of the flange proportions on the ultimate shear strength of the experimental specimens is examined in this section. In each of the three series of specimens cast in this stage of work, the material properties, web geometry, reinforcing percentages and flange depth were identical for each specimen. The only variable in each series was the flange width. The ultimate strength values obtained from the series are used to examine the effect of varying the flange width of a T-beam on the ultimate strength of this type of element.

Examination of the effect of variations in the flange depth requires comparison of results between series. Since there are varying material properties between beam series, the normalised concrete contribution is used in an effort to ensure that material property variations do not affect the results.

5.4.1 Variation of Normalised Concrete Contribution With the Width Ratio for Series 1 Specimens ($d_r=0.33$)

As shown in Figure 5.4-1, the ultimate strength of series 1 results show a sharp increase in the normalised concrete contribution (24% in the average result) for a small increase in the width ratio from $b_f/b_w=1.0$ to $b_f/b_w=1.61$. Beyond this, the gradient of the increase in normalised concrete contribution decreases, and is fairly constant up to a width ratio of $b_f/b_w=4.43$. Beyond this, the increase in the width ratio can be seen to have little contribution to the normalised concrete contribution.

It is noted that the result corresponding to a width ratio of $b_f/b_w=6.64$ could not be repeated, as testing of the first end damaged the shear span of the second end. The result that is presented for the upper, average and lower results is that of the first end test only.

The width ratio at which the increase in ultimate shear strength ceases is $b_r=4.43$. This corresponds to the change of failure mechanisms from beam shear to punching shear as described above in Section 5.3.

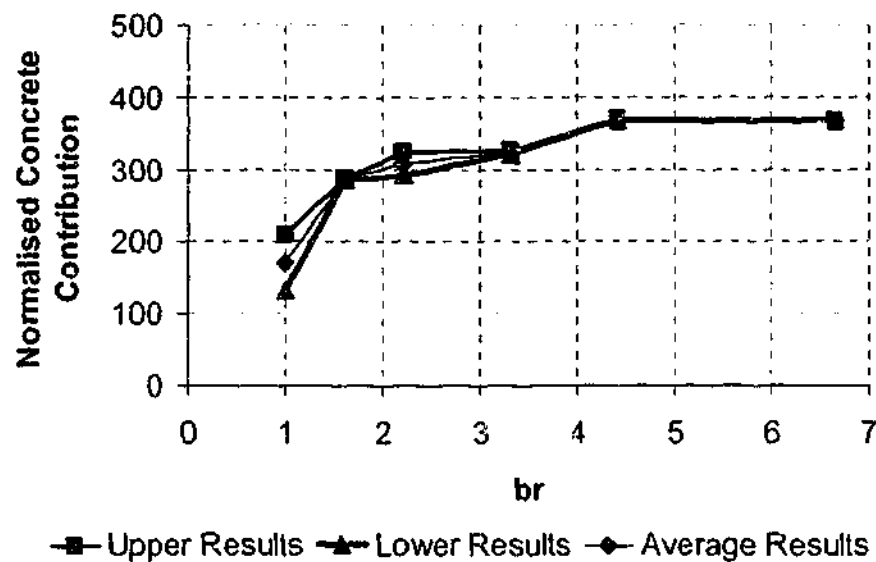


Figure 5.4-1 Normalised concrete contribution vs. width ratio for series 1 specimens

5.4.2 Variation of Normalised Concrete Contribution With the Width Ratio for Series 2 Specimens ($d_r=0.25$)

Figure 5.4-2 shows the variation of the normalised concrete contribution of series 2 specimens with the width ratio of the specimens. This figure shows a significant increase in the normalised concrete contribution (81% in the average result) from a web ratio of $b_f/b_w=1.0$ (the rectangular beam) to $b_f/b_w=2.21$. The trend in the results from this point up to a web ratio of $b_f/b_w=4.43$ is for a steady increase in normalised concrete contribution. The last two average values suggest that no increase in concrete contribution is displayed after $b_f/b_w=4.43$.

As for series one results, the width ratio at which the increase in ultimate shear strength ceases is $br=4.43$. This corresponds to the change of failure mechanism from beam shear to punching shear as described above in Section 5.3.

5.4.3 Variation of Normalised Concrete Contribution With the Width Ratio for Series 3 Specimens ($d_r=0.17$)

Figure 5.4-3 shows the variation of the normalised concrete contribution of series 3 specimens with the width ratio of the specimens. This figure shows variability in the normalised concrete contribution (and hence shear strength) of the specimens with the flange width. It can be noticed that the values of normalised concrete contribution for specimens with width ratio 2.21 and 4.43 (B14 and B12 respectively) are lower than the values of the specimen with smaller flange widths.

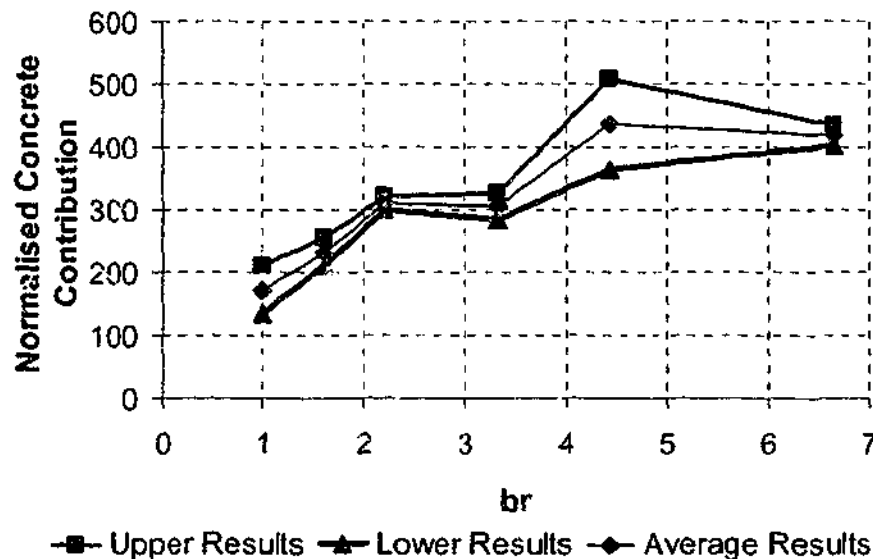


Figure 5.4-2 Normalised concrete contribution vs. width ratio for series 2 specimens

The failure mechanisms were such that all specimens with the exception of those with width ratio 4.43 failed in beam shear. The latter specimen failed by exhibiting the punching shear mechanism. These results suggest that the presence and increase in width of the thin flange in this series of specimens did not provide the significant increases observed in the above two series.

Section 5.2 outlined that the critical diagonal web crack in specimens with width ratio of 4.43 and 2.21 (Specimens B12 and B14 respectively) intersected only one stirrup above the level of the top of the flexural reinforcing. A second stirrup was not intersected in these two

specimens, but the critical shear crack did pass very close to this stirrup. For comparison purposes, the average values of concrete contribution with one stirrup and two stirrups are presented in Figure 5.4-4.

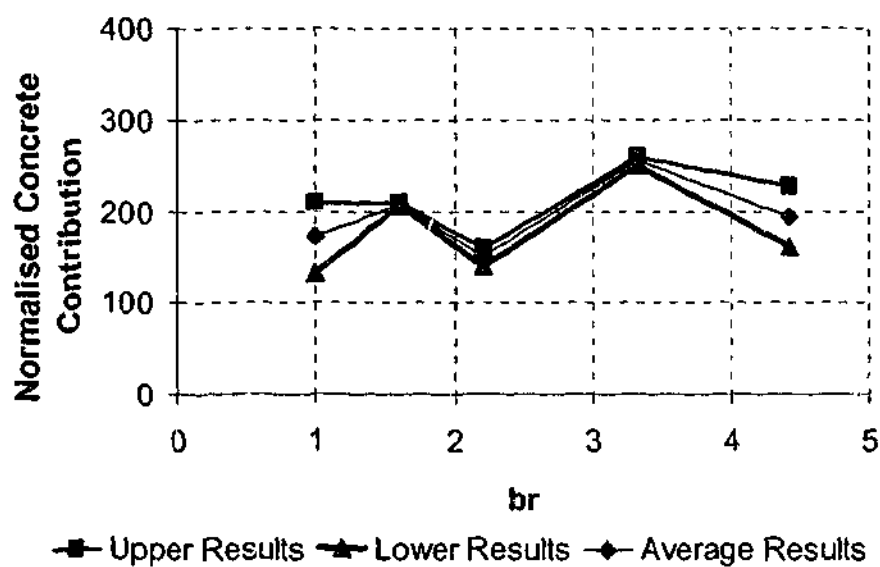


Figure 5.4-3 Normalised concrete contribution vs. width ratio for series 3 specimens

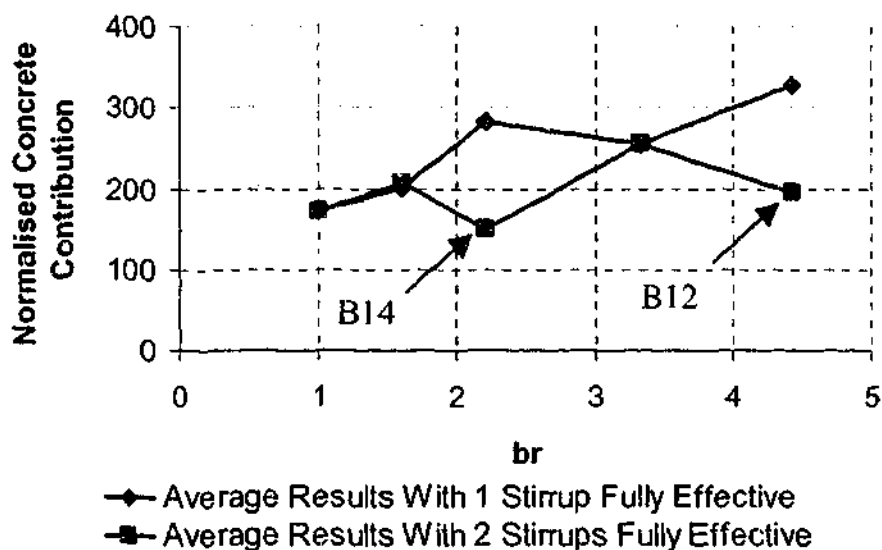


Figure 5.4-4 Comparison of average concrete contribution for series 3 with 1 and 2 stirrups considered effective for Specimens B12 and B14

It can be seen that a significant difference in the concrete contribution is produced when only one stirrup is considered effective in this series. It is thought that a significant contribution by the second stirrup would be made to the shear strength, as the critical crack was so close to the stirrup. The true trend in normalised concrete contribution would therefore be closer to the lower of the two lines. It is noted in general an upward trend in the normalised concrete contribution is observed when combining these average results. For the purpose of comparison with the two other beam series, the normalised concrete contribution with two stirrups considered effective will be used.

To further identify the flange contribution to the shear strength in this series, the values of shear strength obtained are presented in Figure 5.4-5 below against width ratio. These are the values shown in Table 5.2-1. This figure shows the presence and increasing width of the thin flange in this series is not making the significant contribution as seen in series 1 and series 2 specimens. This would further suggest that the flange contribution would have remained fairly constant throughout this series.

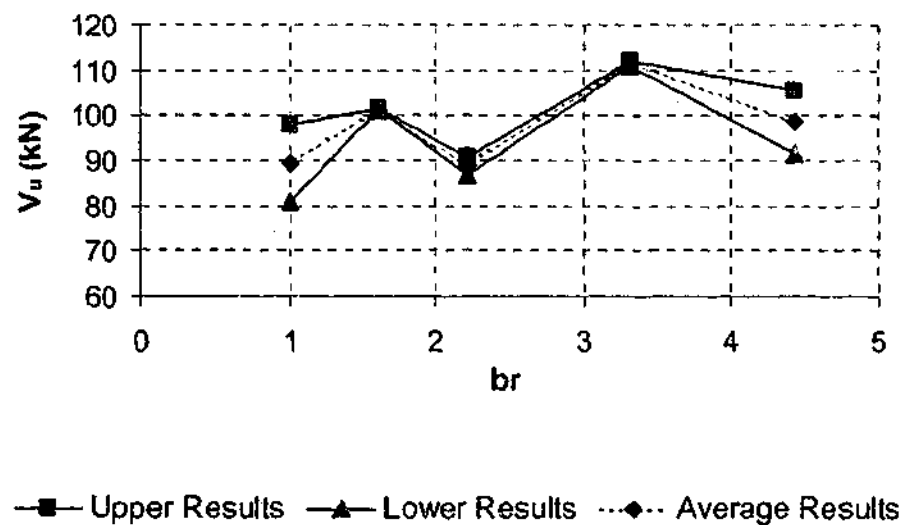


Figure 5.4-5 Ultimate strength vs. width ratio for series 3 specimens

5.4.4 Variation of the Normalised Concrete Contribution With the Depth Ratio

To determine the effect of the variation of the depth ratio (d_f/d_o), the average results of the normalised concrete contribution against width ratio are presented in Figure 5.4-6. Series 1 ($d_f/d_o=0.33$) and series 2 ($d_f/d_o=0.25$) results display a very similar trend in this comparison until the width ratio of $b_f/b_w=4.43$, or the onset of the punching mechanism. This suggests that the increase in ultimate shear strength of specimens failing by a beam shear mechanism in these two series is comparable. As aforementioned, series 3 results show no consistent variation in the normalised concrete contribution with the width ratio. It is concluded here that there is a minimum value of flange depth that is required for the flange to contribute to the resistance of shear. A series of specimens with a flange depth less than this will display no increase in normalised concrete contribution, and hence shear resistance, with an increase in flange width. For specimens that fail in beam shear, any change in width for a flange deeper than this critical value, will yield a similar change in ultimate strength results (and in normalised concrete contribution) regardless of the flange depth.

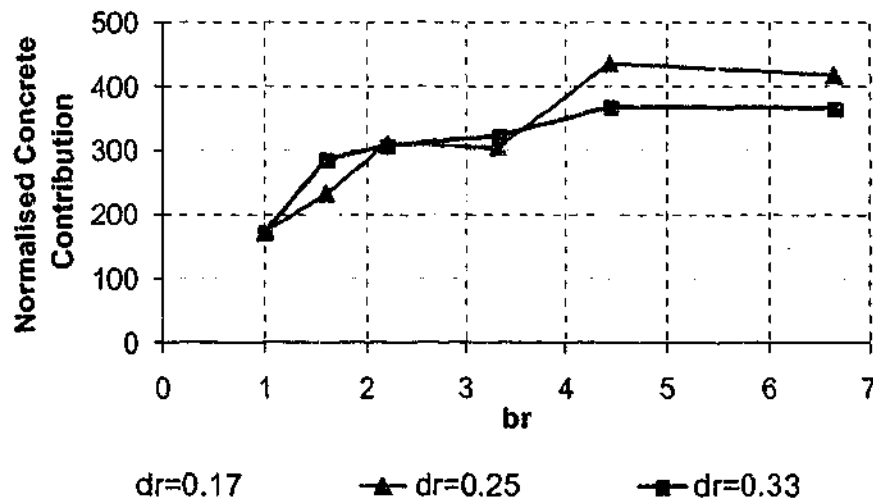


Figure 5.4-6 Average normalised concrete contribution comparison

5.5 The Effect of Lateral Reinforcing Bars on the Ultimate Shear Strength

As discussed in Chapter 3, lateral reinforcing bars that were placed continuously throughout the width of the flange across the web region were included in series 1, and on one end of the series 3 specimens. This section will discuss what effect the inclusion of this reinforcing had on the ultimate strength of the specimens to which they were provided. Firstly, the results of series 3 experiments will be discussed, and then anomalies in the series 1 and series 2 experimental results will be discussed.

5.5.1 Effect of Lateral Reinforcing on Series 3 Ultimate Strength Results

With reference to Figure 5.4-3, the results of ultimate strength for specimens of this series only show a large variation between the shear at ultimate strength for the two end tests for specimens with $br=1.0$ and $br=4.43$. The former of these two is the specimen of rectangular cross section, the variation in these results will not be discussed in this section as it is of different geometry to those which are being considered. The lower results in this graph are from the second end test, and the upper results are from the first end test.

In specimens of T-beam geometry, the specimens which display the beam shear failure mechanism do not display a significant scatter in the ultimate strength results, but it is only the specimen with width ratio $br=4.43$ that exhibits a significant difference in the shear at ultimate strength. This specimen failed by displaying a punching shear mechanism.

5.5.2 Anomalies in Series 1 and Series 2 Results

Referring to Figure 5.4-6, it can be seen that the difference in average shear strength between series 1 and series 2 specimens is not significant where the beam shear mechanism causes failure. Where the punching shear mechanism brings about failure of the specimens (width ratios of $br=4.43$ and 6.64), it can be seen that there is a significant difference between the average ultimate strengths of series 1 and series 2 specimens.

The specimens in series 2 contain lateral reinforcing continuous across the width of the flange, and the specimens of series 1 do not. It is suggested here that the influence of the lateral reinforcing is to increase the strength of the specimens only when they fail with a punching shear mechanism.

5.6 Conclusions from Stage 1 Experimental Work

The above is a presentation of trends in the normalised concrete contribution results calculated from the ultimate shear strength for stage 1 experimental work. Normalised concrete contribution results of each series have been presented together to determine the variations in shear strength that arises from an increasing flange width. To ascertain the effect of increasing the flange depth, the average normalised concrete contribution for each series was compared.

Several facets of the behaviour of this type of specimen as well as the trend in ultimate strength of this type of specimen can be concluded from this stage of experimental work, and normalisation procedure. These are outlined below.

1. A shear critical point loaded RC T-beam that is web reinforced will fail by either one of two mechanisms. The first is a beam shear mechanism in which a diagonal tension crack continues from the web and into the flange. The second is a punching shear mechanism whereby the applied load punches through the flange and the web separates from the flange.
2. The effectiveness of the ratio of flange width to web width (b_f/b_w) on the shear strength of a point loaded RC T-beam is dependent on the ratio of flange depth to the effective depth for shear (d_f/d_o).
3. The flange width is the most significant parameter in increasing the shear strength of a T-beam specimen. In the results presented in this chapter, the flange depth has an insignificant effect on the shear strength of a T-beam.

4. The flange width appears only to have discernable influence on the shear strength of a T-beam when the depth ratio of the specimen is above a certain value. In the three series presented above, this depth ration is $dr=0.16$.
5. The upper bound to the beam shear failure mechanism is provided by the punching capacity of the flange. Once the b_f/b_w ratio is large enough the punching shear mechanism will occur, and the load point will punch through the flange. The shearing resistance of the specimen is suggested to be the sum of the punching capacity of the flange in addition to the shearing capacity of the web. Any further increase in the flange width will not produce an increase in the shear resistance.
6. If the flange of a specimen is wide enough to allow a punching shear failure to occur, the presence of reinforcing running laterally across the width of the flange (continuous over the web) will increase the punching resistance of the flange, hence increasing the overall capacity of the specimen.

Chapter 6 VALIDATION OF THE EXPERIMENTAL ANALYSIS METHOD

6.1 Introduction

The instrumentation system described in Chapter 3 outlines the use of different types of strain gauges to measure strains at different points throughout the width and depth of the flange of an RC T-beam specimen. The intent of measuring the strains at the locations discussed is to calculate stresses, forces, and lever arms for equilibrium considerations.

The use of this instrumentation is prone to many problems. Orthogonal alignment of the gauge in all directions is difficult to achieve, any deviation from the orthogonal direction would result in a reading that is not the strain required. The misalignment of the gauges could be through placing, but also, the location of the embedded gauges could possibly be disturbed through vibration of the concrete after pouring.

The embedded gauges are coated with a material that has a roughened surface. An accurate reading of strain from this type of gauge requires adhesion of the placed concrete to this roughened surface. It can be easily envisaged that vibration in the vicinity of the gauge may not achieve the required adhesion between the concrete and the gauge, perhaps voids may form around the gauge resulting in a strain reading that does not correspond to the strain in the concrete at that location.

It can be seen from Chapter 3 that the strain gauges that were used had slightly different lengths. The surface gauges were approximately 40mm shorter than those that were embedded with in the concrete. The measurement of strain that is recorded from a gauge can be thought of as an 'average' of the measurement over the entire length of the gauge. Although this is not entirely accurate, this analogy illustrates that the difference in lengths of the gauges may have an effect on the reading that is output.

The final concern that arises in the implementation of the procedure in Chapter 3 is the capability of the constitutive relations of the MCFT that are to be implemented to calculate stresses from the strain distributions that were obtained from the experiments. Although these relations have been formulated from experimental work, the combination of the compressive and tensile response in these relationships has not been proven on an experimental basis in any previous work.

For the above reasons, it was decided that a procedure for validation of the instrumentation system be developed, and the system tested. This chapter describes the validation procedure used as well as the results that were obtained from the validation experiments.

6.2 Outline of Validation Procedure

To validate the instrumentation system described in Chapter 3, an identical system to that applied to T-beam flanges was applied to two small slabs prior to the experiments on T-beams being performed. Two slabs were used for validation in order to determine the level of confidence that can be had in the system given the potential sources of experimental error in the system outlined above.

Application of this system to a slab allows for determination of the strain distribution throughout the depth and width of the specimens. The measurement of the distribution throughout the depth allows for calculation of stress distributions, therefore sectional forces and lever arms, and hence total sectional bending moments and shearing forces.

Validation of the instrumentation system and associated analytical procedure can be achieved through analysis of the results that are obtained from this calculation procedure. The comparison of sectional tension and compression forces calculated from measured strains and MCFT relations indicate two things, the accuracy of the measured strains, as well as the ability of the relations in the MCFT to produce accurate results of the axial sectional forces acting on the section of the slab. Comparison of the sectional bending moments calculated using this procedure with equilibrium bending moments indicate the accuracy of the calculation of the lever arm. The results of shear force give an indication of the level of confidence that can be adopted in the system, as well as the accuracy that can be expected when this instrumentation system is applied to the flange of the T-beams.

6.3 Specimen Details

To ensure that the validation produced results that could be compared with known equilibrium values, it was required that the specimens tested had two characteristics. Firstly, a minimum amount of reinforcement ensures that minimum instrumentation is required to determine sectional forces using this procedure. Secondly, the specimens were required to be beam type specimens to ensure that sectional actions could be calculated using equilibrium.

This section outlines firstly the specimens that were designed, as well as the instrumentation system that was adopted. The instrumentation system is based on that outlined for use in T-beam flanges, but slight adaptations were required to suit the geometry of the specimens tested in this validation exercise.

6.3.1 Specimen Geometry and Loading

To ensure that the specimens were of simple nature as required in this procedure, small slabs were used. These were provided only with flexural tension reinforcing. The details of these specimens are illustrated in Figure 6.3-1 - Figure 6.3-2. Both of these specimens were tested under three point loading. The load P in Figure 6.3-2 is a line load over the entire width of the slab. The load P was applied via a controlled displacement of 0.01 mm/sec.

The ultimate strength of the specimens in flexure was estimated using Australian Standard AS3600 (2001), and the shear capacity by the MCFT. The estimated ultimate loads were $P=59\text{kN}$ for shear failure, and $P=79\text{kN}$ for flexural failure.

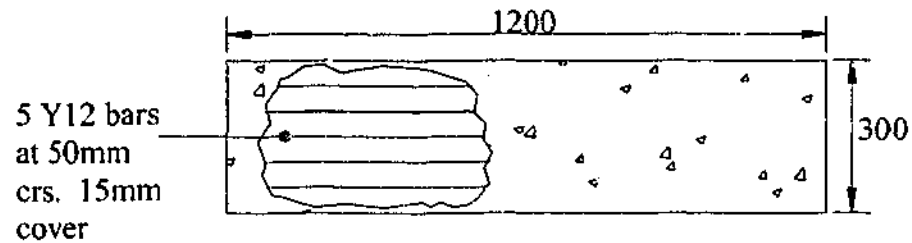


Figure 6.3-1 Plan of specimens S1 and S2

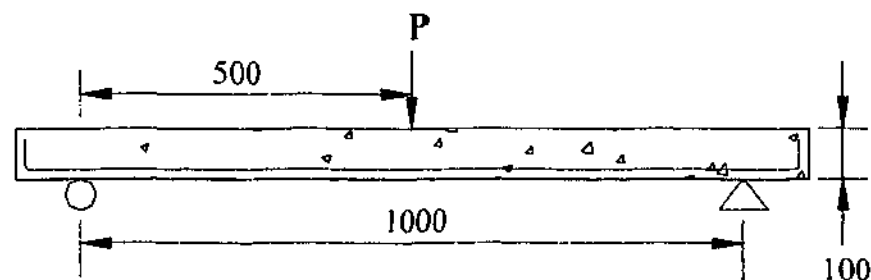


Figure 6.3-2 Elevation of specimen geometry and loading

6.3.2 Specimen Instrumentation

To keep the instrumentation in this series similar to that intended for use in the T-beam flanges, strain gauging was applied at two sections along the span of the slab. At each these cross sections, three gauges were placed on the top surface, three at the centre of depth, and three on the underside of the slab. Figure 6.3-3 - Figure 6.3-4 illustrate the layout of the strain gauges.

Each row of gauges was placed directly underneath the above layer. This ensured that a profile of strain was measured at three points across the width and two points along the span and three locations throughout the depth. The measurement of strain at two locations along the length of the span allows use of dual section analysis to calculate shearing forces.

The reinforcing bars were not instrumented. This was as a result of concern of the influence on the concrete strain results arising from loss of bond in the region of the reinforcing strain gauge. Strains in the reinforcing bars were calculated using concrete strains as discussed below. These calculations assume a perfect bond between the concrete and reinforcing bar.

The gauges positioned at the centre of the concrete cross section were concrete embedment gauges. These are long gauges cast into an epoxy material that had a roughened surface to allow adhesion to the surrounding concrete. The insulating material ensures that the gauge is waterproof. The gauge coating had a Youngs Modulus of 2750MPa. This is much lower than that of concrete and ensures that the gauge does not cause a local stiffening effect.

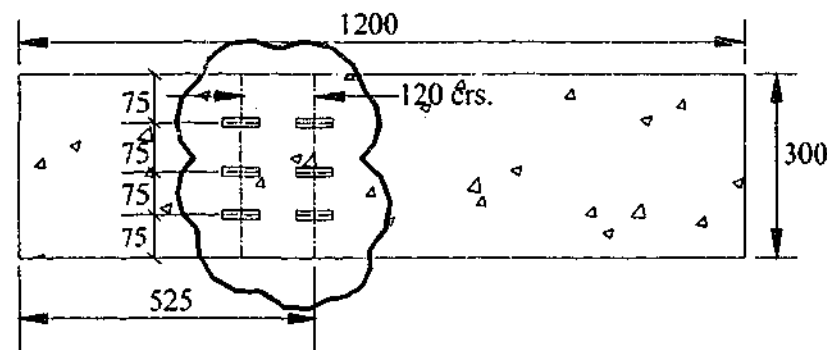


Figure 6.3-3 Plan of surface gauging arrangement

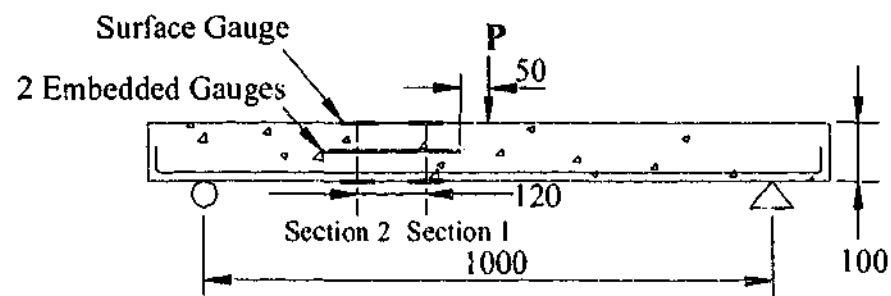


Figure 6.3-4 Elevation of strain gauging arrangement

6.4 Analytical Considerations for Data Analysis

The procedure prescribed for the T-beam flanges needs to be implemented here for the calculation of sectional actions for the slab specimens used in this validation procedure. This adaptation of the system to these slabs introduces some unique aspects that require consideration in this formulation. The most critical of these is the introduction of significant tension forces in the flexural tension reinforcing. This section discusses the above issue of calculating reinforcement tension forces, as well as the implementation of the MCFT and equilibrium relations to calculate sectional actions for the slab specimens.

6.4.1 Extrapolation of Strains

Using the Bernoulli assumption that plane sections remain plane after bending, a linear strain gradient can be assumed throughout the depth of the section. The curvature (strain gradient throughout the depth) was calculated by considering the difference in strain of the top surface (compression) gauges, and the gauges placed at mid depth. The strain in the reinforcing bar was found by simply extrapolating this gradient to the bar and calculating the strain based on the strain on the top surface.

Extrapolation of top surface strain and strain at mid depth was also used to calculate the strain on the underside of the slab. This was due to the fact that strain results on the underside of the slab were unduly affected by the presence of cracking. Results from the experiments that demonstrate this are shown in Section 6.5.2. Validation of the assumption of a linear elastic strain gradient throughout the test (until failure of gauge on the soffit of the slab) is presented in Section 6.6.

6.4.2 Calculation of Concrete Stresses From Strains

As previously stated, the constitutive relations of MCFT were used to transform the strain distributions measured from the experiments into stress distributions which can be used to calculate sectional actions. These relations are re-iterated in Equations 6.4.1 - 6.4.2. Equation 6.4.2 accounts for tension stiffening of the concrete between cracks. Owing to the

long length of strain gauge required for concrete, inclusion of tension stiffening was considered appropriate in order to calculate the average stress from the average strain measured over the length of the gauge.

In these equations, the nomenclature used in Chapter 3 is adopted here. The second part of the compression response equation shows the relations to be used for calculating the response after the strain corresponding to the softened response. For the purpose of calculation of the stress distribution, the tension strain on the bottom surface of the slab was evaluated using the strain gradient calculated by the top surface and mid depth gauges using the same method as for the reinforcing bar.

$$f_{c2} = \begin{cases} f_c \left[2 \left(\frac{\epsilon_2}{\epsilon_o} \right) + \left(\frac{\epsilon_2}{\epsilon_o} \right)^2 \right]; & 0 \leq \epsilon_2 \leq \epsilon_o \\ f_c \left[1 - \left(\frac{\epsilon_2 - \epsilon_o}{\epsilon_o} \right)^2 \right]; & \epsilon_o < \epsilon_2 < 2\epsilon_o \end{cases} \quad 6.4.1$$

$$f_{c1} = \begin{cases} E\epsilon_1; & 0 \leq \epsilon_1 \leq \epsilon_{cr} \\ \frac{f_{cr}}{1 + \sqrt{200\epsilon_1}}; & \epsilon_1 > \epsilon_{cr} \end{cases} \quad 6.4.2$$

6.4.3 Calculation of Resultant Forces From Stress Distribution

Figure 6.4-1 shows a schematic illustration of the strain, stress and force profiles at a section of the slab. This figure is representative of the distribution obtained from the experiment for these two specimens. The difference in the strains measured for these specimens than those outlined in Chapter 3 was that a much higher levels of both tension and compression strains were reached in the specimen. These significant values of strain were well beyond the values of those for which linear interpolation was used to calculate force in the formulation in Chapter 3.

From the stress distributions calculated above, the resultant tension and compression forces acting on each section where the gauging is applied can be calculated via integration of the MCFT relations to the neutral axis. The relationships used in the implementation of this procedure are shown below in Equations 6.4.3 - 6.4.5.

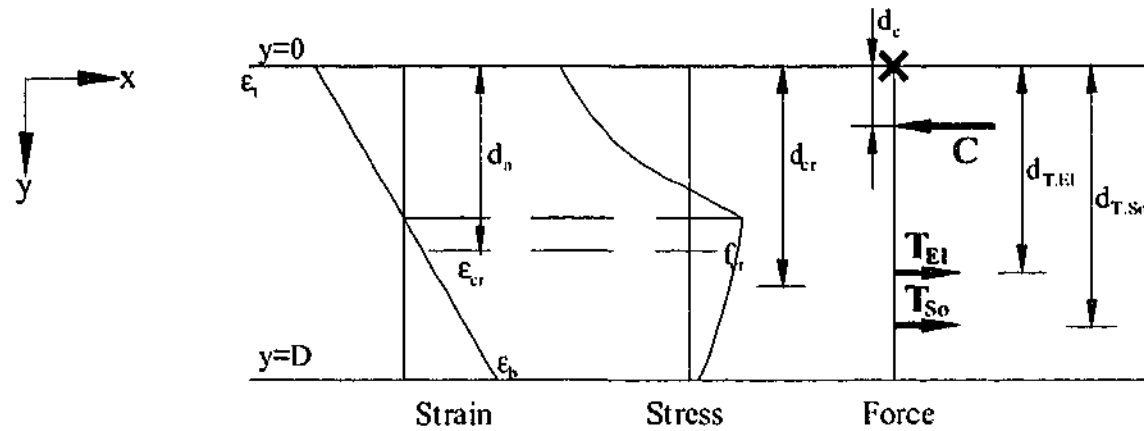


Figure 6.4-1 Profiles assumed for calculation of sectional forces

$$C = b \int_{\epsilon_{cr}}^0 f_p \left[\frac{2\epsilon}{\epsilon_o} - \left(\frac{\epsilon}{\epsilon_o} \right)^2 \right] d\epsilon = b \cdot f_c' \cdot d_n \left[\frac{\epsilon_t}{\epsilon_o} - \frac{1}{3} \left(\frac{\epsilon_t}{\epsilon_o} \right)^2 \right] \quad 6.4.3$$

$$T_{EI} = \frac{1}{2} b E_c \epsilon_{cr} \quad 6.4.4$$

$$T_{So} = b \int_{\epsilon=\epsilon_{cr}}^{\epsilon=\epsilon_b} \frac{f_{cr}}{1 + \sqrt{200\epsilon}} d\epsilon = \frac{b \cdot f_{cr}}{100\kappa} \left[\sqrt{200\epsilon_b} - \ln(1 + \sqrt{200\epsilon_b}) - \sqrt{200\epsilon_{cr}} + \ln(1 + \sqrt{200\epsilon_{cr}}) \right] \quad 6.4.5$$

The lever arm of the forces above was found by calculating the centre of area of the stress distribution in the vertical direction. The formulations used for this (as calculated from the top surface of the specimen) are given below in Equations 6.4.6 - 6.4.8.

$$d_c = d_n^2 \left[\frac{2 f_c' \epsilon_t}{3 C \epsilon_o} - \frac{1}{4} \left(\frac{\epsilon_t}{\epsilon_o} \right)^2 \right] \quad 6.4.6$$

$$d_{T,El} = d_n + \frac{2}{3} (d_{cr} - d_n) \quad 6.4.7$$

$$d_{T,So} = d_{cr} + \frac{b}{TK^2} \left\{ \frac{f_{cr}}{200 \times 10^3} \left[\frac{1}{3} \left((200 \epsilon_b)^{3/2} - (200 \epsilon_{cr})^{3/2} \right) - 100 (\epsilon_b - \epsilon_{cr}) \right. \right. \\ \left. \left. - \left(\ln(1 + \sqrt{200 \epsilon_b}) - \ln(1 + \sqrt{200 \epsilon_{cr}}) \right) + \left(\sqrt{200 \epsilon_b} - \sqrt{200 \epsilon_{cr}} \right) \right] \right\} \quad 6.4.8$$

As discussed in Section 6.4.1, the reinforcing strains were calculated by interpolating the strain gradient obtained from top surface and embedded gauges. The resultant tension force T_R is simply calculated from this, and the location of this was measured before pouring of concrete for these specimens.

6.4.4 Calculation of Sectional Actions

As strain gauges were positioned at two sections along the span, calculation of the sectional forces at these two sections was enabled. A complete check of equilibrium, including the use of dual section analysis to calculate the shearing force was undertaken. Figure 6.4-2 shows a free body diagram of the region enclosed by the two sections to which the instrumentation was applied. The length b shown in this figure was 120mm. This was controlled by the length of the embedment gauges.

Sectional bending moments (M_1 and M_2 in the above figure) were calculated by summation of moments about the line of action of the compression force. This is illustrated as point X in Figure 6.4-2.

To calculate the shearing force, it is firstly assumed that the self weight of the slab over the region being considered is negligible. The magnitude of the sectional shearing force based on this assumption was calculated using dual section analysis. That is, rotational equilibrium of the region above (which includes both sections) was considered by summation of moments

about point A. The resulting formulation of the equation for shearing force is shown in Equation 6.4.9.

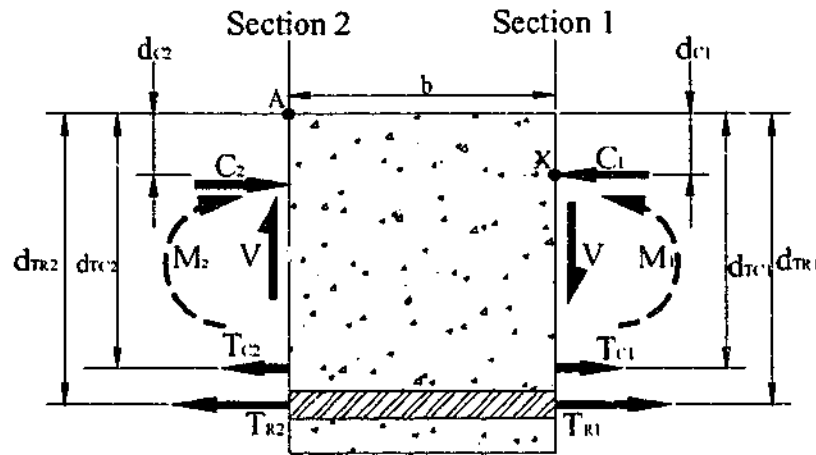


Figure 6.4-2 Free body of region enclosed by strain gauges

$$V = \frac{d_{c1}C_1 - d_{c2}C_2 + d_{TR2}T_{c2} - d_{TR1}T_{c1} + d_{TR1}(T_{R2} - T_{R1})}{b} \quad 6.4.9$$

6.5 Results From the Experiments

Apart from the strain measurements from the instrumentation system outlined above, measurements of the load and midspan displacement were also recorded throughout the experiment. This section discusses some of the trends in these results that are applicable for the following discussion.

The strains that are to be discussed from hereon are the average strain for each row of gauges. That is, the strain on the top surface at section 1 is the average of the strain recorded for the three gauges used over the width. This was required as one of embedded strain gauges was found to be faulty at the time of testing.

6.5.1 *Ultimate Load*

Table 6.5-1 shows the ultimate loads of slabs S1 and S2. It also describes the failure mechanism observed at the ultimate load. The result of ultimate strength is almost identical in each specimen, but the failure mechanism displayed at the ultimate load was different. Although specimen S1 did exhibit a crushing of concrete on the top surface, diagonal shear cracks were present at the ultimate load. This indicates that formation of the shear mechanism was underway when the slab failed in flexural compression.

Table 6.5-1 Ultimate loads and failure mechanisms of specimens

Specimen	Ultimate Load (kN)	Failure Mechanism
Slab S1	69.8	Flexural compression
Slab S2	69.3	Shear

The crushing of the concrete on the surface of slab S1 associated with the flexural compression failure influenced the top surface strain measurement. This is evident in the strain gauge results shown in the following section.

6.5.2 *Results From Strain Gauges*

Figure 6.5-1 shows the results obtained from the average of the strain gauges across the width at section 1 on Slab S1 at each location throughout the depth. Slab S2 displayed very similar results for the gauges present at each section. Results discussed in this section are for section 1 of Slab S1. These are typical of the sectional response of all sections.

It can be seen that at a level of applied load of approximately 63kN, the average compressive strain response of the gauges on the top surface reaches the value of the crushing strain of concrete ($2200 \mu\epsilon$) and begins to increase at a highly non uniform rate. This corresponds to the flexural compression failure mechanism discussed in the proceeding section.

Figure 6.6-1 shows the variation of strain gradient throughout the loading history. This indicates that the strain gradient in the lower half of the slab becomes greater than that of the top layer as the load increases beyond 50kN. This increase with load illustrates that as cracking becomes more excessive, the strain on the bottom is over predicted according to Bernoulli theory.

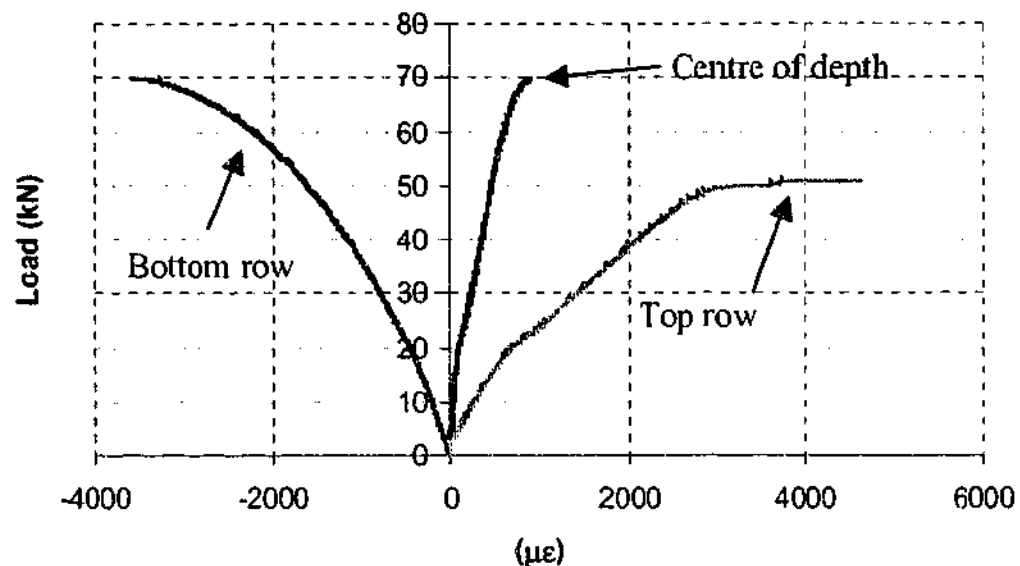


Figure 6.5-1 Average concrete strains produced at the three layers of gauging on section 1 of Slab S1

One other feature of this figure is the linearity of the strain gradient until the level of load at which cracking influences results. This validates the assumption in Section 6.4.1 that a Bernoulli strain distribution is present within the system. It also instils a level of confidence in the instrumentation system to provide compatible results throughout the depth of the specimen.

6.6 Results of Calculations Using Prescribed Analytical Procedure

The above results show a linear distribution of the strain throughout the loading history of the slabs, with the exception of the latter loading stages where cracking has excessive influence on the strain on the bottom surface of the slabs. It has been aforementioned that the above fact influences the decision to use only the strains produced from the two layers of

gauges (top surface and mid depth), coupled with Bernoulli's assumption of a linear strain distribution. This assumption is used to apply the results obtained from the strain gauges to check sectional equilibrium.

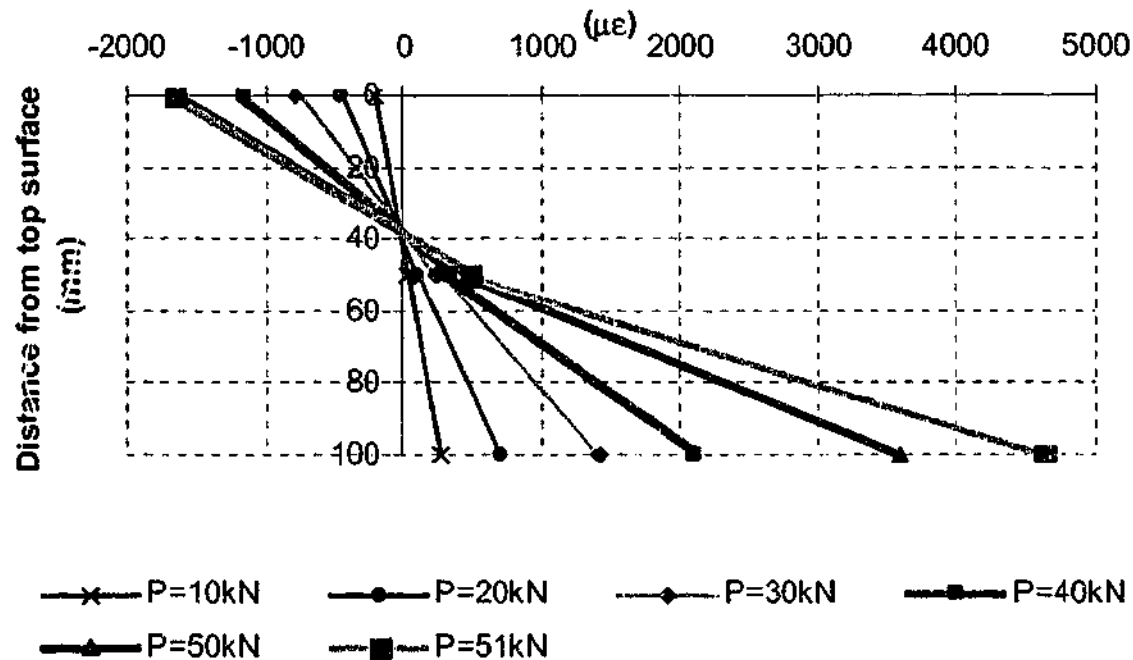


Figure 6.6-1 Variation of strain distribution of section 1 on Slab S1 throughout loading history

In the results analysis given below, strain results between level of applied load of 10kN and 63kN are considered. Between the levels of applied load of 0kN and 10kN, the noise in the system produced a large unrealistic variation in the values of sectional forces that have been calculated. As has already been noted in Section 6.5, Slab S1 exhibited crushing on the top surface near failure. This crushing was deemed to adversely affect the results of strain, hence the calculated values of sectional actions at a level of applied load of 63kN. The results from both specimens were only calculated to this point. It is noted that when this technique was applied to the flange of T-beams, this was not required as tensile strains on the underside of the flange were never high enough to fail the gauges.

6.6.1 Results From the Calculation of Axial Forces

Figure 6.6-2 – 6.6.5 show the results of calculation of the sectional forces for each specimen at both sections. The figures show that the increase in tension and compression forces follows the same trend for each specimen throughout the duration of the loading and that the actual values are very close.

Consider here that the error in these results can be quantified by considering the ratio of the absolute values of the tension and compression forces. For the purpose of analysis in this section, consideration will be given to the average value of this error term throughout the loading history within the bounds considered, as well as value of this error term at the maximum load that was considered ($P=63\text{kN}$).

6.6.1.1 Specimen Slab S1

The results of the calculation of the axial sectional forces for this specimen can be seen in Figure 6.6-2 – 6.6.3. The average value of this error term within the bounds of load considered for this specimen is 8% at section 1 and 23% at section 2. The value of this error term for each of these sections at the maximum applied load considered for discussion ($P=63\text{kN}$) is 7% for section 1 and 16% at section 2. The value of error indicates that the values calculated for the tension and compression force are close at both sections throughout the duration of loading. The plots of the sectional forces indicate that the trend in the variation in these values throughout the duration of the loading is close.

6.6.1.2 Specimen Slab S2

The results of calculation of the axial sectional forces for specimen S2 can be seen in Figure 6.6-4 – 6.6.5. The average value of this error term within the bounds of applied load considered for specimen S1 is 20% at section 1 and 5% at section 2. The value of this error term for each of these sections at the maximum load is 11% for section 1 and 11% at section 2.

These figures again illustrate that the calculation of the sectional forces using the strains measured throughout the experiment coupled with the constitutive relations of the

MCFT produce values of sectional force that are within a reasonable bounds of error. The trend of the variation for these values throughout the loading history again illustrates an almost identical development of the sectional tension and compression forces throughout the duration of the loading.

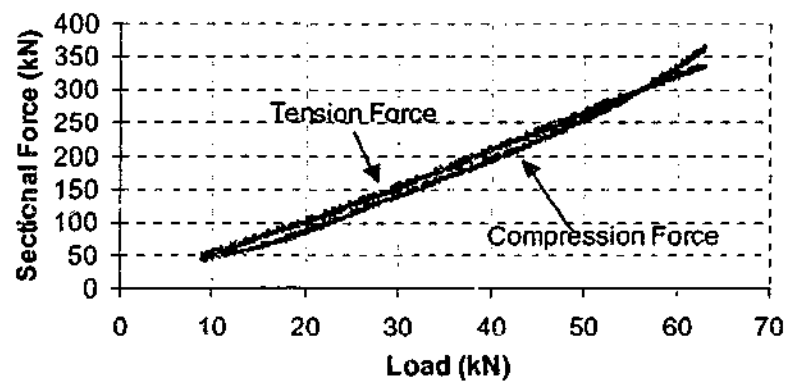


Figure 6.6-2 Slab 1 axial forces on section 1

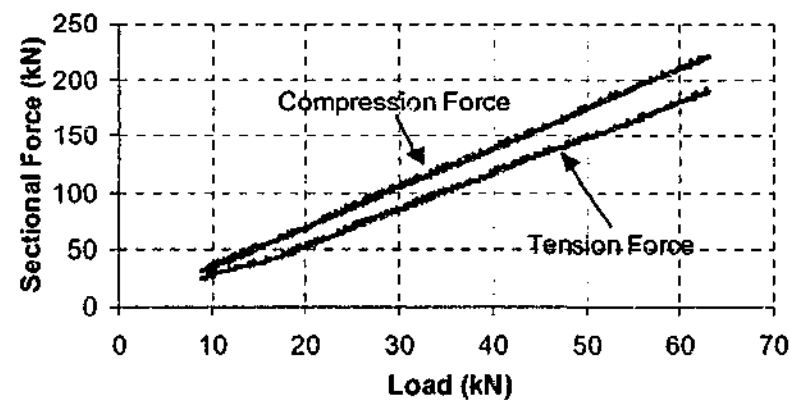


Figure 6.6-3 Slab 1 axial forces on section 2

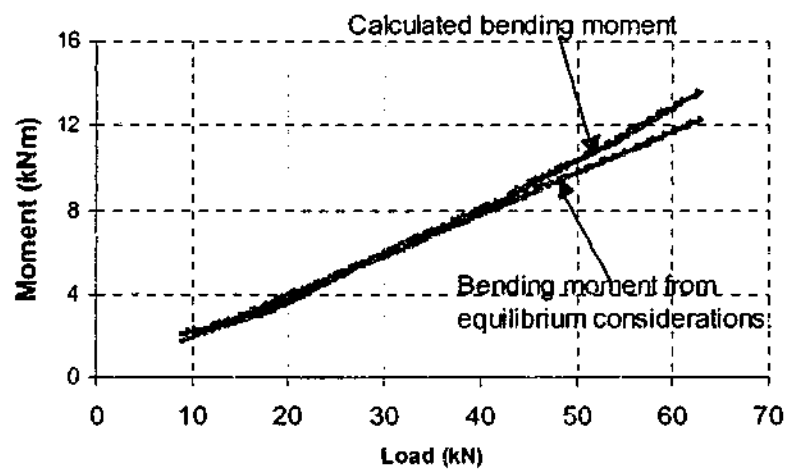


Figure 6.6-4 Slab 2 axial forces on section 1

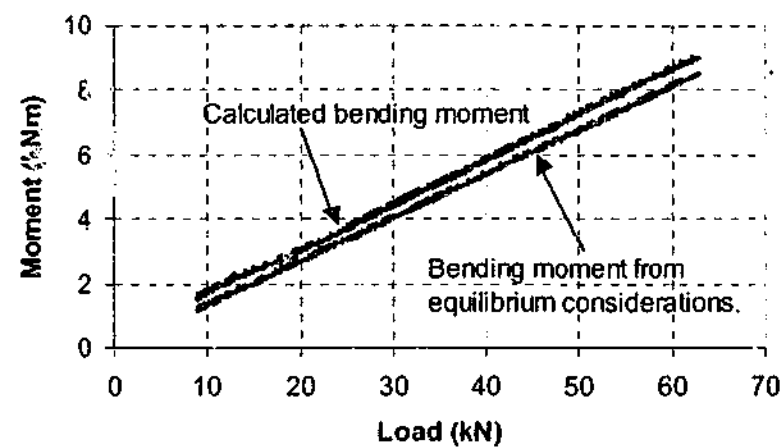


Figure 6.6-5 Slab 2 axial forces on section 2

6.6.2 Results From the Calculation of Sectional Bending Moments

Figure 6.6-6 – 6.6.9 show comparisons of the bending moments calculated using the instrumentation and analytical technique under scrutiny with those calculated using equilibrium consideration throughout the loading history considered.

It is clear from these figures that the bending moments calculated from this technique are in close agreement with those from equilibrium considerations. For the purpose of further analysis of these results, the error considered for this action would be the ratio of bending moment calculated from the instrumentation and analysis technique to the value calculated from equilibrium. Again, the average of this error term throughout the loading duration considered will be used for discussion here.

6.6.2.1 Specimen Slab S1

The results of calculation of the sectional bending moments for specimen S1 can be seen in Figure 6.6-6 – 6.6.8. The average value of the error term within the bounds that are being considered is 2% at section 1 and 9% at section 2. At the maximum load considered ($P=63\text{kN}$), the error is 2% at section 1 and 9% at section 2.

The trend of the variation of the bending moment throughout the loading history at both sections is in close agreement with the linear trend obtained from equilibrium considerations. The values and trend produced from the implementation of this procedure has produced results of bending moment for this specimen that are in excellent agreement with equilibrium values.

6.6.2.2 Specimen Slab S2

The results of calculation of the sectional bending moments for specimen S1 can be seen in Figure 6.6-8 – 6.6.9. The average value of the error term within the bounds that are

being considered is 21% at section 1 and 22% at section 2. At the maximum load considered ($P=63\text{kN}$), the error is 11% at section 1 and 6% at section 2.

The trend of the variation of the bending moment throughout the loading history at both sections is again in close agreement with the linear trend obtained from equilibrium considerations. It is noted that the magnitude of the error has increased somewhat in the calculation of these results for specimen S2. It is suggested that for this specimen, the introduction of the lever arm into the analysis has magnified the error term for this specimen.

6.6.3 Results From the Calculation of Shear Force

Figure 6.6-10 – 6.6.11 show a comparison for both slabs of the shear force obtained using dual section analysis to calculate shear force compared with the sectional shear force obtained from equilibrium. Given the nature of the dual section analysis used to produce these results, the potential error that is introduced into these calculations from the combination of error terms is very high. This is a result of the summation and multiplication of error terms.

In the analysis of these results, consider an error term similar to that used in the analysis of the bending moment results. That is, the error is a ratio of the value calculated using the procedure under scrutiny with the shear force calculated at the midpoint of that of the body considered for dual sectional analysis.

The results for slab 1 show that the average error throughout the loading history considered is 22% with the error at the load of 63kN being 16%. The trend of calculated results does follow that of the equilibrium results, but the accumulation of error that is introduced in the implementation of dual sectional analysis is evident in these results.

The results for slab 1 show that the average error throughout the loading history considered is 12% with the error at the load of 63kN being 16%. The trend of calculated results is much closer for this specimen than those of specimen S1 and provide a good estimate of the shearing force at a section using this technique.

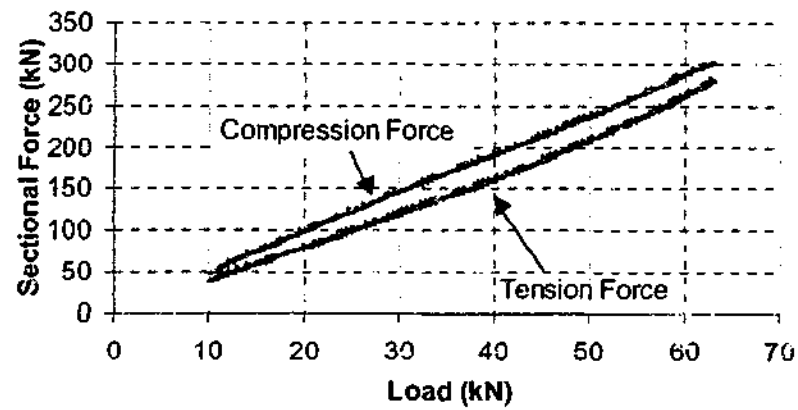


Figure 6.6-6 Slab 1 bending moments on section 1

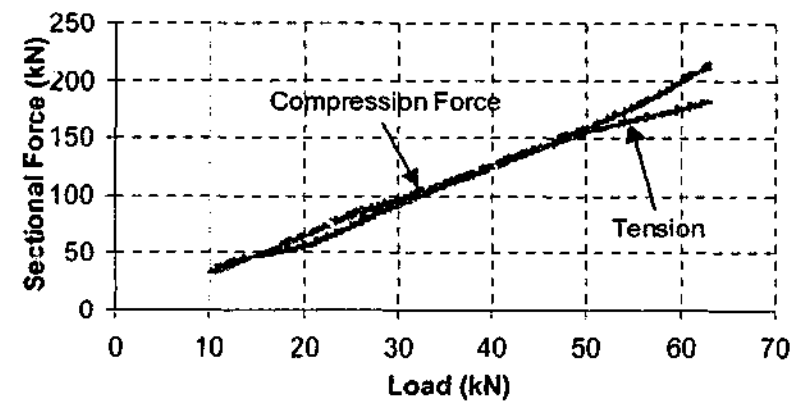


Figure 6.6-7 Slab 1 bending moments on section 2

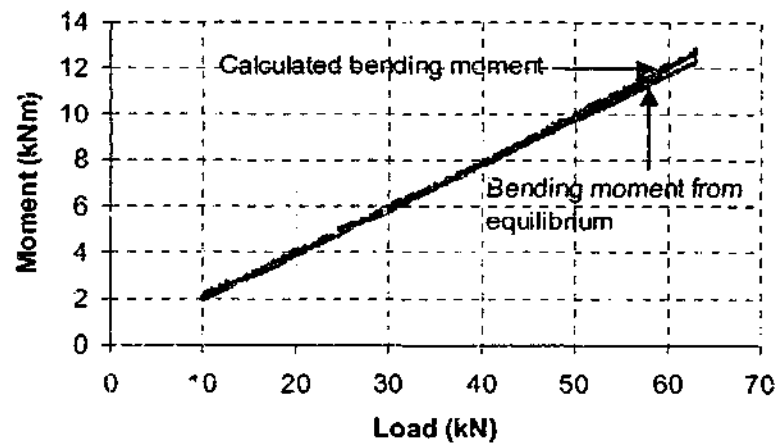


Figure 6.6-8 Slab 2 bending moments on section 1

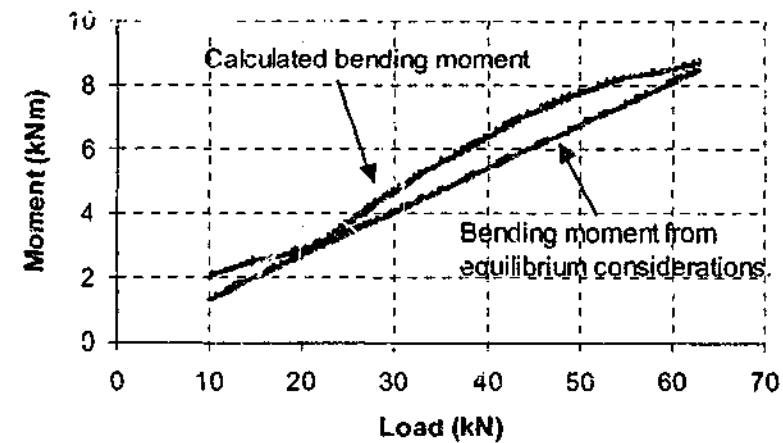


Figure 6.6-9 Slab 2 bending moments on section 2

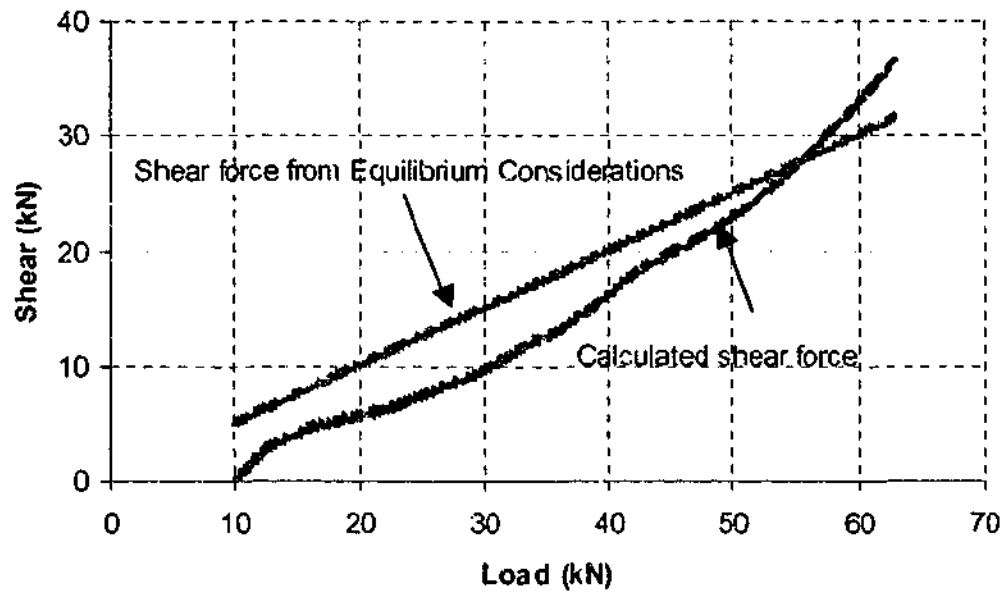


Figure 6.6-10 Shear force on slab 1 from equilibrium and sectional analysis

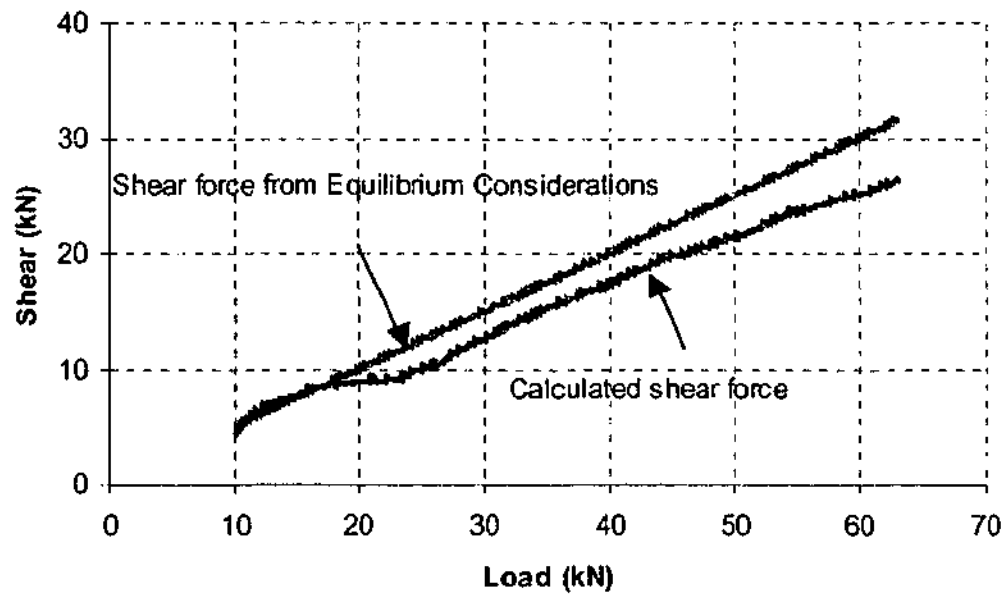


Figure 6.6-11 Shear force on slab 2 from equilibrium and sectional analysis

6.7 Discussion of Experimental Results

The above results indicate that equilibrium actions calculated at each section from the application of the constitutive relations of the MCFT to the strain measurements obtained from

the described technique of instrumentation compare reasonably well to those that are calculated from equilibrium considerations.

This suggests two things. Firstly, if the calculation of sectional net axial force and bending moments are correct, then the method of calculating individual forces and lever arms are correct. This means that the application of Equations 6.4.1 - 6.4.2 are acceptable in the calculation of concrete stresses from strains.

Secondly, for the constitutive relations to be correct in their application, the variable within these relations (axial strain) must be correct. Since the strain on the top surface and at mid depth were used, then it is true that these strains were measured satisfactorily by the instrumentation technique, and that the application of Bernoulli's assumption was an acceptable means of estimating strain in the reinforcing, and on the bottom surface of the slab.

The results of the shear force show that the trend of the equilibrium shear is generally followed throughout the loading duration considered. This dual section analysis procedure as applied to the experimental results introduces many potential sources of error in multiplying and adding errors from all measured results. The technique can be seen to provide results that are capable of producing trends of sectional shear that are consistent with those obtained from equilibrium considerations, and within a reasonable error.

6.8 Conclusions From Validation Experiments

It can be seen from the results that have been presented that an acceptable correlation between the sectional forces calculated from measured strains and equilibrium forces has been achieved using the strain gauging technique described, and constitutive relations of the MCFT.

Given the accuracy of the results that have been obtained from these experiments, the following comments can be made on the issues that were raised in the introduction to this chapter.

1. The location of the gauges in the direction parallel to the span of the of the slab in these experiments was achieved satisfactorily using available tools, and that vibration of the concrete appeared not to misalign embedded gauges.
2. It appears that good adhesion between the embedded gauges and the concrete was achieved, as the distribution of strain throughout the depth produced from this system was linear until cracking on the tension surface of the specimen affected the gauge reading.
3. The difference in length of the surface and embedded gauges has produced no significant errors into the results. This is again obvious from the linearity of the strain gradient throughout the depth until cracking affected the recorded measurements on the gauge on the tension surface.
4. The constitutive relations of the MCFT have proven to produce axial forces on each section that are comparable throughout. This suggests that the tension and compression relations that have been applied were compatible when applied to these specimens.

Given that each of the issues that have been identified as potential sources of introduction of error in this system have been proven to only effect results to a degree of error that is tolerable, this instrumentation system and the accompanying analytical procedure are deemed adequate in reproducing sectional actions for reinforced concrete elements.

Chapter 7 THE CONTRIBUTION OF THE FLANGE TO THE ULTIMATE SHEAR STRENGTH OF A POINT LOADED RC T-BEAM

7.1 Introduction

The results of the experimentation of stage 2 are discussed in this chapter. These results are discussed here based on the outcomes of the validation experiments discussed in Chapter 6. In line with the findings of the previous chapter, it is accepted here that the results of strain, and the calculations of all forces, lever arms, and sectional actions resulting from the strain distribution obtained experimentally are valid to discuss trends and relative proportions of quantities.

The two specimens from stage two displayed different failure mechanisms at the ultimate load. As a result of this, the discussion the results of the two specimens will be undertaken individually. The calculated quantities of shear lag, interface shear and the sectional shear will be discussed.

Some reference is made to Appendix B and C. These appendices present a detailed summary of the results of the instrumentation, including the distributions of strain, neutral axis, and stress across the flange throughout the loading range considered. Although this chapter attempts to remain independent of these appendices, they do provide information that assists with the understanding of some of the aspects of the specimen behaviour outlined below.

Of the measured and calculated quantities discussed in this chapter, several of these are sectional values (i.e. measured or calculated at the two sections to which instrumentation was provided), and some are quantities that are assumed constant throughout the region instrumented (such as the calculated shears). For the sectional quantities, the notation used in Chapter 3 will be used to discuss the results. The two sections of instrumentation will again be referred to as section A and section B. Figure 7.1-1 shows this notation for section labels. Figure 7.1-2 revises the notation used in Chapter 3 to describe rows of gauging across the width and positions throughout the depth of the flange at each section. This notation will be used extensively throughout this chapter.

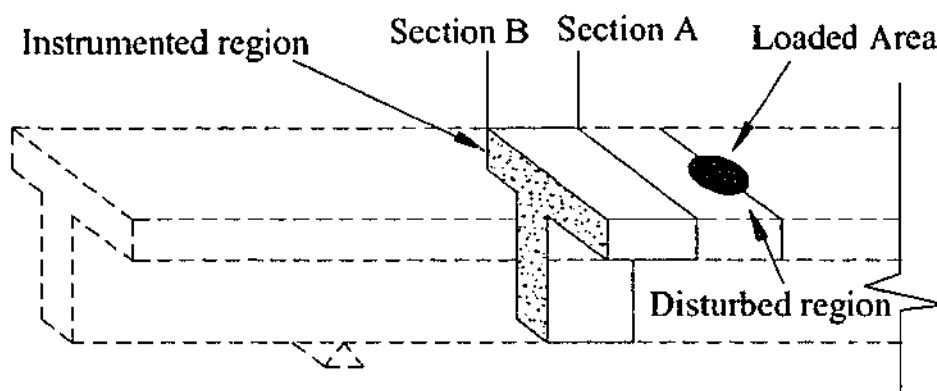


Figure 7.1-1 Identification of Section A and Section B

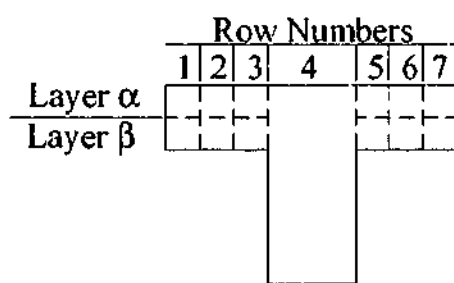


Figure 7.1-2 Notation used for location of flange blocks

7.2 Specimen B16 Analysis

This section presents the results of the overall behaviour of specimen B16, as well as the results of the calculation of the shear lag, interface shear, and the sectional shear in the

region of calculation discussed in Chapter 3. In the determination of the effect of the development of the failure mechanism on the above results presented in this section, some consideration of the longitudinal strain profiles throughout the width and depth of the flange of the specimen, and the variation that they displayed throughout the duration of the loading applied to the specimen was required. These results are presented in Appendix B. Due reference is made to these results in the following discussion where appropriate.

7.2.1 *Ultimate Strength and Failure Mechanism*

The mechanism displayed by specimen B16 at the ultimate load was a punching shear mechanism. Figure 7.2-1 shows a photo of the failure mechanism, and Figure 7.2-2 shows the load deflection curve that was obtained from the experiment of this specimen. On reaching peak load, the specimen exhibited a non-ductile response. The formation of the punching shear mechanism was sudden, as was the resulting loss in load carrying capacity associated with the development of this mechanism. This failure mechanism was displayed at a peak load of $P_u=212\text{kN}$ which corresponds to a peak applied shear of $V_u=155.3\text{kN}$.

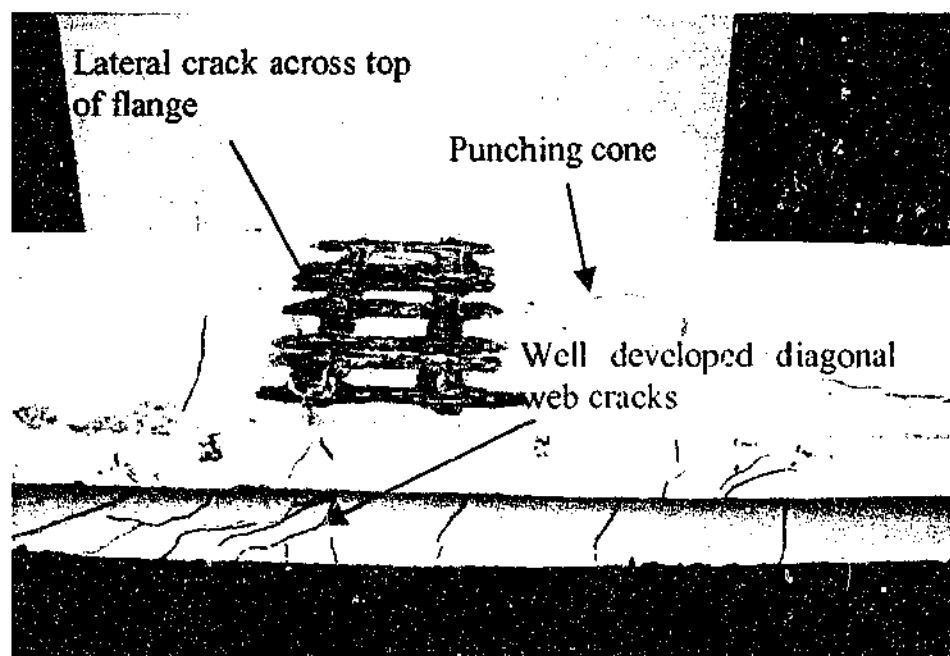


Figure 7.2-1 Photo of B16 failure mechanism

Figure 7.2-2 shows the load deflection curve that was produced by this specimen. Three stages of the development of the failure mechanism are identified on this plot. These

are identified to assist in the analysis of the results of the various shear forces that were calculated from the results of the instrumentation of this specimen.

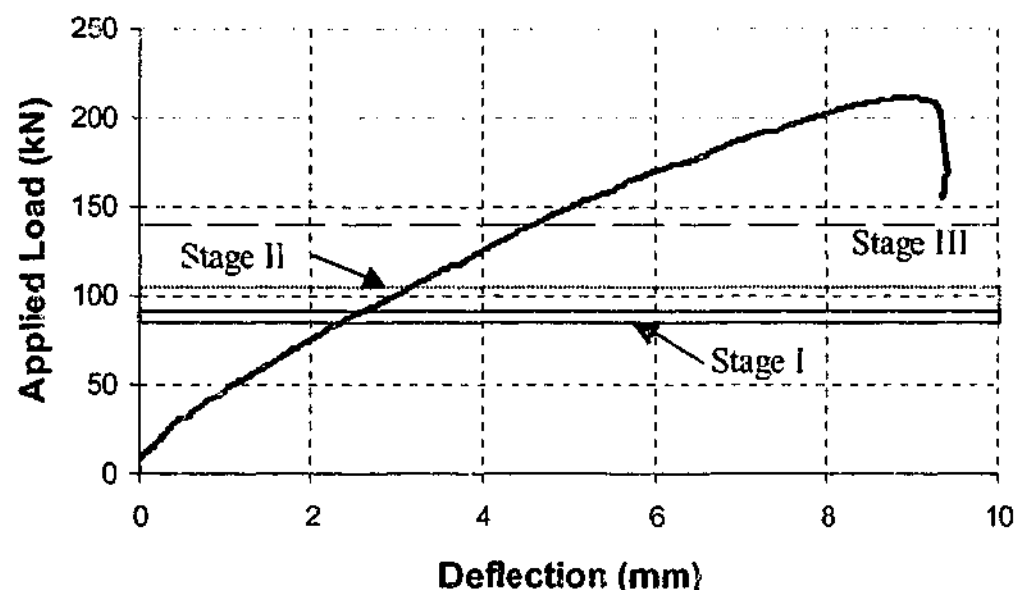


Figure 7.2-2 Specimen B16 Load Deflection Curve

Stage I : This stage is bounded by a level of applied load of 85kN and 91kN. At these levels of load, two diagonal web cracks formed. The crack that formed at a level of applied load of 91kN was observed to form part of the failure mechanism at peak load.

Stage II : This stage is bounded by levels of applied load of 91kN and 105kN. Within these bounds of loads, the stirrups became effective following the formation of the two diagonal web cracks outlined above. It is thought that as this stage develops the stirrups become effective after some slip along the surface occurred during Stage I.

Stage III : This stage corresponds to an applied load of 140kN. Figure B.2-3 in Appendix B shows that it is at approximately at this level of applied load that the rate of increase of compressive strain on the top surface of the flange reverses. This eventually results in the development of a crack across the top of the flange.

Figure B.2-3 Appendix B also illustrates that the tensile strains on the top surface displayed a magnitude corresponding to that of the cracking strain of concrete at a level of applied load of 170kN. This crack can be seen in the Figure 7.2-1 of the failure mechanism. It is noted that the failure mechanism exhibited is very similar to the idealisation presented by Hoang (1997). This level of applied load marks a sudden small increase in the deflection of the specimen as shown in the above figure. Throughout the remainder of this test, this crack on the top surface of the flange, and that of the critical diagonal web crack developed, until the peak load of 212kN when the cracks associated with the punching shear mechanism appeared.

7.2.2 Range of Calculation of Shear Forces

To ensure the accuracy of the results of calculations, checks of equilibrium were performed where possible. Appendix D shows the details of these checks. These checked sectional shear forces by summation of moments about a second point. Comparison of the sectional shear force as calculated by summation of moments about two separate points shows that equilibrium was only satisfied until a magnitude of applied load of 175kN. It has been shown in Chapter 6 that strain gauge readings are in some cases not reliable after the formation of cracks, and it is suggested that the formation of the crack on the top surface (which begins at approximately this load level) has influenced these readings enough to influence the calculations of sectional shear.

Since all checks are not satisfied beyond a level of applied load of 175kN, the discussion below only considers the calculation range of applied load of 0-175kN. All other results are disregarded for the discussion of the calculated shears for this specimen.

7.2.3 Results of the Calculation of Shear Lag Forces

Figure 7.2-3 shows the distribution of shear lag forces at each row of instrumentation at 20kN increments. Figure 7.2-4 show variations of the shear lag at each gauge location with load throughout the loading range considered in this discussion (0-175kN), the individual plots

of this figure correspond to one of the flange overhangs. The shear lag presented in these figures is a force calculated over the entire depth of the flange.

The distribution across the width illustrated by Figure 7.2-3 indicates that in each flange overhang, the maximum magnitude of the shear lag is at the location nearest to the flange, this magnitude decreases the further away from the flange the shear lag is calculated. This figure also shows that the magnitude of the shear lag force is much higher in the right side flange overhang than that of the left side flange overhang. A uniform increase in this trend can be seen in this figure, with the exception of rows 1 and 2 on the left side flange overhang. These decreased in magnitude of the duration of the last load increment considered. Throughout all stages of the experiment, the shear lag in the right side flange overhang was significantly greater than that in the left side flange overhang.

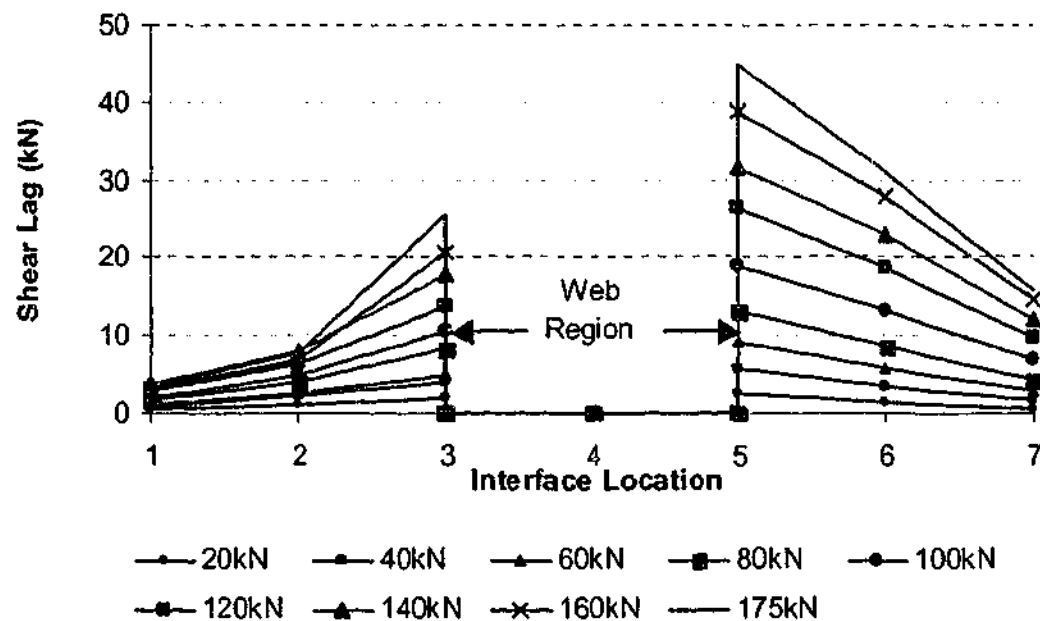
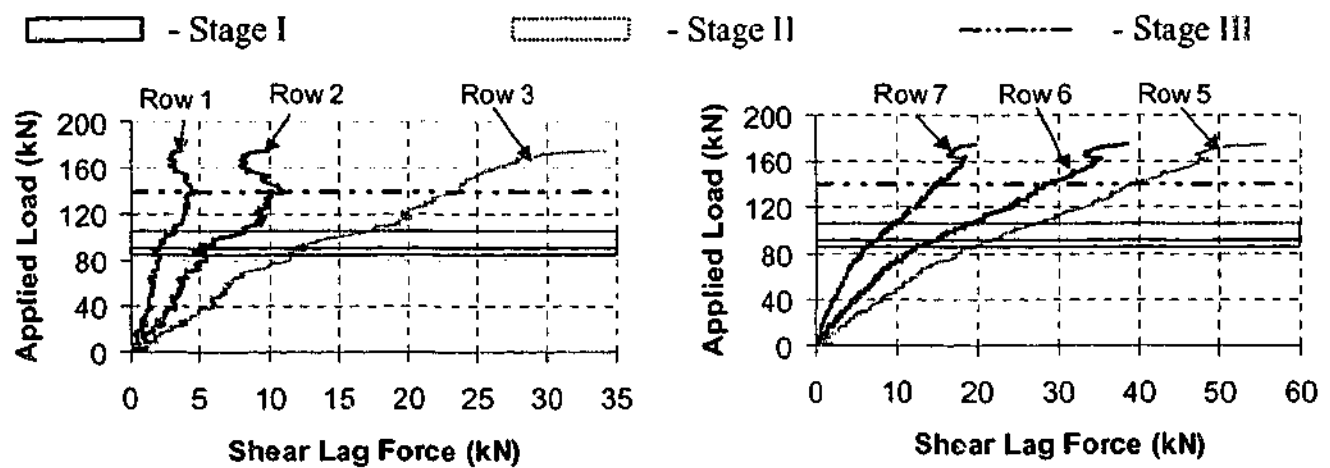


Figure 7.2-3 Shear lag distribution at 20kN load increments for specimen B16

The results shown in Figure 7.2-4 include the stages within the calculation range at which components of the failure mechanism formed. Rows 3, 5, 6, and 7 display a change in gradient of shear lag with applied load at a level of applied load just below that of the start of Stage I. This illustration shows that in Stage II, an increase in gradient of the response of the shear lag with applied load occurred at rows 1 and 2. Only show a small change in gradient of

the response associated with the onset of the stirrup contribution at other rows. Rows 1 and 2 displayed a small reversal in the shear at a level of applied load approximately equal to that of the end of this stage. At rows 3-7, the reversal of strains on the top of the flange at section B at Stage III do not produce a discernable affect on the response of the shear lag. The gradient of the response remains essentially constant after this has occurred. The response of the shear lag at rows 1 and 2 to this strain reversal at section B appears to be a small reduction in magnitude. This was also noted in the discussion of Figure 7.2-3.



(a) Left side flange overhang

(b) Right side flange overhang

Figure 7.2-4 Variations of Shear Lag with Applied Load calculated for Specimen B16

7.2.4 Results of the Calculation of Interface Shear Forces

The interface shear that acts between layer α and layer β is shown below in Figure 7.2-5 and Figure 7.2-6. The first of these figures shows the distribution across the width of the flange in each overhang at increments of 20kN. Figure 7.2-6 shows the variation of the shear lag force at each row throughout the duration of loading considered, as well as the stages of development of the failure mechanism.

It can be seen from Figure 7.2-5 that the distribution of the interface shear force throughout the width of the flange overhangs is essentially constant and of low magnitude throughout until a level of load of 80kN, the load increment immediately preceding the formation of the critical diagonal web crack. Beyond this level of load, the right side flange

overhang carries a higher magnitude of the interface shear force after the formation of the critical web crack. This is consistent with the distribution of the shear lag force. Corresponding to this is the fact that the magnitude of the interface shear forces in the right side flange overhang are significantly greater in the right side flange overhang than in the left side flange overhang. It can also be seen in this figure that a significant increase in the magnitude of the shear lag force occurs between the ranges of load of 140-160kN.

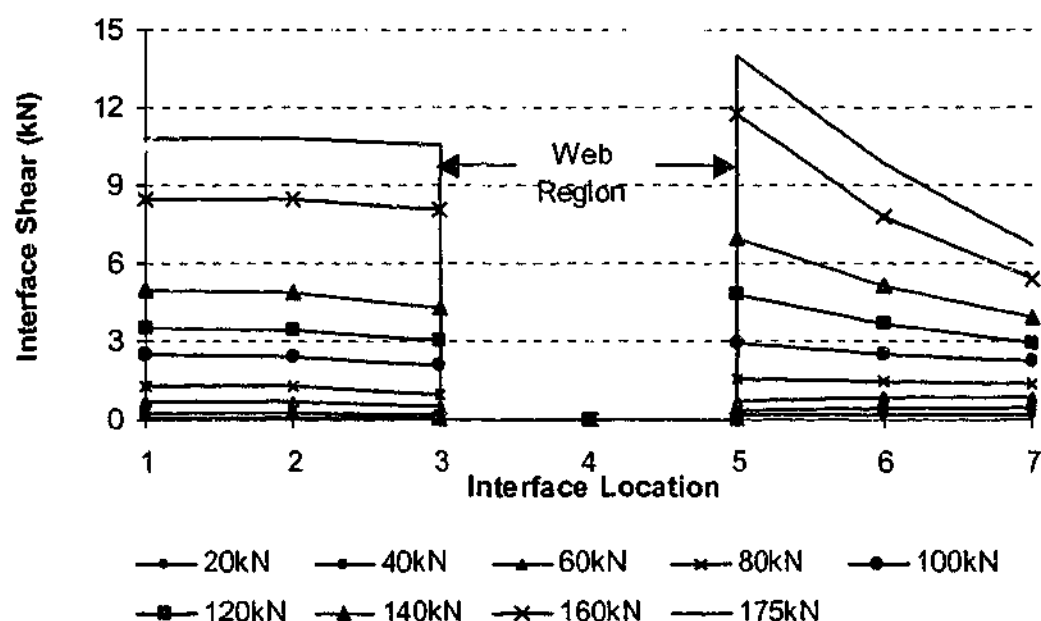
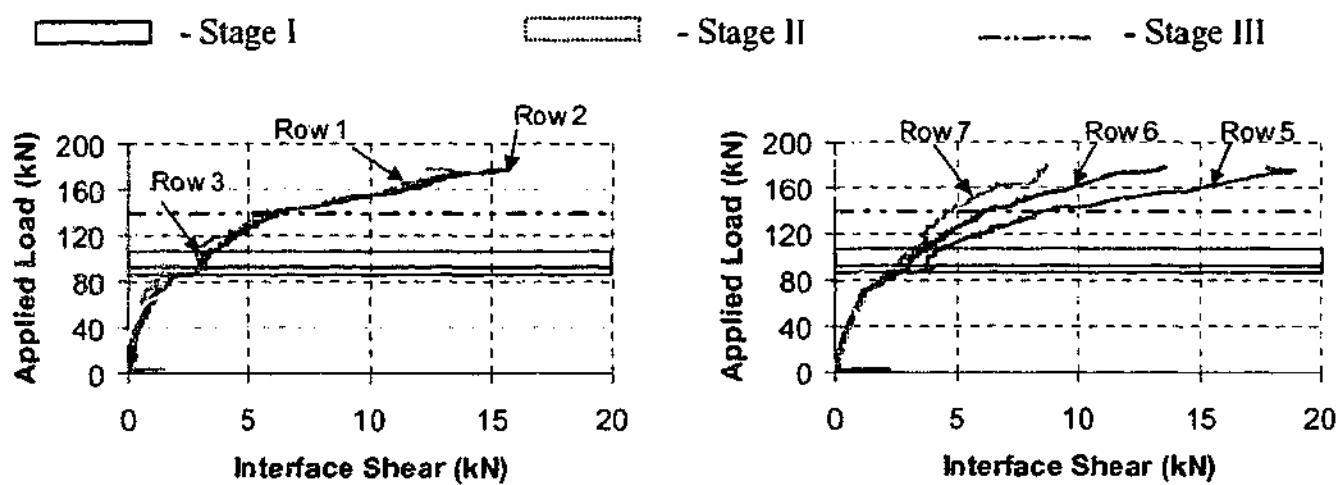


Figure 7.2-5 Distribution of interface shear throughout the width of the flange at 20kN intervals for specimen B16

Figure 7.2-6 illustrates that the formation of the diagonal web cracks in Stage I initiates an increase in gradient of the response of the interface shear with the applied load at all rows. Stage II, however, produces a reversal in the gradient of the interface in Stage II at rows 3 and 5. All other rows across the width of the specimen are not affected within Stage II. The reversal of strain on the top surface of the specimen at section B produces a large increase in the magnitude and in the gradient of the interface shear response at the majority of rows across the width of the flange. Beyond this level of applied load at Stage III, the gradient of the interface shear with the applied load increased significantly. This trend remained constant until the calculation procedure was terminated.



(a) Left side flange overhang

(b) Right side flange overhang

Figure 7.2-6 Variation in interface shear with applied load as calculated for specimen B16

Figure 7.2-8 shows the variation of the percentage of shear force in the flange (V_f/V_{applied} expressed as a percentage) with the applied load. This figure shows the maximum percentage of shear force in the flange is 27.5% that occurs at the maximum load considered ($P=175\text{kN}$). This figure shows within Stage I, the proportion of the total sectional shear being carried by the flange significantly increased. This corresponds to the level of applied load at which the two diagonal cracks formed on the web. In Stage II, the contribution of the flange decreased. This stage has been associated with the onset of stirrup effectiveness. The other change in the trend shown in this figure occurred immediately after Stage III. A sudden decrease in the magnitude of the gradient of the percentage of sectional shear resisted by the flanges with applied load occurred. Stage III corresponds to the level of applied load at which the strains on the top surface at section B began to reverse.

It can be seen in Figure 7.2-8 that at a level of applied load of 10kN, the variations in the results were significant. This is attributed to the electrical noise in the instrumentation system at these low stages of load. It was considered that this noise was too significant for the results below a level of applied load of 10kN to be reliable. Therefore, results analysis was not considered until after a level of applied load of 10kN.

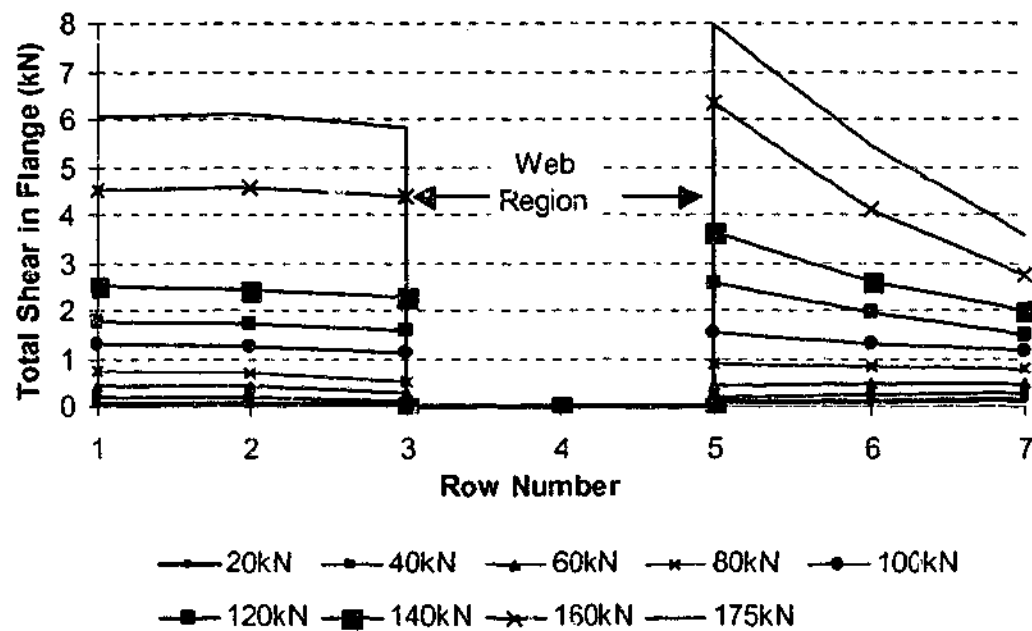


Figure 7.2-7 Distribution of sectional shear throughout the width of the flange as calculated for specimen B16

Figure 7.2-9 shows the distribution of sectional shear force across the width of the flange as calculated in each the two layers of the flange considered. The behaviour of both layers of the flange at all rows considered is identical to the behaviour of the flange throughout the entire depth (shown in Figure 7.2-7). This graph also shows that the magnitude of the sectional shear force that is carried in each layer is similar.

7.2.5 Flange Effectiveness of Specimen B16

As each component of the failure mechanism formed, the percentage of the total shear force resisted by the flange increased. This illustrated in Figure 7.2-8. This is a result of the development of each stage of the failure mechanism requiring redistribution of the longitudinal compression stresses to accommodate their formation.

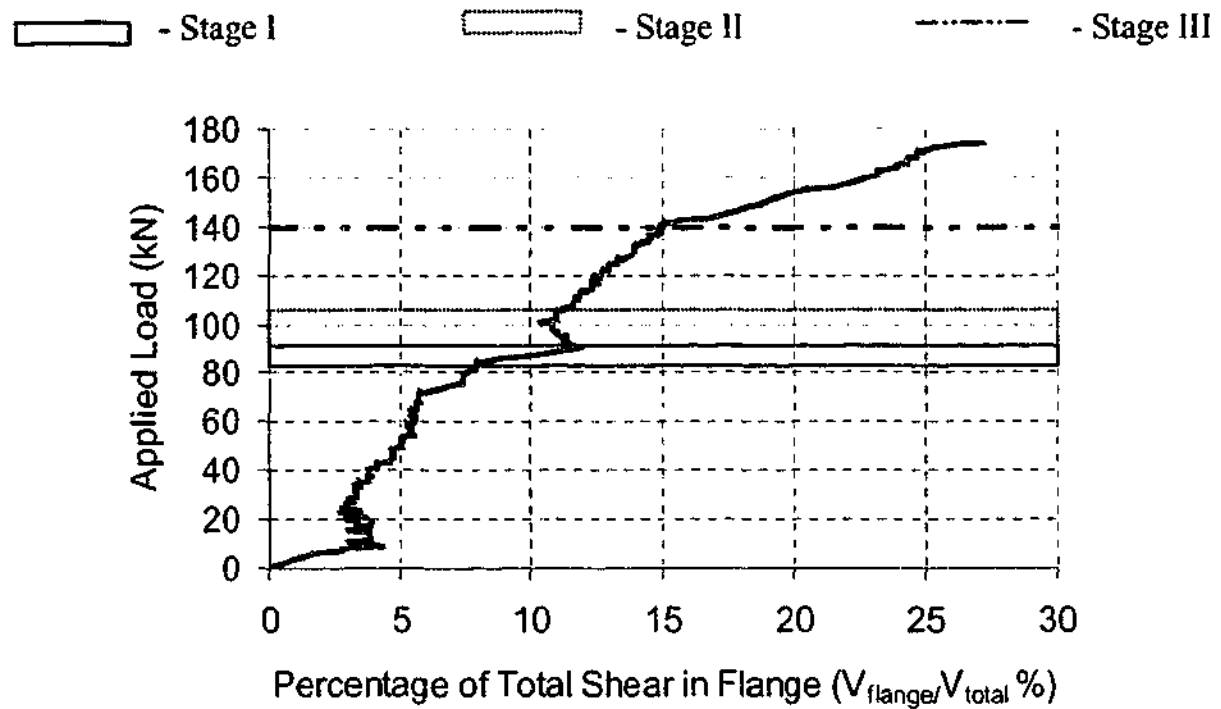


Figure 7.2-8 Variation of percentage of total sectional shear in flanges for specimen B16

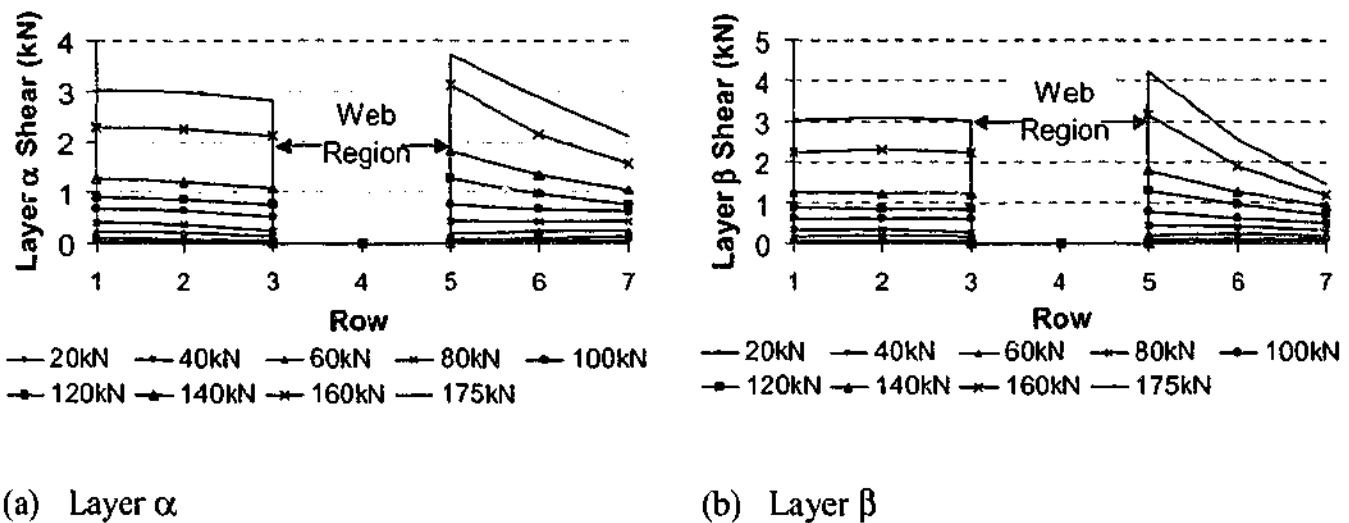


Figure 7.2-9 Variation of shear in each layer at 20kN intervals for specimen B16

The formation of the critical diagonal web crack at stage I, a significant relocation of the neutral axis across the width of the flange at section A. This can be seen in Figure B.3-1 in Appendix B. Following the initiation of this crack, the neutral axis penetrated deep into the web. The longitudinal stress distribution throughout the width of the specimen remained essentially constant, with the magnitude in the flange overhangs and the web being close to equal (again, refer Figure B.3-1 in Appendix B). Since the depth of the neutral axis decreased

in the web, and the compression stress remained constant throughout the width of the specimen, it is suggested that the specimen 'shed' compressive force into the flanges following the formation of the critical diagonal web crack.

This is reiterated in the results of the shear lag shown in Figure 7.2-4. It is through this action of shear lag that the compression force is 'transported' from the web to the flange. The significant change in the gradient of the shear lag with applied load shown in Figure 7.2-4 is in the vicinity of Stage I that corresponds to formation of the critical web crack. This increase in shear lag not only shows this redistribution across the width of the flange, but as a result of the dependence of this quantity on the difference in compression forces between sections, this increase in gradient signifies an increase in the difference in net compression force acting on the flanges between the section A and B.

The onset of the stirrup effectiveness marked a significant decrease in the interface shear at rows 3 and 5 (shown in Figure 7.2-6), a significant increase in the gradient of the shear lag with the applied load (shown in Figure 7.2-4), and a slight decrease in the magnitude of the percentage of shear resisted by the flanges (shown in Figure 7.2-8). These phenomena occurred within Stage II, indicating a gradual onset of stirrup effectiveness, or a lag in the full response of the stirrups. This lag is associated with slip between the concrete and the plain round bars that were used for stirrups. Once the stirrups were fully effective (when the slip between concrete and stirrups ceased), the percentage of sectional shear resisted by the flanges increased, but the rate at which this increased with applied load was not as high as that during the formation of the diagonal web cracks in Stage I. This is a result of the greater web shear stiffness with the full effect of the stirrups. This is illustrated in Figure 7.2-8.

The formation of the tensile crack on the top surface of the flange started with a reversal of strain recorded by the gauges at section B at a load level of $P=140\text{kN}$. This is outlined in the discussion in Appendix B. The discussion in this appendix also shows that the compression strains are transferred downward throughout the depth of the flange beyond this level of applied load. This is required of sectional equilibrium to ensure that the magnitude of the total compression force at section B equals the magnitude of the tension force at this section.

Corresponding to this, the magnitude of the interface shear can be seen to have significantly increased following this redistribution. It is through this action that the compression forces are 'transported' throughout the depth of the flange following the reversal of strains on the top of the flange. Through equilibrium between section A and B, the interface shear is dependant on the difference in compression force acting on a flange block, as well as the difference in shear lag acting on either side of the block. The increase in gradient of the shear lag was relatively insignificant following the load level of 140kN in comparison to the interface shear. The difference in compression forces acting on the flange blocks within this load level was high resulting in a large gradient of the interface shear.

Through equilibrium, the sectional shear was calculated using the shear lag, interface shear, and the compression force acting on each side of a flange block. Through the equilibrium relations, an increase in the rate of increase of the percentage of sectional shear resisted by the flange was found to occur at Stage III, and a subsequent increase in the gradient of this quantity with applied load was found to occur until the upper limit of the load range considered.

The formation of the cracks that defined the failure surface of this specimen throughout the duration of loading required redistributions of longitudinal strain, hence stresses throughout the width and depth of the flange to accommodate their development. The shear lag and interface shear were the actions through which the required redistributions took place. The change in flange compression gradient (between the sections considered) that resulted from these redistributions that occurred to accommodate the failure mechanism, increased significantly. It is the increase in compression gradient, and compression forces acting on the flange that result in the greater flange effectiveness for this specimen until the maximum loading value considered.

7.3 Specimen B17 Analysis

This section presents the results of the overall behaviour of specimen B17, as well as the results of the calculation of the shear lag, interface shear, and the sectional shear in the stage of calculation discussed in Chapter 3. In the determination of the effect of the formation of components of the failure mechanism on the results presented in this section, some consideration of the longitudinal strain profiles throughout the width and depth of the flange of the specimen, and the variation that they displayed throughout the duration of the loading applied to the specimen is required. These results are presented in Appendix C, due reference is made to these results in the following discussion where appropriate.

7.3.1 *Ultimate Strength and Failure Mechanism*

Specimen B17 exhibited a ductile flexural compression failure. Figure 7.3-2 shows a photo of the failure mechanism and Figure 7.3-2 shows the load deflection curve that was obtained from the experiment from this specimen. This curve shows that on reaching the peak load, the specimen exhibited very large plastic deflections. On exhausting all load carrying capacity, the concrete on the top surface of the specimen crushed, and the strength of the specimen decreased sharply. The peak load reached by the specimen was $P_u=238\text{kN}$ as indicated on the figure. This corresponded to a sectional shear at the peak load of $V_u=174.4\text{kN}$.

Figure 7.3-2 defines four stages on the load deflection curve. These correspond to key magnitudes of applied load at which stages of the failure mechanism formed throughout the experiment. These are categorised below.

Stage 1: This stage is bounded by a level of applied load of 78kN and 86kN. At each of these levels of load, a diagonal web cracks formed. Neither of these cracks became part of the shear mechanism that formed. It is noted that this mechanism was not exhausted at the end of the experiment.

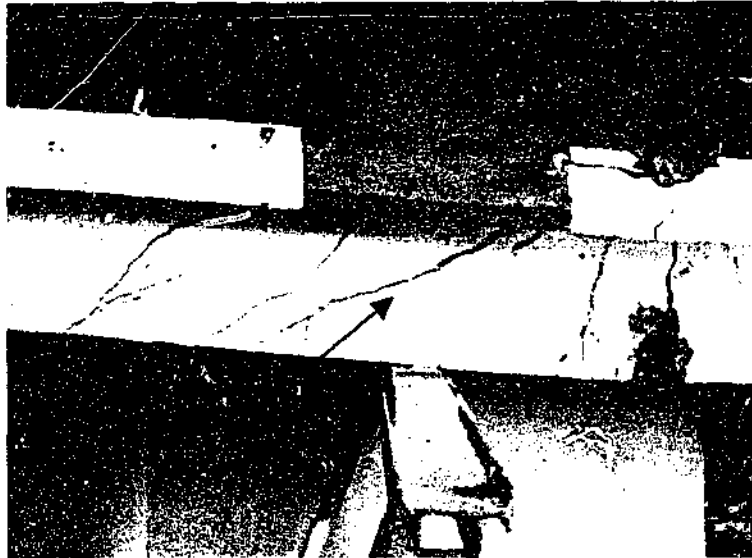


Figure 7.3-1 Specimen B17 failure mechanism

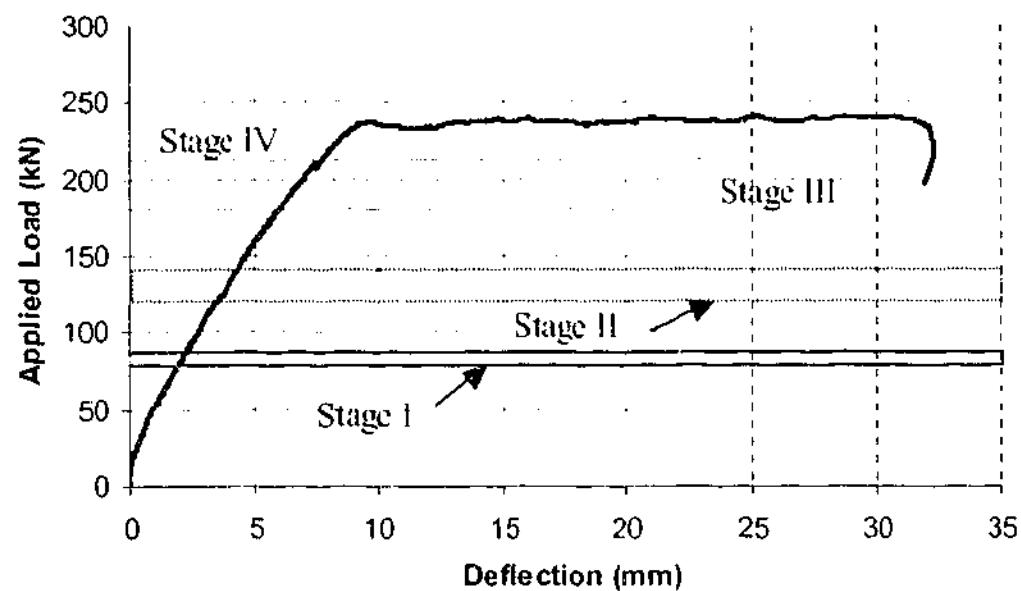


Figure 7.3-2 Specimen B17 load deflection curve

Stage II : This stage is bounded by a level of applied load of 120kN and 140kN. Between these levels of applied load, the gradient of increase in strain on the underside of the flange reversed. Prior to this level of applied load, the strains on these rows increased in tensile magnitude, within the load level, a redistribution of strain prevailed that saw this trend reverse. This is associated with the initiation of a shear compression that did not fully

develop throughout the experiment, as the flexural capacity was not high enough to allow this to occur. This was evident from examination of the longitudinal strain gradients. An analysis of these results is presented in Section C.2.1 in Appendix C. A small discontinuity in the load deflection curve is evident within this stage.

Stage III : This stage corresponds to an applied load of 180kN at which the neutral axis at section B moved to a location outside the underside of the flange at all rows in the flange overhangs. At the location of the centre of width of the web, the neutral axis remained within the depth of the flanges at all levels of applied load. A detailed analysis of the distribution of the neutral axis depth across the width of the specimen is given in Section C.3 Appendix C.

Stage IV : This stage corresponds to the level of applied load at which a significant diagonal web crack formed (212kN). Although this specimen failed in flexural compression, the formation of this crack coupled with the strain distribution formed in Stage II developed a shear compression mechanism. This mechanism did not develop to cause failure. A small discontinuity of the load deflection curve occurred at this level of load.

Although Stage II produced a discontinuity in the load deflection curve, there was no physical attribute in the test that could be attributed to the formation of this. Stage III does not cause any change to the load deflection curve, but it will become clear throughout the discussion in this chapter that the movement of the neutral axis outside of the flange overhangs produced significant influence on the effectiveness of the flange in the resistance of the applied sectional shear. As stated in their classifications, these reason for changes in the load deflection curve and flange effectiveness plots at these levels of applied load were deduced from the longitudinal strain distributions. A discussion of this is presented in Appendix C.

7.3.2 Range of Calculation of Shear Forces

The checks on the calculations of the shear forces briefly described in Section 7.2.2 were also undertaken for specimen B17. These can be seen in Appendix D. The checks of the

interface shear, and the sectional shear force calculated using the results of the longitudinal gauges indicated that the calculations satisfied equilibrium checks throughout the entire range of loading. Therefore, the results of the analysis of the quantities of shear lag, interface shear, and sectional shear are considered up to the value of peak load of 237.8kN illustrated in Figure 7.3-2.

7.3.3 Results of the Calculation of Shear Lag Forces

Figure 7.3-3 - 7.3-3 show the variation of the shear lag force displayed by specimen B17 throughout the duration of applied load. Figure 7.3-3 shows the variation of the shear lag force at each instrumented location across the width of the flange of the specimen at 20kN intervals, and Figure 7.3-4 shows the variation of the shear lag with applied load displayed by the specimen at each of the locations to which instrumentation was applied. Each part of the latter figure shows the variation of shear lag in one of the flange overhangs. The Figure 7.3-4 also shows the stages and points that were significant in the formation of the failure mechanism as outlined in Section 7.3.1 above.

The results of the distribution of the shear lag across the width of the flange shown in Figure 7.3-3 indicate that the profile across the width of the flange remained essentially constant throughout the duration of loading. This distribution always displayed a maximum magnitude at the rows closest to the flange-web interface, and these values decreased as the distance from the flange-web interface increased. This distribution showed an increasing trend with the load increments illustrated.

Figure 7.3-4 shows that the shear lag as calculated at all instrumented rows is affected by the formation of diagonal web cracks in Stage I. This is evident from the change in gradient of the shear lag with applied load that occurs at all rows within this stage. The initiation of the shear compression mechanism that occurs in Stage II causes a shift in the shear lag distribution at rows 1, 2, 3, 6 and 7. After this shift, there is a change in gradient of the shear lag distribution at these rows with the exception of row 3. The gradient of the shear lag with applied load at rows 3 and 5 is largely unaffected by the redistribution, as is the magnitude of the shear lag at row 5.

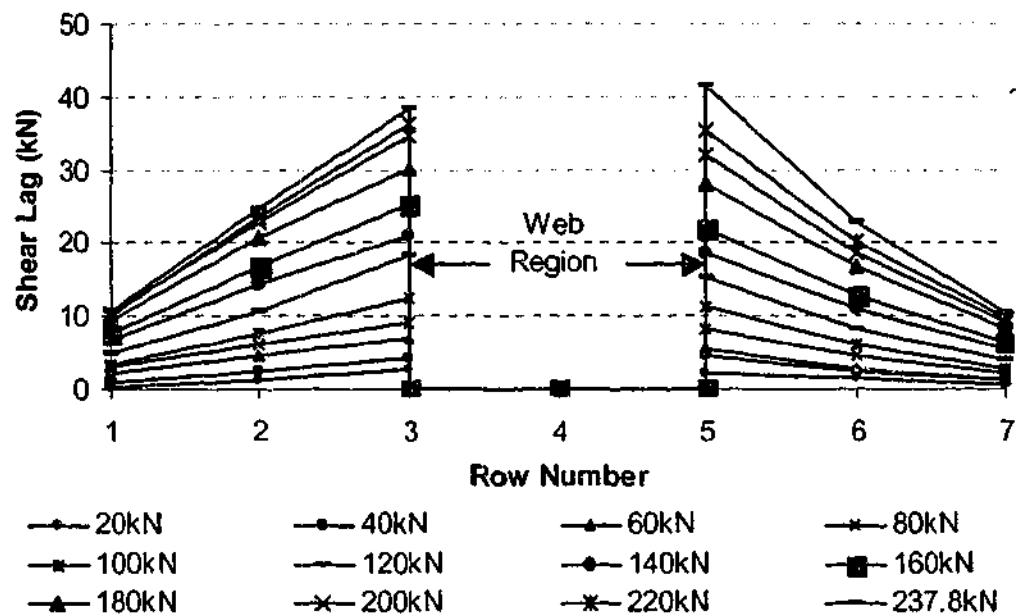
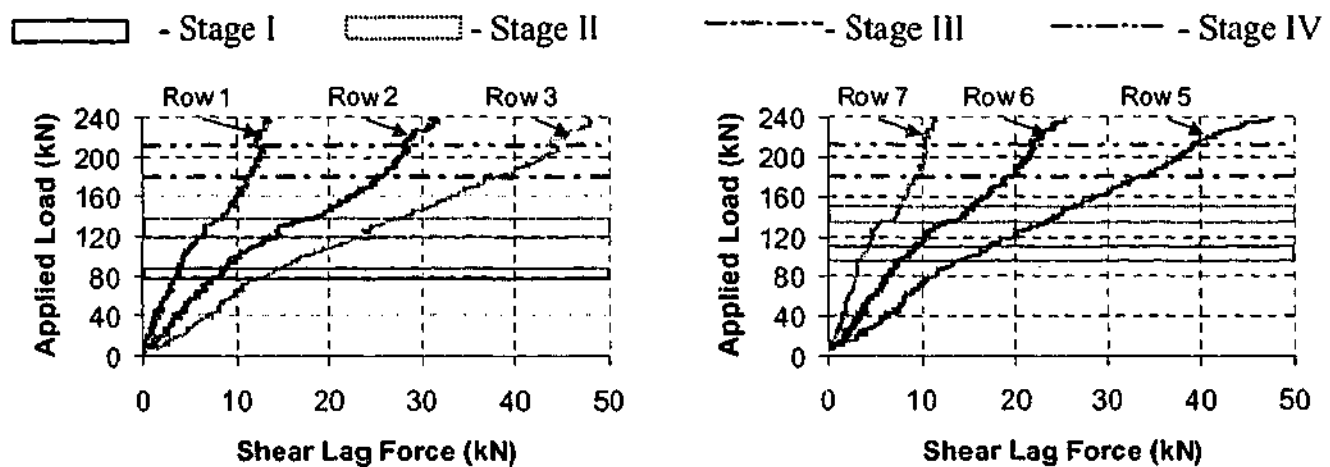


Figure 7.3-3 Shear lag distribution at 20kN increments for specimen B17



(a) Left side flange overhang

(b) Right side flange overhang

Figure 7.3-4 Variations of shear lag with applied load for specimen B17

It can also be seen from these figures that the appearance of the diagonal web crack at Stage IV (a level of applied load of 212kN) produces some variations in the response of the shear lag. The gradient of the response with the applied load remains essentially constant at each gauge location corresponding to the formation of this crack, but some discontinuity in the response can be seen in the figures.

7.3.4 Results of the Calculation of Interface Shear Forces

The results of the calculation of the interface shear that acts between layer α and layer β are shown below in Figure 7.3-5 – 7.3-5. The first of these figures shows the distribution of the calculated value of interface shear across the width of the flange at each gauge location in the flange overhangs. Figure 7.3-6 show the variation of the interface shear with the applied load at each gauge location. Each part of the latter figure shows results in one flange overhang. Figure 7.3-6 also shows the stages that were significant in the formation of the failure mechanism as outlined in Section 7.3.1 above.

Figure 7.3-5 shows that at all rows in the left side flange overhang, the distribution of the interface shear throughout the width remained essentially constant across the width of the flange. There are some small variations in the value of interface shear that occurred in this overhang at some load levels, but these considered insignificant in this discussion given the level of error that may be produced in the results. The right side flange overhang also shows an even distribution of the interface shear force at each row at low levels of applied load. At a level of applied load of 120kN a significant change in the distribution of the interface shear occurs in this overhang. Beyond this level of load, the value of the interface shear at the row nearest the flange-web interface decreases slightly moves to become a local minimum in this overhang, and remained so for the remainder of the loading history. The general trend at the remaining two rows is for the magnitude of the interface shear to increase with distance from the flange-web interface.

Figure 7.3-6 shows that this specimen displayed a very complex response of the interface shear to the formation of the components of the mechanism that developed throughout the loading history. It is evident from the longitudinal strain profiles that tensile stresses in the web at the level of the underside of the flange were at values equivalent to the cracking strain on concrete at levels of applied load of approximately 50kN. As can be observed from the figure below, all rows experienced a significant increase in the gradient of the interface shear with applied load resulting from the development of these cracking strains. The formation of the diagonal web cracks in Stage I can be seen to have decreased this gradient a small amount in the rows on the left side flange overhang, but had very little effect

on the rows on the right side flange overhang. Stage II produced a reversal in the gradient of interface shear with applied load at all rows in the left side flange overhang, and also at row 5. Interface shear values at rows 6 and 7 locally increased in magnitude as a result of the redistributions in Stage II. The gradients at all rows displayed at the end of Stage II can be seen to have reverted back the value that they were prior to Stage II. The appearance of the critical diagonal web crack at Stage IV caused a local increase in magnitude of the interface shear at all rows. The gradient of the interface shear with applied load displayed by all rows following the formation of this crack remained essentially constant after this shift.

7.3.5 Results of the Calculation of Sectional Shear Forces

Figure 7.3-7 shows the distribution of sectional shear forces calculated throughout the entire depth of the flange at each row in the flange overhangs. These results show a distribution that was essentially constant distribution across the width of the flange until a level of applied load of 120kN. Beyond this applied load, the specimen appears to have redistributed more shear force into the flange overhangs, resulting in a magnitude of shear at the in the flange blocks closest to the web being a minimum in both overhangs, and the magnitude increasing as the distance from this interface increases. This distribution remained essentially constant throughout the test on this specimen. An increase can be seen at each row with the increasing load for the most of the experiment. This is not the case at the increment of 120kN, and in the right side flange over hang at a level of applied load of 237.8kN.

Figure 7.3-8 shows the variation of the percentage of total shear force in the flanges (V_f/V_{applied}) with the level of applied load. The maximum contribution of the flange to the resistance of the applied sectional shear occurred at the peak load. This corresponded to a percentage of the sectional shear force resisted by the flanges of 24.0%. Line A on this figure represents the value of applied load which is the lower bound of applied load at which results of percentage of sectional shear resisted by the flanges were considered. At levels of load below this line, the electrical noise in the system produced variations in results that rendered the calculated values as inaccurate.

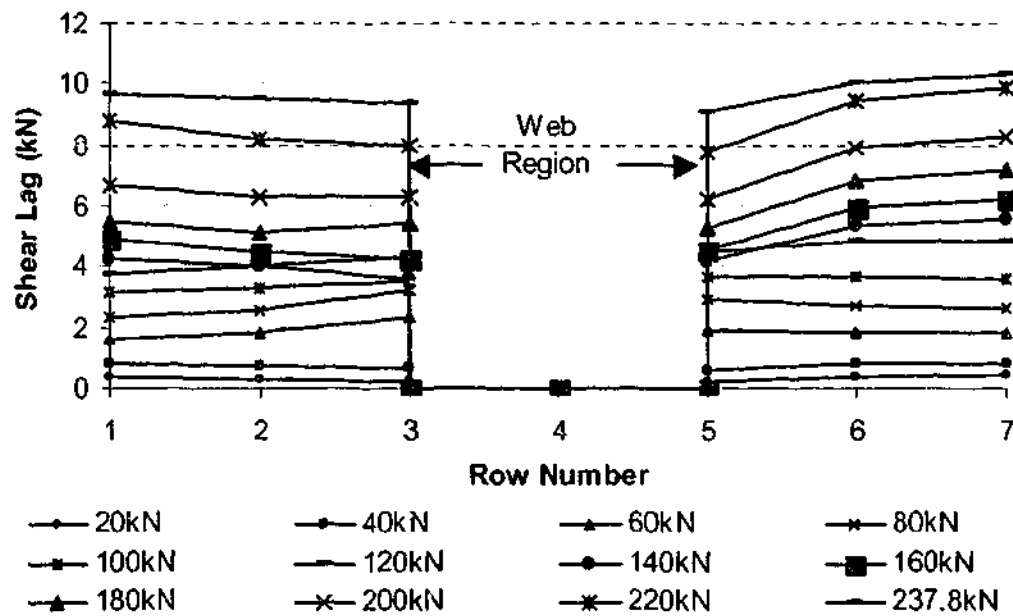
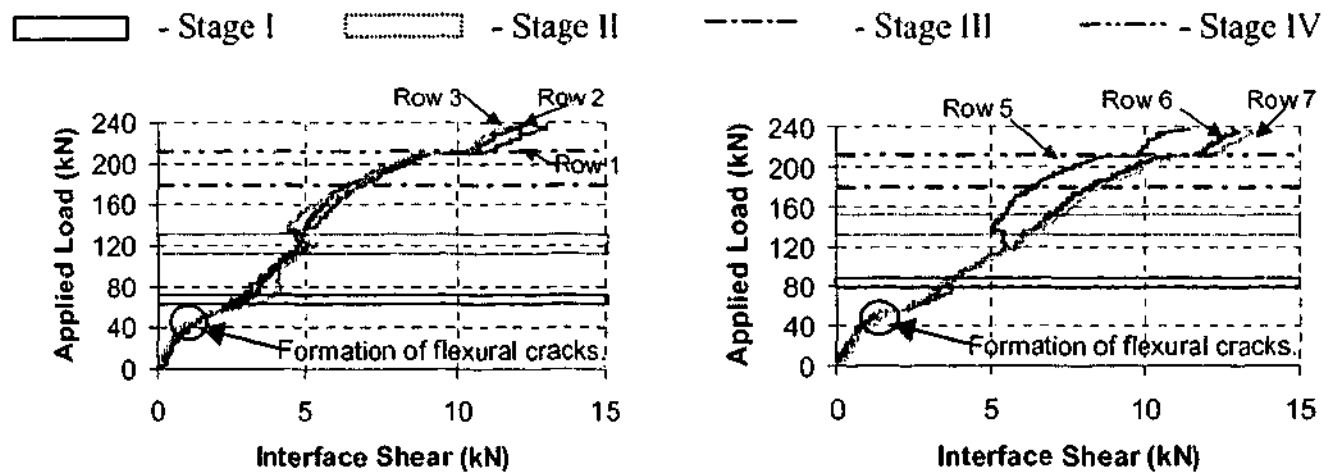


Figure 7.3-5 Distribution of interface shear throughout the width of the flange at 20kN intervals for specimen B17



(a) Left side flange overhang

(b) Right side flange overhang

Figure 7.3-6 Variation of interface shear with applied load at rows

The gradient of the percentage of sectional shear resisted by the flanges with applied load remains essentially constant from 30kN until Stage I. The formation of the diagonal web cracks in Stage I produced a decrease in the percentage of sectional shear resisted by the flanges. Beyond this stage, the gradient of this quantity with applied load was less than that

prior to Stage I. Stage II marks a significant reduction in the percentage of shear carried by the flanges. Throughout this stage, the magnitude of this quantity decreased at a uniform rate with the applied load. This occurred in both layers, but is most prominent in layer α . Beyond this stage, the contribution of the flange to the resistance of shear remained constant until Stage III. This point marked the level of applied load at which the neutral axis at section B moved outside of the flange. The appearance of the critical diagonal web crack caused a sudden, local, and significant increase in the percentage of shear carried by the flanges at stage IV. Beyond this point, the rate of increase of this quantity with the applied load increased at a slow rate.

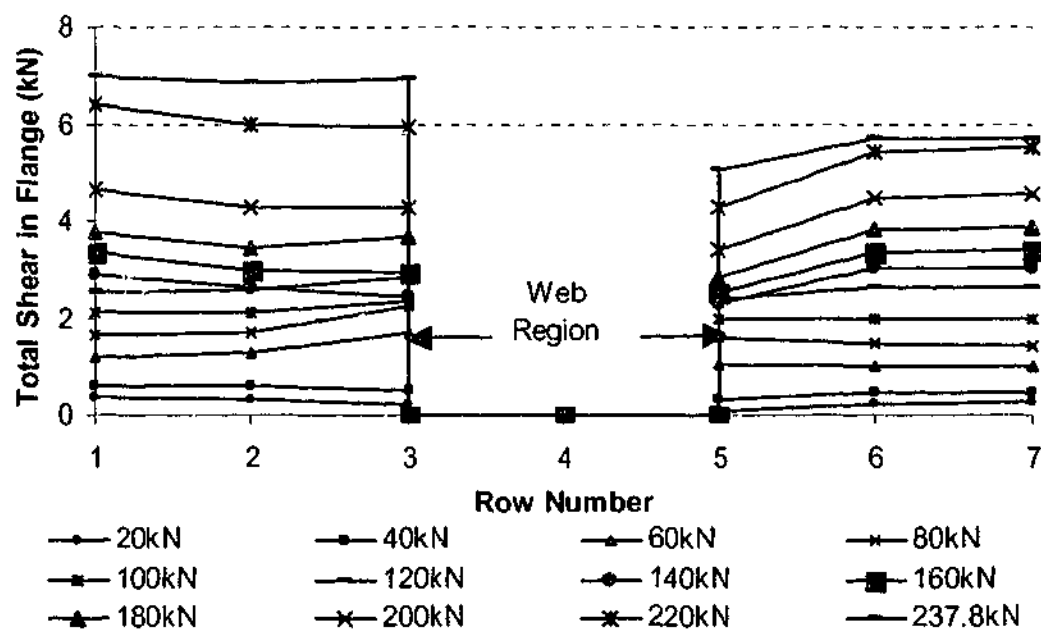


Figure 7.3-7 Distribution of sectional shear throughout the width of the flange as calculated for specimen B17

Figure 7.3-9 shows the distribution of shear force across the width of the flange that was calculated in each layer of the flange. In considering the total sectional shear force carried by each layer, layer α has a magnitude of sectional shear force smaller than layer β from the level of applied load of 30kN until the formation of the critical diagonal web crack at 212kN. Beyond this level of applied load, the rows in layer β resist more of the total shear than those in layer α . The magnitudes of the each row in the figure below reflect this.

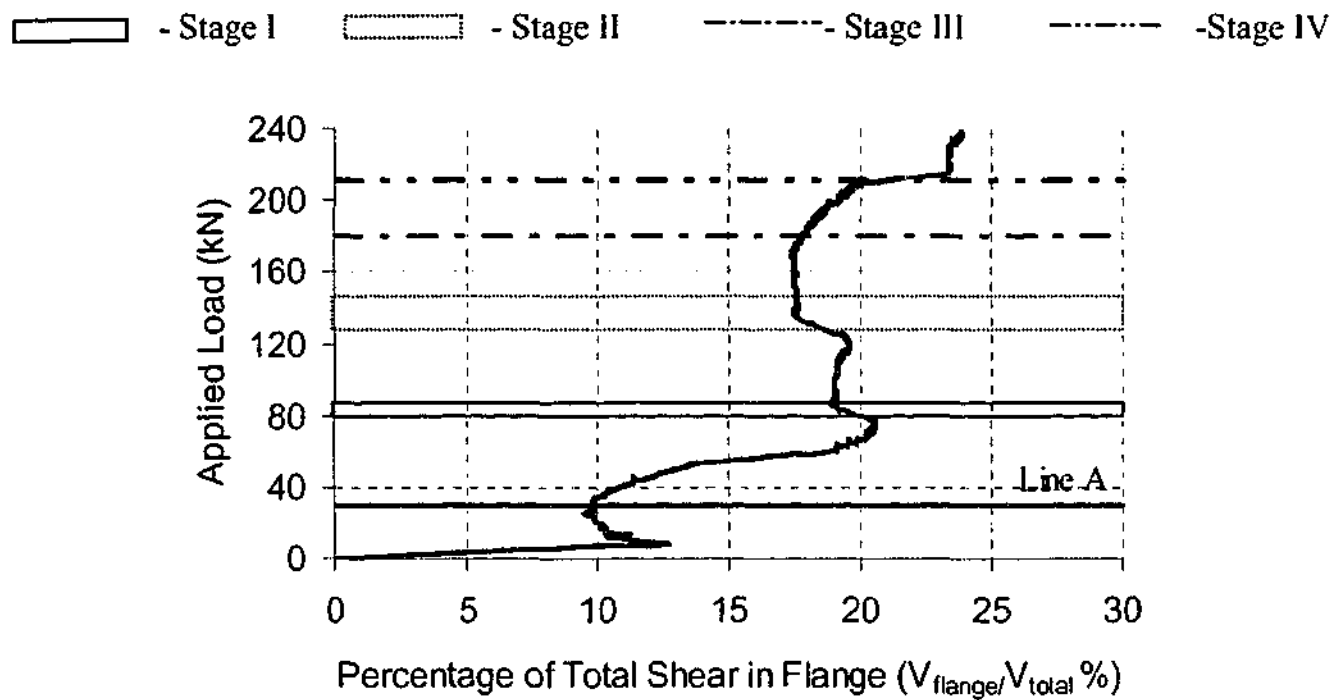
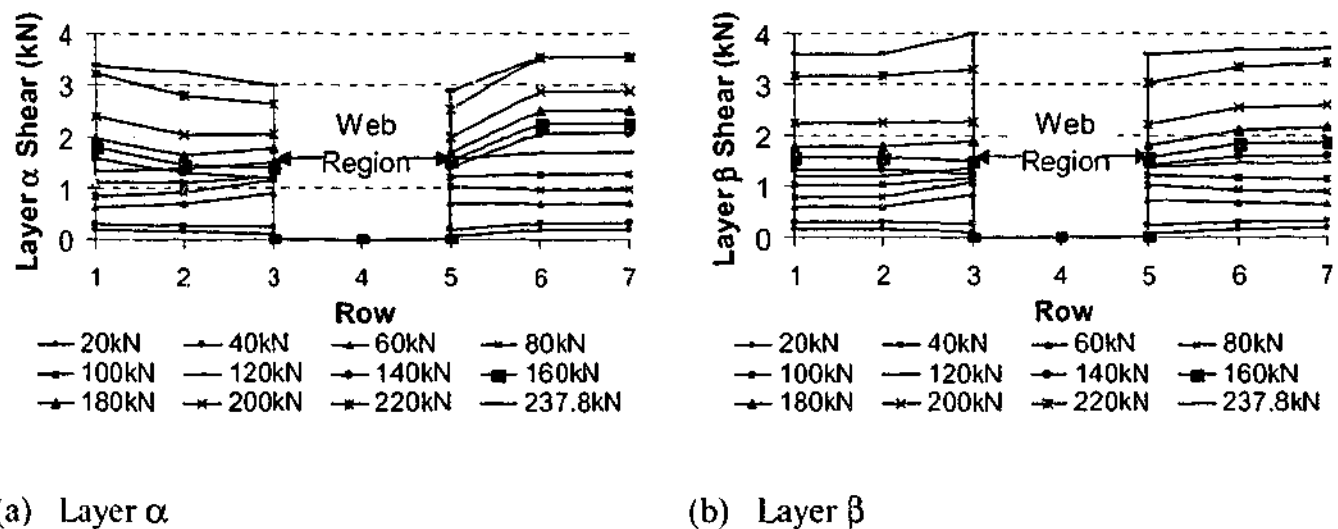


Figure 7.3-8 Variation of percentage of total sectional shear in flanges for specimen B16



(a) Layer α

(b) Layer β

Figure 7.3-9 Variation of shear in each layer at 20kN intervals for specimen B17

7.3.6 Flange Effectiveness of Specimen B17

From the initial level of applied load at which results of the calculations were considered (at $P=30\text{kN}$), the contribution of the flange (as indicated by the percentage of the total shear force carried by the flange) increases at a uniform and sharp rate. The formation of the first two diagonal web cracks in Stage I (range of applied load of 78-86kN) marked the end of this trend. Figure C.3-2 Appendix C shows that within this stage, the neutral axis

position at all rows in section B moved closer to the top surface of the specimen at a rapid rate. An increase in shear lag at all rows shown in Figure 7.3-4 was calculated, and a slight decrease in the interface shear shown in Figure 7.3-6 at all rows can be observed. As shown in Figure 7.3-8, the flange effectiveness decreased in this stage, the reason suggested for this is the onset of the stirrup effectiveness, and some slip between the concrete and the stirrups as the diagonal web cracks form.

Stage II saw a strain redistribution at both sections that is associated with the formation of a shear compression mechanism. Figure 7.3-5 shows that it is within this stage that a local increase in the shear lag was calculated at rows 1, 2, 6, and 7. This local increase in the shear lag indicates that compression forces were 'carried' from the web to the flange within this stage, and also that there was an increase in the compression gradient between the two sections at these rows.

Figure 7.3-6 shows a reversal of gradient in the interface shear calculated at rows 1, 2, 3, and 5. In addition to this, a local increase in the interface shear was calculated at rows 6 and 7, with these rows resuming the same gradient of increase with applied load following this local increase.

The net result of the above changes in the distributions of shear lag and interface shear produce an accompanying decrease in the percentage of sectional shear resisted by the flanges. The trend at which this decreases is consistent with that of the interface shear, showing the heavy reliance of the sectional shear on the interface shear.

As stated earlier, Stage III (applied load of 180kN) marked the level of applied load at which the neutral axis in the flange overhangs of section B moved to a depth greater than that of the flange depth. The steady increase in the compression force at this section increased the gradient of the compression force between section A and section B as the load progressed. This steady increase in the compression gradient between the sections produced an accompanying increase in the gradient of the percentage of the shear force resisted by the flanges with the applied load. The cause of the increase in the neutral axis depth at this section was the reduction in strains on the top surface similar to that of specimen B16. It is

apparent that the reversal of strain associated with the formation of a crack across the width of the flange had been initiated during this experiment, but the flexural capacity of the specimen was exhausted before the crack could fully form.

This steady increase in gradient of the flange effectiveness continued throughout the remainder of the experiment until the peak load. This is shown in Figure 7.3-8. The only other significant influence on the percentage of shear carried by the flanges was the appearance of the critical diagonal web crack at Stage IV. The results in Appendix C show that the appearance of this crack produced an accompanying sharp decrease in the strains on the top surface of the flanges at all rows, and increased the magnitude of the compressive strain on the underside of the flange at all rows. An increase in the difference in the compression force carried by each section is noted to have occurred as a result of the formation of this diagonal web crack.

Figure 7.3-6 shows that the interface shear increased locally at Stage IV as a result of the appearance of this critical diagonal web crack. This indicates that an increase in the magnitude of compression force 'carried' from layer α to layer β resulted from the appearance of this diagonal web crack. This is further reflected in Figure 7.3-9 where the distribution of shear in layer β shows values of greater magnitude of shear resisted than those in layer α . Therefore, the appearance of the diagonal web crack forced a redistribution of sectional shear forces throughout the depth of the flange.

7.4 A Further Examination of Stage 1 Failure Mechanisms

Examination of the above variation of the flange effectiveness of both specimens with applied load coupled with the discussion in Appendix B and C illustrates that as the shear failure mechanism develops, the flange becomes more effective. This effectiveness has been calculated at above 25%, and is therefore very significant in the shear resistance mechanism. It is now pertinent to examine the results of Stage 1 in light of these findings.

The discussion in Section 5.3 outlines the two failure mechanisms that were exhibited in Stage I of the experimental work. These failure mechanisms were the beam shear failure mechanism and the punching shear failure mechanism. Further examples of these can be seen below in Figure 7.4-1 - Figure 7.4-3.

The pictures in these figures, illustrate that both the beam shear failure mechanisms and the punching shear failure mechanism exhibit the key stages of the development of the shear failure mechanism that were outlined in this chapter to be correlated with significant increases in the gradient of increase in flange effectiveness with applied load. These are the appearance of the critical diagonal web crack and the reversal of the compressive strains on the top surface. Note that the latter is observed from the presence of the lateral crack on the top surface of the flange.

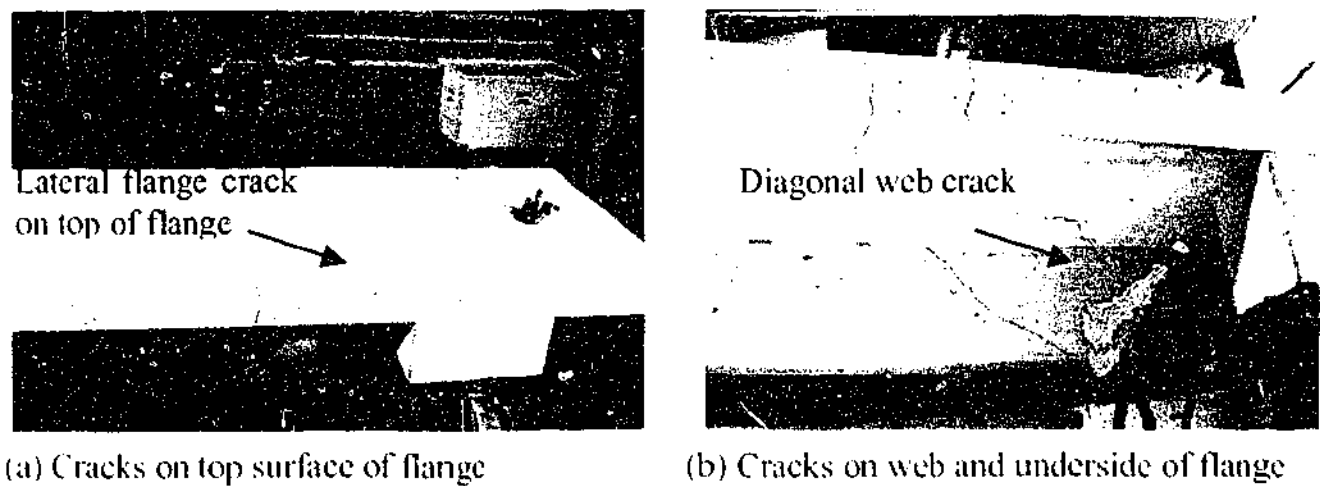


Figure 7.4-1 Cracks on specimens B1 (punching shear failure mechanism) at failure

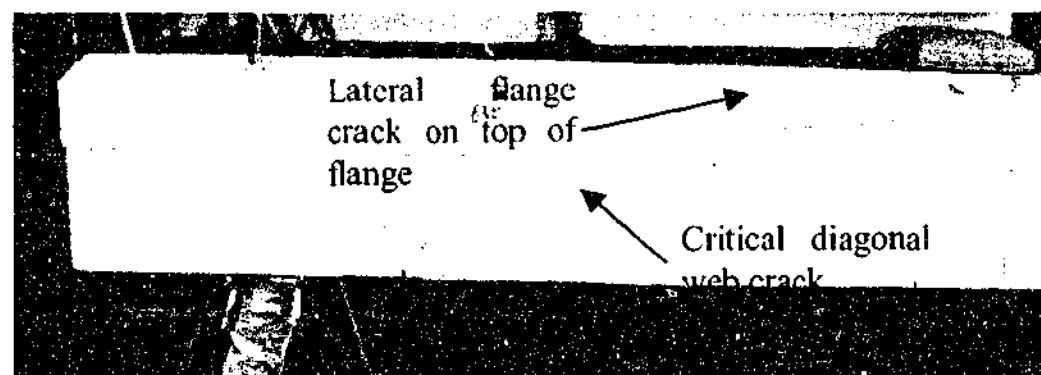


Figure 7.4-2 Cracks on specimen B5 at failure (beam shear mechanism)

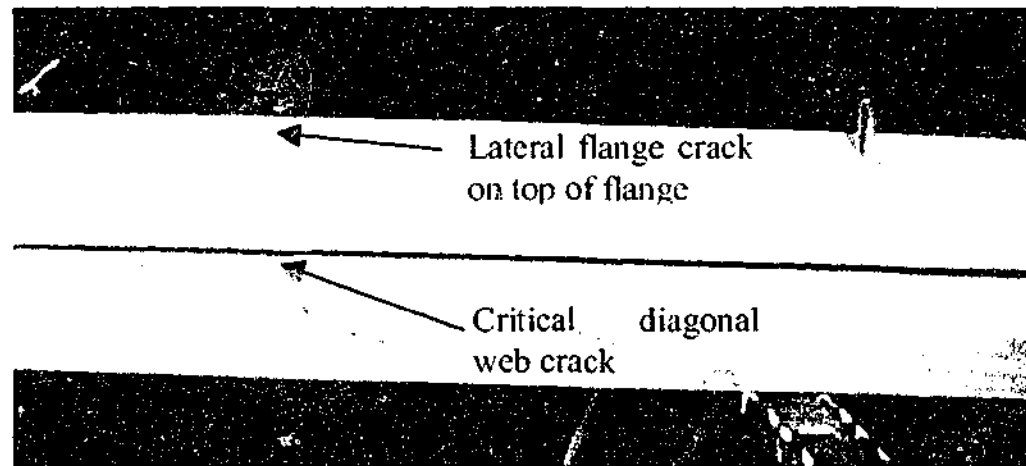


Figure 7.4-3 Cracks on specimen B3 at failure (beam shear failure)

It is the significant increase in the gradient of the increase in flange effectiveness that has been shown in Sections 7.2.5 and 7.2.6, and the identical development of the failure mechanism displayed in all specimens in Stage I that suggests that the increase in shear strength with the flange proportions of stage I specimens is highly dependent on the propagation of shear forces into the flange of the specimen.

Stage II experimental work has indicated that approximately 25% of shear force is resisted by the flange. This was true for specimen B16 at termination of the calculation procedure at 75% of the peak load (showing a trend for increase beyond this level of applied load), and for specimen B17 that failed by exhibiting a flexural compression mechanism. It is suggested that these figures are indicative of a minimum value of the flange effectiveness of a point loaded RC T-beam specimen with web reinforcing subjected to a point load. This value would therefore be a minimum contribution to the shear resistance in stage I experiments where a significant increase in shear strength is observed. The thin dimension of the flange in specimens of series 3 in stage I experimental work is thought to limit the propagation of shear forces in the flange, therefore resulting in minimal increasing shear strength through this redistribution.

7.5 Conclusions

The above presents results of the application of the instrumentation technique and accompanying analysis procedure developed in Chapter 3 to the flanges to two point loaded RC T-beam specimens. Confidence in the results that are discussed in this section is drawn from the validation work discussed in Chapter 6.

The most important conclusion from these two tests is that the increase in contribution to the resistance of shear that arises from the presence of the flange on a web reinforced RC T-beams subjected to a concentrated point load is at least partly due to propagation of shear stresses into the flange.

Conclusions regarding the nature of this and the redistributions of this are outlined below.

1. The proportion of the shear force resisted by the flange increases throughout loading suggesting that shear stresses are redistributed from the web of an RC T-beam specimen to the flange. The maximum percentages of the total shear resisted by the flange calculated using this procedure were 27.5% in specimen B16 at 75% of the peak load (which was the termination point of the calculation procedure), and 24.0% in specimen B17. The latter was calculated at the peak load.
2. The development of the shear failure mechanism throughout the tests outlined above significantly increases the contribution of the flange to the resistance of shear.
3. After the full development shear failure mechanism, the contribution of the flange increases throughout the application of the loading to these specimens, such that the peak contribution is at either the peak load or the maximum load at which the calculations were performed (the figures in point 1 above demonstrate this).

4. The significant value of the contribution of the flange at the termination of the calculation procedure is associated with the redistribution of the longitudinal strains that occur as the specimen accommodates the individual stages of the failure mechanism.
5. The redistribution of the shear forces throughout the width and depth of the flange is achieved through the actions of the shear lag and the interface shear forces.
6. Since specimens in stage 1 and 2 in series 1 experimental work exhibited identical development of the shear failure mechanism, the significant increase in the shear strength can be at least in part attributed to the contribution of the flange.
7. The negligible increase in shear strength in series 3 of stage 1 experimental work is attributed to the depth of the flange to be too small to allow propagation of shear forces into this region, therefore allowing for no increase in shear strength from the flange contribution.
8. The increase in the contribution of the flange is associated with the redistribution of longitudinal strains that occur as the specimen accommodates the failure mechanism. The transportation of the shear stresses across the width of the flange is achieved by the action of the shear lag, and the transportation of the shear throughout the depth is achieved by the action of the interface shear.

Chapter 8 RESULTS OF THE FINITE ELEMENT STUDY

8.1 Introduction

This chapter presents the results of the finite element study that was outlined in Chapter 4. The finite element study was performed in three stages as follows.

1. Stage I

- Implement modelling aspects such as mesh size and optimum solution scheme that have already been established by previous investigations (outlined in Section 4.6), and examine the effect of the selection of material models, and size of displacement increment on the typical specimens that represent those of stage I experiments.

2. Stage II

- Determine the ability of the selected material model combination and step increment to predict the peak loads, load deflection behaviour, crack patterns, reinforcing stains at peak load, and failure mechanisms of the three series of specimens tested in stage one experimental work.
- Determine the ability of the solution scheme to predict longitudinal strains in the experimental work.
- Calculate the percentage of the shear force predicted to be in the flange of the specimens for comparison with experimental values.

3. Stage III

- Knowing the limitations of the modelling strategy determine the predicted values of peak loads, and the load deflection response of three series of beams that with constant material properties, with variable flange geometry.

This chapter presents the implementation of the finite element procedure to examine the above.

8.2 Stage I – The Parametric Study

This study was applied to two specimens from series 1 of stage 1 experimental work. These are specimens B2 and B5. These specimens displayed the two different types of failure mechanism that were observed throughout the experimental work; the beam shear and punching shear mechanisms.

8.2.1 *Material Model Study*

To determine the most suitable combination of material models to describe the behaviour of the concrete within the specimen, the following comparisons were made.

1. Comparison of the load vs. displacement plots obtained for each of the Drucker-Prager and Crack Model Based on Total Strain models with those produced in the experimental work. These models are outlined in Section 4.4.1.
2. Comparison of peak load from experimental work (P_E) with the peak load obtained from NLFEA (P_{NLFEA}).
3. Comparison of the crack patterns from the experiments with those obtained from the finite element analysis.

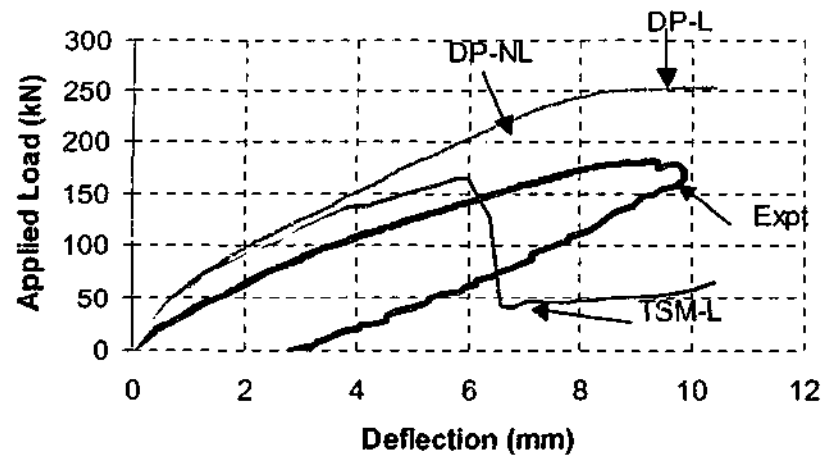
It would be useful to compare the stirrup contribution (measured in terms of the number of stirrups that were at yield at the peak load), however, the results from the experimental work only gave strains at one point on two stirrups within the shear span. It was highly possible that the locations instrumented did not correspond to a location on a stirrup that was at yield. Since it is the number of stirrups at yield that indicate the stirrup contribution, and no direct comparison can be made of this, it was decided that this would not be considered in the parametric study. The results of the stirrup (and flexural tension) reinforcing strains will be discussed later in the application of the procedure to individual specimens.

8.2.1.1 Comparison of Load-Deflection Response

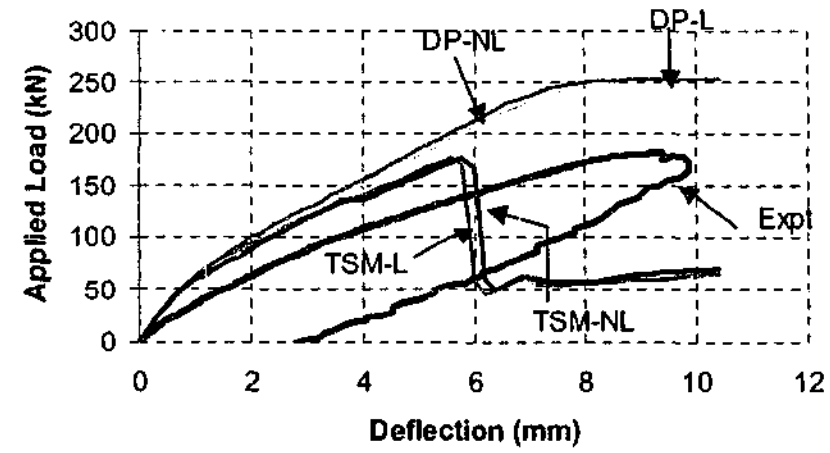
The load deflection response of each of the combinations of the constitutive models that were considered in this study was compared with the load deflection curve obtained from the experimental work. The results of this are presented below in Figure 8.2-1 - Figure 8.2-2. These figures show the variation in the load deflection response of the four combinations of constitutive models investigated in this parametric study for each value of the shear retention factor (β).

Some values are not shown on these plots for specimens that diverged early as a result of numerical instability. Table 8.2-1 and Table 8.2-2 outline which specimens this applies to.

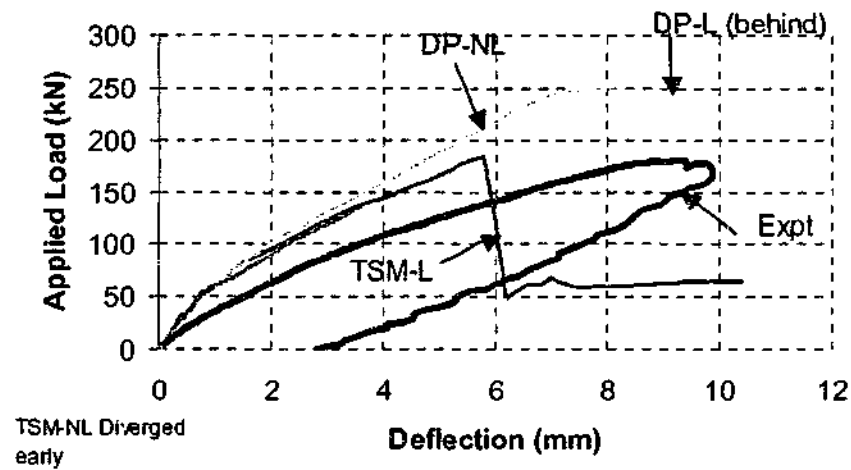
It is clear from Figure 8.2-1 and Figure 8.2-2 above that the Crack Model Based on Total Strain produces a significantly better prediction of the load deflection behaviour than the Drucker – Prager model. This is the case regardless of the value of β . In all cases, the Drucker – Prager model predicts a ductile response beyond the peak load and does not produce any overall softening, whereas, the TSM model predicts a softening after the peak load. The softening in the latter case is brittle for specimen B2, and smooth for specimen B5.



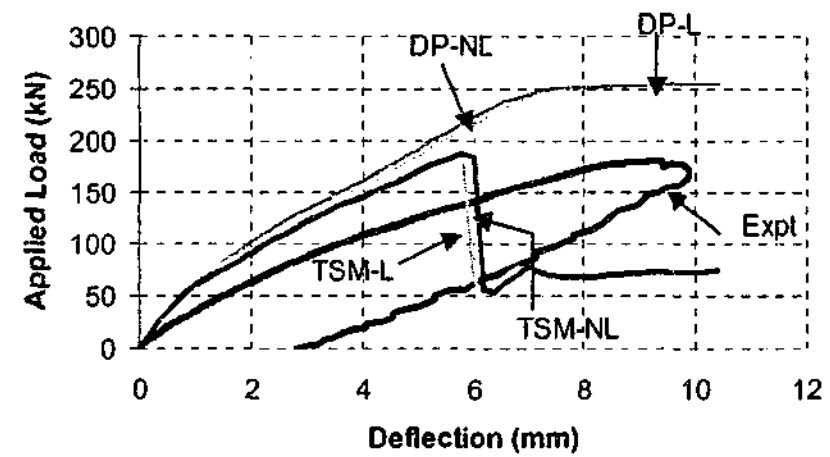
(a) $\beta=0.05$



(b) $\beta=0.10$

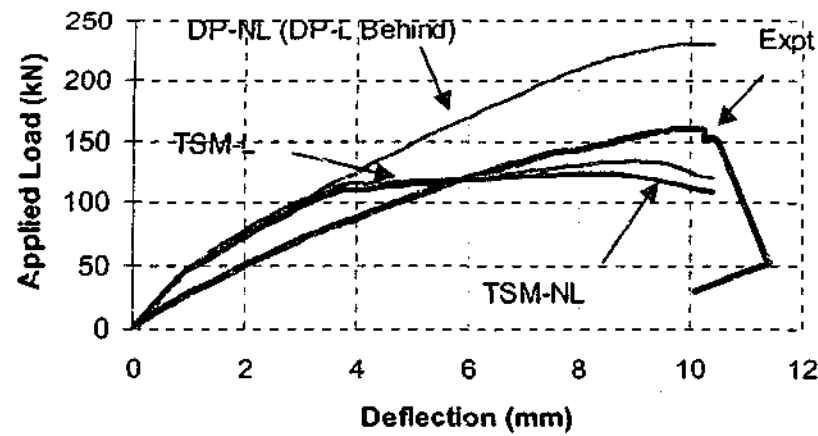


(c) $\beta=0.15$

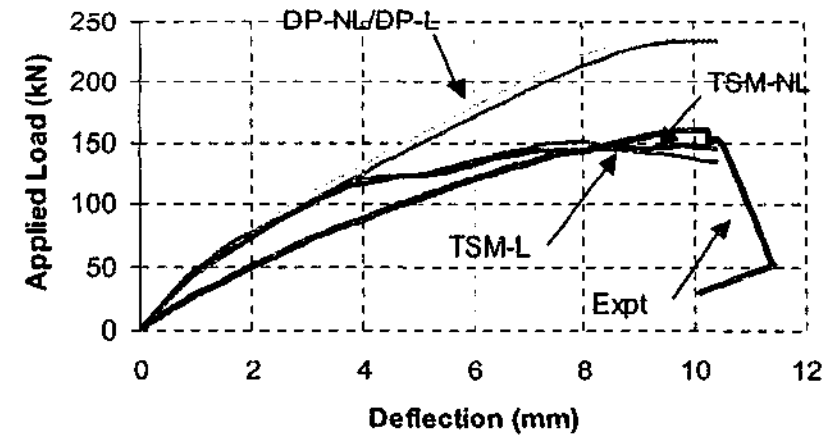


(d) $\beta=0.20$

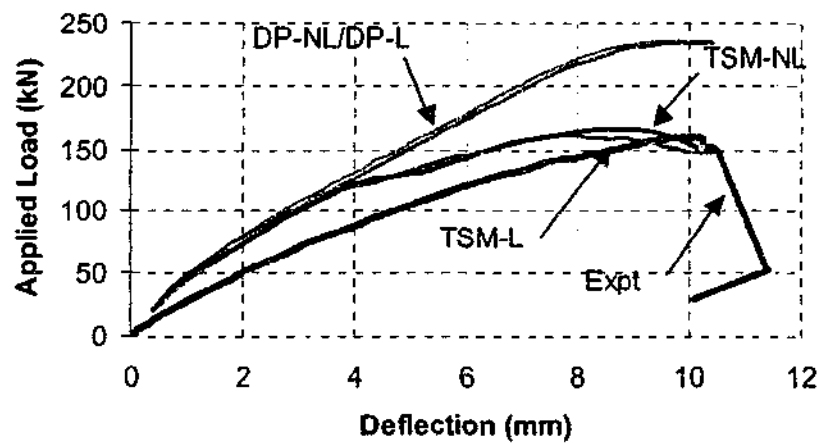
Figure 8.2-1 Comparison of load deflection plot for varying values of β and varying constitutive model combinations for Specimen B2



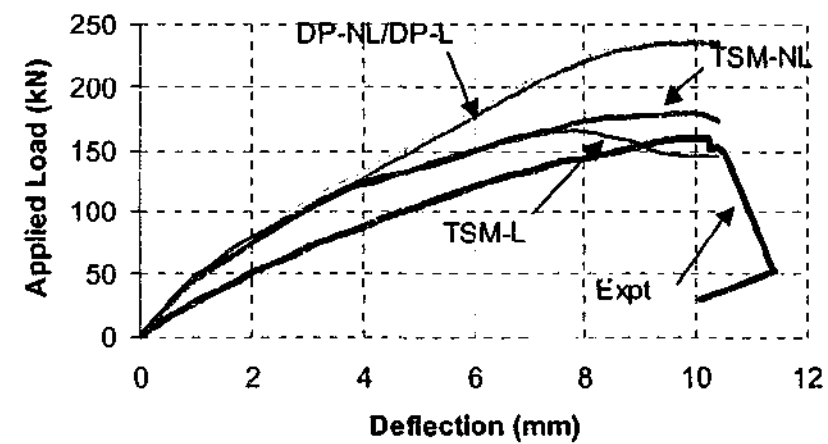
(a) $\beta=0.05$



(b) $\beta=0.10$



(c) $\beta=0.15$



(d) $\beta=0.20$

Figure 8.2-2 Comparison of load deflection plot for varying values of β and varying constitutive model combinations for Specimen B5

For each value of β that was investigated, it is clear that combining the Drucker – Prager material model with a linear or nonlinear tension softening model only makes a slight difference to the overall load deflection response. The combination of the Total Strain Based Crack Model however shows that for specimen B2, the use of a nonlinear tension softening model predicts a higher deflection at peak load when compared to results that incorporate the linear tension softening model. The results of specimen B5 indicate that the use of the nonlinear tension softening model produces a more ductile post peak response (the actual specimen was brittle in failure) than the linear response model.

8.2.1.2 Comparison of Peak Loads

The comparison of the peak loads obtained from each analysis (P_{NLFEA}) between the experimental results is given below in Table 8.2-1 for Specimen B2, and in Table 8.2-2 for Specimen B5. These tables show the effect of the value of the Shear Retention factor (β) as well as the combination of the constitutive models considered on the two specimens used for the parametric study. It was considered appropriate that the combination of material behaviour models was discussed rather than each tension and compression model in isolation because of the effect of tension response on the compression response that is particularly apparent in the Crack Model Based on Total Strain. The peak load presented in this table, and from this point onward is the sum of the reactions obtained from the solution.

Both of these tables above show a consistent and significant over estimate of the peak load by the Drucker – Prager material model. This overestimate is true for both specimens, and is independent of the value of β and tension response model.

The prediction of the peak load for the constitutive model combinations that involve the use of the Crack Model based on Total Strain are significantly better than those predicted by material model combinations that include the Drucker – Prager model. Table 8.2-1 and Table 8.2-2 show that the increase in the value of β generally increases the peak load. In addition to this, the use of the nonlinear tension softening model in combination with this compression model generally increases the peak load.

Table 8.2-1 B2 peak load comparison ($P_E = 181.0\text{kN}$)

Shear Retention Factor (β)	Constitutive Model Combination	Peak Load (P_{NLFEA}) (kN)	(P_{NLFEA}/P_E)
0.05	DP-L	252	1.39
	TSM-L	165	0.91
	DP-NL	*	NA
	TSM-NL	*	NA
0.10	DP-L	253	1.40
	TSM-L	175	0.97
	DP-NL	251	1.39
	TSM-NL	175	0.97
0.15	DP-L	254	1.40
	TSM-L	185	1.02
	DP-NL	254	1.40
	TSM-NL	*	*
0.20	DP-L	254	1.40
	TSM-L	188	1.04
	DP-NL	251	1.39
	TSM-NL	188	1.04

* - These specimens diverged early. The combination of constitutive models that produced divergence were not presented as it is apparent from the load deflection comparisons that this divergence was numerical rather than an exhaustion of capacity of the specimen. These results are therefore redundant in this discussion.

As noted below the Table 8.2-1, specimens marked * displayed exceptionally high relative energies, and sudden divergence for both compression models considered. The results of peak load corresponding to this divergence were not consistent with the experimental results nor with those of the other numerical analyses. It is thought this is a problem with the numerical solution scheme. Since this is the case, the combination of nonlinear tension softening with the Crack Model Based on Total Strain will be disregarded owing to potential numerical instabilities; the linear tension softening model was adopted.

Table 8.2-2 B5 peak load comparison ($P_E = 159\text{kN}$)

Shear Retention Factor (β)	Constitutive Model Combination	Peak Load (kN)	(P_{NLFEA}/P_E)
0.05	DP-L	230kN	1.45
	TSM-L	127	0.80
	DP-NL	230	1.45
	TSM-NL	108	0.68
0.10	DP-L	236	1.48
	TSM-L	151	0.95
	DP-NL	233	1.47
	TSM-NL	140	0.88
0.15	DP-L	236	1.48
	TSM-L	145	0.91 ^A
	DP-NL	235	1.48
	TSM-NL	165	1.04
0.20	DP-L	237	1.49
	TSM-L	163	1.03
	DP-NL	235	1.48
	TSM-NL	175	1.11

Either a value of β of 0.10 or 0.15 produce ultimate strength results that are close to those obtained experimentally. The ultimate strength result for specimen B5 with the constitutive model combination of TSM-L and $\beta=0.15$ (marked with a superscript ^A) went against the general trend that was produced in the ultimate strengths obtained from this constitutive model combination both for this specimen and specimen B2. This inconsistency led to the use of the value of $\beta=0.10$. The constitutive model combination used in the ensuing analysis is summarised by $\beta=0.10$: TSM-L.

8.2.1.3 Crack Patterns Produced From the Analysis

Figure 8.2-3 and Figure 8.2-4 below show the crack patterns that were predicted by the NLFEA procedure for the two specimens examined in this parametric study. To verify that

the modelling procedure is capable of predicting results that are representative of those produced in the experiment, it was required that the crack pattern represent those that form the mechanisms by which the specimens failed in the experimental work.

In the experiment, specimen B2 failed by the mechanism of punching shear. The crack pattern predicted by the NLFEA procedure shown below in Figure 8.2-3 shows a crack pattern of similar characteristics to the punching shear mechanism. A diagonal web crack is formed, and there is the presence of local cracks in the vicinity of the load point consistent with the punching mechanism.

Specimen B5 failed by exhibiting a beam shear mechanism in the experimental work. Figure 8.2-4 shows the crack pattern predicted by NLFEA for this specimen. It shows that a diagonal web crack is present, and predicts this crack will extend along the underside of the flange to meet with a crack on the edge of the flange at failure. This crack was then predicted to continue to the centreline of the specimen. This pattern of cracking is consistent with the beam shear crack pattern obtained from the experiment.

The two types of failure mechanism observed in the experimental work are produced by the NLFEA solution scheme, and are predicted to occur on the corresponding specimens in this study. This combination of material models is deemed sufficient in predicting the crack patterns for the experimental specimens.

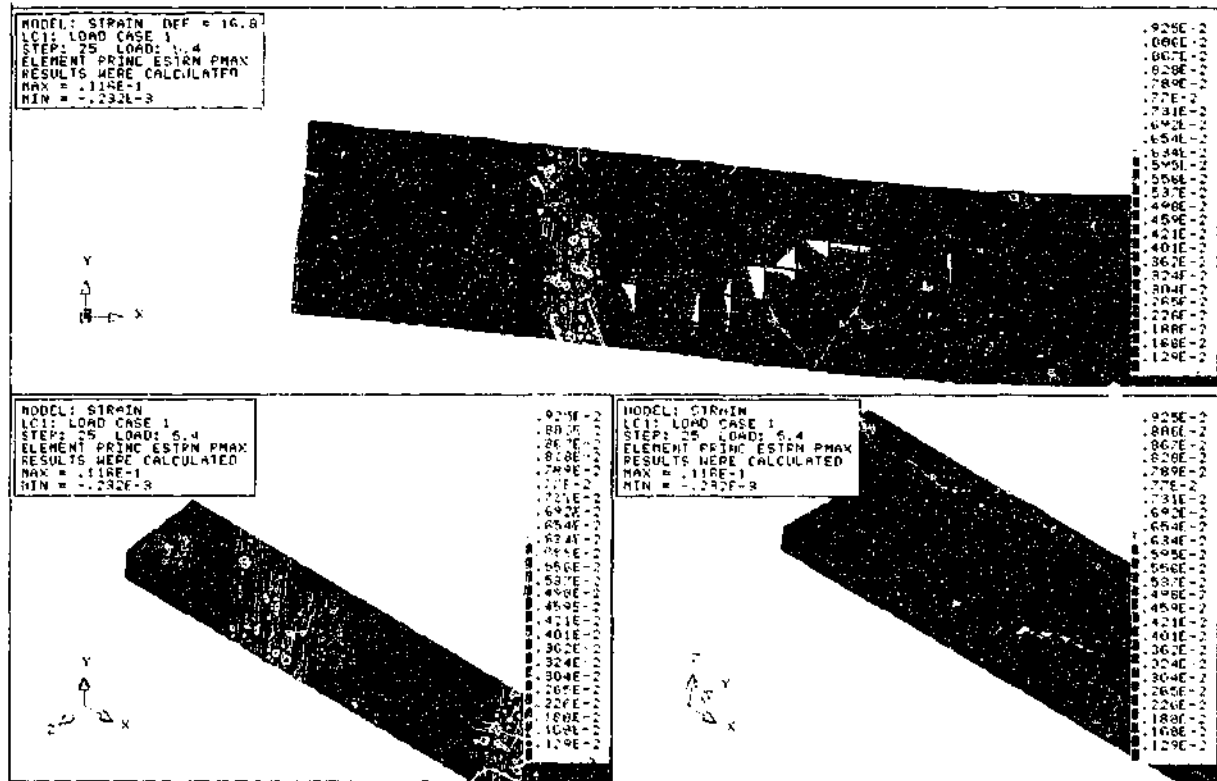


Figure 8.2-3 Crack pattern obtained for B2 using $\beta=0.1$: TSM-L

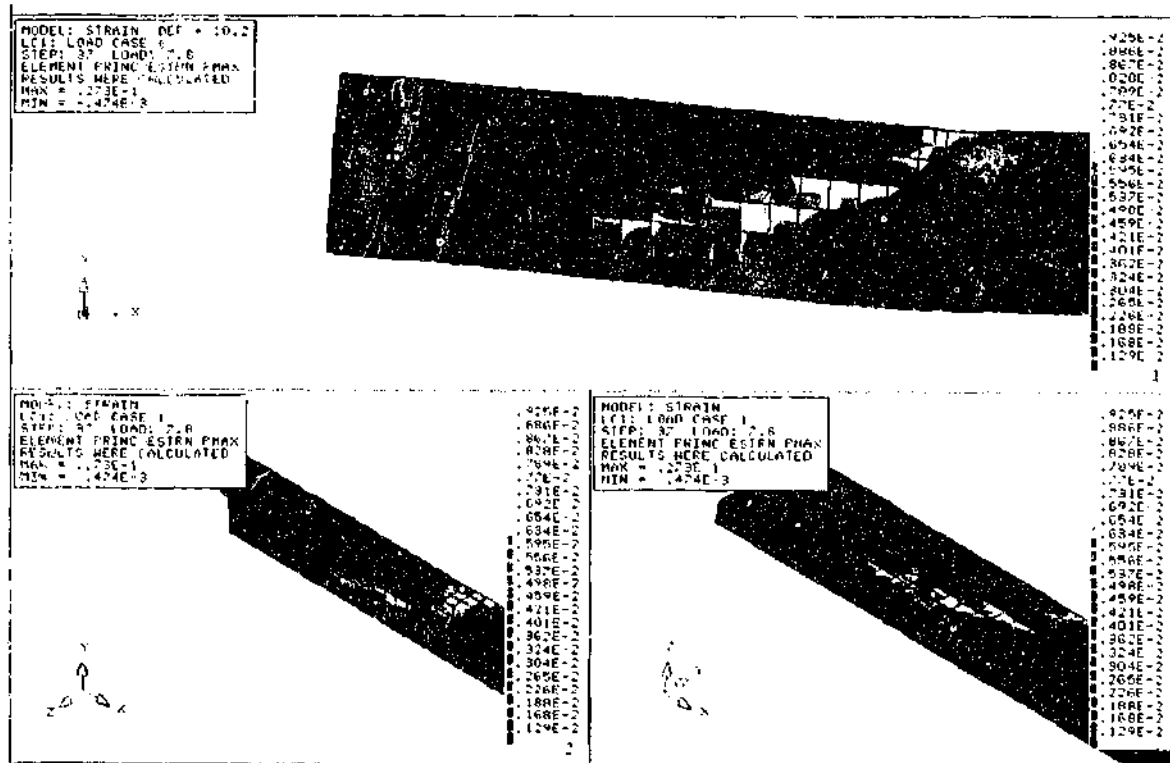


Figure 8.2-4 Crack pattern obtained for B5 using $\beta=0.1$: TSM-L

8.2.2 Load Step Size Study

Using the combination of the crack model based on total strain and the linear tension softening for the description of the behaviour of concrete, it was deemed necessary to determine the influence of the step size on the load deflection behaviour. This was to ensure that the step increment did not over step the values of applied load that result in the formation of the failure mechanisms. This study was performed on specimen B5.

The displacement increments that were selected are (as outlined in Chapter 4); an initial displacement increment of $D_i=0.2\text{mm}$ for two steps followed by 0.1mm thereafter, an initial displacement increment of $D_i=0.4\text{mm}$ for two steps followed by 0.2mm thereafter, an initial displacement increment of $D_i=0.5\text{mm}$ for two steps followed by 0.25mm thereafter, an initial displacement increment of $D_i=1.0\text{mm}$ for two steps followed by 0.5mm thereafter. A comparison of the load deflection plots for these specimens is shown in Figure 8.2-5.

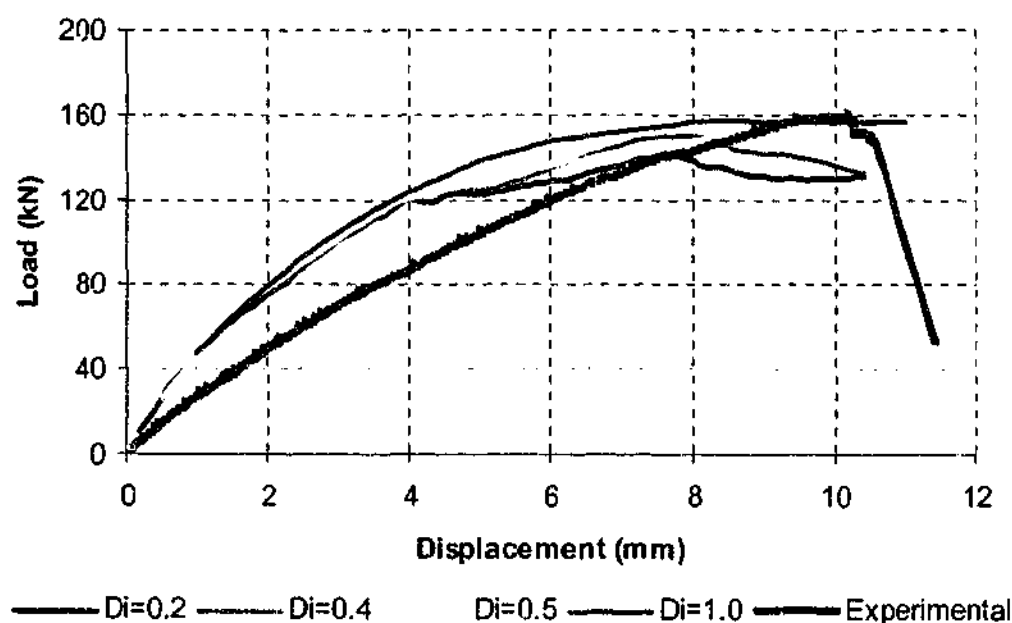


Figure 8.2-5 Comparison of load displacement plots for different increments of displacement

Figure 8.2-5 shows that at early stages of loading, the analyses performed with higher increments of displacement ($D_i=0.5\text{mm}$, and $D_i=1.0\text{mm}$) produce comparable load-displacement curves as the lower values of this increment ($D_i=0.2\text{mm}$, and $D_i=0.4\text{mm}$). However, as cracking starts to influence the behaviour of this specimen (at a level of applied

displacement of approximately 4.0mm), the sensitivity of the response to cracking is seen in this figure to reduce as the increment of displacement increases.

The two smaller displacement increments displayed a trend of load deflection similar to that of the experimental curve, particularly in reference to slope changes with cracking. Of these two analyses, the analysis performed with $D_i=0.4\text{mm}$ produced a peak load that was close to that given in the experiment. As this was the case, a displacement increment of 0.4mm for the first two steps, and then 0.2mm was used in the ensuing analysis.

8.3 Stage II – The Specimen Study

Application of the combination of the Crack Model based on Total Strain in combination with the linear tension softening model and an increment of initial displacement of $D_i=0.4\text{mm}$ (and subsequent displacement increment of 0.2mm) was applied for numerical modelling of all experimental specimens. These models included exact properties of both materials as calculated from cylinder tests and tensile tests results. This section presents a comparison between the NLFEA results and those obtained from the experimental work. In line with the objectives outlined in Section 4.2, the results of ultimate strength, load-deflection response, crack patterns, and reinforcing strains at the peak load are compared with stage 1 experimental work, and an examination of the predicted failure mechanisms. In addition to this, concrete strains and the flange contribution to the shear resistance is compared to stage 2 experimental work.

8.3.1 *Ultimate Strength*

Table 8.3-1 below shows the comparison between the peak loads obtained from experimental work with those obtained from numerical analysis as well as the relative error between these. In general, the NLFEA procedure has predicted values of the peak load with an average ratio of the numerical to peak loads of 1.01, and a standard deviation of 0.13.

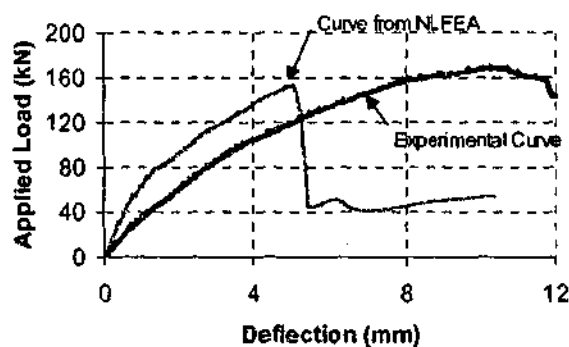
NLFEA significantly over predicted the peak load of specimens B9, B12, and B13. The remainder of this section outlines the load deflection response, crack patterns, reinforcing

strains, and failure mechanisms. The overestimates are dependant on the failure mechanisms, and this over prediction is discussed in Section 8.3.5 that outlines all failure mechanisms observed throughout the numerical modelling implementation.

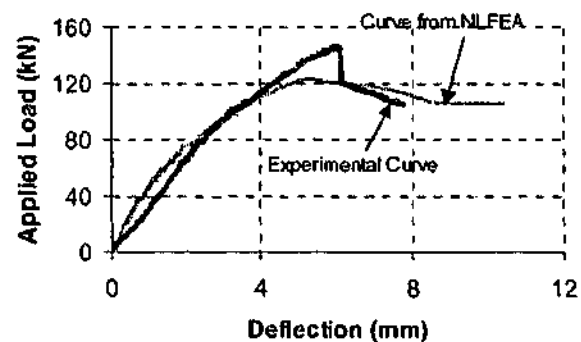
8.3.2 Load Deflection Response

For the purpose of this discussion, only two load deflection curve comparisons from each series of specimens will be presented in this section. Load deflection curves for all specimens are presented in Appendix E. The comparisons are shown below in Figure 8.3-1 - Figure 8.3-2. Note again that the load presented in the finite element results is the sum of the reactions.

In general NLFEA has produced results of the load-deflection response that display the trend of the experimental results. The results of all specimens shown above indicate that the slope of the load-deflection curve from the NLFEA procedure is very close to that of the experiments, and is an overprediction of this slope when compared to the experimental curves particularly at the early stages of loading. In some instances (such as B11, B12 and B14 above), the onset of cracking reduces the stiffness to well below that observed experimentally. The results for specimens B2 and B7 obtained from the finite element study show that the reactions suddenly decrease when the peak load is reached. The other load-deflection curves presented show that the reactions decrease smoothly once the peak load has been reached.



(a) Comparison of load-deflection curves for specimen B7

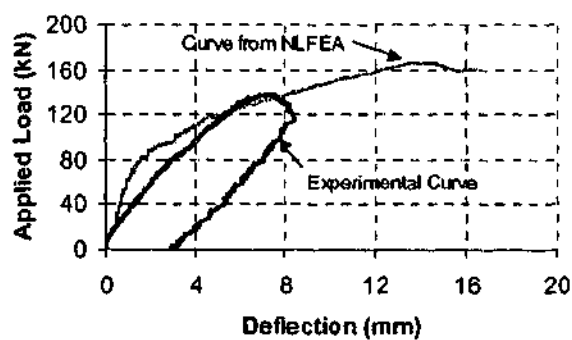


(b) Comparison of load-deflection curves for specimen B11

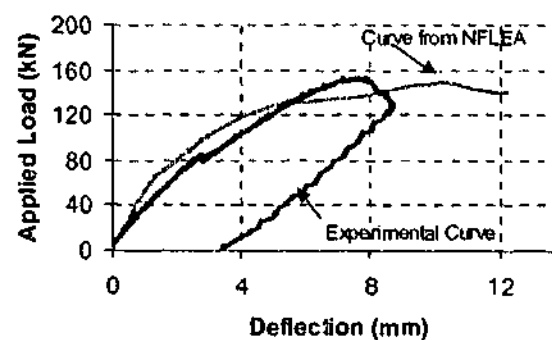
Figure 8.3-1 Comparison of two load-deflection curves for series 2 specimens

Table 8.3-1 Comparison of peak loads obtained from experimental work and NFLEA

	SPECIMEN	P_E (kN)	P_{NLFEA} (kN)	P_{NLFEA}/P_E
SERIES 1	B1	180.8	177.2	0.98
	B2	180.7	175.5	0.97
	B3	167.0	172.2	1.03
	B4	158.2	177.6	1.12
	B5	159.8	150.6	0.94
	B6	110.2	113.6	1.03
SERIES 2	B7	168.3	152.7	0.91
	B8	185.0	148.6	0.80
	B9	134.8	171.0	1.27
	B10	144.2	135.1	0.94
	B11	145.8	121.6	0.83
SERIES 3	B12	138.3	166.8	1.21
	B13	153.0	180.6	1.18
	B14	153.0	148.8	0.97
	B15	138.0	130.9	0.95
Average				1.01
Standard Deviation				0.13



(a) Comparison of load-deflection curves for specimen B12



(b) Comparison of load-deflection curves for specimen B14

Figure 8.3-2 Comparison of two load-deflection curves for series 3 specimens

Figure 8.3-3 below shows the load deflection curves for all specimens in series 1. It can be seen that this type of sudden decrease in the magnitude of the reactions noted above is seen in specimens B1 ($br=6.64$), B2 ($br=4.43$), B3 ($br=3.32$), and B4 ($br=2.21$). The other two specimens in this series show the smooth decrease in the magnitude of the reactions beyond the peak load. It is noted that the results of series 2 specimens show that specimens with flange width $br=6.64$, $br=4.43$, and $br=3.32$ show the sudden decrease in reaction magnitude at failure. No specimens from the series 3 analysis displayed this trend in load-deflection behaviour.

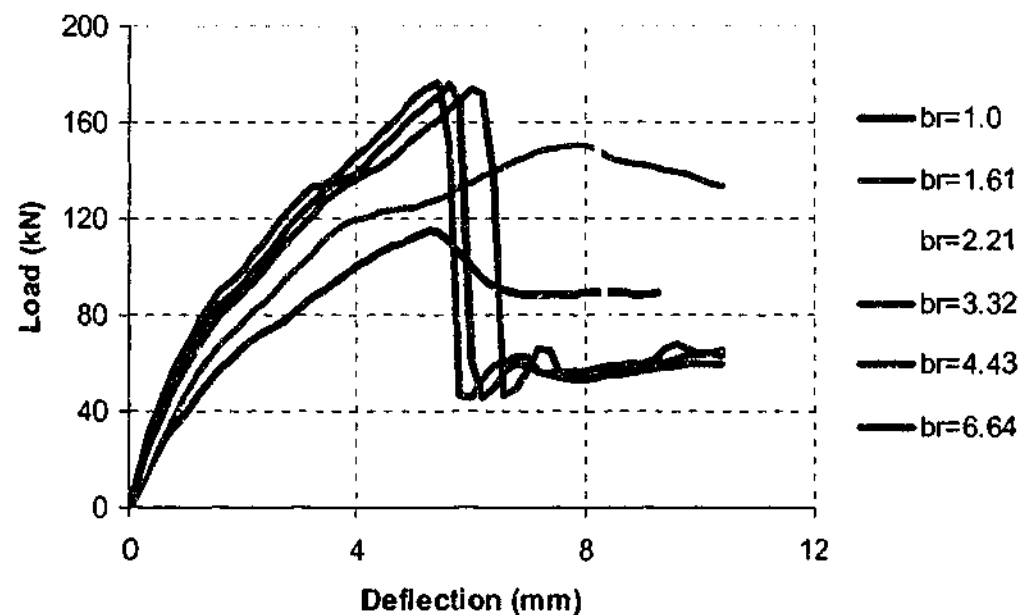


Figure 8.3-3 Comparison of load-deflection behaviour obtained from NLFEA for series 1 specimen

8.3.3 Crack Patterns

Crack visualisation in DIANA can be achieved through a number of methods. For the purpose of presentation, the method used here was to calculate the ultimate crack strain (i.e. the strain corresponding to the point where a concrete element has exhausted capacity to resist any applied stress). If the maximum principal tensile strain was greater than this value, the element was considered cracked. These values are shown as a contour plot in the ensuing figures; where the crack strain is shown to be higher than the ultimate strain and a contour is displayed, the following discussion will simply refer to a crack at the given location. The

recommendation in the DIANA manual for the value of the ultimate strain of a concrete element in tension is given in Equation 8.3.1.

$$\epsilon_u = \epsilon_e + \epsilon_u^{cr} = \frac{f_t}{E_c} + \frac{2G_f}{f_t h} \quad 8.3.1$$

The values of the symbols in this equation are the same as those defined in Chapter 4.

NLFEA predicted different types of crack patterns throughout this series of analysis. These are shown at the end of this section in Figure 8.3-4 - Figure 8.3-6 along with the corresponding crack patterns obtained from experimental work for these specimens.

Figure 8.3-4 shows that for specimen B2, NLFEA predicted that there were cracks on the web of the specimen from the underside of the flange at the point of the applied load to a point at the bottom of the web close to the support. These cracks are representative of the web crack shown in the experimental specimen. The method also predicted cracks in this specimen that run vertically from the bottom of the web to the underside of the flange; these are consistent with flexural cracks obtained in the experiments. On the underside of the flange, the diagonal web cracks were predicted to continue laterally along the width of the flange of the edge to the flange (from this specimen). This crack formation is also seen on the experimental specimen that is shown. On the top surface of the flange, there is a localised region of cracking in the vicinity of the region at which the controlled displacement was applied. The crack pattern shown from the experiment shows some cracking on the top surface of the flange, but this is not as localised as the NLFEA results predicted.

Figure 8.3-5 shows that for specimen B5 the NLFEA procedure predicted a similar pattern of diagonal web (and vertical web) cracks at the peak load as described above for specimen B2. The procedure predicted that the on the underside of the flange for specimen B5, cracks propagated from the intersection of those on the web to the edge of the flange; the crack on the edge of the flange visible in the photo of the experimental specimen joined with the diagonal web crack through a crack of this type on the underside of the flange. The NLFEA procedure predicted that a crack on the top surface of the flange was present in the

region of the point of applied displacement, but for this specimen, the crack was not localised, but propagated laterally along the top surface of the flange and intersected with the crack on the edge of the flange. It can be seen from the photo of the experimental specimen that a crack propagated on the top surface of the flange; this crack intersected with the cracks on the edges of the flange.

Figure 8.3-6 shows the crack pattern predicted by NLFEA on specimen B12 is similar to that of B2 shown above, but an additional crack was present that propagated along the edge of the web on the top and bottom surface of the flange within the shear span. This crack was of great significance on the prediction of the ultimate strength from the NLFEA analysis. The prediction of this crack on this specimen (as well as a similar crack on specimen B13) were observed to produce significant errors in the prediction of the peak load as will be discussed in Section 8.3.5.

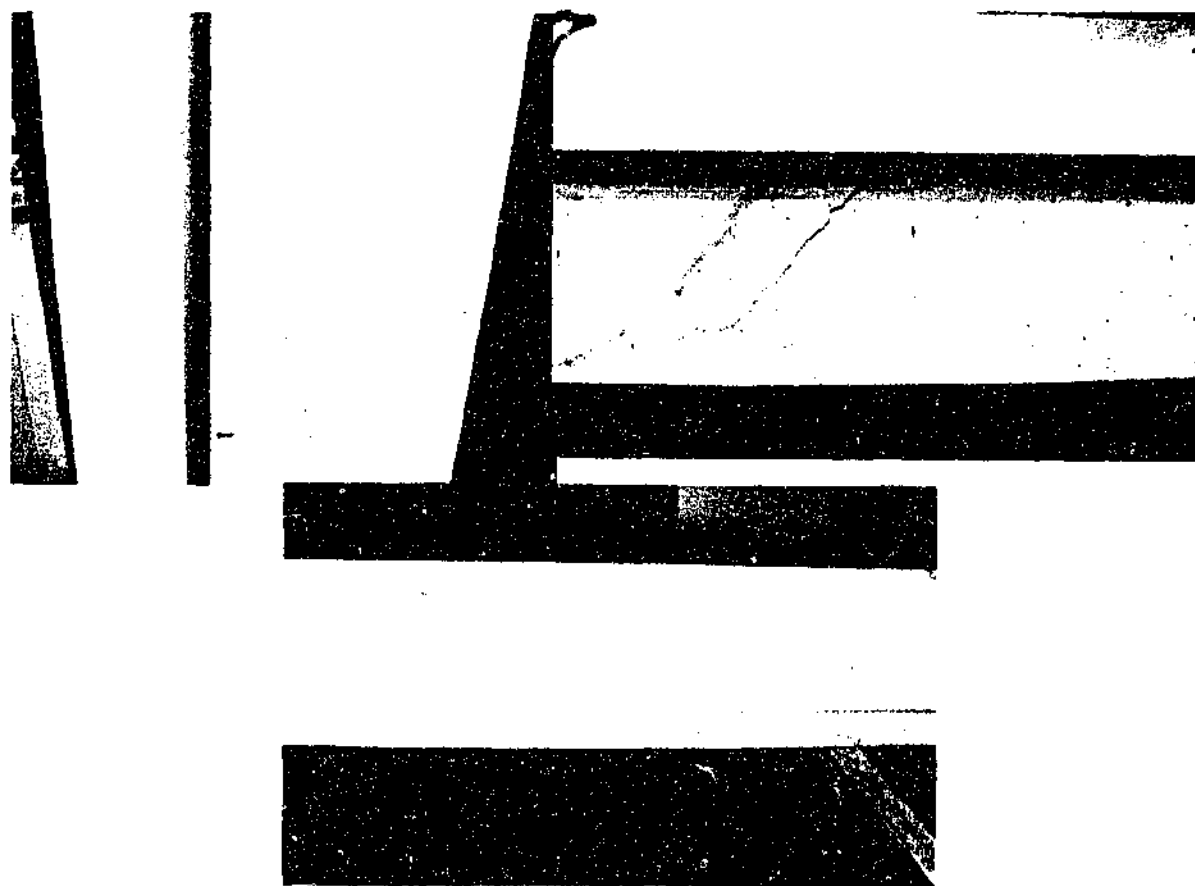
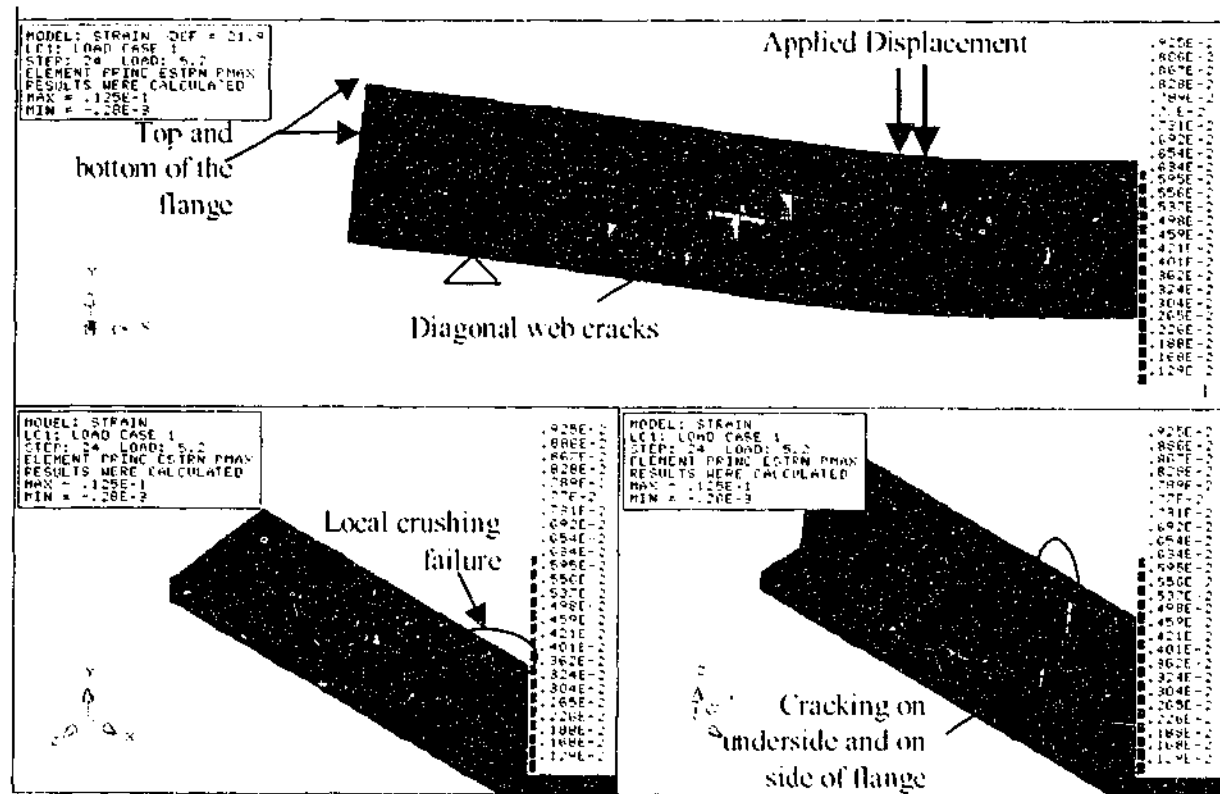


Figure 8.3-4 Comparison of predicted crack strains and exhibited on specimen B2 during experiment

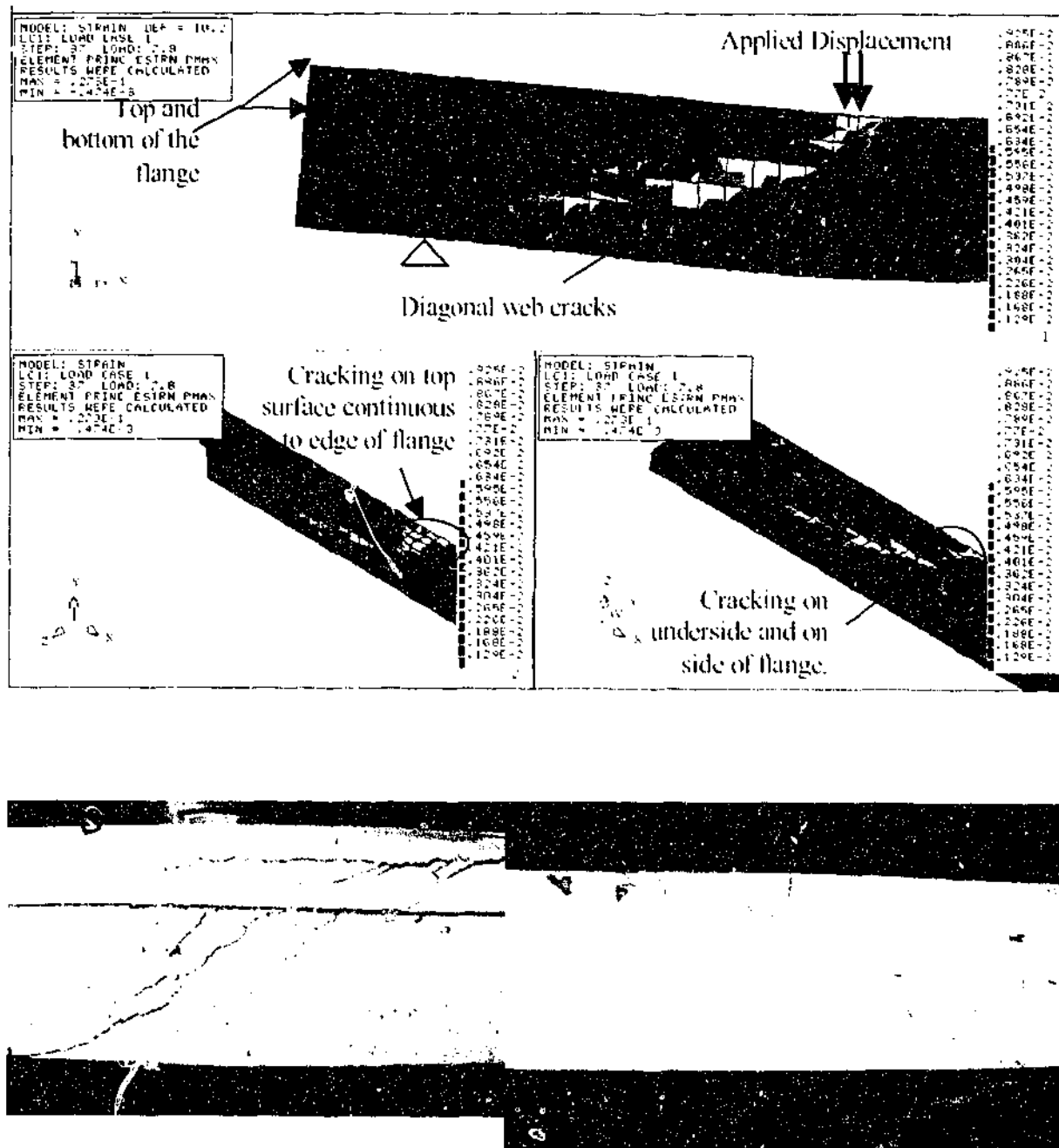


Figure 8.3-5 Comparison of predicted crack strains and exhibited on specimen B5 during experiment

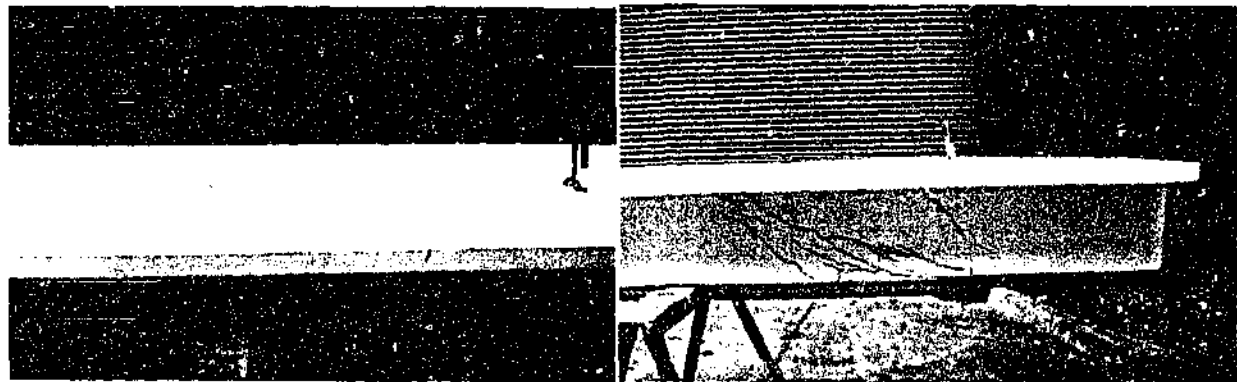
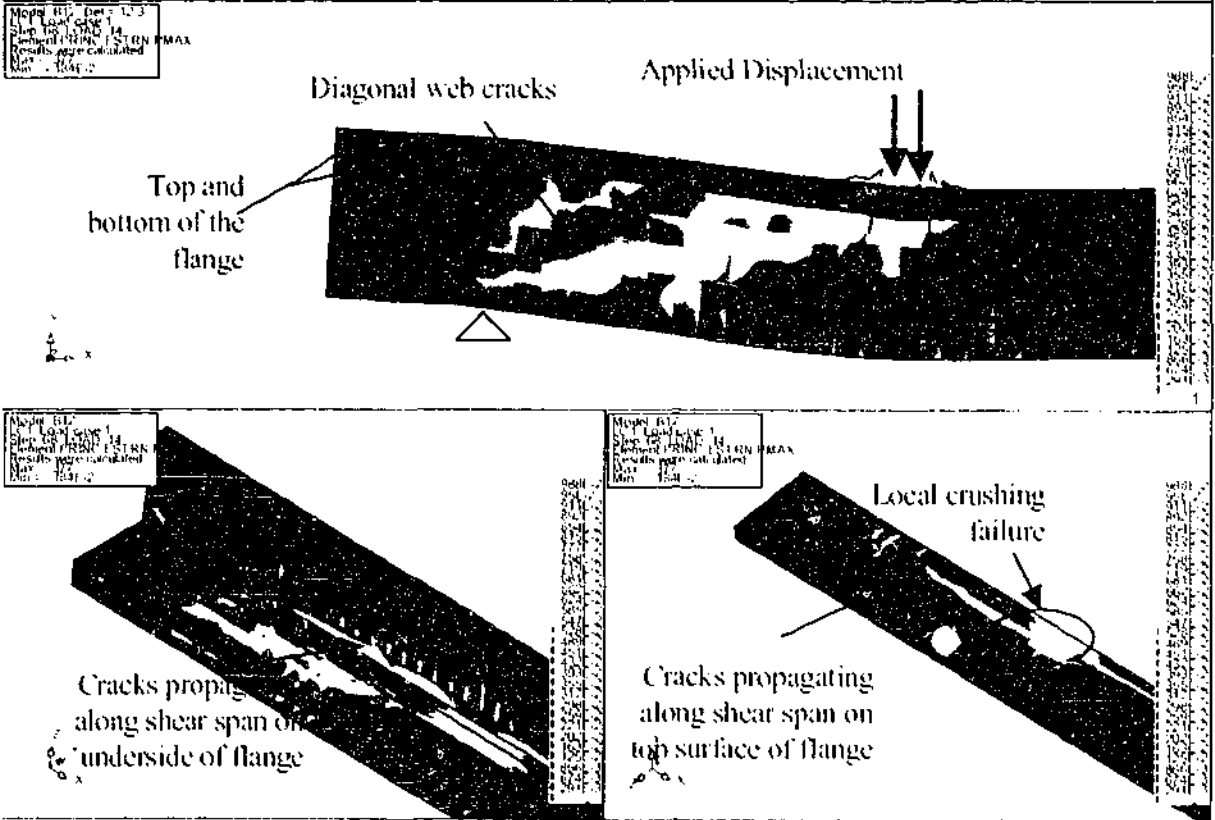


Figure 8.3-6 Comparison of predicted crack strains and exhibited on specimen B12 during experiment

8.3.4 Reinforcing Strains

Strain gauges were provided on series 1 and series 2 specimens on locations on the stirrups and on the main tensile reinforcing. Figure 8.3-7 illustrates these locations. This figure also outlines the notation used to compare the results of the strains output from the NLFEA procedure with those obtained in the experiments. This comparison is shown below in Table 8.3-2 for the stirrups and in Table 8.3-3 for the longitudinal bars. Note that at these locations, both legs of the stirrups of the experimental specimens were instrumented and two longitudinal reinforcing bars were instrumented. The subscripts 1 and 2 shown in Figure 8.3-7 are used in order to show the results from both strain gauges from the experiment. In this table, 'NA' is used in the instance of faulty gauges or a gauge that has failed during the experiment.

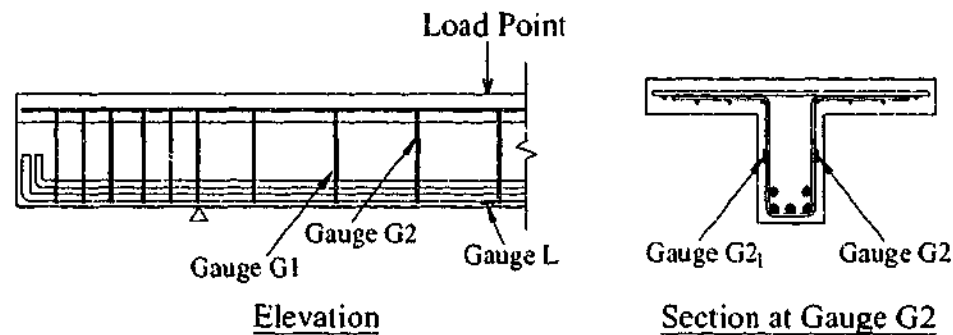


Figure 8.3-7 Notation used for comparison of strain gauge results

The comparison between stirrup strains at the peak load is shown in Table 8.3-2. In most cases, at least one gauge reading from the experiment indicated that a stirrup had failed during the experiments, but the NLFEA showed that in all except one analysis, the stirrups did not yield at the location where the gauges were provided during the experiments. NLFEA did predict that at least one stirrup on each specimen would reach yield strain during the loading. For series 1 and 2 specimens, it generally predicted one stirrup at yield if a punching mechanism formed, and two at yield if a beam shear mechanism formed. This generalisation could not be made for series 3 predictions.

The results below in Table 8.3-3 show that with the exception of specimen B4, the NLFEA solution scheme was able to predict that at the location of maximum moment,

significant flexural tensile strains developed in series 1 specimen, but they did not yield. In series 2, this was also the case, one anomaly on specimen B9 was observed. NLFEA predicted a very high peak load for this specimen, and it is thought that this high value of strain corresponds to the relative increase in the number of steps taken to achieve this overestimate of load. The comparison of the results of the flexural tensile strains indicates that NLFEA has significantly better capacity to predict strains on the flexural tensile reinforcing than those on the stirrups.

Table 8.3-2 Comparison of stirrups strains at the peak load (Positive strains are tension)

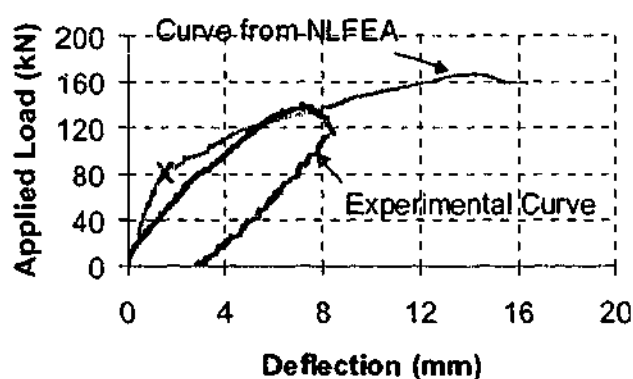
Specimen		$\epsilon_{st,f}$ From Experiment ($\mu\epsilon$)				$\epsilon_{st,f}$ From NLFEA ($\mu\epsilon$)	
		Gauge G1 ₁	Gauge G1 ₂	Gauge G2 ₁	Gauge G2 ₂	Gauge G1	Gauge G2
Series 1	B1	NA	NA	2436	3085	832	1386
	B2	1214	486	3053	7018	878	1247
	B3	NA	NA	2503	-992	1375	1628
	B4	634	NA ($>\epsilon_{y,v}$)	903	3370	1374	1628
	B5	5623	3307	651	700	1140	1290
	B6	3259	3744	326	283	660	275
Series 2	B7	3977	NA	866	643	7	1345
	B8	5799	5512	3184	NA	1092	1337
	B9	NA ($>\epsilon_{y,v}$)	NA	310	300	2090	958
	B10	NA	NA	238	NA	1025	1432
	B11	2285	2619	110	207	1078	1478

* $\epsilon_{st,f}$ denotes stirrup strain at failure
 Series 1 stirrups yield $\epsilon_{y,v}=1990\mu\epsilon$
 Series 2 stirrups yield $\epsilon_{y,v}=1500\mu\epsilon$

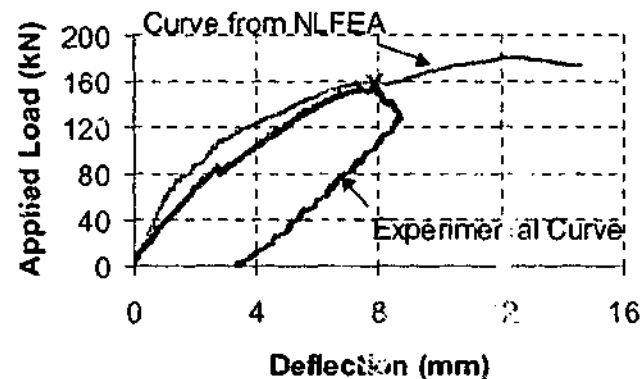
8.3.5 Specimens B12 and B13

NLFEA has been shown above to overpredict the peak load of specimens B12 and B13 as well as predict a crack along the web flange interface that forms part of the failure mechanism of these specimens. This crack is predicted only for these specimens.

Figure 8.3-8 shows the load deflection curve for these two specimens. On both of these figures, an X is marked. This point is the level of applied displacement at which a sudden decrease in stiffness of the specimens can be observed. It is thought that at this point, the influence of the longitudinal crack along the web flange interface influences the stiffness of the structure producing the softer structure that is evident in the load deflection response presented below. The peak load that is predicted is also a result of the change of failure mechanism. The mechanism that is predicted with this crack along the web flange interface has a higher capacity than an ordinary beam or punching shear mechanism.



(a) Specimen B12



(b) Specimen B13

Figure 8.3-8 Load - deflection curves for specimens B12 and B13

These specimens have very wide flanges in proportion to their depth ($b_f/d_f=12.4$ for specimen B12 and $b_f/d_f=9.3$ for specimen B13). These ratios of flange width to flange depth are suggested to be representative of specimens with thin wide flanges. The results of these two specimens suggest that the NLFEA strategy that is employed may require special attention for these two specimens, and more generally for specimens with thin wide flanges.

8.3.6 Failure Mechanisms as Predicted by NLFEA

The NLFEA always predicted that at least one stirrup would produce yield by peak load, and in general, longitudinal bars were generally not predicted to yield. Along with the crack patterns presented above, the results always suggest a shear failure mechanism.

Table 8.3-3 Comparison of flexural reinforcing strains at the peak load

Specimen		$\epsilon_{1,r}$ at From Experiment ($\mu\epsilon$)		$\epsilon_{1,r}$ at From NLFEA ($\mu\epsilon$)
		Gauge L ₁	Gauge L ₂	Gauge L
Series 1	B1	1501	1594	1225
	B2	NA	NA	1405
	B3	1525	NA	1465
	B4	1203	1395	1715
	B5	1434	NA	1615
	B6	975	1061	1065
Series 2	B7	1437	1413	1250
	B8	NA	1697	1265
	B9	1108	1097	1710
	B10	1310	1284	1660
	B11	957	NA	1230

* $\epsilon_{1,r}$ denotes flexural reinforcing bar strain at failure
 Flexural reinforcing yield $\epsilon_y = 1700\mu\epsilon$

In line with the observation in Section 8.3.3, those specimens that failed in a similar manner to specimen B2 all displayed a sharp decrease in the sum of the reactions at the peak load. In series 1, this failure mechanism was displayed by specimen B1, B2, B3, and B4; in series 2, this failure mechanism was displayed by specimens B7, B8, and B9. All other specimens in these series' displayed crack patterns illustrated in Figure 8.3-5 above. The crack pattern of specimen B2 and the corresponding sudden decrease in the sum of the reactions is associated with a prediction by NLFEA of the formation of a punching shear mechanism. The crack patterns of the remainder of the specimens are consistent with the beam shear mechanism. The over prediction of peak load of specimen B9 is attributed to the NLFEA scheme predicting a punching shear mechanism at failure rather than the beam shear failure exhibited during the experiment.

In series 3, specimen B12 displayed a similar crack pattern to that for specimen B2. Figure 8.3-6 shows that this type of crack pattern was indicative of a punching shear type

failure, but showed the formation of a crack that propagated along the edge of the web throughout the shear span. The other two specimens in this series failed by the beam shear mechanism as outlined above. The crack pattern for specimen B13 shows a similar facet to that predicted for specimen B12; a crack propagates along the length of the span at the flange web interface.

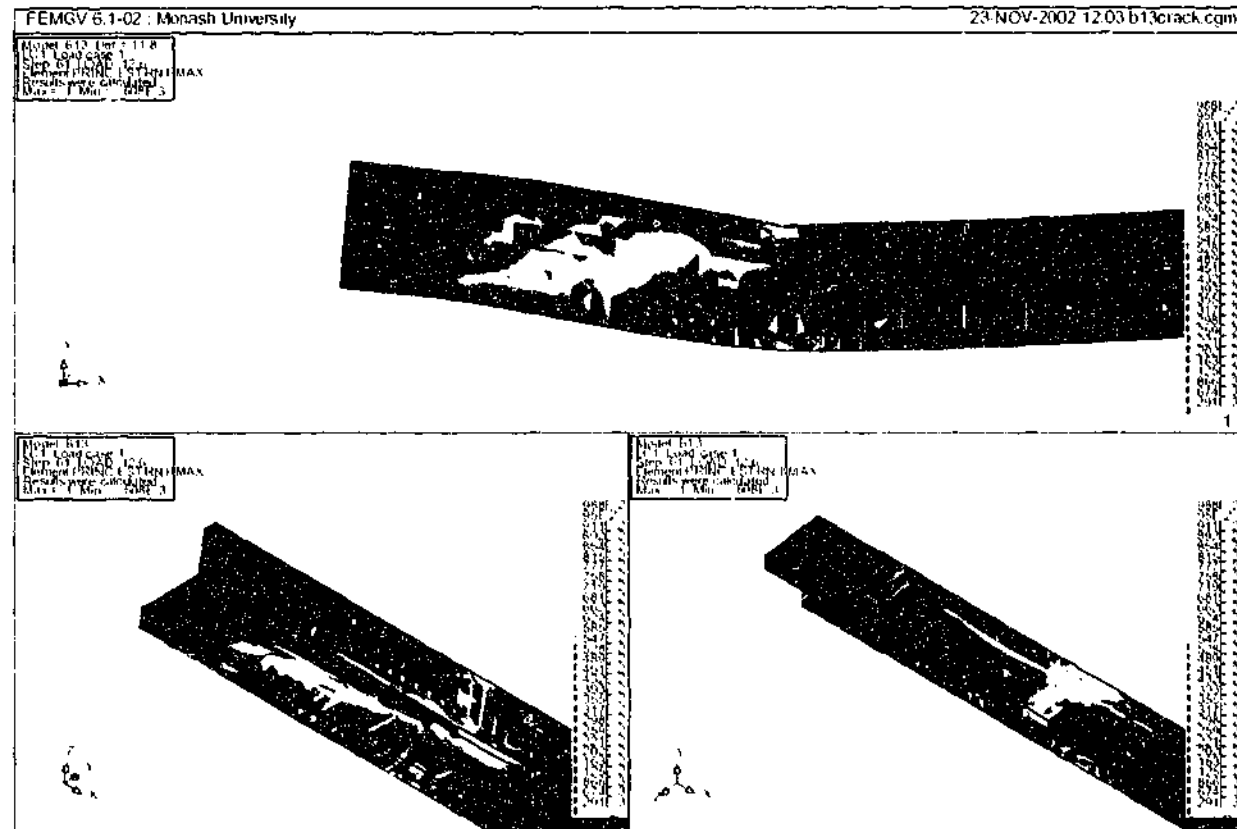


Figure 8.3-9 Failure mechanism predicted for specimen B13

As the width ratio decreased throughout series 1 and 2 specimens, the predicted failure mechanism changed from a punching shear to a beam shear mechanism. The first specimen to display the beam shear mechanism had a peak load higher than the punching shear mechanisms. It is apparent that the NLFEA solution scheme has over predicted the strength of these specimens. The prediction of the strength of specimens failing in beam shear improved as the width ratio decreased.

A summary of the comparison of failure mechanisms exhibited by the experiment and NLFEA are given below in Table 8.3-4. It is seen that in general NLFEA predicts the failure mechanism well, but there are instances where it is incorrectly predicted.

Table 8.3-4 Comparison of failure mechanisms from experimental and NLFEA work

Specimen	Experiment	NLFEA	Specimen	Experiment	NLFEA
B1	Punching	Punching	B9	Beam	Punching
B2	Punching	Punching	B10	Beam	Beam
B3	Beam	Punching	B11	Beam	Beam
B4	Beam	Punching	B12	Punching	Punching*
B5	Beam	Beam	B14	Beam	Beam*
B6	Beam	Beam	B14	Beam	Beam
B7	Punching	Punching	B15	Beam	Beam
B8	Punching	Punching			

* Indicates that crack along the length of the span was shown in the NLFEA results as outlined in Section 8.3.5

The failure mechanism of specimens B9, B12, and B13 were incorrectly predicted by NLFEA. Specimen B9 is incorrectly predicted as a punching mechanism, and the mechanisms predicted for B12 and B13 are inconsistent with the remainder of the mechanisms for the other specimens as outlined above in Section 8.3.5. It is these incorrect predictions of the failure mechanisms which is attributed to the over prediction in peak load by NLFEA. The latter cracking is associated to form only on two specimens with thin wide flanges.

8.3.7 Prediction of Longitudinal Flange Strains

The solution scheme predicted that specimen B16 would fail by a punching shear mechanism, and that B17 would fail by a ductile flexural compression failure. NLFEA estimated that B16 would reach a peak load of 229kN (compared with 212kN from experiment), and that B17 would reach a peak load of 234kN (compared with 238kN from the experiment). The load deflection comparison can be seen in Appendix E.

Comparison of the longitudinal strains in the flange predicted by the NLFEA procedure with the results obtained from the experimental work of stage 2 are described in this section. To identify the locations within the flanges at which this comparison is undertaken,

Figure 8.3-10 is shown. Gauges are described as being in layers; there is a top layer of gauges (TL), and middle layer of gauges (ML), and a lower layer of gauges (LL). To be consistent with the convention used in Chapter 3, section A is the section closest to the load point, and section B is the section of gauges farthest from the load. The numbering system can be seen in the figure below. For the purpose of the ensuing discussion, compressive strains are shown as positive.

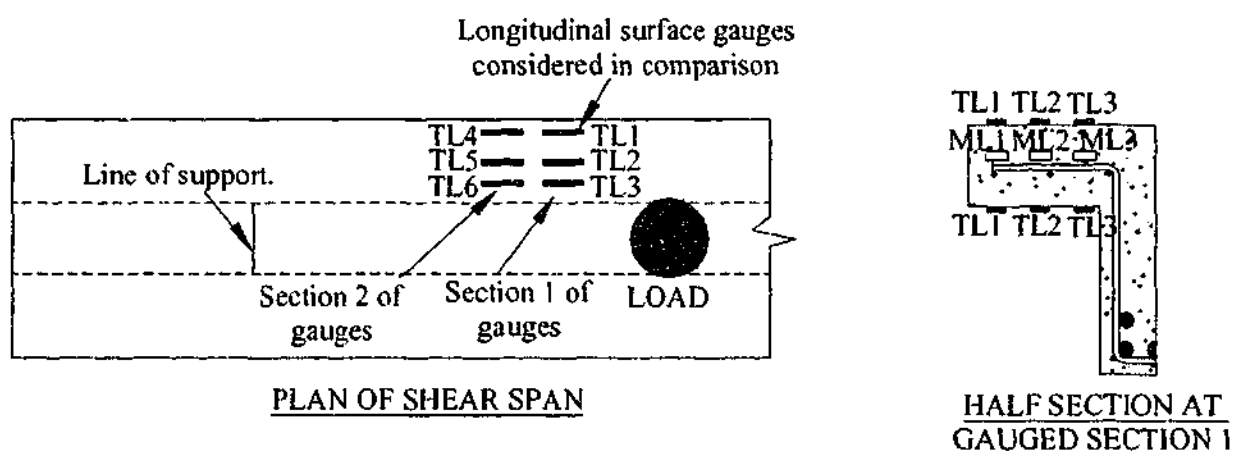


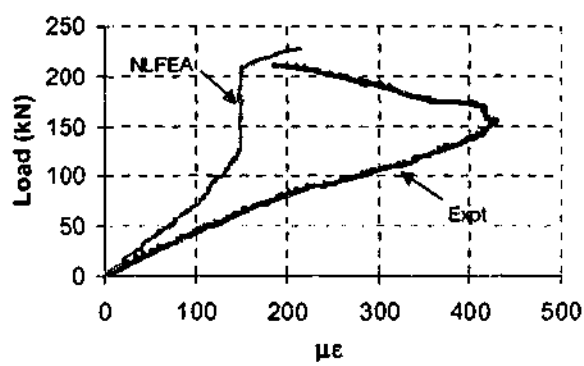
Figure 8.3-10 Notation used for description of gauge location

8.3.7.1 Specimen B16

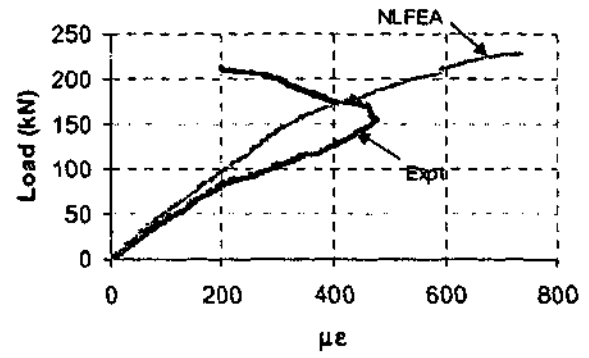
Figure 8.3-11 shows the comparison of the results of the longitudinal strains at section A gauge locations. The results for gauges TL2-3 initially show a close correlation between the NLFEA and experimental results. This correlation remains close until the reversal of strain on the top surface of the flange recorded during the experiment. The NLFEA solution procedure does not predict this; however, it is interesting to note that at the reversal of strain at gauge TL1, the NLFEA predicts a range of load where there is little increase in strain, and at the other two gauge locations on the top surface NLFEA predicts an increase in the strain gradient at approximately the level of load at the strain reversal.

The results of the comparison between the experimental results and NLFEA at the middle layer of gauges (shown in Figure 8.3-11) show very similar characteristics to the above. The difference between this layer and the above is that the strain reversal occurs at a

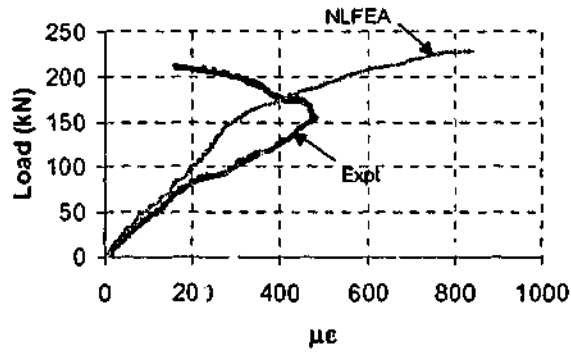
higher load on these gauges, and is much less severe. This leads to a much better correlation between results at these locations.



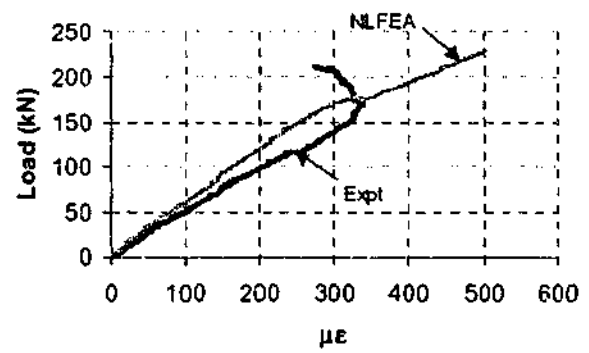
(a) TL1



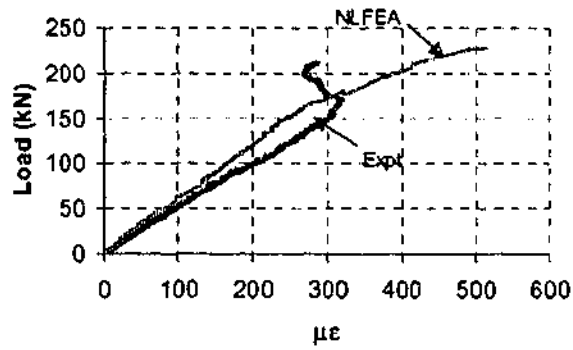
(b) TL2



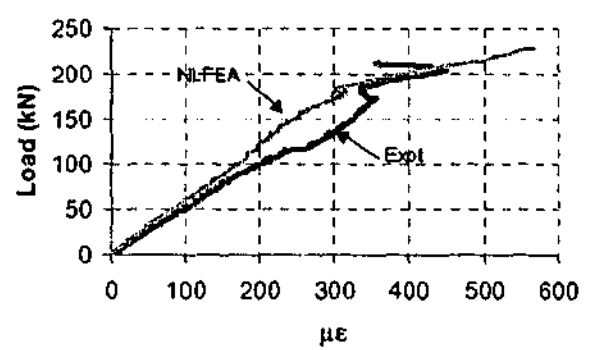
(c) TL3



(d) ML1



(e) ML2



(f) ML3

Figure 8.3-11 Comparison of longitudinal strains in specimen B16 section A

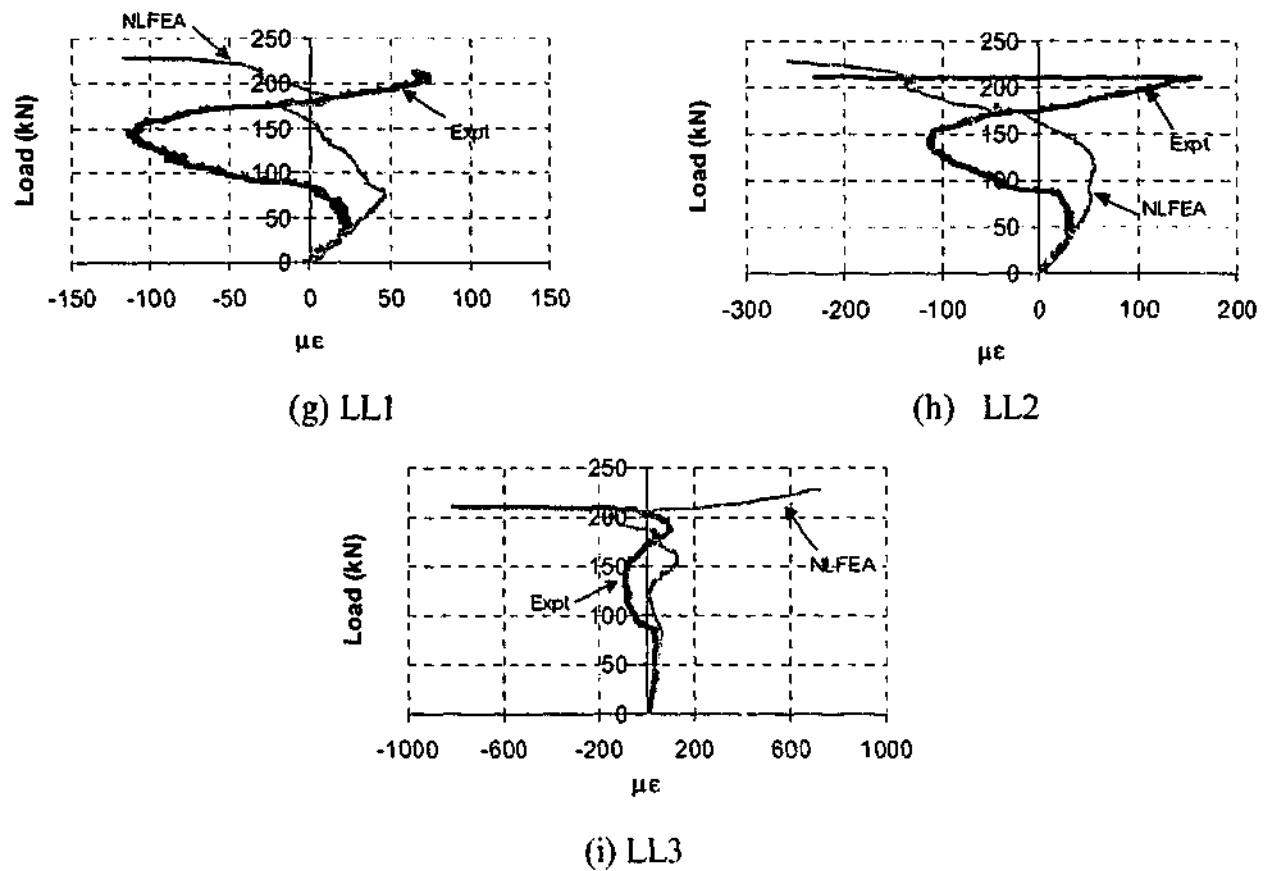
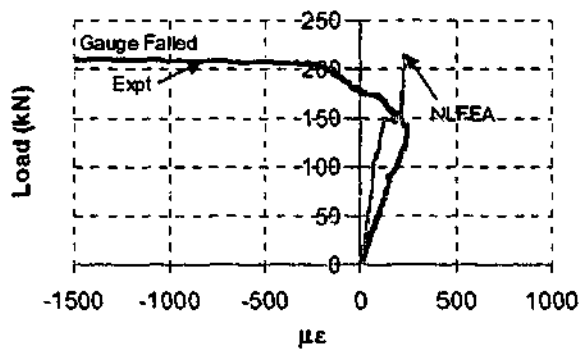


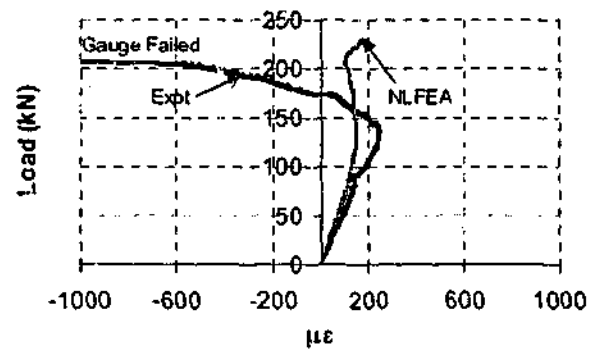
Figure 8.3-11 Continued

The results of the NFLEA at the lower gauge layer are comparable to the experimental results in that the propagation of the neutral axis into the flange developing a reversal of strains at the early stages of loading is predicted by NLFEA. However, NLFEA did not predict the reversal of strain corresponding to the formation of the failure mechanism on the underside of the flange.

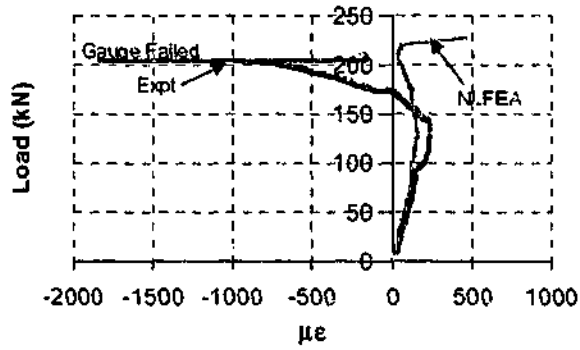
Figure 8.3-12 shows the comparison between strains at section B measured from the experiments and predicted by the NLFEA solution scheme. The results from TL4-6 show that the NLFEA solution predicts the strains well at the early stages of load, but did not predict the tensile strains that developed during the experiment. Some discontinuity in the trend of the strain increase in the NFLEA results is present at a level of applied load close to that corresponding to the beginning of the reversal. This is also true for the gauges at the middle layer; gauges ML4-6. Large increases in compressive strain were predicted at the location of gauges ML5 and ML6.



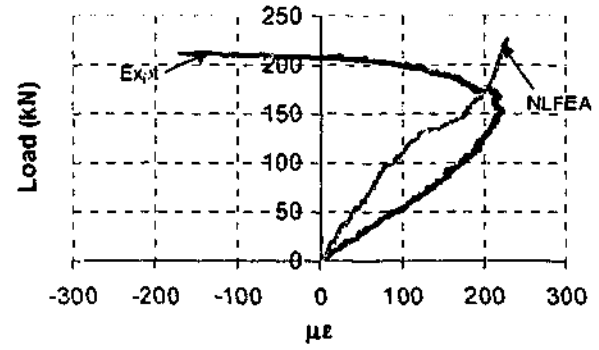
(a) TL4



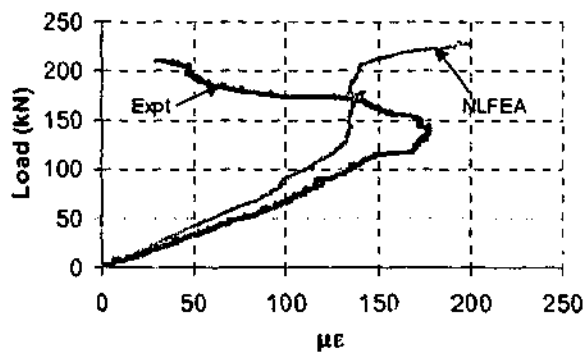
(b) TL5



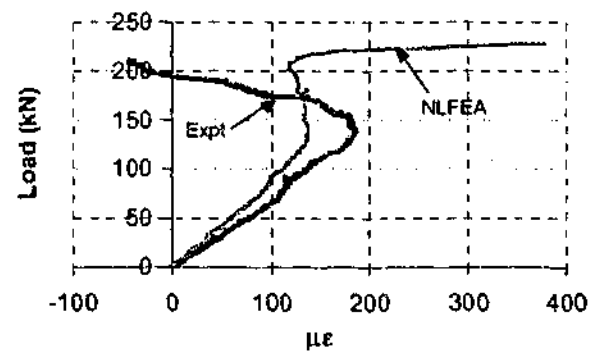
(c) TL6



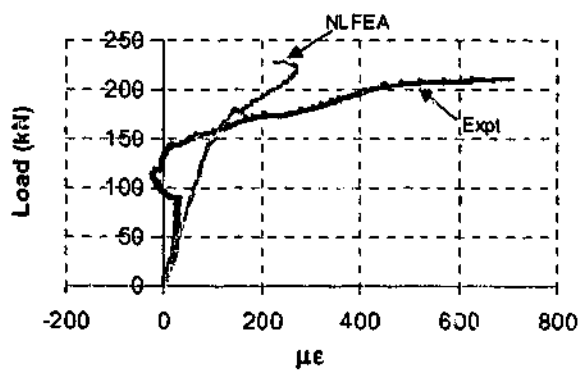
(d) ML4



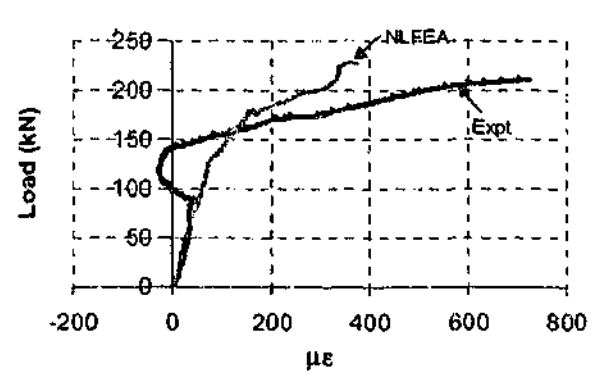
(e) ML5



(f) ML6

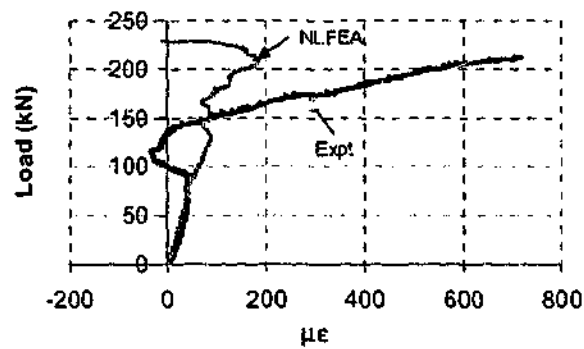


(g) LL4



(h) LL5

Figure 8.3-12 Comparison of longitudinal strains in specimen B16 section



(i) LL6

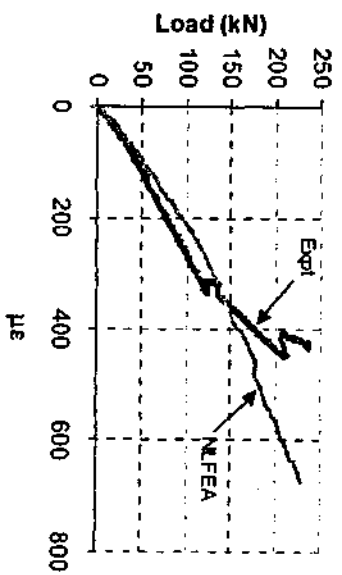
Figure 8.3-12 Continued

The results of strain on the lower layer at this section from the NLFEA procedure are in general agreement with the trend recorded from the experimental results. They show a low level of compression strain at the low levels of load, then an increase in the gradient of this response at a level of applied load close to that which occurred at failure in the experiment. NLFEA predicted that the strain corresponding to gauge location LL6 reversed close to the peak load.

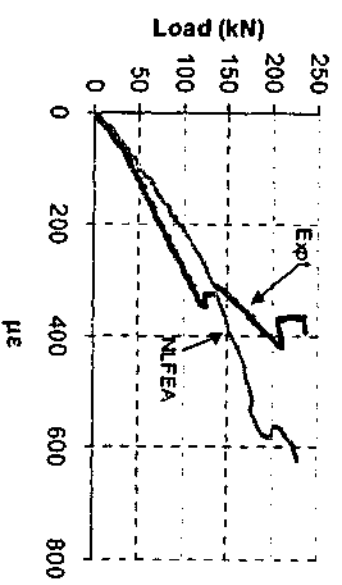
8.3.7.2 Specimen B17

Figure 8.3-13 shows the comparison between the strains predicted by NLFEA and the results of strain gauges from the experiments at locations at section A in the flange. The results of strain from NLFEA at locations on the top surface show good correlation with the trend of increasing compressive strain on the top surface of the flange. Discontinuities in the trend displayed in the experiment resulting in a decrease in the strain increase gradient are not predicted by the NLFEA procedure.

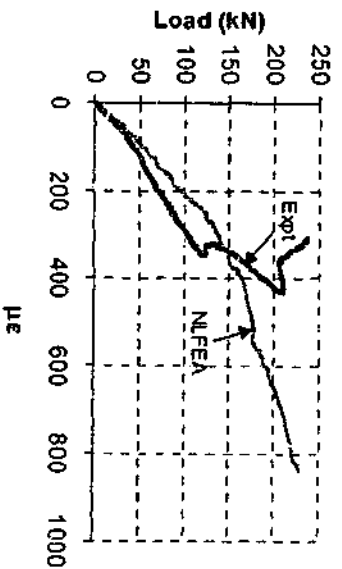
The predictions from the NFLEA solution scheme of strains at the middle layer of the specimen are close to those measured in the experiment. The general trend is well predicted, and the magnitudes are close. The NLFEA procedure did not detect some discontinuities displayed in the experimental results.



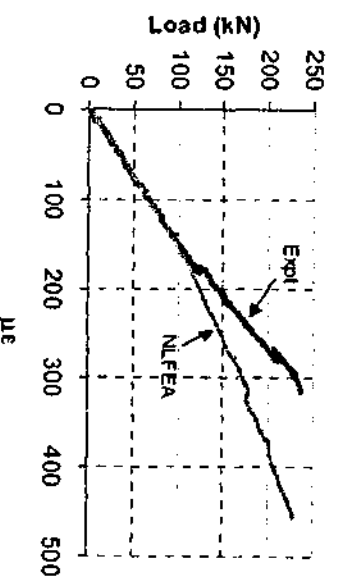
(a) TL1



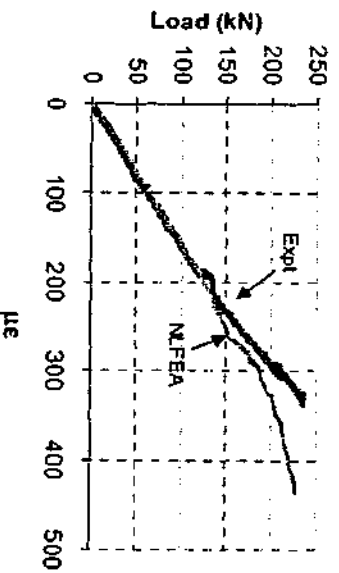
(b) TL2



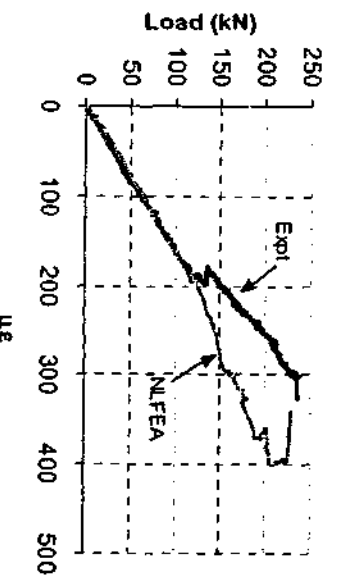
(c) TL3



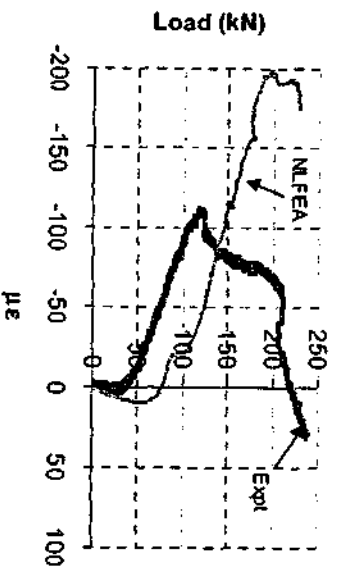
(d) ML1



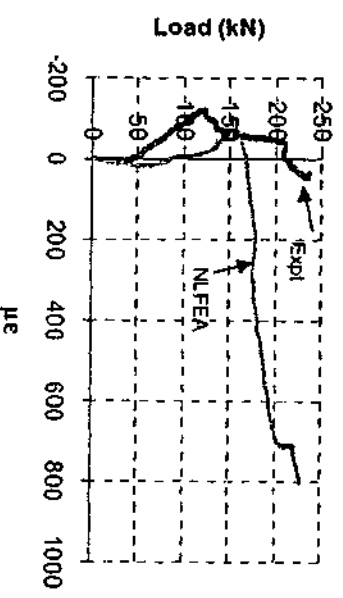
(e) ML2



(f) ML3

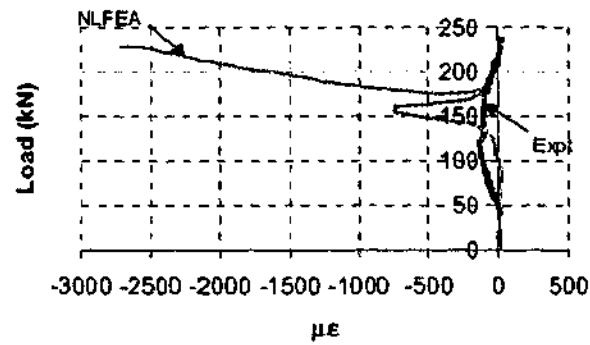


(g) LL1



(h) LL2

Figure 8.3-13 Comparison of longitudinal strains at section A in specimen B17 at locations in the flange



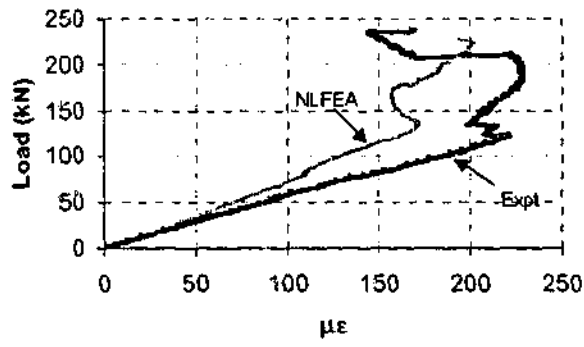
(i) LL3

Figure 8.3-13 Continued

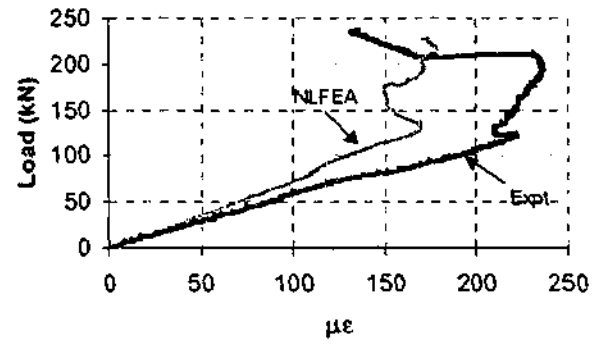
The NLFEA solution procedure predicted the trend and magnitudes of strain at the lower layer of gauges at low levels of load. However, at higher levels of load, the results were not well predicted. There is no general correlation between the strains produced from each set of data at this location.

Figure 8.3-14 shows the comparison of strains from the NLFEA solution scheme with those measured in the experiment of section 2 on specimen B17. The results of the gauges on the top surface are well predicted by NLFEA at this section, including the reversal of strain that occurs. This strain reversal corresponds to Stage II as discussed in Chapter 7. The magnitude of the compression strains before the reversal was lower in the NFLEA prediction than in the experiment. The sudden decrease in strain corresponding to the formation of the diagonal web crack at 212kN was not predicted by NLFEA.

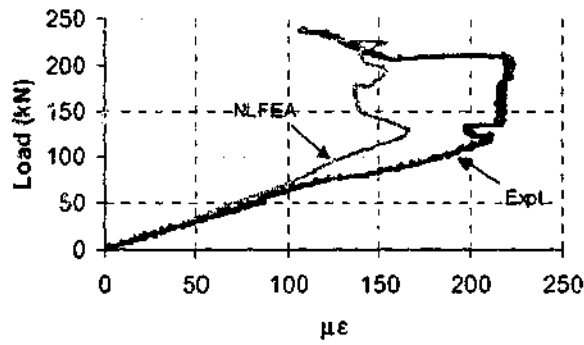
The results of strain from the NFLEA procedure at locations at the middle layer of gauges again show very close agreement with those values measured in the experiment. The level of applied load of discontinuities in the trend of the increase in strain measured in the experiment is well predicted by NLFEA; however, the nature of these discontinuities was not well predicted. The reversal of strain at gauge ML6 close to the peak load is not predicted by the NLFEA solution scheme. Again, sudden reversals in strain observed throughout the experimental work at the formation of the diagonal web crack at 212kN were not predicted by NLFEA, although some discontinuity in the trend of the NLFEA was observed at approximately this load.



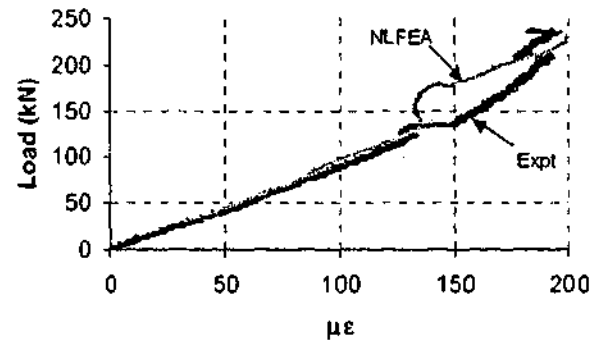
(a) TL4



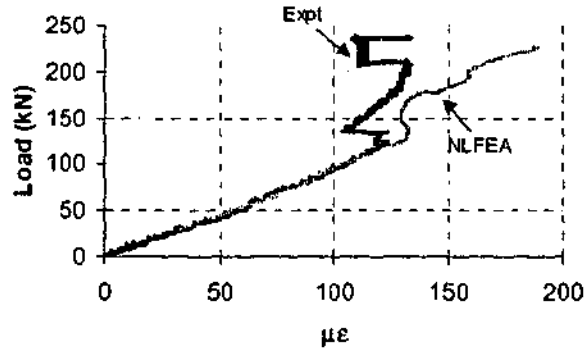
(b) TL5



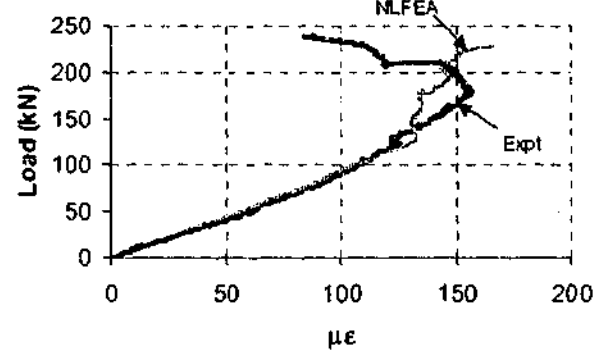
(c) TL6



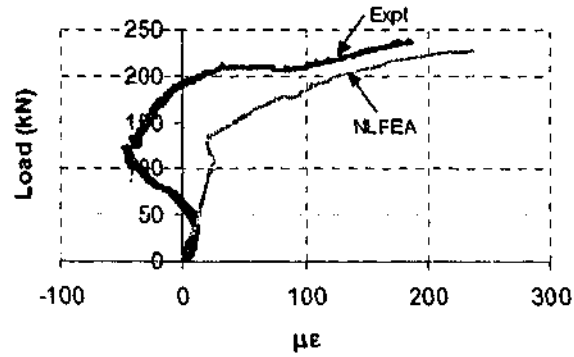
(d) ML4



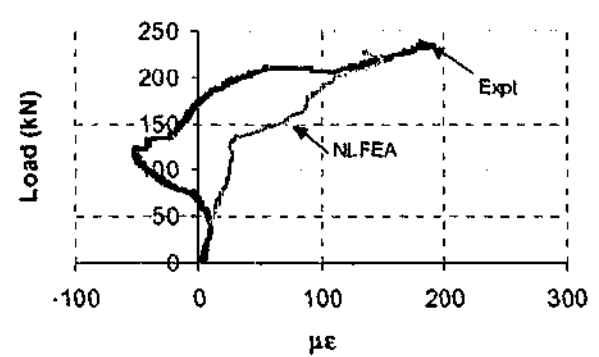
(e) ML5



(f) ML6

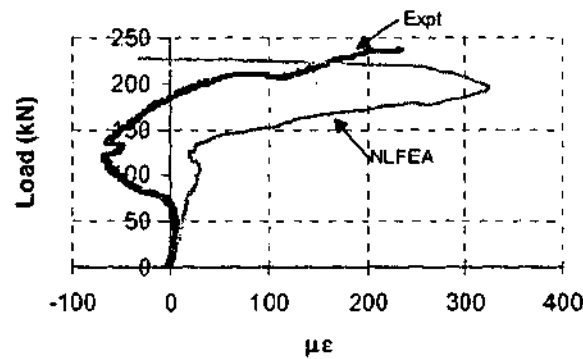


(g) LL4



(h) LL5

Figure 8.3-14 Comparison of longitudinal strains at section B in specimen B17 at locations in the flange



(i) LL6

Figure 8.3-14 Continued

The trend of the variation of strains on the lower layer of gauges is well estimated by the NLFEA procedure, with peak values of strain predicted by the scheme being very close to those recorded in the experiment. The NLFEA scheme did not predict any tension on the underside of the flange. This was shown in the experiments. In addition to this, a reversal of strain at location LL6 was predicted by NFLEA that did not occur in the experiment.

8.3.7.3 NLFEA and the Prediction of Longitudinal Strains in the Flange of an RC T-beam

The strains predicted in the flange using the NLFEA solution show in general the capacity to replicate the trends that were apparent from the experimental work, at low levels of load. The above results show that the prediction of longitudinal strains in the flange using the NLFEA procedure were generally more accurate in both the prediction of trends for specimen B17 than for specimen B16. Specimen B17 failed in flexure, and specimen B16 failed in punching shear.

In the prediction of the strains in B17, the NLFEA procedure was able to capture the discontinuities in the trend of the increase in strains that prevailed throughout the loading. These were decreases in the gradient of the strain response with the applied load throughout the experiment on the top and middle layers of the specimen. Also, the increase in the strain response on the lower layer at section B was captured by NLFEA. The solution scheme predicted high values of strain on the lower layer of the flange at section A where they did not occur.

Specimen B16 displayed reversals of strain at a late stage of loading in the experiment. These prevailed to accommodate the formation of the failure mechanism. NLFEA did not predict these sharp changes in strain at this location. In the instances where they did not occur (at the middle layer at section 1), the NFLEA procedure was able to predict these trends.

8.3.8 Estimation of the Flange Contribution to Shear Resistance

The application of the instrumentation and accompanying analytical technique to evaluate the sectional shear in the flange of the beam specimens presented in Chapters 3 and 7 above require the difference in compression force on a small element of the concrete along the length of the span. Strain gauges were provided at two sections along the length of the span. For comparison with the NLFE model, the calculated shear force was interpreted to be at a point equidistant from the centre of the two rows of gauges.

As the above region over which averaging was performed in the experiments corresponded to two elements along the length of the span in the finite element model, an average of the sectional shears in these two elements over the width of the flange was taken to obtain a value that was representative of that calculated from the experimental work.

Implementing the above, a value of the sectional shear was calculated from the results of the models on the two corresponding experimental specimens for which this result was obtained. The load at which this was taken was the load from the experimental work at which the last calculation was performed. For specimens B16, this was a level of applied load of 175kN (83% of the peak load), and for specimen B17, the last calculation was made at the peak load of 238kN. Note that as the NLFEA estimate of the peak load of specimen B17 was lower than obtained from the experiment, the value at the estimated peak load was obtained for comparison. The values of the shear in the flange are presented below as percentages of the total shear as this value is representative of the flange contribution.

At a level of applied load of 175kN in specimen B16, the implementation of the instrumentation and analytical technique into the experimental work estimated a flange

contribution of 27.5%; NLFEA estimated a flange contribution of 10.6%. At a peak load of specimen B17, the implementation of the instrumentation and analytical technique into the experimental work estimated a flange contribution of 24.0%; NLFEA estimated a flange contribution of 22.1%.

8.3.9 Discussion of the Results of Stage II NLFEA

The above examination of the results of NLFEA from modelling of the specimens tested during of the experimental work in this research indicate the following:

1. NLFEA predicts a significant increase in the shear strength of a web reinforced RC T-beam specimen that from increasing the width of the flange. No significant increase in strength is produced from increase the flange depth.
2. The peak load predicted by the solution scheme is in close agreement with the values obtained from the experimental work in series 1 and series 2 results. The best values of peak load are obtained for specimens that are predicted to fail in punching shear. The ability of NLFEA to predict the peak load of specimens in series 3 with thin wide flange appears limited, and seems to require mesh refinement.
3. The NLFEA solution scheme predicts less deflection for an applied load on each specimen. That is, the specimens are predicted to be stiffer using NLFEA than they were when tested.
4. Crack patterns predicted from the solution scheme are indicative of those associated with the failure mechanisms described in Chapter 5. Some influence of the web on the failure mechanism is series 3 specimens resulted in over prediction of ultimate strength. This was noted to occur when cracks were predicted along the length of the span at the flange web interface.

5. NLFEA displayed the ability to predict the magnitude of the strains on the flexural tensile reinforcing in the region of maximum moment on these specimens. It did not show the same ability to determine the strain in the stirrups. It is thought that the inability to predict the precise location and path of propagation of the crack is a result of the smeared cracking procedure implemented into NLFEA.
6. The NLFEA solution procedure has shown reasonable correlation in the prediction of the strains on the flange of the specimens of stage 2 experimental work, more so when predicting the flexural failure mechanism that was exhibited by specimen B17, than that of the shear mechanism exhibited by specimen B16. It is noted that a punching shear mechanism was recorded for this specimen in the experiment, and NLFEA also predicted a punching shear mechanism. The high localisation of the punching area predicted by the NLFEA is thought to prevent the redistributions of strain into the region instrumented in the experimental work thus limiting the solution scheme to predict the strain reversals in this region.
7. The output of the sectional shear from NLFEA showed that this procedure predicted that the flange resisted a significant percentage of the shear force. The prediction of the level of shear in the flange was much more accurate for specimen B17 (predicted flange contribution of 22.1%) than that of specimen B16 (predicted flange contribution of 10.6%). It is again thought that the prediction of the localisation of the punching shear failure mechanism as predicted by NLFEA solution scheme led to predicted values of the flange contribution to the shear resistance that were lower for specimen B16 than those calculated from experimental work.

8.4 Stage III - Flange Geometry Study

Since comparative trends of the load deflection response predicted by NLFEA with that of the ultimate strength and load-deflection response were obtained in the proceeding

section, the solution scheme was applied to specimens identical to those of the experiments without any variation in material properties. This study investigates the predicted variation of applied loads with the flange proportions and the failure mechanisms predicted by NLFEA for this set of specimens using the material models and displacement increment scheme outlined in Section 8.2, and material properties outlined in Section 4.7.

8.4.1 *Ultimate Strength*

The results of the ultimate strength predicted for each specimen with the width ratio are presented below in Table 8.4-1. This table also indicates the values of the width ratio, br , for each specimen, the values of the depth ratio, dr , are given at the bottom of the table.

NLFEA predicted that the first four specimens of series 1 (specimens CMP-B1 - CMP-B4) had almost identical peak loads. Specimens CMP-B3, and CMP-B4 are slightly higher in magnitude. The remaining two values in this series decrease in magnitude with the width ratio. As the depth ratio was decreased in series 2, NLFEA predicted that specimens CMP-B7 - CMP-B9 have values of peak strength that are approximately equal. The value of the peak strength for specimen CMP-B9 was predicted to be a little higher than the other two of these specimens. The remainder of this series showed a decrease in the peak strength with the width ratio. As the depth ratio was again decreased further, NLFEA predicted that specimens CMP-B12 CMP-B14 have a peak load that is equal, with this value of peak load decreasing with the width ratio from specimen CMP-B15. It is noted that these values for series 3 are higher in all cases (with the exception of CMP-B15) than specimens with deeper flanges. This will be further discussed in Section 8.4.2.3.

Figure 8.4-1 shows the above trend graphically. It can be seen that the peak load for each value of dr for the value of br is corresponding to the peak strength increase is approximately equal. It is also predicts that the peak strength for $dr=0.33$ is higher for values of $br=3.32$ and 2.21 than those specimens in the same series with a higher width ratio. Similarly, the value of peak strength predicted for series 2 ($dr=0.25$) specimen with $br=3.32$ is higher than those with a higher width ratio.

Table 8.4-1 Comparison of peak loads produced from the flange geometry study

	SPECIMEN	br	P _E (kN)
SERIES 1	CMP-B1	6.64	176
	CMP-B2	4.43	176
	CMP-B3	3.32	188
	CMP-B4	2.21	185
	CMP-B5	1.61	150
	CMP-B6	1.00	101
SERIES 2	CMP-B7	6.64	184
	CMP-B8	4.43	183
	CMP-B9	3.32	199
	CMP-B10	2.21	154
	CMP-B11	1.61	143
SERIES 3	CMP-B12	4.43	187.6
	CMP-B13	3.32	187.6
	CMP-B14	2.21	184.3
	CMP-B15	1.61	140.0

Note: Series 1; dr=0.33
 Series 2; dr=0.25
 Series 3; dr=0.16

8.4.2 Load Deflection Response

As established in Section 8.3.5, the load-deflection curves give an indication of the failure mechanism that is predicted by implementation of the NLFEA procedure. This section will extrapolate this to the Flange Geometry Study to correlate the peak loads and the failure mechanisms.

8.4.2.1 Series 1

Figure 8.4-2 shows the load-deflection curves that were obtained from the NLFEA procedure for all specimens in series 1 of this study. These results show that the specimens with br=6.64, 4.43, and 3.32 all exhibit the sharp loss of capacity at the peak load. Using the

above correlation between failure mechanisms, it is noted that these NLFEA predicted the punching shear for these specimens.

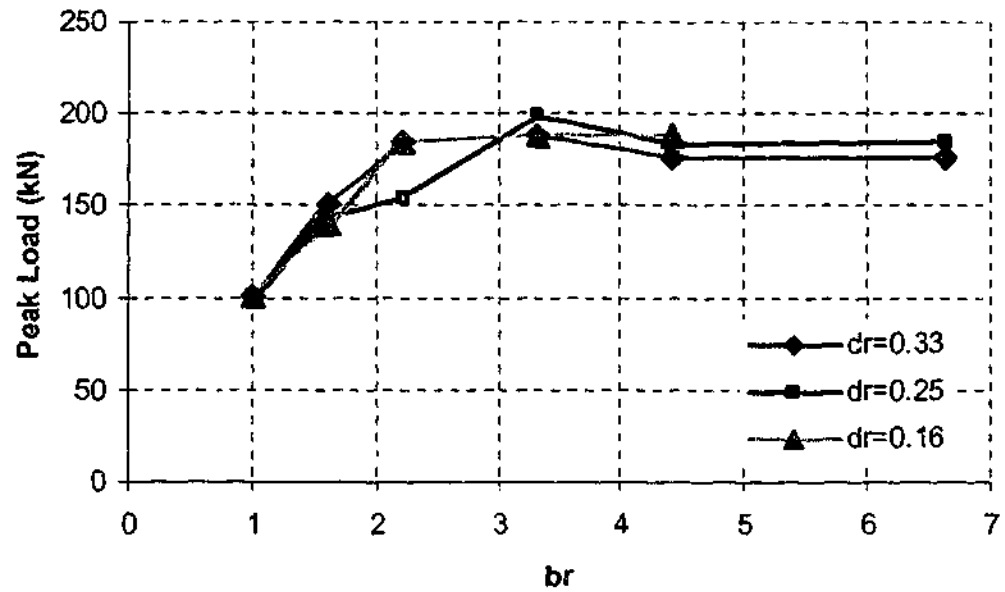


Figure 8.4-1 Variations in the ultimate strength with width ratio predicted by NLFEA for Stage III NLFEA

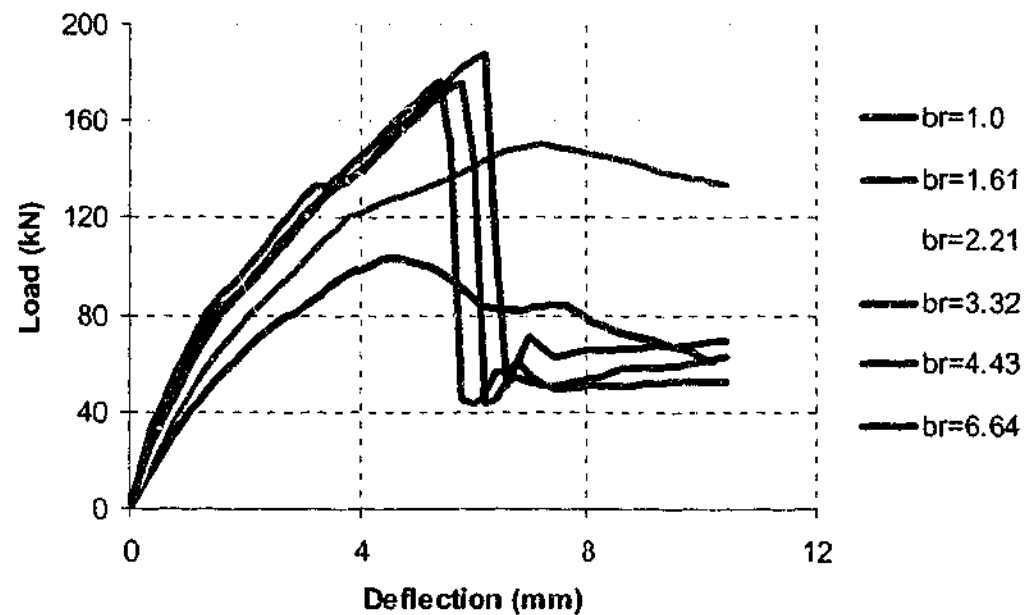


Figure 8.4-2 Load deflection curves for all specimens in series 1 of the Flange Geometry Study

Specimens with $br=2.21$, 1.61 and 1.0 all exhibited a smooth reduction in the sum of the reactions once the peak load was reached. Using the above correlation between failure mechanism and the load-deflection curve, these specimens all failed by exhibiting a beam shear mechanism.

8.4.2.2 Series 2

Figure 8.4-3 shows the load-deflection curves that were obtained from the NLFEA procedure for all specimens in series 2 of this study. These results show that the specimens with $br=6.64$ and 4.43 exhibited the sharp loss of capacity at the peak load. Using the above correlation between failure mechanisms, it is noted that these NLFEA predicted are punching shear failure mechanism for these specimens.

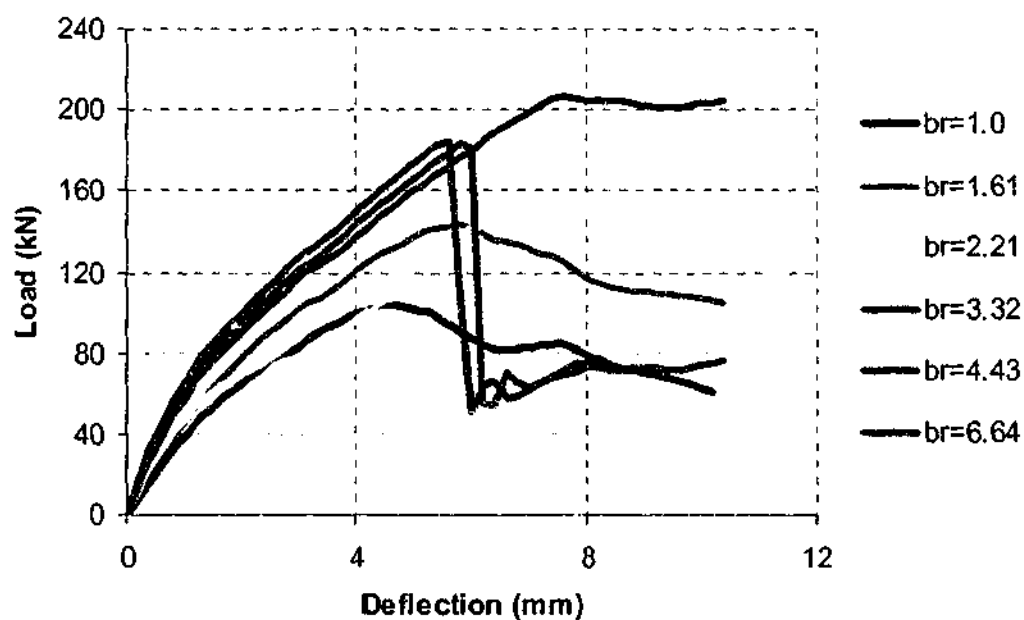


Figure 8.4-3 Load deflection curves for all specimens in series 2 of the Flange Geometry Study

Specimens with $br=3.32$, 2.21 , 1.61 and 1.0 all exhibited a smooth reduction in the sum of the reactions once the peak load was reached. Using the above correlation between failure mechanism and the load-deflection curve, these specimens all failed by exhibiting a beam shear mechanism.

8.4.2.3 Series 3

Figure 8.4-4 shows the load-deflection curves that were obtained from the NLFEA procedure for all specimens in series 3 of this study. These results show that all specimens exhibited a smooth reduction in the sum of the reactions once the peak load was reached. Using the failure mechanisms outlined in Section 8.3.5, it was found that the solution scheme predicted that specimen B12 would fail by exhibiting a punching shear mechanism, specimen B13 would fail by beam shear. Both of these two specimens were predicted to have longitudinal cracks at the flange web interface similar to those shown in Figure 8.3-6 and Figure 8.3-9. Specimens B14 and B15 were predicted to fail with a beam shear mechanism as determined by the crack patterns produced.

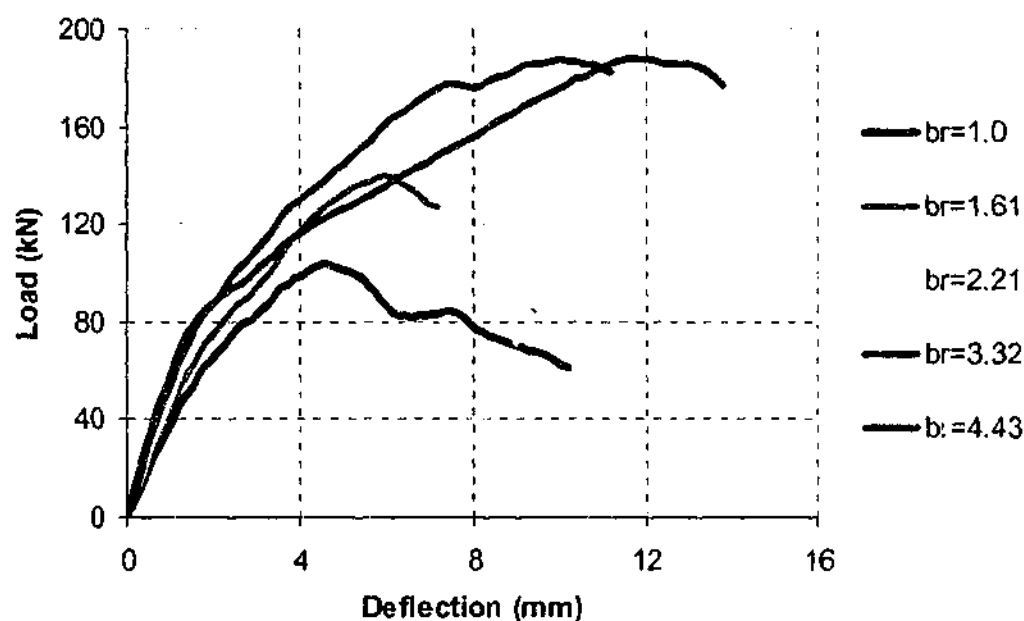


Figure 8.4-4 Load deflection curves for all specimens in series 3 of the Flange Geometry Study

The trend shows by this series of specimens is dissimilar to that of the experimental work. The outstanding issue is the high value of load predicted by specimens CMPB12 and CMPB13 ($br=4.43$ and 3.32 respectively), these values are higher than those predicted for series 1 and 2 specimens that have deeper flanges. Similar to Stage II experimental work, it is apparent that for a fixed mesh density, the NLFEA is having difficulty predicting the peak

strength consistently for specimens these specimens that are thought to be representative of wide and thin flanges.

8.4.3 Discussion of Results

The above study shows that the NLFEA solution procedure predicted an increase in the shear capacity of a series of T-beams that arises from increases in the proportions of the flange of an RC T-beam that is subjected to a concentrated point load without any variations in the material properties.

The predicted peak loads are estimated for specimens that were predicted to fail by the punching shear mechanism are essentially constant, and are estimated to be independent of the flange depth (as shown from the results between series 1 and series 2). As the flange width ratio decreased in series 1 and series 2, the beam shear mechanism became the mode of failure. The results for these series indicate that the predicted peak load for the specimen with the highest width ratio failing with a beam shear mechanism is higher than those predicted for specimens predicted to fail by punching. The peak load of two specimens that have wide thin flanges is higher than specimens that have identical flange widths but deeper flanges. This is a result of longitudinal cracks along the flange web interface being predicted by the solution scheme.

The solution procedure does not predict any significant variation in the peak load for specimens that display the punching shear mechanism regardless of the width ratio or the depth ratio. As the beam shear mechanisms began to prevail, NLFEA predicts that a higher strength is attained for specimens with greater flange proportions. The solution scheme predicts a higher dependency on the flange width than the flange depth in the increase in peak load with the flange proportions. The latter was also predicted from experiments.

8.5 Conclusions From the Finite Element Study

The above presents a three stage investigation into the ability of NLFEA to replicate experimental results and further predict the influence of the flange on the shear capacity of a web reinforced RC T-beam. The study examined the sensitivity of the solution scheme to

combinations of material models that described the tension and compression response of concrete, as well as the effect of the displacement increment on the solution obtained. Once the optimum combination of these was established, the procedure was implemented to investigate the accuracy of predicting peak strengths, load-deflection response, reinforcing strains, failure mechanisms, concrete strains and flange contribution to shear resistance as compared with the experimental work. A fixed mesh density was used throughout for consistency. Once the capabilities and limitations of the scheme were established, it was applied to a set of specimens with only flange proportions as the variables. The following was concluded from this study.

1. The accuracy of the scheme, and the prediction of the load deflection response is highly dependent on the choice of the compression response of the concrete. It is concluded that a concrete compression model that explicitly includes the effect on the compressive response from co-existing perpendicular tensile strains is most suited to this type of specimen. It is suggested that this would be the case in general for shear critical members.
2. The ultimate strength results predicted from NLFE modelling of the experimental specimens are in general in close agreement with those recorded during the experimental work. The exception to this is specimens B12 and B13. It is suggested that analysis of web reinforced T-beam specimens using NLFEA requires particular attention to mesh density in the region of the load point as well as the increment of applied displacement.
3. NLFEA predicted crack patterns at failure consistent with those that are displayed by the two failure mechanisms displayed during the experimental work with the exception of specimens B12 and B13.
4. NLFEA has reasonable prediction of longitudinal strains in the flange. This was particularly the case for specimen B17 that failed in flexure. It appears that the prediction of the wrong failure mechanism by the NLFEA solution scheme has led to an inaccurate estimate of the redistribution of the strains in the flange at failure.

5. NLFEA predicts that the width ratio and the depth ratio of a flange has a significant bearing on the shear strength of a shear critical, web reinforced T-beam subjected to a concentrated point load.
6. NLFEA has shown that flange contribution to the resistance to shear is significant. Excellent correlation of this result with the experimental work was produced for specimen B17. The result was not as good for specimen B16; it is again thought that the prediction of the wrong failure mechanism resulted in an inaccurate estimate for the flange contribution.
7. NLFEA predicts that the width ratio has a much more significant effect on the shear strength of an RC T-beam specimen subjected to a concentrated point load than the depth ratio.

Chapter 9 **CONCLUSIONS AND RECOMMENDATIONS**

9.1 **Overview of the Research Undertaken**

The research presented in this thesis implemented strategies to examine the contribution of the flange of a web reinforced RC T-beam subjected to a concentrated point load to the resistance of shear. This task was undertaken in three tiers of work, these were as follows.

- Determination of the variation in peak load and failure mechanisms obtained from a group of 15 specimens with varying flange width and depth, but constant overall depth and reinforcing ratio to examine the overall behaviour.
- Evaluation of the contribution of the flange to the resistance of shear by development of an experimental technique, and associated analytical relations that enable calculation of the sectional shear in the flange of a T-beam. This technique was applied to two specimens.
- Implementation of the NLFEA procedure to predict both the failure loads, load-deflection behaviour, crack patterns, strains (both concrete and steel strains), and percentage of total shear force in the flange.

The main conclusion drawn from this research is that increasing the flange proportions of a web reinforced RC T-beam subjected to a concentrated load will increase the shear resistance of that specimen. A significant contributing factor to this increase in shear capacity is the

redistribution of shear stresses into the flange from the web associated with the formation of the failure mechanism.

9.2 **Conclusions From This Research**

It is the purpose of this section to draw general conclusions from this research. The conclusions specific to each of the three tiers of the work are presented at the end of the relevant section. These general conclusions are as follows.

Failure mechanisms of web reinforced RC T-beams subjected to a concentrated point load

A web reinforced RC T-beam subjected to a concentrated point load will fail by either one of two mechanisms. Firstly, a beam shear mechanism which is a similar mechanism to that observed in rectangular beams, and secondly a punching shear mechanism whereby the load point tries to punch through the flange of the T-beam. The latter is a local phenomenon and arises from the concentration of the applied load over the width of the web during the experiments outlined above.

Ultimate strength of web reinforced RC T-beams subjected to a concentrated point load

Within a series of specimens that has an increasing flange width from a rectangular specimen upward, the shear strength will continue to increase until the punching shear mechanism forms. Once the flange is wide enough for the punching mechanism to form, any further increase in the flange width will not result in an increase in the shear strength.

Significant geometric variations in flange proportions

Of the two geometrical proportions of the flange, variations in the flange width results in much more significant variations in the shear strength of these specimens failing in beam shear than that of the flange depth. Results of the experimental work indicated that a thin flange may not provide any additional capacity to shear resistance.

The role of the flange in the resistance of shear

The significant increase in the shear strength of an RC T-beam with flange width is a result of the propagation of shearing stresses into the flange. The development of the failure mechanism (i.e. formation of the cracks that make up the failure mechanism at failure) results in redistributions of longitudinal strain in the flange that are required to accommodate the failure mechanism. It is these redistributions that necessitate a higher contribution of the flange to the resistance of shear. The full development of the failure mechanism results in a high effectiveness of the flange.

Implementation of the NLFEA solution scheme

Implementation of the NLFEA solution scheme with solid elements, a nonlinear elastic constitutive compression model with secant unloading for the concrete, and a linear tension softening has shown the ability to predict the above. This tool is suitable for the investigation of more subtle variations of the ultimate shear strength of a web reinforced RC T-beam specimen subjected to a concentrated point load with flange width. This is the case for specimens with flange proportions similar to that of series 1 and series 2 outlined in this study. The relative flange depths of these specimens are representative of those common in structural engineering application. The solution scheme appears to have difficulty in predicting the peak strength of specimens with thin wide flanges.

Amendment of provisions in current concrete codes of practice

The current codes of practice for the assessment of the shear strength of a T-beam are inadequate. Some provision should be made for the increase in the shear strength of a T-beam with increases in the flange proportions particularly for the purpose of evaluating existing structures.

9.3 **Suggestions for Future Work**

The work undertaken in this thesis has drawn attention to several areas that require further attention. These are as follows.

Failures resulting from localisation of load on wide flanged T-beam specimens

This research has shown that a concentrated load on a wide flanged T-beam produce a punching mechanism as a result of the localisation of the load. Consideration of the nature of the localisation (i.e. size and shape of load point, width of web, width and depth of flange) and the effect of this on the formation of the punching mechanism should be the major focus of such a study. The possibility of a beam shear failure mechanism being a subset of the punching shear failure mechanism should also be given special attention.

Elimination of unintended variations in material properties

The experimental work presented in this thesis required a normalisation procedure as ultimate strength results included unintended material properties that arose from the need to separate experimental work into three specimens. The examination of the experimental work for the effect of the flange depth required use of these procedures. It is suggested that the flange depth be investigated as a primary variable of an investigation, with experiments prepared in such a way that the same concrete and steel batches are used for each specimen to eliminate as many potential variations as possible.

T-beams without web reinforcing

There is some discrepancy between results obtained from previous investigations at the University of Glasgow (Fok (1972) and Chong (1980)) and the results of this and numerous other investigations. A normalisation procedure outlined above has indicated that the method of precluding variations in material properties used in the Glasgow studies may have hidden the increase in shear strength with increase in flange proportions. It is suggested that this statement should be validated by further

experimental work. This should particularly be the case for a specimen with a concentrated point load similar to that used in this investigation.

The contributions to the shear resistance of an RC beam

The adaptation of the instrumentation technique and the accompanying analytical technique to rectangular beams is suggested. This coupled with sufficient instrumentation on the stirrups could also be used to indirectly quantify the joint combination of aggregate interlock and dowel action.

Finite element analysis of these specimens

Although the NLFEA did adequately predict the strength of the specimens, it is thought that implementation of more sophisticated constitutive models may prove more successful in the prediction of the critical value of the flange width at which the punching mechanism forms. The inadequacy of NLFEA to predict the peak strength of beams with thin wide flanges should also be given further attention.

In situ T-beams in parallel

Structures such as a T-beam bridge deck comprise of a series of T-beams (of similar proportions to those tested in this research) in parallel. As one girder (which is a T-beam) is subjected to a point load from a truck, it may be such that the effective flange width for resistance of shear of this girder overlaps with the adjacent girder. This could significantly increase the shear strength of the deck further, and is suggested that this effect be the subject of detailed investigation.

Effects on other components of the shear mechanism from the increase in flange proportions

The above research has proven a contribution of the flange to the resistance of shear. An investigation into the effect that the increase in the flange proportions on the effect of dowel action and aggregate interlock should also be undertaken.

REFERENCES

- ACI 318 (1999) *Building Code Requirements for Structural Concrete*, American Concrete Institute, Detroit.
- Adepegba, D. (1966), "A Theory of Failure for Reinforced Concrete Beams without Web Reinforcing Subjected to Bending and Shear" PhD, University of Leicester.
- ASCE-ACI Committee 445 (1998), "Recent Approaches to Shear Design of Structural Concrete", *Journal of Structural Engineering*, **124** (12), pp. 1375-1417.
- Al-Alusi, A. F. (1957), "Diagonal Tension Strength of Reinforced Concrete T-Beams with Varying Shear Span", *ACI Journal*, **53**, pp. 1067-1077.
- Al-Mahaidi, R., Taplin, G., Giaccio, C. and Bouilly, G. (2000), "Strength and Load Distribution Analysis of a T-Beam Bridge Deck", *Austrroads 4th Bridge Engineering Conference*, Adelaide, pp. 261-274.
- Al-Mahaidi, R., and Taplin, G., Guifre, A. (2000), "Load Distribution and Shear Strength Evaluation of an Old Concrete T-Beam Bridge", *Transportation Research Record*, **1**(1969), pp. 52-62.
- Al-Mahaidi, R. S. and Taplin, G. (1998), "Analysis and Full Scale Testing of a Reinforced Concrete T-Beam Bridge", *Australasian Structural Engineering Conference*, Auckland, pp.
- AS3600 (2001) *Concrete Structures*, Standards Australia, Sydney.
- Austrroads (1996) *Australia Bridge Design Code*, Austrroads, Sydney.
- Averbuch, D. and de Buhan, P. (1999), "Shear Design of Reinforced Concrete Deep Beams: A Numerical Approach", *Journal of Structural Engineering-ASCE*, **125** (3), pp. 309-317.
- Baumann, T. (1968) *Tests for Studying the Dowel Effect of Flexural Tensile Reinforcement in a Reinforced Concrete Beam*, Technischen Hochschule Munchen, pp. 51 (in German).
- Beal, D. B. (1982), "Load Capacity of Concrete Bridge Decks", *Journal of Structural Engineering*, **108** (ST4), pp. 814-832.
- Beal, D. B. (1985), "Strength of Concrete T-Beam Bridges", *ACI SP-88*, 143-164.
- Belarbi, A. and Hsu, T. T. C. (1990), "Stirrup Stresses in Reinforced Concrete Beams", *ACI Structural Journal*, **87** (5), pp. 530-538.

- Belarbi, A. and Hsu, T. T. C. (1995), "Discussion of "Compression Response of Crack Reinforced Concrete"", *Journal of Structural Engineering*, **121** (7), pp. 1151-1152.
- Bentz, E. E. (2000), "Sectional Analysis of Reinforced Concrete Members" PhD, Graduate Department of Civil Engineering, University of Toronto.
- CEB-FIP (1993) *CEB-FIP Model Code 1990*, Comite Euro-International du Beton.
- Chong, O. Y. (1980), "Ultimate Shear Strength of Uniformly Loaded Reinforced Concrete Tee Beams" Masters Thesis, Department of Civil Engineering, University of Glasgow.
- Collins, M., Vecchio, F. J. and Mehlhorn, G. (1985), "An International Competition to Predict the Response of Reinforced Concrete Panels", *Canadian Journal of Civil Engineering*, **12** (3), pp. 626-644.
- Collins, M. P. (1998a), "Opinion Procedure for Calculating the Shear Response of Reinforced Concrete Elements: A Discussion", *Journal of Structural Engineering*, **124** (12), pp. 1485-1488.
- Collins, M. P. (1998b), "Procedures for Calculating the Shear Response of Reinforced Concrete Elements: A Discussion", *Journal of Structural Engineering-ASCE*, **124** (12), pp. 1485-1488.
- CSA A23.3 (1994) *Design of Concrete Structures 1994*. CSA International, Ontario, Canada.
- Darvall, P. L. P. (1987) *Reinforced and Prestressed Concrete*, Macmillan.
- Darwish, M. N., Gesund, H. and Lee, D. D. (2000), "A Discussion of "Recent Approaches to Shear Design of Structural Concrete"", *Journal of Structural Engineering*, **126** (7), pp. 853-854.
- Dei Poli, S., Di Prisco, M. and Gambarova, G. (1990), "Stress Field in Web of RC Thin-Webbed Beams Failing in Shear", *Journal of Structural Engineering*, **116** (9), pp. 2496-2515.
- DIANA (1998) *Finite Element Analysis User's Manual, Release 7.0*, TNO Building and Construction Research.
- El-Neima, E. I. (1988), "Investigation of Concrete Haunched T-Beams under Shear", *Journal of Structural Engineering*, **114** (4), pp. 917-930.
- Ferguson, P. M. and Thomson, J. N. (1953), "Diagonal Tension in T-Beams without Stirrups", *ACI Journal*, **50** 665-675.
- Fok, W. K. (1972), "The Shear Strength of Reinforced Concrete T Beams with Unreinforced and Shear-Reinforced Webs" PhD Thesis, Department of Civil Engineering, University of Glasgow.
- Giaccio, C., Al-Mahaidi, R. S. and Taplin, G. (2000), "Flange Effectiveness in the Shear Strength of RC T-Beams", *APSEC 2000*, K.L., pp. 462-472.

- Hoang, L. C. (1997) *Shear Strength of Non-Shear Reinforced Concrete Elements Part 2. T-Beams*, Technical University of Denmark, pp. 32.
- Hognestad, E. (1951) *A Study of Combined Bending and Axial Load in Reinforced Concrete Members*, University of Illinois.
- Hseih, S. S., Ting, E. C. and Chen, W. F. (1979), "An Elastic-Fracture Model for Concrete", *Third Engineering Mechanics Division Specialty Conference*, Austin, Texas, pp. 437-440.
- Hsu, T. T. C. (1988), "Softened Truss Model Theory for Shear and Torsion", *ACI Structural Journal*, **85** (6), pp. 624-635.
- Hsu, T. T. C. (1998a), "Stresses and Crack Angles in Concrete Membrane Elements", *Journal of Structural Engineering-ASCE*, **124** (12), pp. 1476-1484.
- Hsu, T. T. C. (1998b), "Unified Approach to Shear Analysis and Design", *Cement and Concrete Composites*, **20** 419-435.
- Hsu, T. T. C., Mau, S. T. and Chen, B. (1987), "Theory of Shear Transfer Strength of Reinforced Concrete", *ACI Structural Journal*, **84** (2), pp. 149-160.
- Ibell, T. J., Morley, C. T. and Middleton, C. R. (1997), "Plasticity Approach to the Assessment of Shear in Concrete Beam-and-Slab Bridges", *Structural Engineer*, **75** (19), pp. 331-338.
- Klein, G. J. and Popovic, P. L. (1985), "Strength Evaluation of Existing Bridges", *Publication SP ACI 88*, 199-224.
- Kollegger, J. and Melhorn, G. (1990), "Material Model for the Analysis of Reinforced Concrete", *Computational Mechanics*, **6** (5-6), pp. 341-357.
- Kotsovos, M. D. (1983), "Mechanisms of 'Shear' Failure", *Magazine of concrete research*, **123** (35), pp. 99-106.
- Kotsovos, M. D. (1986), "Behaviour of Beams with Shear Span-to-Depth Ratios Greater Than 2.5", *ACI Journal*, **83** (6), pp. 1026-1034.
- Kotsovos, M. D., Bobrowski, J., Eibl, J. (1987a), "Behaviour of Reinforced Concrete T-beams in Shear", *The Structural Engineer*, **65B** (1), pp. 1-10.
- Kotsovos, M. D. (1987b) "Shear Failure of Reinforced Concrete Beams", *Engineering Structures*, **9** (1), pp. 32-38.
- Kotsovos, M. D. (1988), "Compressive Force Path Concept: Basis for Reinforced Concrete Ultimate Limit State Design", *ACI Structural Journal*, **85** (1), pp. 68-75.
- Kotsovos, M. D. and Bobrowski, J. (1993), "Design Model for Structural Concrete Based on the Concept of the Compressive Force Path", *ACI Structural Journal*, **90** (1), pp. 12-20.

- Kotsovos, M. D. and Lefas, I. D. (1990), "Behaviour of Reinforced Concrete Beams Designed in Compliance with Concept of Compressive-Force Path", *ACI Structural Journal*, **87** (2), pp. 127-139.
- Kotsovos, M. D. and Pavlovic, M. N. (1995) *Structural Concrete: Finite Element Analysis for Limit State Design*, T. Telford, London.
- Lee, D. D. and Hsu, T. T. C. (2000), "Stresses and Crack Angles in Concrete Membrane Elements", *Journal of Structural Engineering*, **126** (5), pp. 631-633.
- Litton, R. W. (1974), "A Contribution to the Analysis of Concrete Structures under Cyclic Loading" PhD, University of California.
- Loov, R. E. (2000), "Shear Design of Concrete-ac Simpler Way", *Annual Conference of the Canadian Conference of Civil Engineers*, Ontario.
- Morsch, E. (1906) *Der Eisenbetonbau Seine Anwendung Und Theorie*.
- Ngo, D. and Scordelis, A. C. (1967), "Finite Element Analysis of Reinforced Concrete Beams", *ACI Journal*, **64** (3), pp. 152-163.
- Pang, X.-B. and Hsu, T. T. C. (1995), "Behaviour of Reinforced Concrete Membrane Elements in Shear", *ACI Structural Journal*, **92** (6), pp. 665-679.
- Pang, X.-B. and Hsu, T. T. O. (1996), "Fixed Angle Softened Truss Model for Reinforced Concrete", *ACI Structural Journal*, **93** (2), pp. 197-207.
- Placas, A. and Regan, P. E. (1971), "Shear Failure of Reinforced Concrete Beams", *ACI Journal*, **68** 763-773.
- Reinhardt, H. W. (1984), "Fracture Mechanics of an Elastic Softening Material", *Heron*, **29** (2), pp.
- Ritter, W. (1899), "Die Bauweise Hennebique", *Schweizerische Bauzeitung*, **33** (7), pp. 59-61.
- Rodrigues, C. P. and Darwin, D. (1987), "Shear Strength of Lightly Reinforced T-Beams in Negative Bending", *ACI Structural Journal*, **84** (1), pp. 77-88.
- Sargin, M. (1971) *Stress-Strain Relations for Concrete and the Analysis of Structural Concrete Sections, Study No 4*, University of Waterloo, Waterloo, Ontario, Canada.
- Selby, R. G. (1993), "Three-Dimensional Relations for Reinforced Concrete" PhD Thesis, Graduate Department of Civil Engineering, University of Toronto.
- Selby, R. G., Vecchio, F. J. and Collins, M. P. (1996), "Analysis of Reinforced Concrete Members Subject to Shear and Axial Compression", *ACI Structural Journal*, **93** (3), pp. 306-315.
- Seraj, S. M., Kotsovos, M. D. and Pavlovic, M. N. (1992), "Three-Dimensional Finite-Element Modelling of Normal- and High-Strength Reinforced Concrete Members, with Special Reference to T-Beams", *Computers & Structures*, **44** (4), pp. 699-716.

- Stevens, N.J., Uzumeri, S.M., Collins, M.P., Will, G.T. (1991), "Constitutive Model Analysis for Reinforced Concrete Finite Element Analysis"; *ACI Structural Journal*, **88** (1), pp. 49-59.
- Swamy, N. and Qureshi, S. A. (1971), "Strength, Cracking and Deformation Similitude of Reinforced T-Beams under Bending and Shear", *ACI Journal*, **68**, 187-195.
- Swamy, R. N. (1969), "Shear Failure in Reinforced Concrete Beams without Web Reinforcement", *Civil Engineering and Public Works Review*, 237-243.
- Taplin, G. and Al-Mahaidi, R. (2000), "Experimental Investigation of Shear Critical T-Beams", *3rd Structural Specialty Conference, Canada*, pp. 486-492.
- Thorenfeldt, E., Tomaszewicz, A. and Jensen, J. J. (1987), "Mechanical Properties of High Strength Concrete and Applications and Design", *Symposium on the Utilisation of High Strength Concrete*, Trondheim.
- Timoshenko, S. P. (1970) *Theory of Elasticity*, McGraw-Hill, New York.
- Vecchio, F. J. (1989), "Nonlinear Finite Element Analysis of Reinforced Concrete Membranes", *ACI Structural Journal*, **86** (1), pp. 26-35.
- Vecchio, F. J. (1990), "Reinforced Concrete Membrane Element Formulations", *Journal of Structural Engineering*, **116** (3), pp. 730-751.
- Vecchio, F. J. (2000), "Disturbed Stress Field Model for Reinforced Concrete: Formulation", *Journal of Structural Engineering*, **126** (9), pp. 1070-1077.
- Vecchio, F. J. (2001), "Disturbed Stress Field Model for Reinforced Concrete: Implementation", *Journal of Structural Engineering*, **127** (1), pp. 12-20.
- Vecchio, F. J. and Collins, M. (1986), "The Modified Compression-Field Theory for Reinforced Concrete Elements Subjected to Shear", *ACI Journal*, **83** (2), pp. 219-231.
- Vecchio, F. J. and Collins, M. (1988), "Predicting the Response of Reinforced Concrete Beams Subjected to Shear Using the Modified Compression Field Theory", *ACI Structural Journal*, **85** (3), pp. 258-268.
- Vecchio, F. J., Lai, D., Shim, W. and Ng, J. (2001), "Disturbed Stress Field Model for Reinforced Concrete: Validation", *Journal of Structural Engineering*, **127** (4), pp. 350-358.
- Vecchio, F. J. and Selby, R. G. (1991), "Toward Compression-Field Analysis of Reinforced Concrete Solids", *Journal of Structural Engineering*, **117** (6), pp. 1740-1758.
- Vecchio, F. J. and Collins, M. P. (1993), "Compression Response of Cracked Reinforced Concrete", *Journal of Structural Engineering*, **119** (12), pp. 3590-3610.
- Wagner, H. (1929), "Ebene Blechwandtrager Mit Sehr Dünnem Stegblech", *zeitschrift für flugtechnik und motorluftschiffahrt*, **20** (8-12), pp.

Warner, R. F., Rangan, B. V. and Hall, A. S. (1993) *Reinforced Concrete*, Longman Cheshire, Melbourne, Australia.

Appendix A COMPRESSION SOFTENING DUE TO PERPENDICULAR TENSILE STRAINS IN SPECIMENS B16 AND B17

A.1 Introduction

Softening of the compressive response resulting from perpendicular tensile strain is a characteristic of the response of concrete that has only received attention in the last twenty years. The original formulation of the MCFT involved testing of 30 reinforced concrete panels to determine the stress-strain characteristics of such an element. The resulting constitutive relations that were borne from that study were the first to attempt to quantify this phenomenon. The authors of the MCFT then embarked on a large testing program that isolated this phenomenon and attempted to describe its behaviour more accurately. The discussion on this paper that followed by Belarbi and Hsu (1995) indicated many shortcomings that exist in the determination of the influence of tension strains on the compressive response, including a lack of generally agreed upon method to measure tensile strains of concrete with large cracks. The authors of this discussion had proposed their own set of equations to predict the compressive response of concrete subject to large perpendicular tensile strains prior to this publication in Pang and Hsu (1995) (note that these relations were formulated by Belarbi and Hsu in July 1991 in a departmental publication at the University of Houston). Other authors have given treatment to this problem, but as it is not a major focus of this research, only a representative model will be considered for this discussion.

The research above has not determined an agreed upon method of calculating the influence of the perpendicular strains on the compressive response of concrete. In the examination of the potential effect of this phenomenon on the calculation of compression forces in the flange of an RC T-beam, the relationships determined by Vecchio and Collins (1993) are used, as the pool of data used for the determination of these relations is the largest. It is thought that the large data pool should yield the most statistically reliable results.

A.2 Determination of the Influence of Perpendicular Tensile Strains Using DSFM

As outlined in Chapter 3 the DSFM requires calculation of the softening parameter using the relationship in Equation A.A.2.1.

$$\beta_d = \frac{1}{1 + C_s C_d} \leq 1.0 \quad \text{A.2.1}$$

The parameter C_s is a parameter that accounts for the relative reinforcing percentages in the two directions in plane stress. Vecchio and Collins (1993) suggest a value of 0.55 where equal reinforcing is provided in both orthogonal directions, or a value of 1.0 otherwise. Given the arrangement of reinforcing in the flanges of the specimens tested, the value of C_s is taken as 1.0 for this procedure. The parameter C_d is the parameter that takes into account the effect of the tensile strain perpendicular to the principal compressive direction. The DSFM considers two methods of calculation of the value of this parameter. These are shown in Equations A.2.2 and A.2.3.

$$C_d = 0.27(-\epsilon_{c1} / \epsilon_0 - 0.37) \quad \text{A.2.2}$$

$$C_d = 0.35(-\epsilon_{c1} / \epsilon_{c2} - 0.28)^{0.8} \quad \text{A.2.3}$$

Equation A.2.2 relates the parameter C_d to the value of the principal tensile strain (ϵ_{c1}), and the strain at the peak cylinder stress (ϵ_o). Using the value of ϵ_o recommended by the CEB-FIP Model Code ($\epsilon_o=0.0022$), this equation yields a value of principal tensile strain of $814\mu\epsilon$ as the minimum magnitude of tensile strain that is required to be present in the direction perpendicular to the principal compressive strain. The authors recommend this equation for use in design procedures when the level of compressive strain is unknown. This formulation implicitly assumes that the concrete has reached the peak stress in the principal compressive direction. During stage 2 tests, the concrete at the location of the gauges did not crush, nor did the perpendicular tensile strain reach $814\mu\epsilon$.

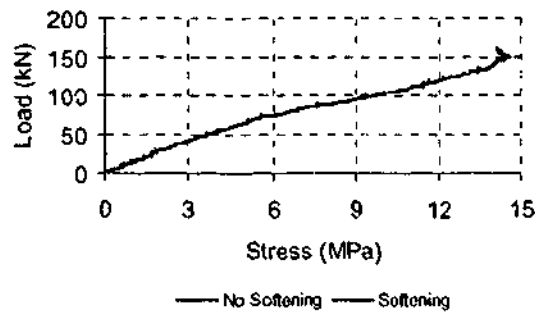
Equation A.2.3 depends on the ratio of the principal tensile strain to the principal compressive strain (ϵ_{c2}). A discussion of the value of the softening parameter calculated using this formulation, as well as the values of compressive stress calculated using this value is given in the following section.

A.3 Results of the Calculation of the Softening Coefficient

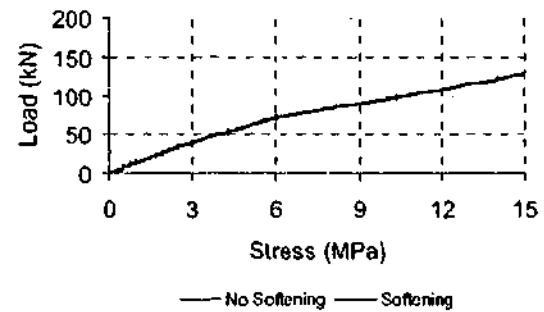
The lateral and longitudinal surface gauges in specimens B16 and B17 were coincident at the locations where lateral gauges were applied. Within the depth of the flange, the lateral gauges were offset half of one embedded gauge thickness. This is considered negligible for the purpose of the calculations presented below. Therefore, at any given location where lateral and longitudinal gauges are coincident, ϵ_{c1} in Equation A.2.3 is the result of the gauge in the lateral direction, and the term ϵ_{c2} is the result of the gauge in the longitudinal direction. For the purpose of this discussion, Equation A.2.3 is only valid if ϵ_{c2} is a compressive strain.

The gauges were coincident at three locations across the width of the specimen. With reference to Figure 7.1-2 in Chapter 7, these are at row 2, 4, and 6. Row 4 results are not relevant to this discussion because this row is in the web and not considered in these calculations. The effect of the softening coefficient as calculated at row 2 and row 6 is considered in this discussion.

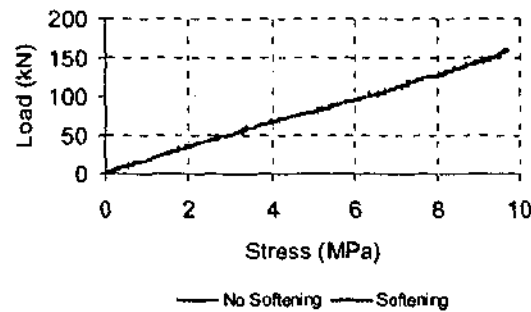
Figure A. 3-3 – A.3-4 presented at the end of this appendix show the variation of the stresses calculated at row 2 and row 6 with the applied load. These figures present the results of stresses both with and without the inclusion of the softening coefficient. These figures show that (with the exception of results of specimen B17 gauges at row 2 embedded in the flange at section A and section B) consideration of softening does not influence the value of the calculated stress.



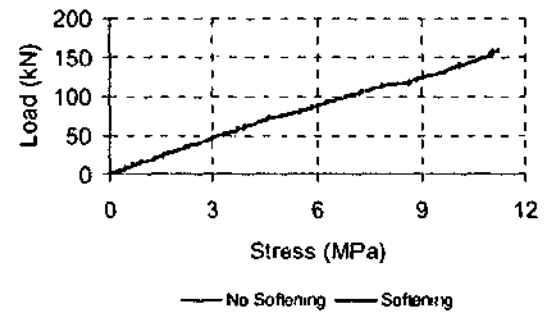
(a) Top Surface Row 2



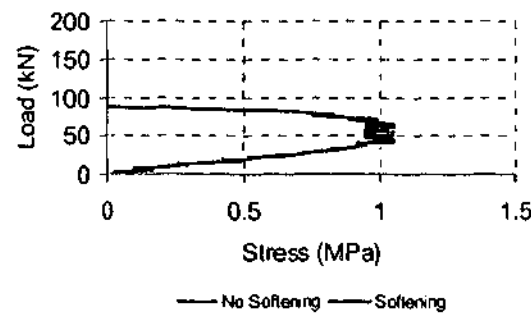
(b) Top Surface of Flange at Row 6



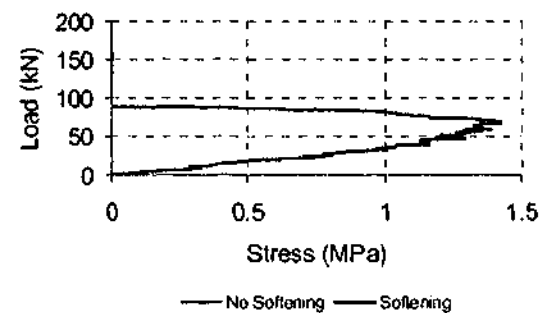
(c) Middle of Flange at Row 2



(d) Middle of Flange at Row 6



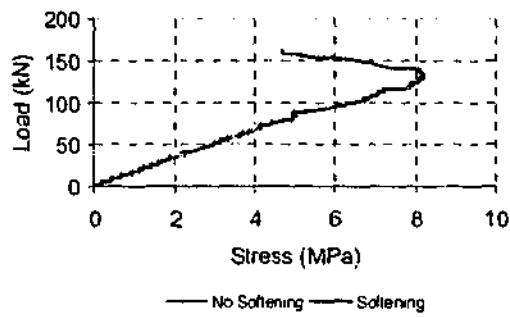
(e) Underside of Flange at Row 2



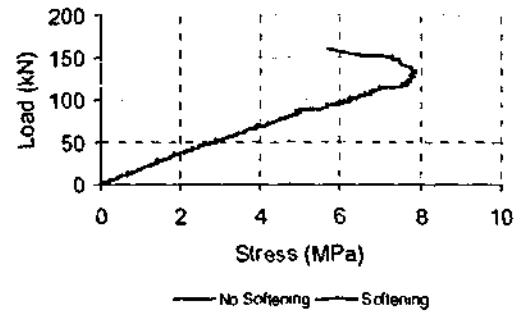
(f) Underside of Flange at Row 6

Figure A. 3-1 Comparison Of Stresses Calculated With And Without Softening Considerations For Specimen B16 At Section A

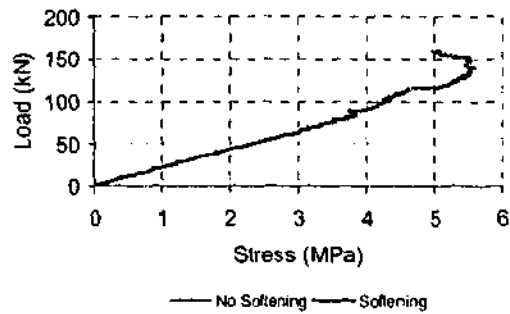
Considering the ratio of calculated stresses (stress calculated with softening considered/stress calculate without softening considered) expressed as a percentage, it is found that the maximum variation at section A, row 2 is 2.0%, and at section B row 2 is 3.5%. These values are small and negligible in the use of these stresses to calculate force over the area of one flange block in specimen B17. Based on these results, the effect of softening is ignored in the discussion of the calculation of flange stresses hereon.



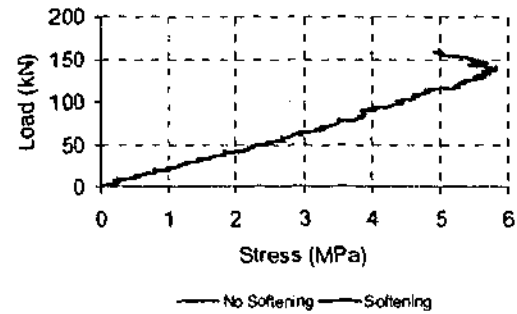
(a) Top Surface Row 2



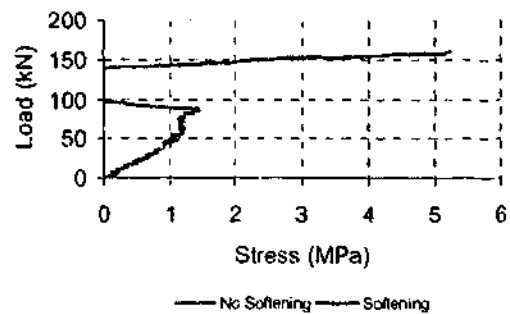
(b) Top Surface of Flange at Row 6



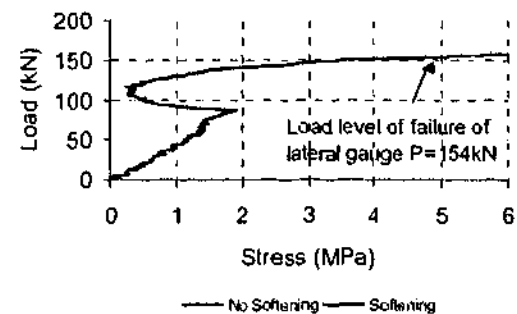
(c) Middle of Flange at Row 2



(d) Middle of Flange at Row 6

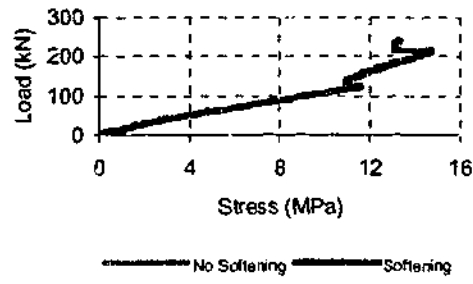


(e) Underside of Flange at Row 2

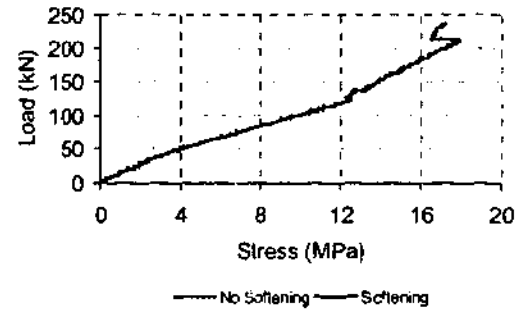


(f) Underside of Flange at Row 6

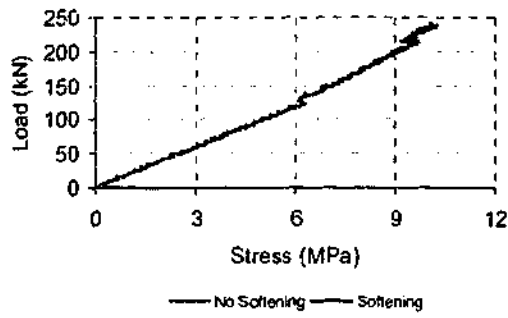
Figure A. 3-2 Comparison Of Stresses Calculated With And Without Softening Considerations For Specimen B169 At Section B



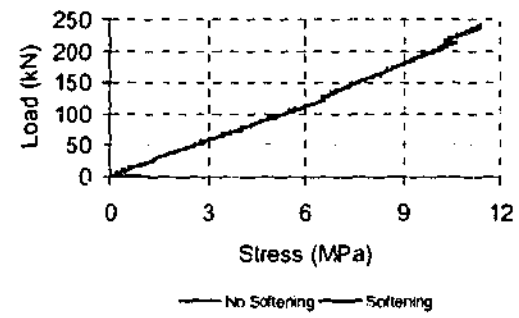
(a) Top Surface Row 2



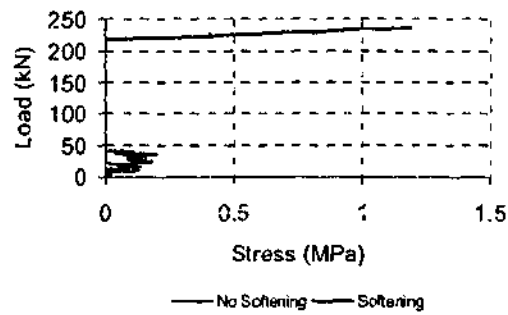
(b) Top Surface of Flange at Row 6



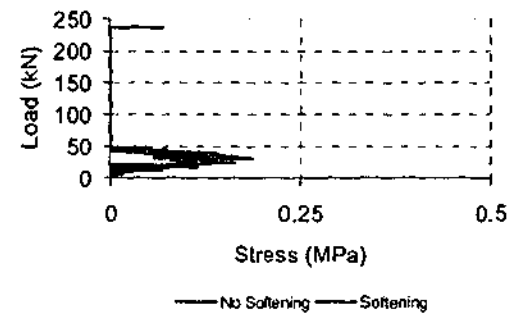
(c) Middle of Flange at Row 2



(d) Middle of Flange at Row 6

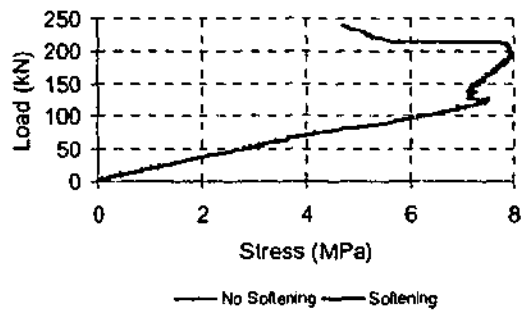


(e) Underside of Flange at Row 2

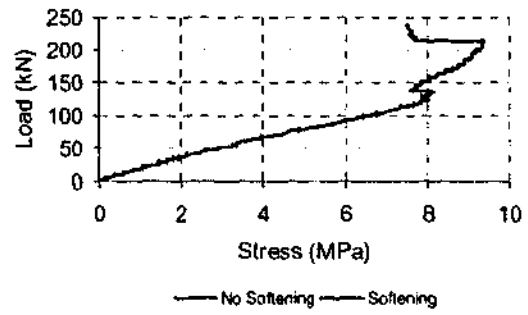


(f) Underside of Flange at Row 6

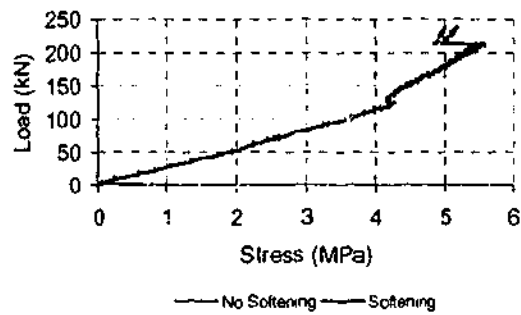
Figure A. 3-3 Comparison Of Stresses Calculated With And Without Softening Considerations For Specimen B17 At Section A



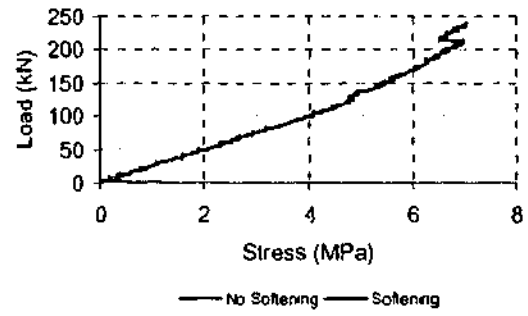
(a) Top Surface Row 2



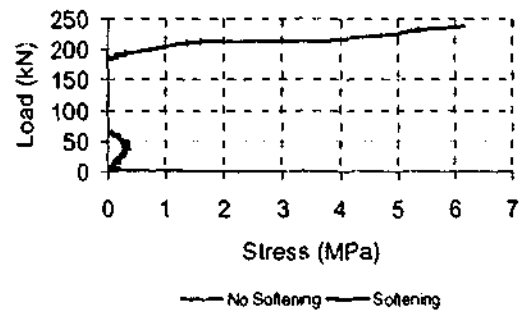
(b) Top Surface of Flange at Row 6



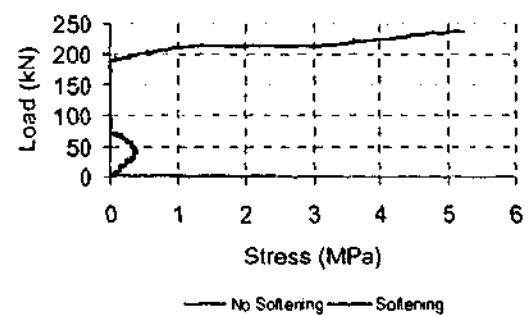
(c) Middle of Flange at Row 2



(d) Middle of Flange at Row 6



(e) Underside of Flange at Row 2



(f) Underside of Flange at Row 6

Figure A. 3-4 Comparison Of Stresses Calculated With And Without Softening Considerations For Specimen B17 At Section B

Appendix B LONGITUDINAL STRAINS, REDISTRIBUTIONS AND THE FAILURE MECHANISM OF SPECIMEN B16

B.1 Introduction

This appendix is intended to take the reader through the process of analysis of longitudinal strain results that was undertaken in an effort to determine the redistributions of strain that occurred throughout the loading history, and the effect that these redistributions had on the distribution of compression throughout the width of the flange. Several stages of the development of the failure mechanism were discussed for this specimen in Chapter 7, this appendix shows the relationship of these stages with the longitudinal strain distributions obtained from the experimental procedure.

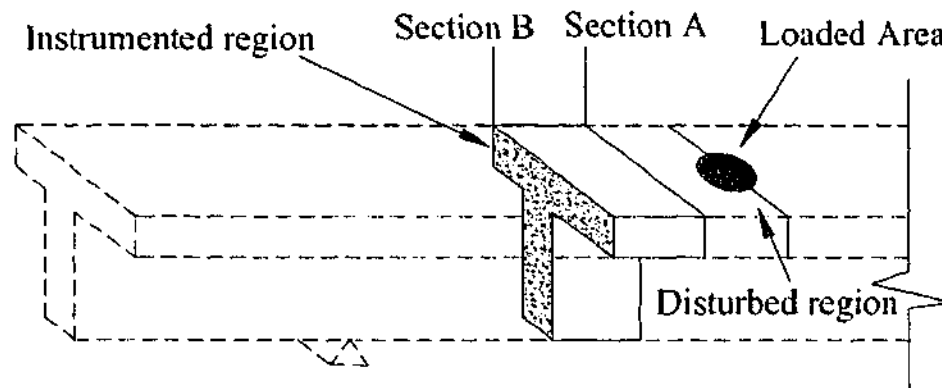


Figure B. 1-1 Identification of Section A and Section B

This appendix presents the results of the strain gauges, results of the calculation of neutral axis depth and top fibre stress, as well as a discussion of the stages of strain redistribution associated with the formation of the failure mechanism that significantly influenced the effectiveness of the flange in the resistance of shear. This appendix uses some notation that was defined in Chapter 3. Figure B. 1-1 outlines the relevant definitions.

B.2 Distribution of Longitudinal Strains

The results of strain gauging in the longitudinal direction at the two sections can be seen in Figure B. 2-1 – B.2-3. The results of strain gauging are presented as distributions throughout the width and depth. Figure B. 2-1 shows the distributions of strain across the width of the flange at three locations throughout the depth at section A, Figure B. 2-2 shows the same distributions at section B, and Figure B. 2-3 shows the shows the distribution of strain throughout the depth of the flange at section A and B in the web (row 4), and at one location that is representative of the behaviour exhibited at each row in the flange (row 2). The illustrations in Figure B. 2-1 and Figure B. 2-2 show distributions of strain across the width of the flange on the top surface of the flange, at the centre of the depth of the flange, and at the underside of the flange. Linear interpolation was used to produce results at exactly the centre of the depth of the flange. In all of the illustrations, the convention of compression as positive is used for stresses and strains.

B.2.1 Section A

Figure B. 2-1 (a) – (h) show that the distribution of compressive strain on the top surface of the specimen remains uniform until a level of load of 140kN. This distribution is essentially constant throughout the width, with the strain in the flange overhangs being equal to that at the centre of the width of the web. Beyond this level of applied load, the magnitude of strain in the right side flange overhang can be seen to be higher than that in the left side flange overhang as is shown in part (i) – (j) of Figure B. 2-1.

Examination of Figure B. 2-3 (a) shows that the rate of increase of the compressive strain on the top surface of the flange overhangs remained essentially constant until a level of load of 91kN. This level of applied load marked the appearance of the critical diagonal web

crack. Beyond this level of applied load, the gradient of increase in the compressive strain with applied load increased until a level of 140kN. This level of applied load marked the beginning of a reversal of strain on the top surface of the flange, with the decrease in magnitude beginning at a level of applied load of 160kN. Beyond this level of applied load, a uniform decrease in the compressive strain on the top surface of the flange prevailed. Although difficult to see in part (b) of this figure due to the large tensile strains that formed, this trend was generally reflected by the strain gauges located at the centre of the width of the web of the specimen.

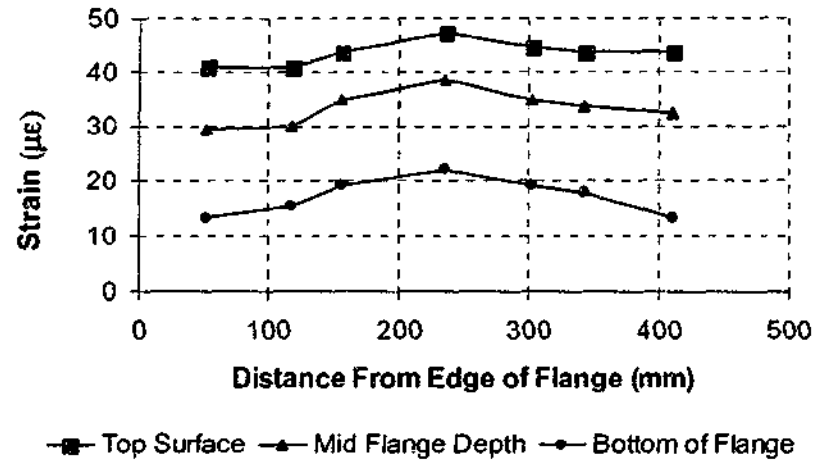
The strain on the underside of the flange can be seen to be in compression and small in magnitude between applied loads of 0-60kN at this section as shown in Figure B. 2-1 (a) – (c). Comparison of strains on the underside of the flange at a load level of 60kN and 80kN (Figure B. 2-1 (c) and (d)) show that the development of strain within these load increments is not consistent with the development from previous load stages. Between these load increments, the magnitude of the compression strains generally decreases within this range; this is thought to be associated with the redistribution required for the formation of the critical diagonal web crack. Beyond a load level of 91kN, the strains on the underside of the flange at section A become tensile, and increase in magnitude until a level of load of 140kN as indicated by Figure B. 2-1 (e)-(g). Beyond this level of load, the magnitude of the tensile strains begins to decrease, as can be seen by Figure B. 2-1 (g) – (h). This trend is continued until a level of applied load of 170kN. Beyond this level of load, there is a trend for the strains on the underside to become small compressive strains as is shown in part (i) and (j) of this figure.

All results at the centre of depth indicate that in the flanges, the strain is compressive and increasing until failure. However, the gauge that was embedded at the centre of the width of the web indicates that a tensile strain develops from an applied of load of 160kN onward. This can be seen in Figure B. 2-1 (h)-(j).

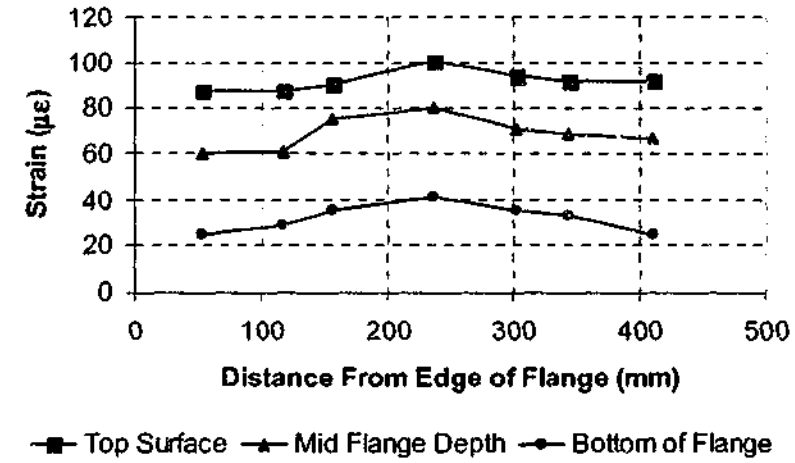
The results from the strain gauges on the underside of the flange and those embedded within the flange indicate that only the web exhibits significant tensile strains. As the specimen approaches failure the crack that initiates failure does not penetrate the edges of the

flange within the range of loading considered in these plots at section A, it only penetrates the web region of the specimen.

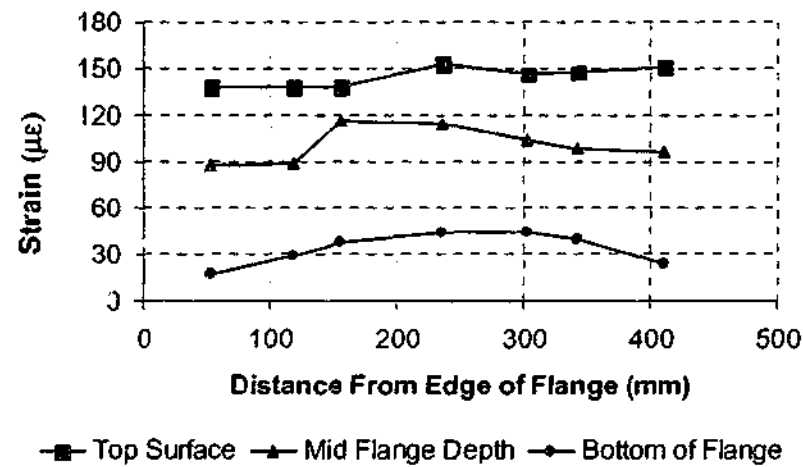
The results at section A show that in general, if gauges show compression throughout the entire width of the flange, the right hand flange overhang has a higher level of compression than the left hand overhang. It can also be seen from these figures that re-distributions corresponding to the formation of the critical cracks outlined above shed more strain to the over hang on the right hand side of the flange.



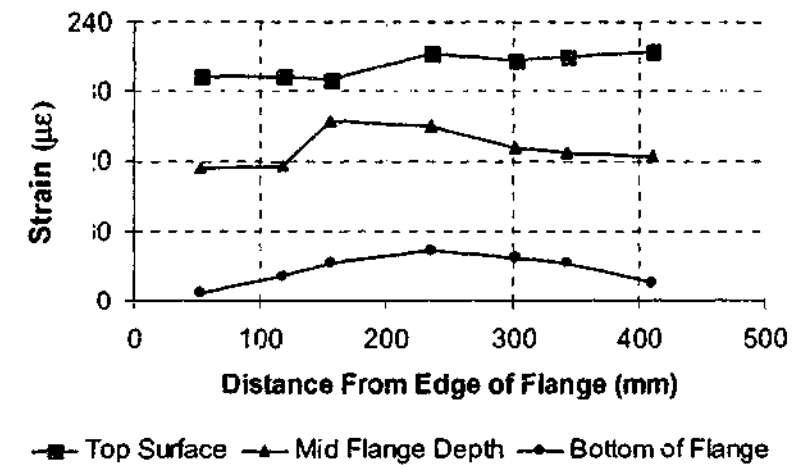
(a) Section A at 20kN



(b) Section A at 40kN

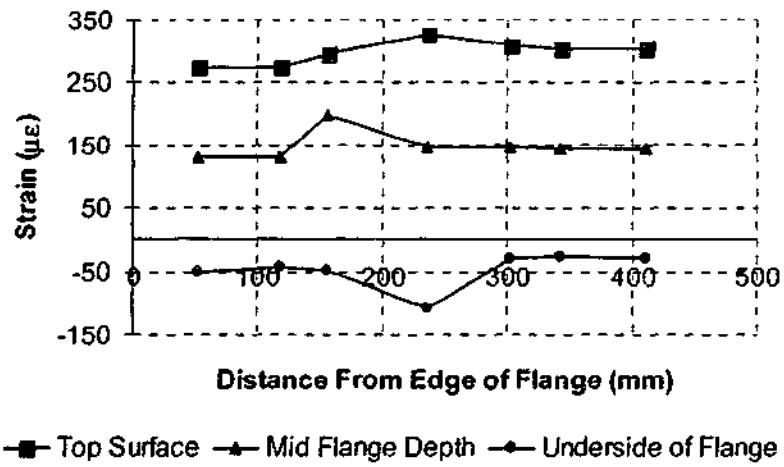


(c) Section A at 60kN

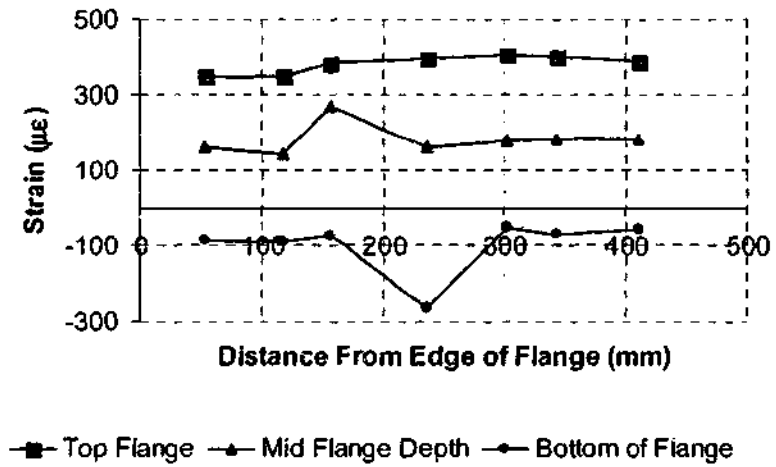


(d) Section A at 80kN

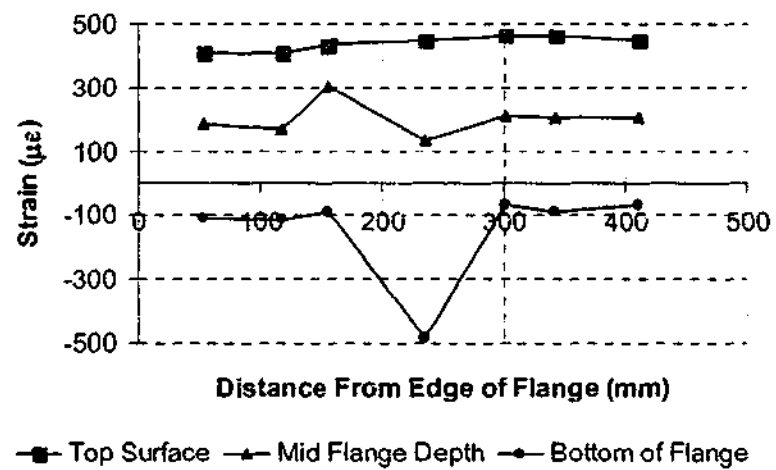
Figure B. 2-1 Distributions of longitudinal strain on section A of specimen B16 at 20kN intervals



(e) Section A at 100kN

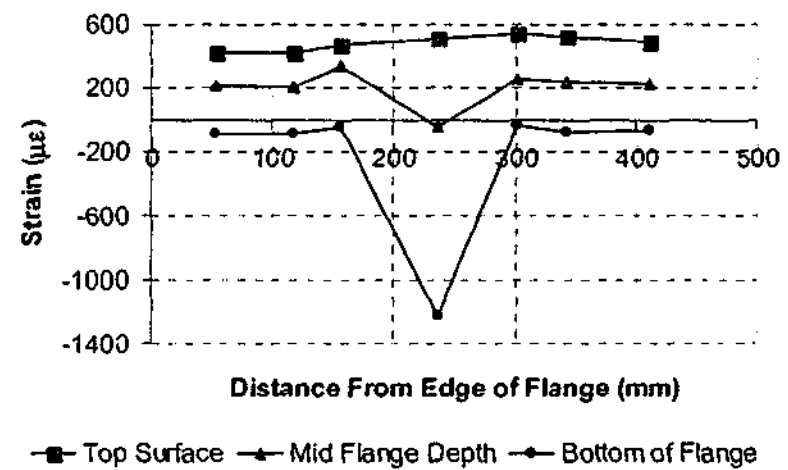


(f) Section A at 120kN

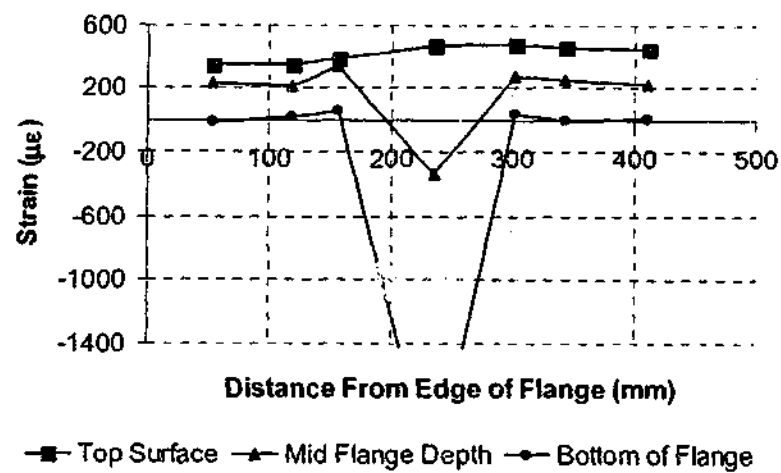


(g) Section A at 140kN

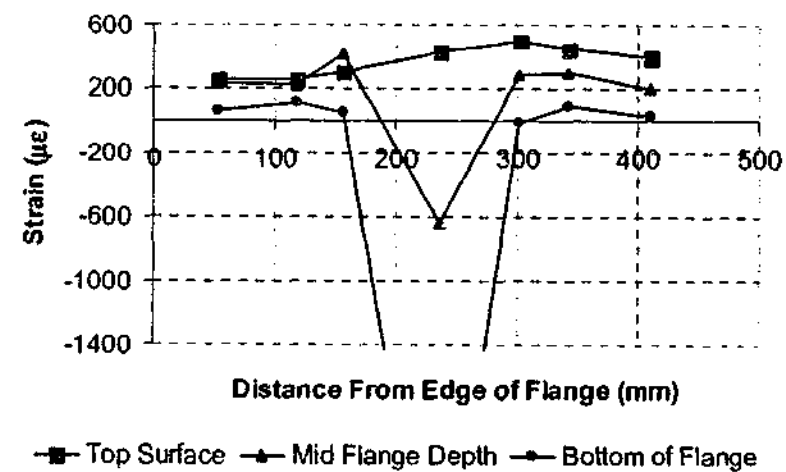
Figure B. 2-1 Continued



(h) Section A at 160kN



(i) Section A at 180kN
Figure B. 2-1 Continued



(j) Section A at 200kN

B.2.2 Section B

From the initial loading stage until a level of applied load of 141kN, the strain on the top surface of the flange at section A can be seen to increase uniformly in magnitude of compressive strain. This is shown for the distribution in Figure B. 2-2 (a) – (g), as well as for the individual gauges in Figure B. 2-3. Beyond this level of load, a reversal of top surface strains begins. Figure B. 2-3 shows that this reversal of strain produces tensile strains on the top surface at a level of load of approximately 175kN. Figure B. 2-2 (i) and (j) show that tensile strains were displayed at all rows across the width of the specimen with the exception of row 2. Strains of magnitude significant enough to produce crack were reached at a level of load of approximately 180kN.

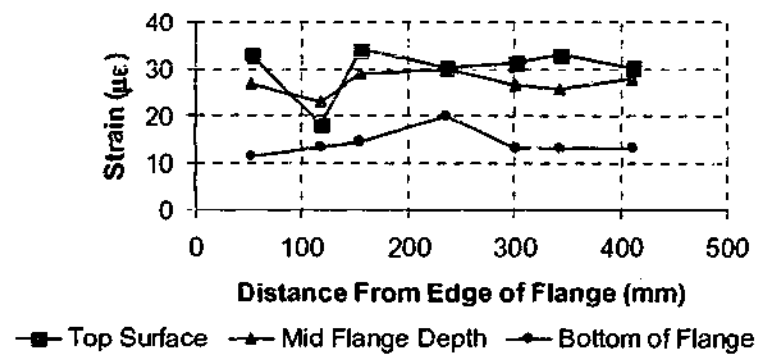
At the early stages of loading on section B, the strain on the underside of the flange is small in magnitude and compressive. This remains so until a level of applied load of 91kN, and is shown in Figure B. 2-2 (a) – (d) and in Figure B. 2-3. Beyond this level of applied load, a reversal in the trend in the magnitude of the strain with the applied load, culminating in the development tensile strains on the underside of the flange at a level of applied load of approximately 100kN (this varied row to row). Figure B. 2-3 shows that the strain on this surface again remains fairly low in magnitude on the flange overhangs, but decreases in magnitude at a slow rate at the centre of width of the web. This trend continued until a level of applied load of 140kN. The variations throughout the width of the specimen showing the local maximum at the centre of the width of the web are shown in Figure B. 2-2 (f) – (g). Beyond a level of applied load of 140kN, the strain on this surface becomes compressive throughout the width of the flange and continues to increase in magnitude until the end of the loading range considered in this discussion. As is shown in Figure B. 2-2 (h) – (j), and in Figure B. 2-3, compressive strains develop throughout the entire width of the specimen on this surface (including at the centre of the width of the web).

It is noted here that as the crack on the top surface (shown in Section 7.2) begins to penetrate the depth of the flange, the compressive strains on the underside of the flange increase. This indicates some vertical redistribution of compressive strains throughout the

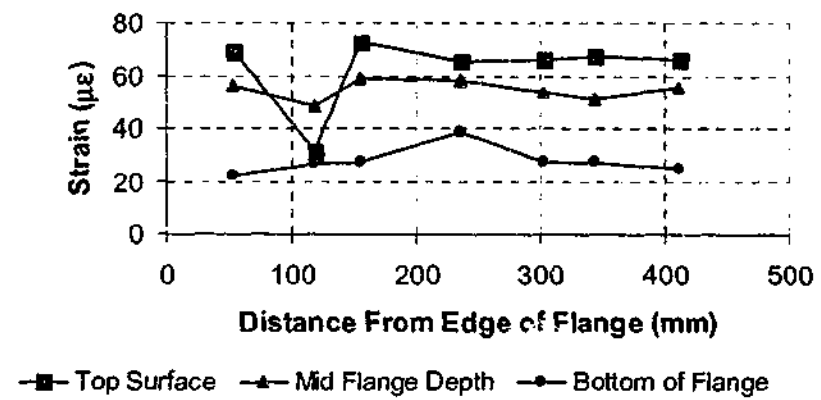
depth of the flange corresponding to the failure mechanism that exhausts the strength of the specimen.

Figure B. 2-3 shows that the strain at the centre of depth of the flange at section B remained in compression throughout the duration of the loading and increased essentially uniformly throughout the experiment until a level of applied load of 140kN. The magnitude of the strain is small only slightly exceeding $200\mu\epsilon$ in the figures shown below. Beyond this level of load, the magnitude of the compressive strain in the flange overhangs can be seen to have decreased, and the strain at the centre of the width of the web can be seen to have increased in compressive magnitude with applied load at a slower rate than prior to this level of applied load. The results shown in Figure B. 2-2 reflect the above distributions across the width of the specimen.

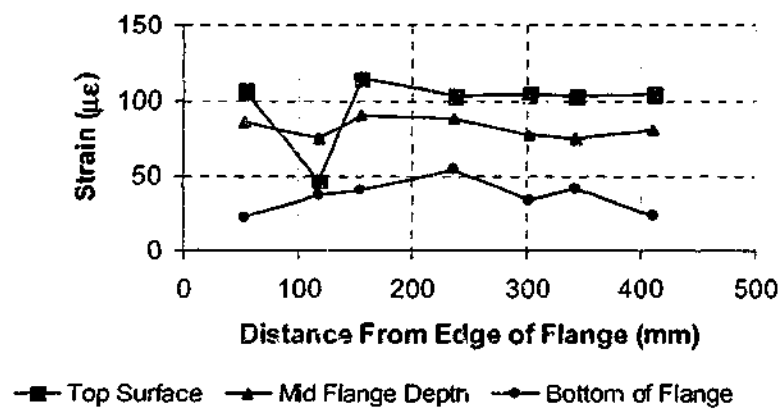
The results from the gauge at row 2 (second row from the left hand edge) on the top surface of the specimen at section B is inconsistent with the other results that are produced. The results from this gauge do not exceed $100\mu\epsilon$. In the early stages of the loading history, it can be seen that the results from this gauge are much lower than the rest at this section. Results from section A, and the remainder of the gauges at section B indicate that the distribution should be constant throughout the width at a low level of load. Since this is not the case, it is assumed that this gauge failed prior to the commencement of the test. The calculations of the shearing forces throughout the width of the flange use a value of strain at this point that is linearly interpolated from adjacent gauges.



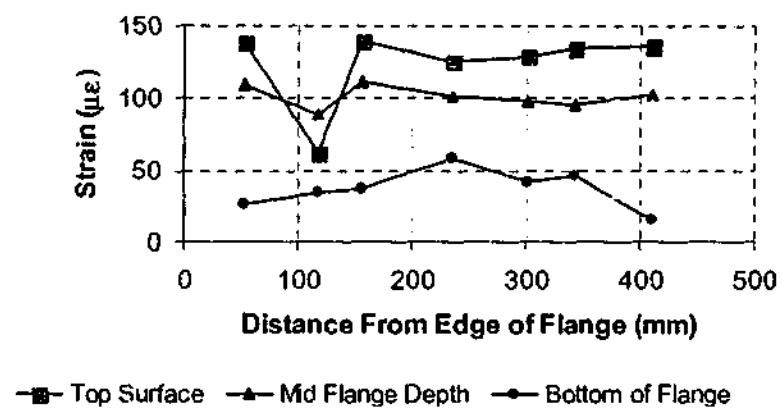
(a) Section B at 20kN



(b) Section B at 40kN

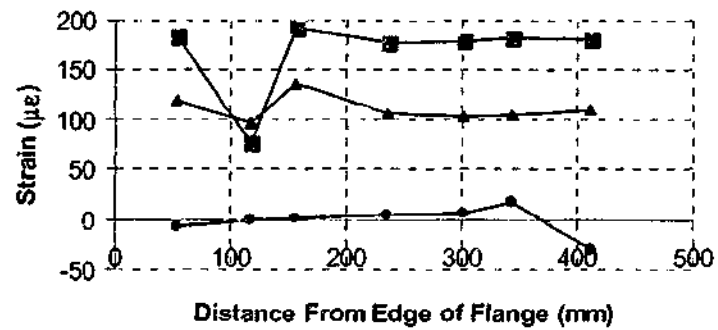


(c) Section B at 60kN



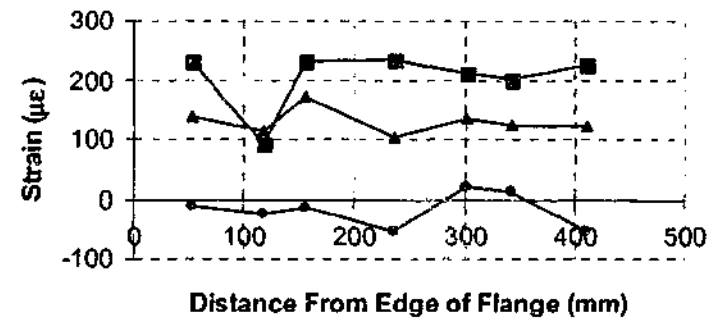
(d) Section B at 80kN

Figure B. 2-2 Distributions of longitudinal strain on section B of specimen B16 at 20kN intervals



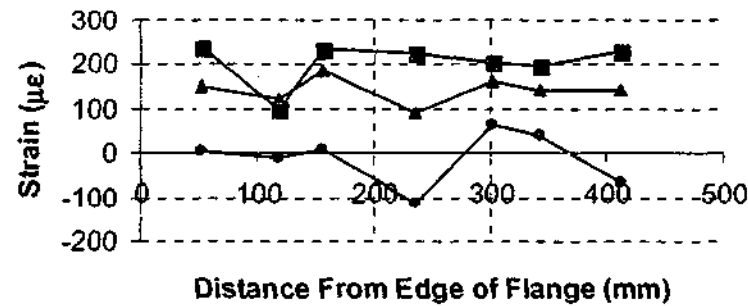
■ Top Surface ▲ Mid Flange Depth ● Bottom of Flange

(e) Section B at 100kN



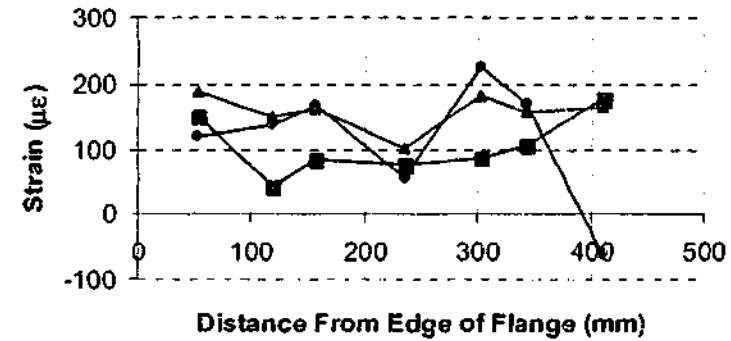
■ Top Surface ▲ Mid Flange Depth ● Bottom of Flange

(f) Section B at 120kN



■ Top Surface ▲ Mid Flange Depth ● Bottom of Flange

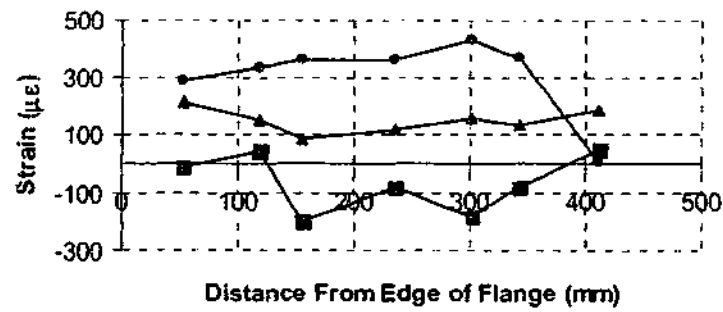
(g) Section B at 140kN



■ Top Surface ▲ Mid Flange Depth ● Bottom of Flange

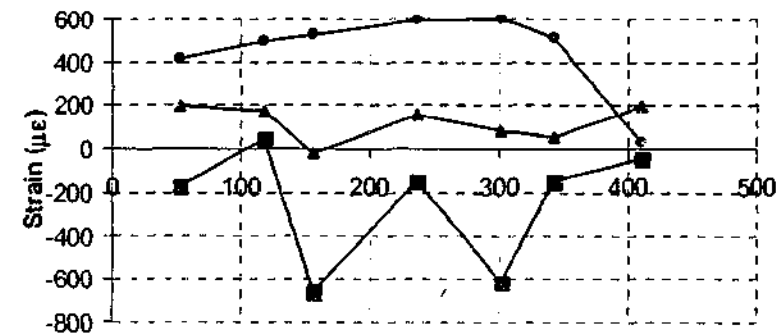
(h) Section B at 160kN

Figure B. 2-2 Continued



■ Top Surface ▲ Mid Flange Depth ● Bottom of Flange

(i) Section B at 180kN
Figure B. 2-2 Continued



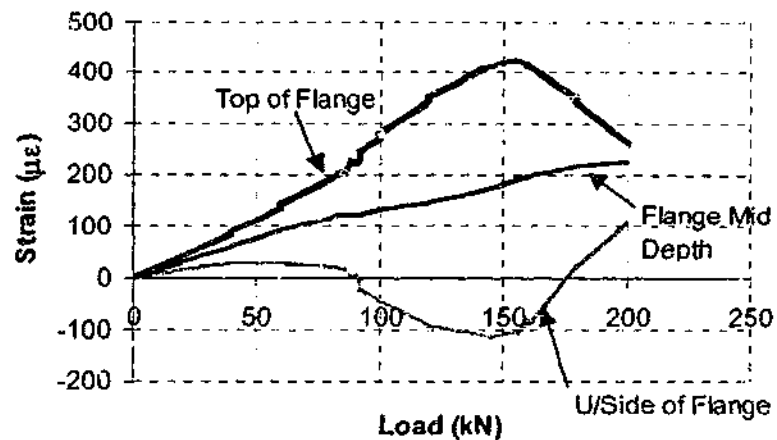
■ Top Surface ▲ Mid Flange Depth ● Bottom of Flange

(j) Section B at 200kN

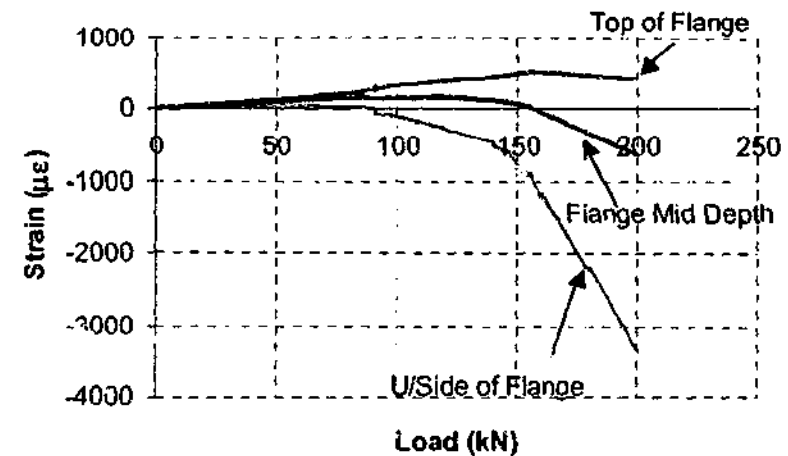
B.2.3 Comparison of Results Between Sections

As the specimen approaches failure, a crack develops on the top surface. The crack intersected the majority of the gauges positioned at section B on this specimen. The formation of this crack is inline with observations made by Hoang (1997) for reinforced concrete, shear critical beams without web reinforcing (as outlined in Section 2.2.3). As this crack develops, the longitudinal compressive strains are redistributed vertically throughout the depth of the flange in this section.

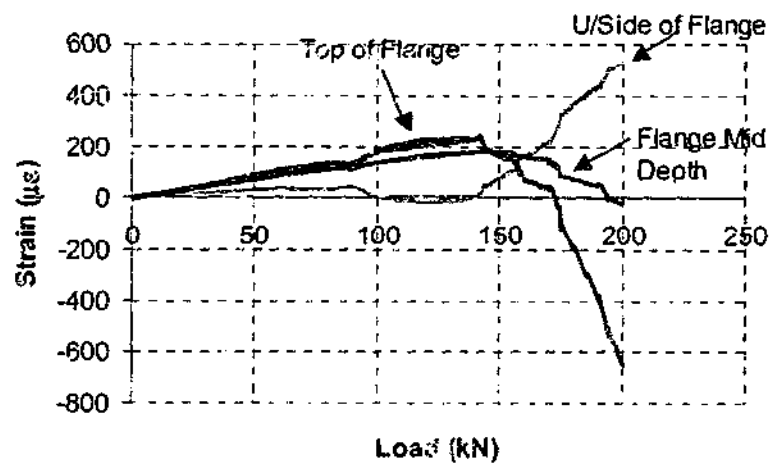
Similarly, the level of strain on the top surface of section A can also be seen to decrease after the initiation of the failure mechanism. This section also shows some redistribution of strain throughout the depth with the gauges on the underside of the flange displaying compressive results after the formation of the crack on the top surface. However, at this section, the level of tensile strain at the centre of the width of the web at the location of the underside of the flange is high. Since this specimen failed in punching shear, the excessive cracking in the web is though to be associated with the formation of the punching cone.



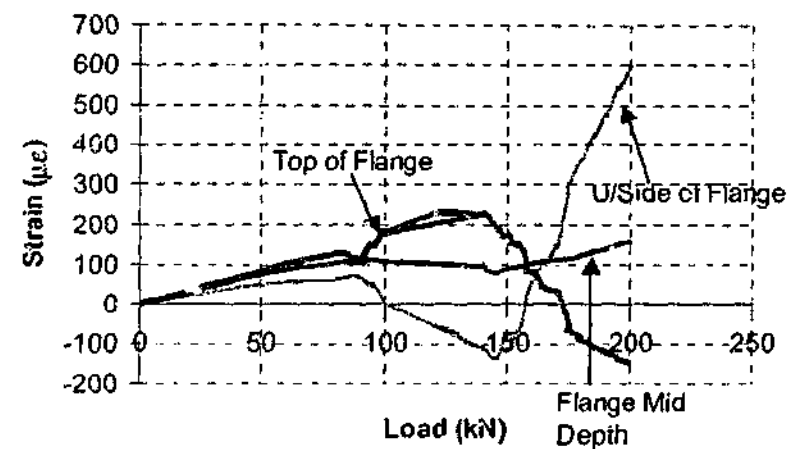
(a) Distribution throughout depth of flange at row 2 at Section A



(b) Distribution throughout depth of flange at row 4 at Section A.



(c) Distribution throughout depth of flange at row 2 at Section B



(d) Distribution throughout depth of flange at row 4 at Section B.

Figure B. 2-3 Variations of distribution of strain throughout the depth of specimen B16 with applied load

B.3 Distribution of Neutral Axis Location and Top Fibre Stresses

Figure B. 3-1 – B. 3-2 show results of calculations of the neutral axis depth, as well as the calculation of the stress on the top surface using the DSFM relations at 20kN intervals. These results are presented at each row throughout the width of the flange in an effort to show the effect that redistributions of strain associated with the formation of the failure mechanism have on the location of the neutral axis within the flange and the web.

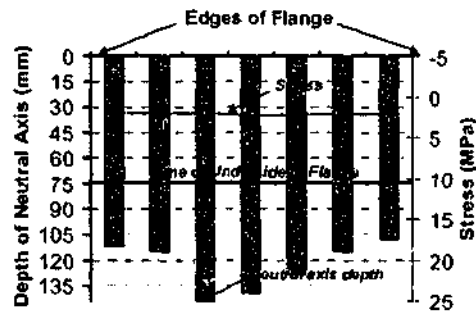
The neutral axis depth was calculated using linear interpolation of the results of the strain at the top and bottom surface of the flange to calculate the depth at which the strain was zero. In positions where gauges failed as a result of cracking at that location, the strain at location of the embedded gauge was used to calculate the location. At the centre of the web, the embedded gauge at the location of the flange web interface was used for this calculation. Values of stress on the top surface of the flange were calculated using the relations of the DSFM as discussed in Section 3.3.1.

B.3.1 Section A

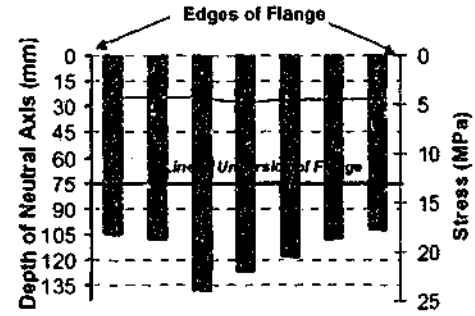
The movements of the neutral axis at section *A*, throughout the loading history considered is consistent with linear elastic theory until the formation of the critical diagonal web crack at an applied load of 91kN. This is shown in Figure B. 3-1 (a)-(d). Prior to this level of load, the trend is for a lower neutral axis depth at the centre of the web, and the remainder of the neutral axis positions at the section (in the flange) are at locations closer to the top surface of the flange. The stress distribution on the top surface at this section until this applied load is in general constant across the width of the flange.

At the level of applied load of 90kN, the neutral axis position suddenly moved up throughout the width of the flange to become closer to the top surface of the concrete. This is reflected by the significant difference in the distributions shown in part (d) and (e) of Figure B. 3-1. Parts (e) – (h) show that as the loading progressed up to a level of load at which the crack on the top surface of the flange formed (approximately 180kN), the level of the neutral axis in the flange remained constant, whereas the depth decreased at the centre of the width of

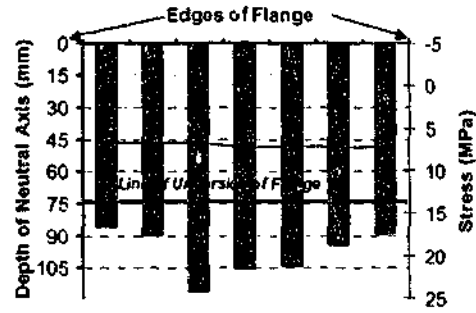
the web. The levels of stress within this range of applied load increased at a fairly uniform rate, and the distribution of compressive stress across the width of the flange did not remain uniform as for previous loading stages, the magnitude of the stresses at rows on the right hand flange overhang were higher than that on the left side flange overhang, but of similar magnitude to those at the centre of width of the web.



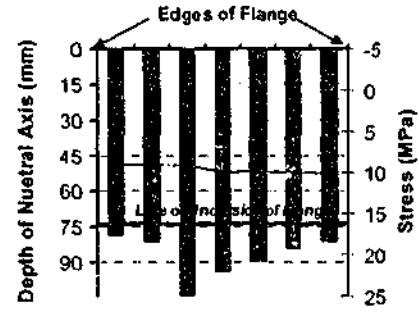
(a) Section A at 20kN



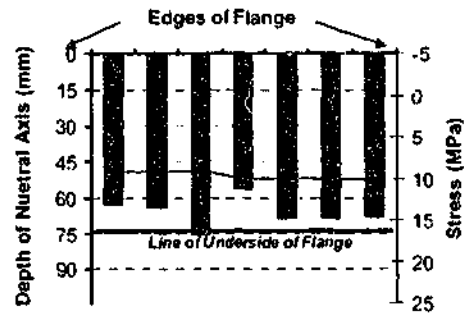
(a) Section A at 40kN



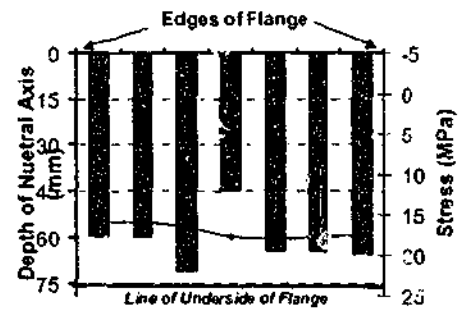
(c) Section A at 60kN



(d) Section A at 80kN

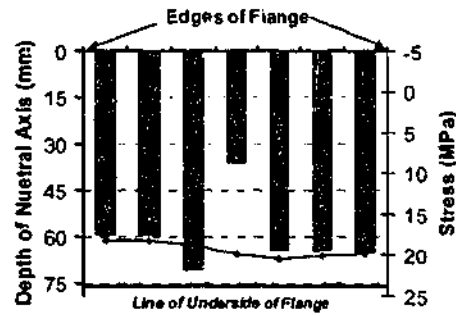


(e) Section A at 100kN

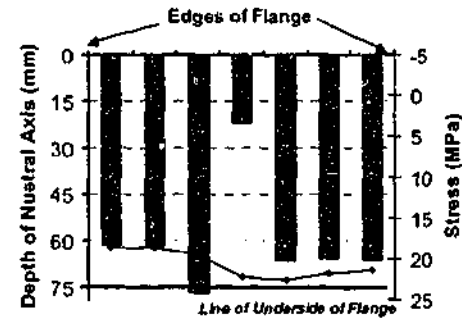


(f) Section A at 120kN

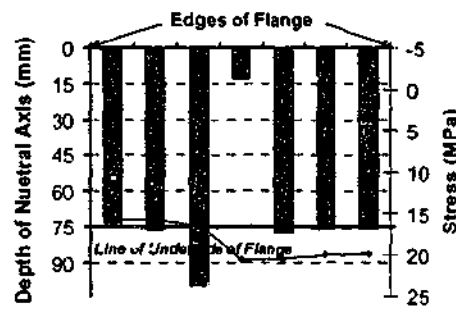
Figure B. 3-1 Distributions of neutral axis and top fibre stress on section A of specimen B16 at 20kN intervals



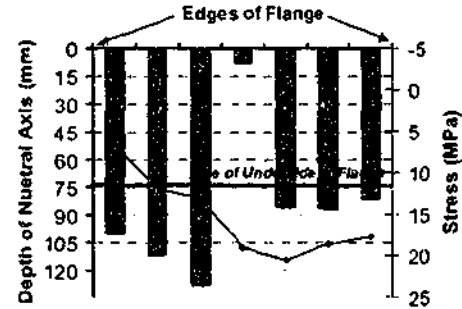
(g) Section A at 140kN



(h) Section A at 160kN



(h) Section A at 180kN



(i) Section A at 200kN

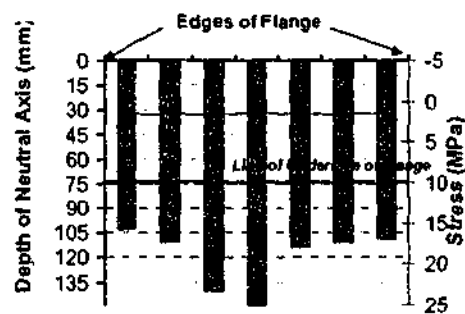
Figure B. 3-1 Continued

B.3.2 Section B

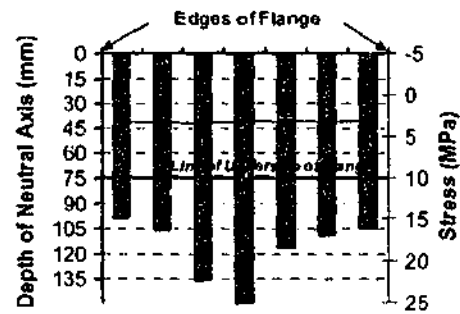
The distributions of the neutral axis across the width of the flange at section B illustrated in Figure B. 3-2 show similar features to the distributions of section A. The maximum depth of neutral axis is at the location of the centre of width of the web until a level of load of 90kN, with the appearance of the critical web crack producing a sharp decrease in the depth of the neutral axis. The latter can be seen by comparison of Figure B. 3-2 (d) and (e). The distribution of compressive stresses on the top surface of the flange throughout this loading range is constant throughout the entire width.

At a level of load of 140kN, the neutral axis depth throughout the entire width of the flange is poorly predicted by the linear interpolation between strains on the top and bottom surface of the concrete. Beyond this loading range, a vertical re-distribution of strains is apparent throughout this section. The tension surface is in the process of switching from being the underside of the flange to being the top of the flange. As this occurs the entire flange is in compression for some ranges of load at which stage the interpolation of strains produces unrealistic results of the depth of the neutral axis. This is seen in Figure B. 3-2 (h).

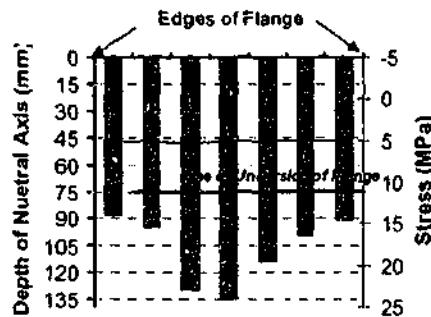
Figure B. 3-2 (i) shows the neutral axis location with the stresses on the top surface of the flange being mostly in tension. This is not the case at the location of the gauge on the outer left hand edge of the specimen, as the tension strains had yet to reach this point in the test. Figure B. 3-2 (j) shows that distribution of the neutral axis depth corresponding to the entire specimen being in tension on the top surface across the width of the flange. The levels of tension stress on the top surface of the specimen at a load level of 200kN are shown to be small in magnitude. This is fairly uniform at high levels of tension strain as the softening limb of the tension stress-strain response described by the DSFM relations is quite gradual.



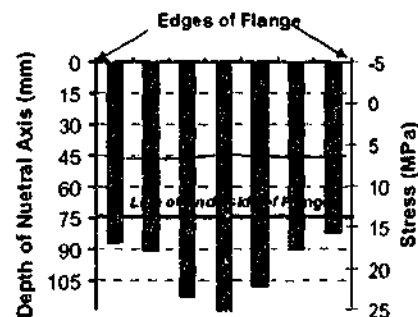
(a) Section B at 20kN



(b) Section B at 40kN

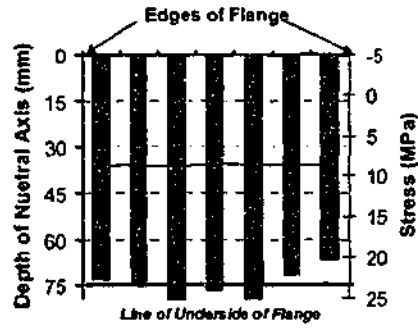


(c) Section B at 60kN

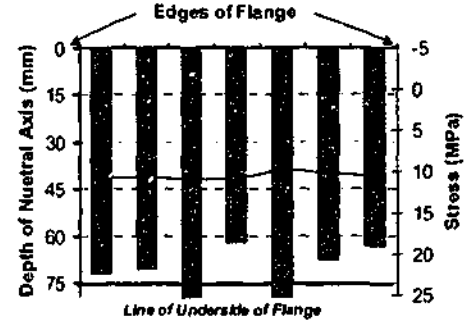


(d) Section B at 80kN

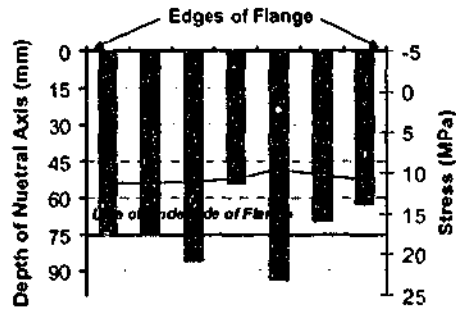
Figure B. 3-2 Distributions of neutral axis on section A of specimen B16 at 20kN intervals



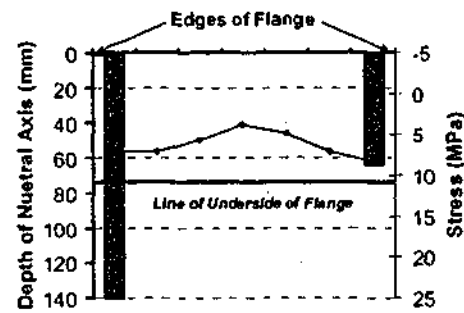
(e) Section B at 100kN



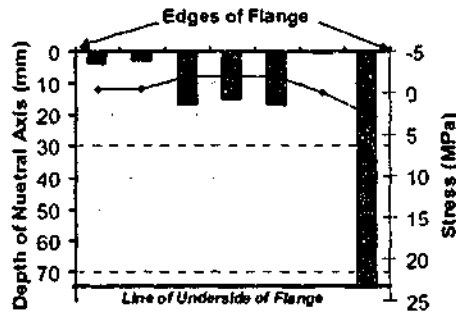
(f) Section B at 120kN



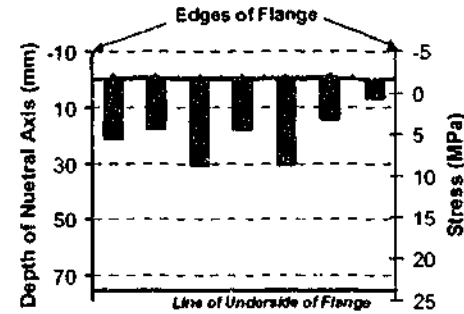
(g) Section B at 140kN



(h) Section B at 160kN



(i) Section B at 180kN



(j) Section B at 200kN

Figure B. 3-2 Continued

B.3.3 Comparison of Results Between Sections

It is apparent from the above analysis that the formation of the failure mechanism results in substantial redistributions of compressive stress throughout the specimen at section A. After the formation of the critical diagonal web crack, the depth of the neutral axis at this section decreased at the centre of width of the specimen while the distribution of compressive stresses across the width of the flange remained fairly constant. This suggests that the flange region is carrying more compression force than the web region. Therefore, there is a lateral redistribution of compressive stresses into the flange following the formation of the critical shear crack.

As discussed in section B.2.3, the formation of the lateral crack on the top surface of the flange also initiates a redistribution of stresses. This redistribution is a vertical redistribution with the compressive stresses of the flange at this section moving from being on the top surface of the flange to being the bottom surface of the flange.

Appendix C LONGITUDINAL STRAINS, REDISTRIBUTIONS AND THE FAILURE MECHANISM OF SPECIMEN B17

C.1 Introduction

This appendix is intended to show the process of analysis of longitudinal strain results that was undertaken to determine the redistributions of strain that occurred throughout the loading history, and the effect that these redistributions had on the distribution of compression actions throughout the width of the flange. Several stages of the failure mechanism have been outlined for this specimen in Chapter 7, this appendix shows the relationship of these stages with the longitudinal strain distributions obtained from the experimental procedure.

This appendix presents the results of the strain gauges, results of the calculation of neutral axis depth and top fibre stress, as well as a discussion of the stages of strain redistribution associated with the formation of the failure mechanism that significantly influenced the effectiveness of the flange in the resistance of shear. This appendix uses some notation that was defined in Chapter 3. Figure C. 2-1 outlines the relevant definitions.

C.2 Distribution of Longitudinal Strains

The results of strain gauging in the longitudinal direction at two sections can be seen in Figure C. 2-2 – C.2-4. These results are presented as distributions of strain throughout the

width and depth of the flange. Figure C. 2-2 shows the distribution of strains across the width of the flange at three locations throughout the depth at section A, Figure C. 2-3 shows the same distributions at section B, and Figure C. 2-4 shows the distribution of strain throughout the depth of the flange at section A and B in the web (row 4), and at one location in the flange that is representative of the behaviour exhibited at each row in the flange of the specimen (row 2). The illustrations in Figure C. 2-2 – C.2-2 show the distribution of strain across the width of the flange at 20kN load increments at the top of the flange, centre of depth of the flange, and on the underside of the flange. Linear interpolation was used to generate results that are equidistant across the width of the flange, and also to generate strains exactly at the centre of the depth. The process of the linear interpolation used is outlined in Appendix F. The convention of a positive strain representing a compression strain is again used in the analysis of this specimen.

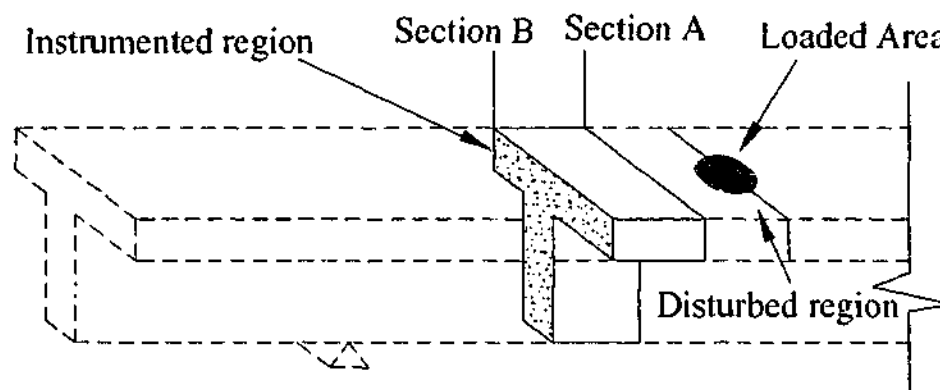


Figure C. 2-1 Identification of Section A and Section B

These results have been shown at 20kN increments to be consistent the analysis of specimen B16. The discussion that follows will focus on the redistribution of longitudinal strain profiles throughout the width and the depth of the flange, the movement of the neutral axis throughout the application of load to the specimen, and the variations in stress on the top surface of the specimen throughout the experiment. All strain gauges remained intact throughout the entire duration of the test, allowing analysis of strains and calculated stresses and neutral axis positions to be considered at all levels of load. This discussion considers strain gauging results, and subsequent calculations, until the peak load of $P=238\text{kN}$. The notation of sections used in these figures is similar to that in Chapter

C.2.1 Section A

The strain distribution on the top surface of the flange shown in Figure C. 2-2 remained essentially uniform across the width of the flange until a level of applied load of 140kN (refer part (a) – (g) of this figure). Beyond this level of load, it is apparent that more compressive strain was in the right side flange overhang. PartS (k) and (l) of Figure C. 2-2 indicate that a significant reduction in the magnitude of the strain occurred at the centre of the web, relative to the flanges, as the load on the specimen approached the peak load.

The rate of increase in the magnitude of the compressive strains on this surface was uniform until a load level of 120kN as illustrated in Figure C. 2-4 (a) and (b). At a level of applied load of 120kN, a sudden small decrease in the magnitude of the strain on this surface occurred. This decrease was sudden, and was followed by a redistribution that prevailed within a load range of 120-140kN as shown in this figure. Beyond this value of load, the rate of increase again continued at a constant rate, but a lesser rate than before this load level. The increase continued until a level of load of 212kN when another sharp decrease occurred, accompanying the formation of the critical diagonal web crack.

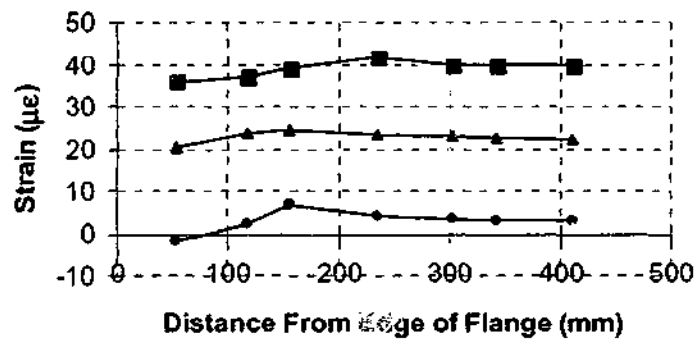
The first two load increments in Figure C. 2-2 shows that an even distribution across the width of the flange of compression strain at the centre of the depth prevailed. Between levels of applied load of 60-200kN, the strain at the centre of width of the flange was lower than that in the flanges. This is most likely due to the influence of a flexural crack that was at this location in the web. This distribution across the width of the flange was consistent until near the peak load. Parts (k) and (l) of Figure C. 2-2 show an even distribution across the entire width of the specimen followed the formation of the critical diagonal web crack.

Figure C. 2-4 shows that the rate of increase of compressive strain in row 2, and at row 4 with the applied load was constant until a level of applied load of 120kN. Between levels of applied load of 120-140kN, there was a redistribution of strain throughout the depth of the flange that caused a sudden drop in the magnitude of the strain at the centre of depth of the flange. As shown in Figure C. 2-4 (a) and (b), this was most significant in the web region (at

row 4). Beyond the level of load of 140kN, the rate of increase of the compressive strain at each location remained constant.

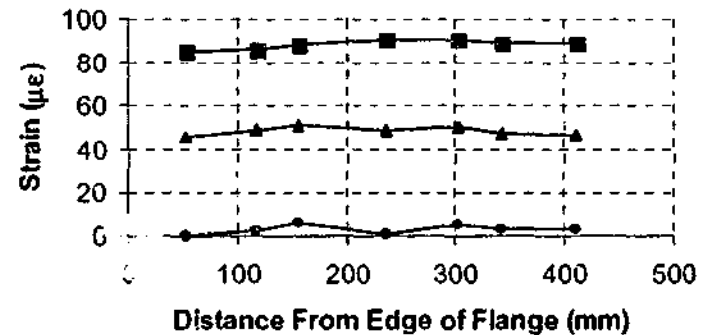
The strains on the underside of the flange at this section remained close to zero until a level of applied load of 44kN. From this level of load until a level of applied load of 120kN, tension strains developed on this row of gauges, increasing at a uniform rate with the loading, with the maximum tension strain being at the centre of the web. This is illustrated in part (c)-(f) of Figure C. 2-2. The distribution of these strains across the width of the specimen was constant in the flanges, and at a maximum tensile magnitude in the web. At a level of load of 212kN, the strains in the flange rapidly reduced to magnitude of approximately zero, and the strain in the web became compressive.

The distribution of strain throughout the depth shown in Figure C. 2-4 (a) – (b) shows that a constant increase in the magnitude of the tensile strain in the flanges and the web prevailed until a magnitude of applied load of 120kN. At a level of applied load of 120kN, a sudden reversal of trend of strain increase with load on the underside of the flange occurred. This reversal occurred between levels of applied load of 120-140kN. Following this sudden reversal, the specimen, as shown in this figure, displayed a uniform decrease in magnitude of the tension strain. This uniform rate of decrease continued until a level of applied load of 212kN, when a sudden decrease in magnitude of the tensile strain on the underside of the flange occurred, resulting in small compression strains at this row of gauges. This sudden reversal accompanied the sudden appearance of the diagonal web crack.



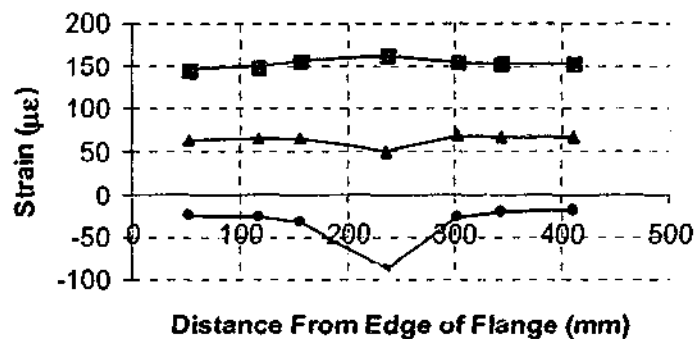
■ Top Surface ▲ Mid Flange Depth ● Bottom of Flange

(a) Section A at 20kN



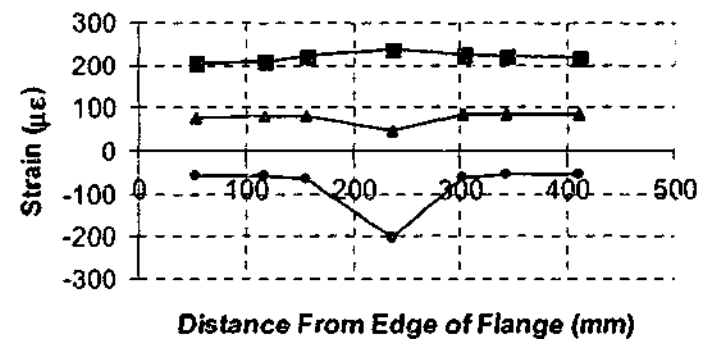
■ Top Surface ▲ Mid Flange Depth ● Bottom of Flange

(b) Section A at 40kN



■ Top Surface ▲ Mid Flange Depth ● Bottom of Flange

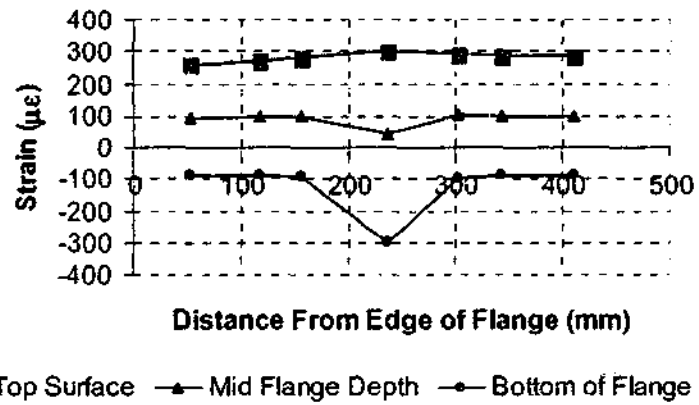
(c) Section A at 60kN



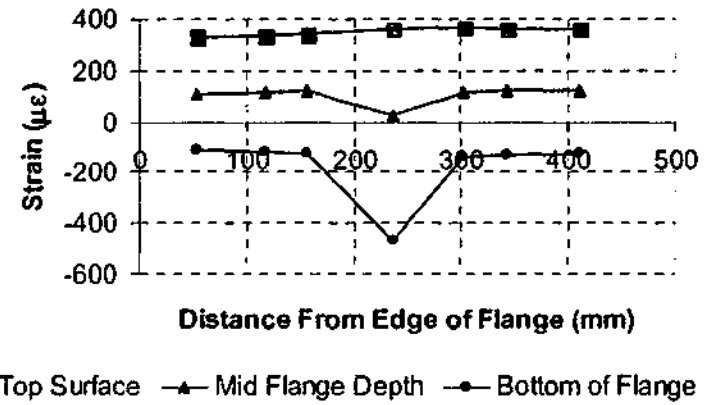
■ Top Surface ▲ Mid Flange Depth ● Bottom of Flange

(d) Section A at 80kN

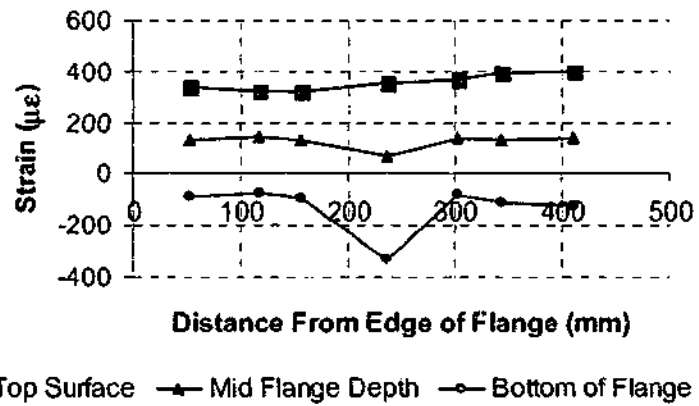
Figure C. 2-2 Distributions of longitudinal strain on section A of specimen B17 at 20kN intervals



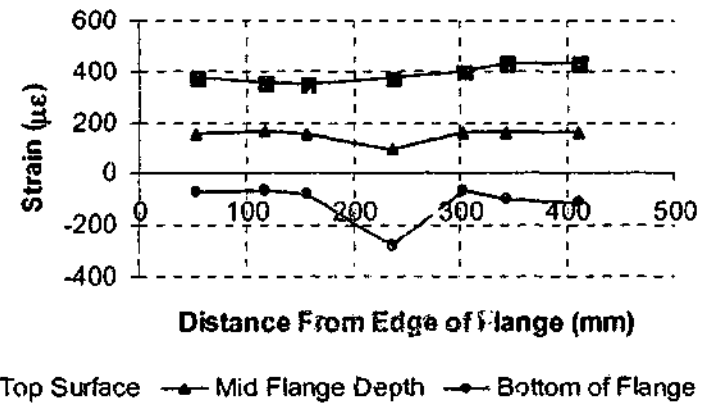
(e) Section A at 100kN



(f) Section A at 120kN

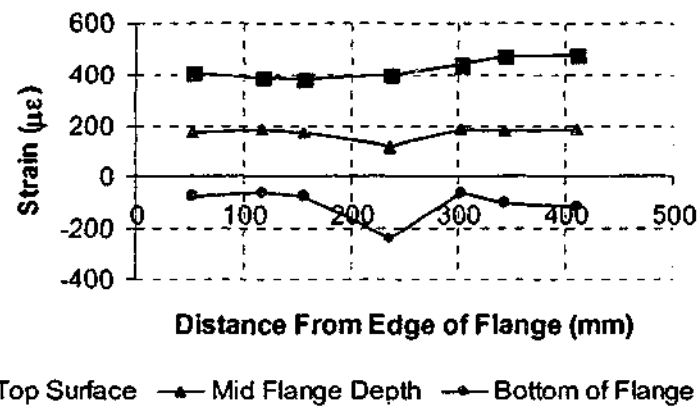


(g) Section A at 140kN

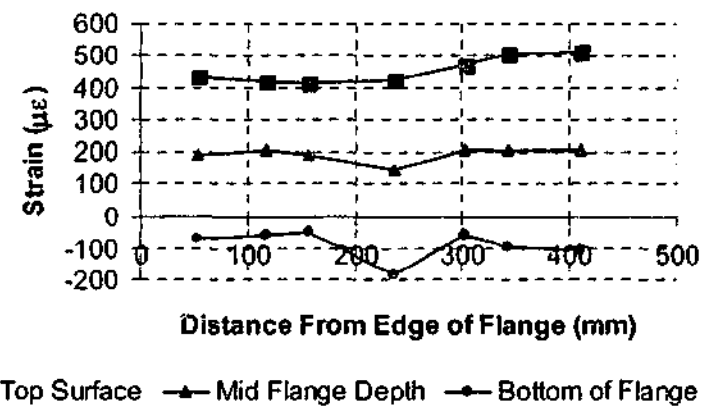


(h) Section A at 160kN

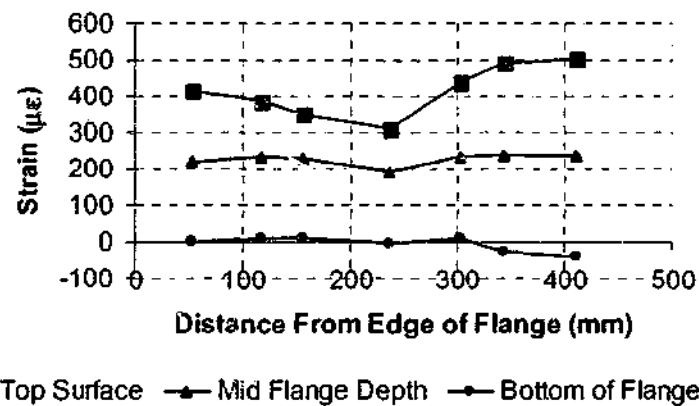
Figure C. 2-1 Continued



(i) Section A at 180kN

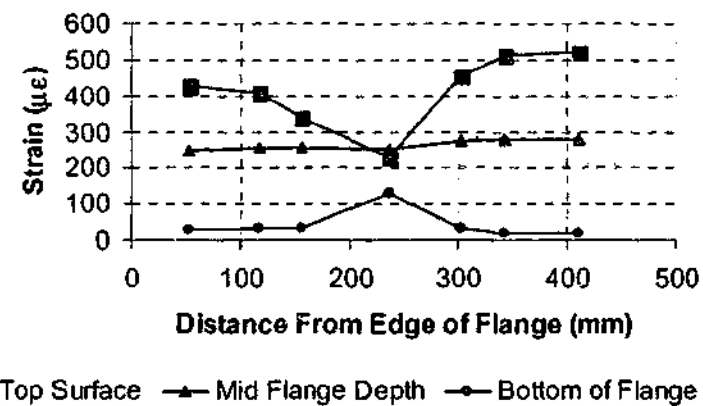


(j) Section A at 200kN



(k) Section A at 220kN

Figure C. 2-1 Continued



(l) Section A at 238kN

C.2.2 Section B

Figure C. 2-3 shows that the distribution of compression strains across the width of the flange at section B is similar to that of section A. The distribution remains essentially uniform across the width of the flange until a level of applied load of 140kN (refer part (a) – (g) of this figure). Beyond this level of load, it is apparent that more compressive strain was in the right side flange overhang. Part (k) and (l) of Figure C. 2-3 indicates that a significant reduction in the magnitude of the strain occurred at the centre of the web, relative to the flanges, as the load on the specimen approached the peak load. This reduction in strain occurred at a level of applied load of 212kN, corresponding to the formation of the critical diagonal web crack.

The variation throughout the depth of the top surface strain with the applied load was also similar at section B to that at section A. Figure C. 2-4 (c) and (d) shows that the rate of increase in the magnitude of the compressive strains on this surface was uniform until a load level of 120kN. At a level of applied load of 120kN, a sudden small decrease in the magnitude of the strain on this surface occurred. This decrease was followed by a redistribution that occurred between applied load levels of 120-140kN as shown in these figures. Beyond this value of load, the rate of increase again continued at a constant rate, this was at a much lower rate than that preceding the redistribution, almost constant. The increase continued until a level of load of 212kN when another sharp decrease occurred, accompanying the formation of the critical diagonal web crack.

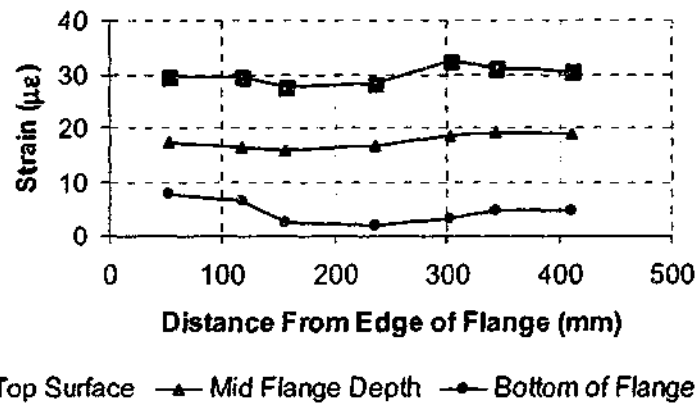
Figure C. 2-3 shows an even distribution of compression strain at the centre of depth of the flange across the width of the flange until a level of applied load of 85kN, this is reflected in part (a) –(d) of this figure. Beyond this level of applied load, the strain at the centre of the web decreased slightly, most probably due to the influence of flexural cracking in the specimen. This distribution across the width essentially remained constant until failure.

Figure C. 2-4 (c) and (d) shows that the rate of increase of compressive strain in row 2 and at row 4 with the applied load is constant until a level of applied load of 120kN. A very small redistribution of strains that occurred between levels of applied load of 120-140kN is evident in these figures. This was much less significant than that at section A, but did occur.

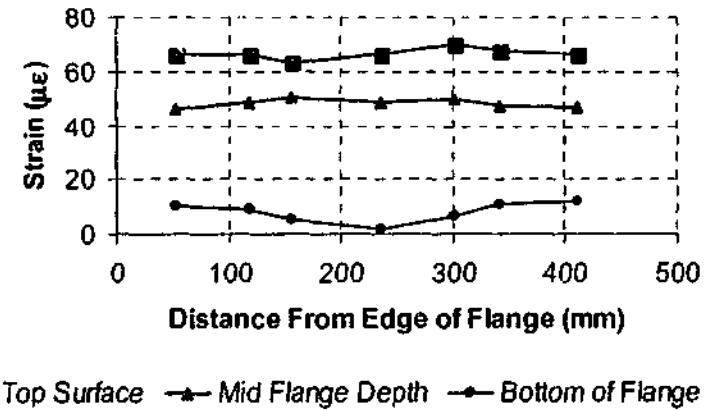
Beyond the level of load of 140kN, the rate of increase of the compressive strain at each location remained constant, and equal in gradient to that prior to the redistribution. There was a sudden decrease in the magnitude of the strain at the centre of the depth of the flange at a level of applied load of 235kN. This can be most clearly seen by comparing Figure C. 2-3 (k) and (l).

The strains on the underside of the flange at this section remained close to zero until a level of applied load of 67kN. Beyond this level of applied load (as shown in Figure C. 2-3 (d) – (k)), the strain at the centre of the web became tensile, and increased in magnitude, while the strains on the underside of the flange remained close to zero. This trend remained constant until a level of applied load of 212kN, where a sudden shift in the strains throughout the entire width on this surface occurred. The strain on the soffit of the flange became compressive, and the magnitude of the tensile strain at the centre of the web decreased sharply. This is illustrated in part (k)-(l) of Figure C. 2-3.

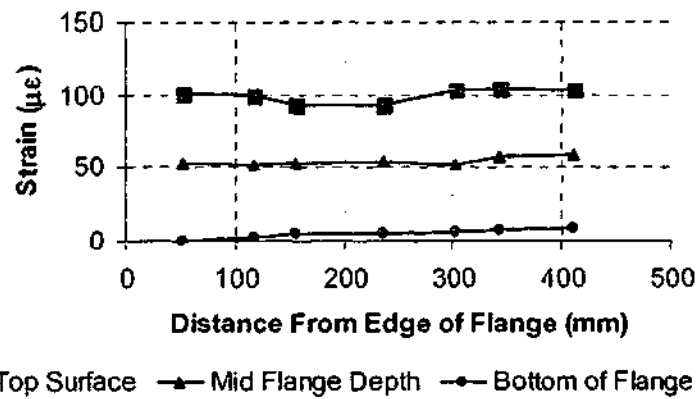
The distribution of strain throughout the depth shown in Figure C. 2-4 (c) – (d) indicates that a constant increase in the magnitude of the tensile strain in the flanges, and the web prevailed with a range of applied load of 67 - 120kN. At a level of applied load of 120kN, a sudden reversal of trend in strain increase on the underside of the flange occurred. This reversal occurred between levels of applied load of 120-140kN. Following this sudden reversal, the specimen, as shown in this figure, displayed a uniform decrease in magnitude of the tension strain. This uniform rate of decrease continued until a level of applied load of 212kN, when a sudden decrease in magnitude of the tensile strain on the underside of the flange occurred, resulting in compression strains at this row of gauges. This sudden reversal accompanied the sudden appearance of the diagonal web crack. It is noted that compression strains on the underside of the flange developed at a level of load of 173kN as shown in Figure C. 2-4 (c).



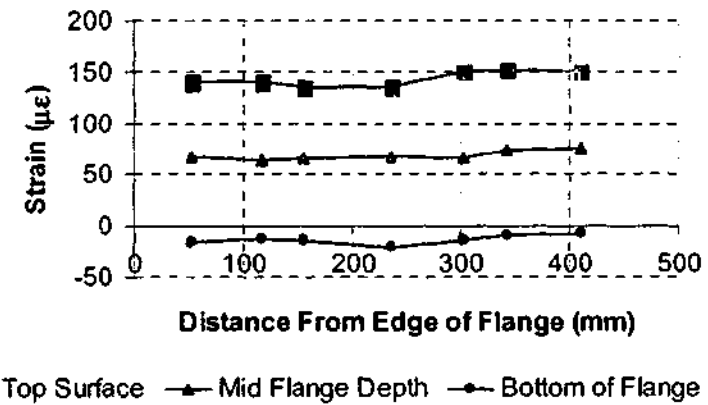
(a) Section B at 20kN



(b) Section B at 40kN

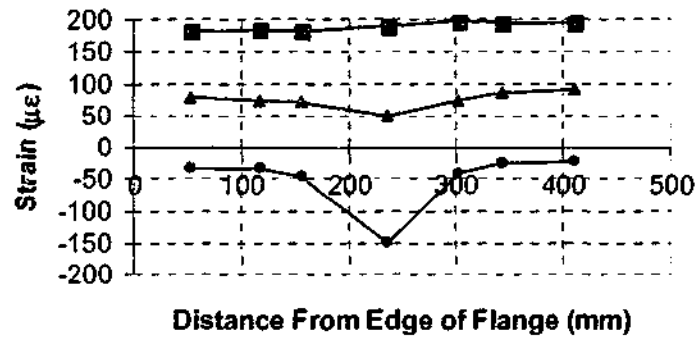


(c) Section B at 60kN



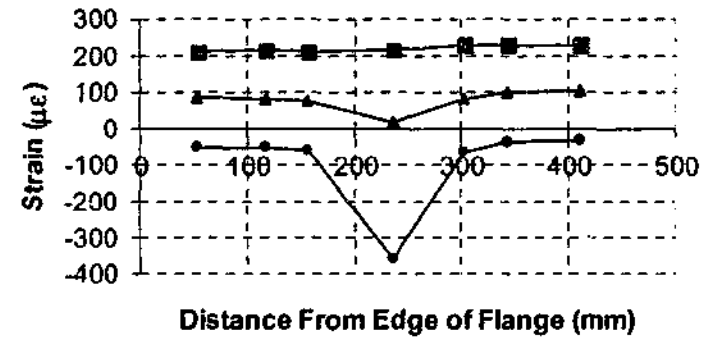
(d) Section B at 80kN

Figure C. 2-3 Distributions of longitudinal strain on section B of specimen B17 at 20kN interval



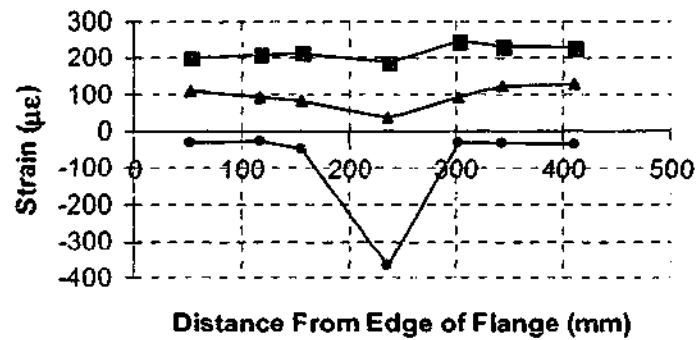
■ Top Surface ▲ Mid Flange Depth ● Bottom of Flange

(e) Section B at 100kN



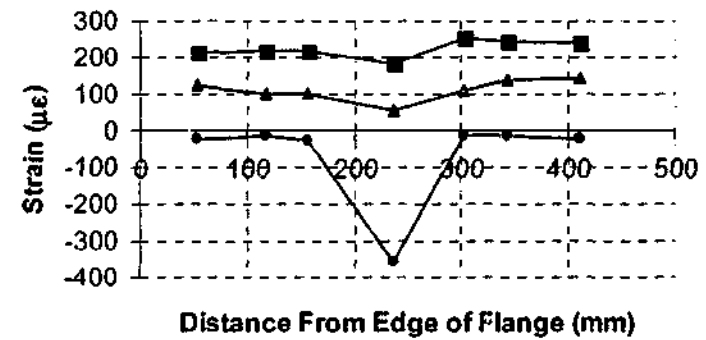
■ Top Surface ▲ Mid Flange Depth ● Bottom of Flange

(f) Section B at 120kN



■ Top Surface ▲ Mid Flange Depth ● Bottom of Flange

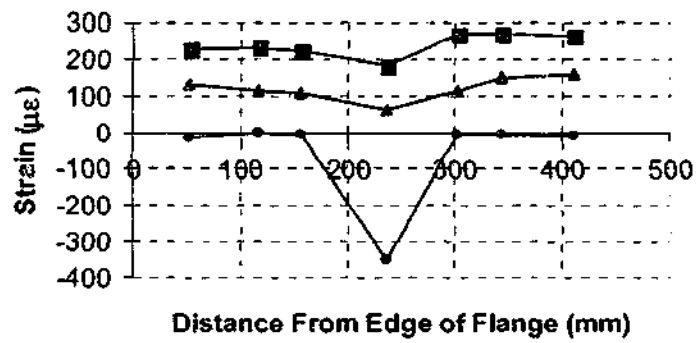
(g) Section B at 140kN



■ Top Surface ▲ Mid Flange Depth ● Bottom of Flange

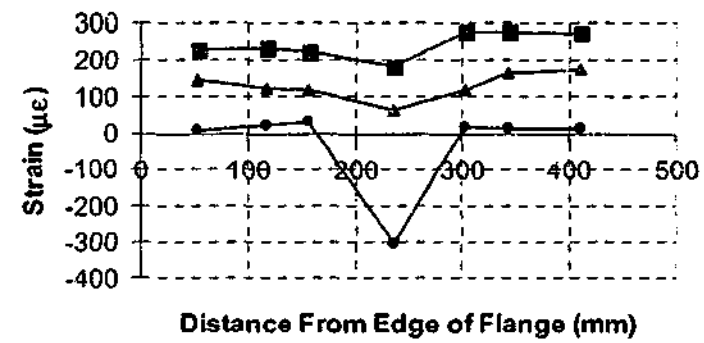
(h) Section B at 160kN

Figure C. 2-2 Continued



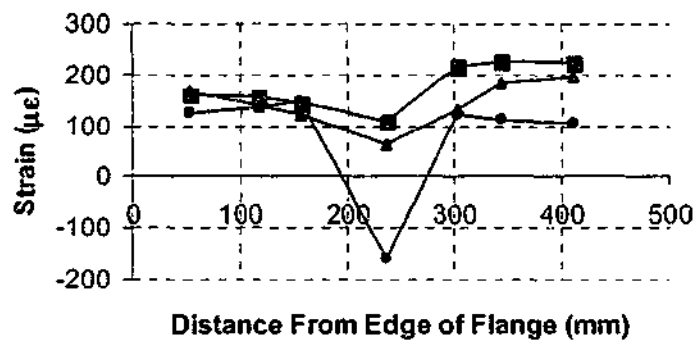
■ Top Surface ▲ Mid Flange Depth ● Bottom of Flange

(h) Section B at 180kN



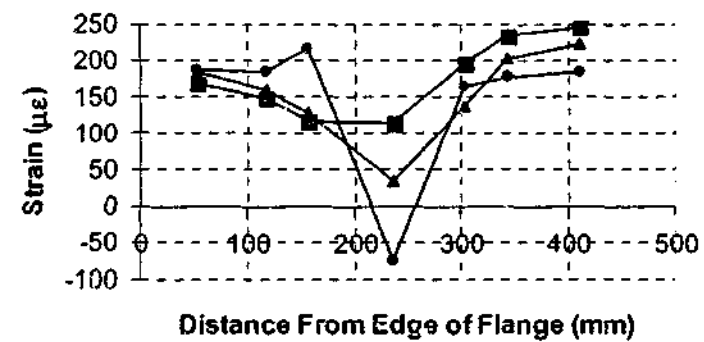
■ Top Surface ▲ Mid Flange Depth ● Bottom of Flange

(j) Section B at 200kN



■ Top Surface ▲ Mid Flange Depth ● Bottom of Flange

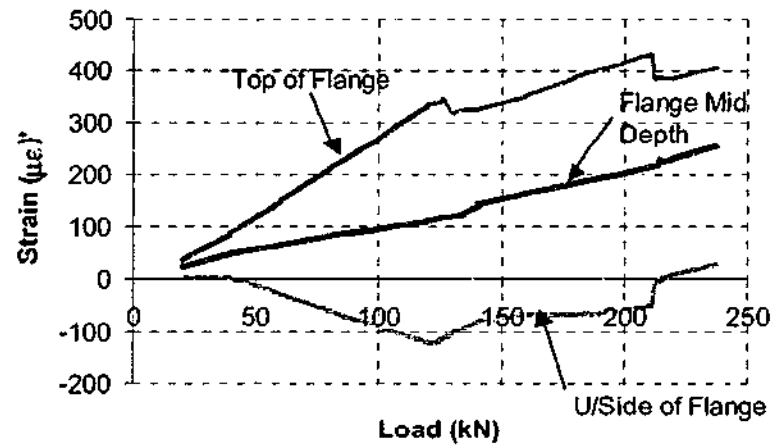
(k) Section B at 220kN



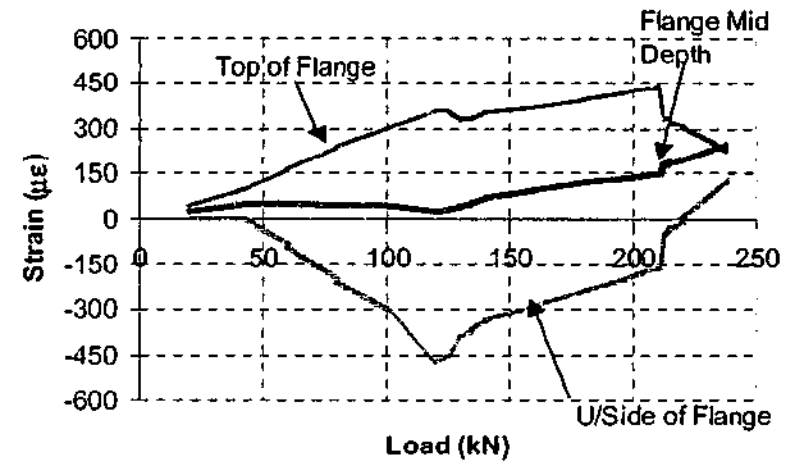
■ Top Surface ▲ Mid Flange Depth ● Bottom of Flange

(l) Section B at 238kN

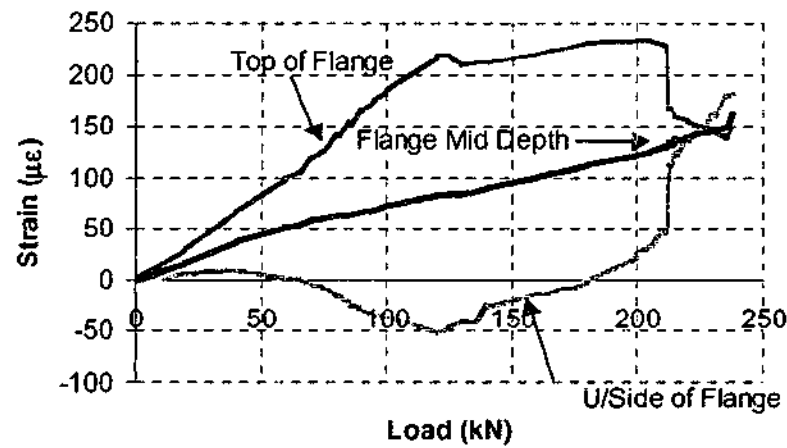
Figure C. 2-2 Continued



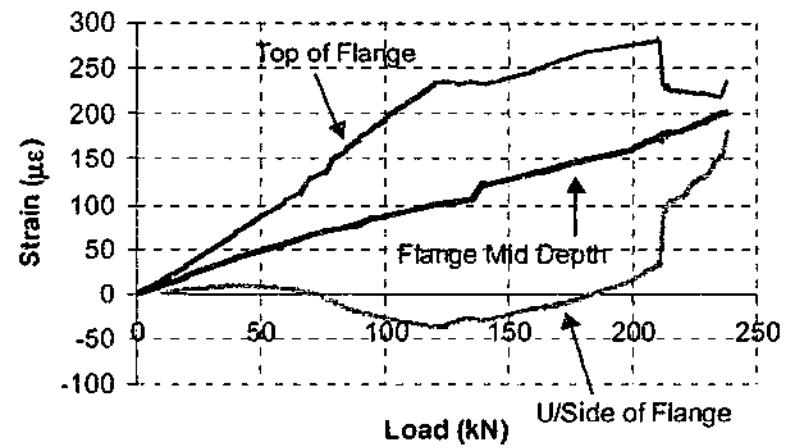
(a) Distribution throughout depth of flange at row 2 Section A



(b) Distribution throughout depth of flange at row 4 at Section A



(c) Distribution throughout depth of flange at row 2 at Section B



(d) Distribution throughout depth of flange at row 4 at Section B

Figure C. 2-4 Variations of distribution of strain throughout the depth of specimen B17 with applied load.

C.3 Distribution of Neutral Axis Location

Figure C. 3-1– C. 31-4 show results of calculations of the neutral axis depth, as well as the calculation of the stress on the top surface using the DSFM relations at 20kN intervals. These results are presented at each row throughout the width of the flange in an effort to show that effect that redistributions of strain associated with the formation of components of the failure mechanism have on the location of the neutral axis within the flange and the web.

The neutral axis depth was calculated using linear interpolation of the results of the strain at the top and bottom surface of the flange to calculate the depth from the top surface of the specimen at which the strain was zero. At the centre of the web, the embedded gauge at the location of the flange web interface was used for this calculation. Values of stress on the top surface of the flange were calculated using the relations of the DSFM as stated in Chapter 3.

C.3.1 Section A

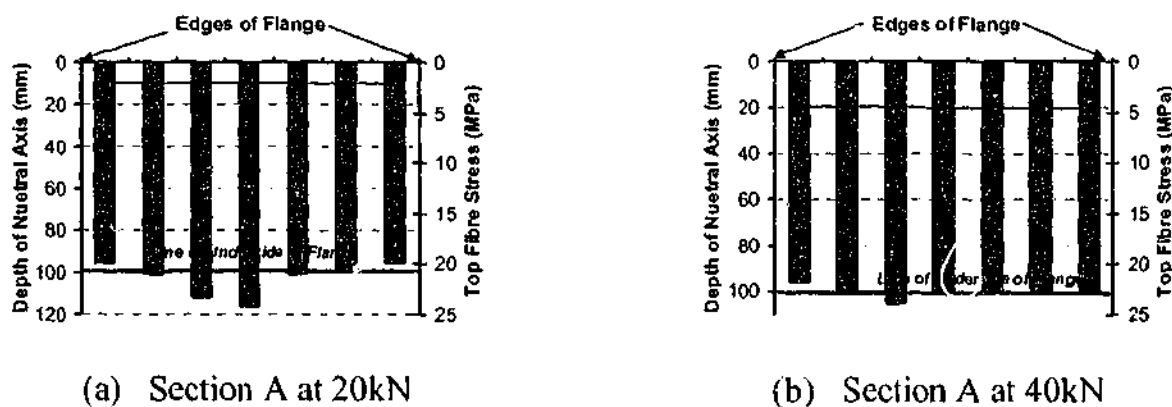
Figure C. 3-1 (a) shows a distribution of neutral axis that is consistent with that given by linear elastic theory. This profile was consistent from the start of the loading on the specimen until a level of load of 30kN. Between applied load levels of 30kN and 86kN, the neutral axis decreased in depth throughout the entire width of the specimen, including at the centre of width of the web. Figure C. 3-1 (b)-(d) show this trend. The applied load of 86kN marked the appearance of the second diagonal web crack.

From a level of applied load of 86kN, and until 120kN (corresponding to the reversal of strain on the bottom surface of the flange), the rate of decrease of the depth of the neutral axis with applied load decreased significantly. This is shown in Figure C. 3-1 (e)-(f). The level of applied load of 120kN marked a reversal of the movement of the neutral axis. With the reversal of the strain gradient on the underside of the flange, the neutral axis began to move away from the top of the flange of the specimen at a slow rate (this can be seen in Figure C. 3-1 (f)-(j)). At a level of applied load of 212kN (the load level at which the critical

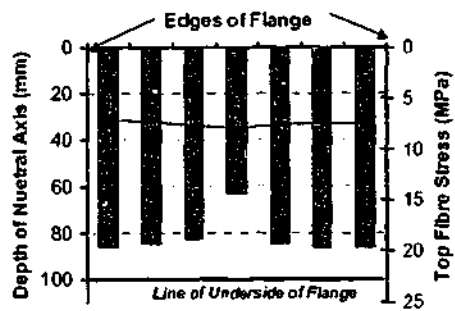
diagonal web crack formed), this trend ceased, and the position of the neutral axis sharply moved away from the top surface of the flange. An indication of the magnitude of this movement is given by comparing Figure C. 3-1 (j) and (k). Beyond the level of applied load of 212kN, and after this sudden shift, the neutral axis continued its movement deeper into the flange of the specimen.

The distribution of stresses across the top surface of the flange remained essentially constant throughout the range of loading until a level of applied load of 212kN. It is noted that similar to the strain distribution, the level of compressive stress is higher in the right side flange overhang beyond a level of applied load of 140kN. Following the formation of the critical diagonal web crack, the stress at the centre of the width of the web was significantly lower in magnitude than that in the flange overhangs.

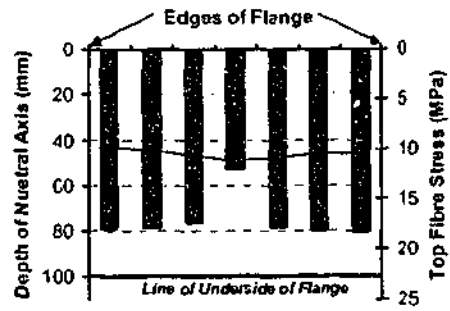
Coupled with the effect of a deeper neutral axis in the flange than in the web, the fact that the stresses are higher in the flanges than in the web indicates that as the failure mechanism formed, there was a tendency for the specimen to shed compressive forces into the flange region. These redistributions are highlighted by components of the mechanism forming as the load progressed.



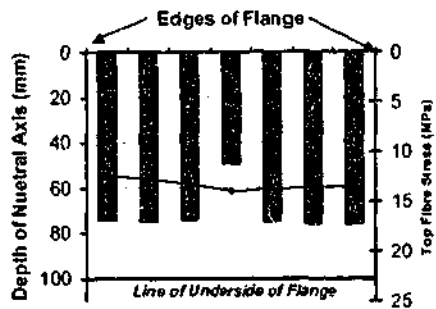
(a) Section A at 20kN (b) Section A at 40kN
 Figure C. 3-1 Distributions of neutral axis on section A of specimen B17 at 20kN intervals



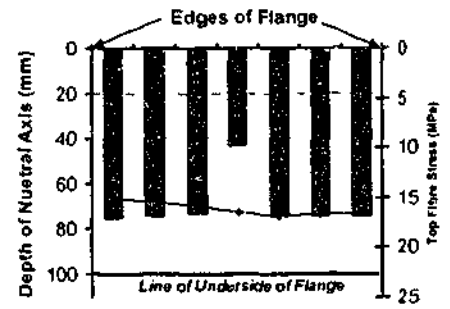
(c) Section A at 60kN



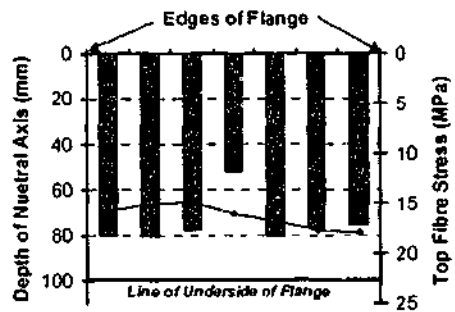
(d) Section A at 80kN



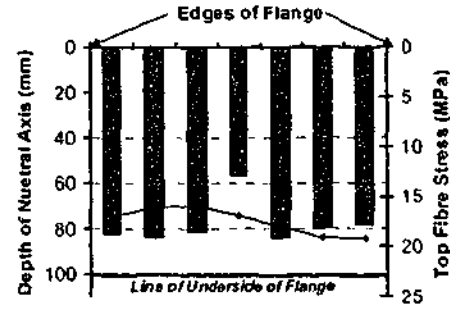
(e) Section A at 100kN



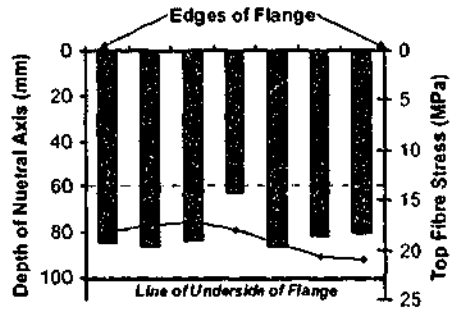
(f) Section A at 120kN



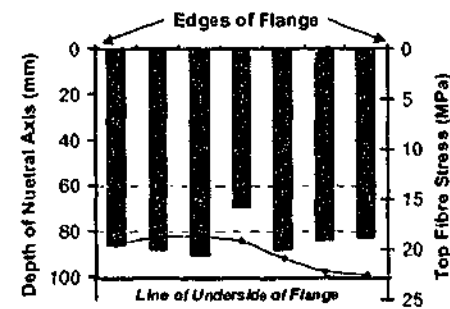
(g) Section A at 140kN



(h) Section A at 160kN

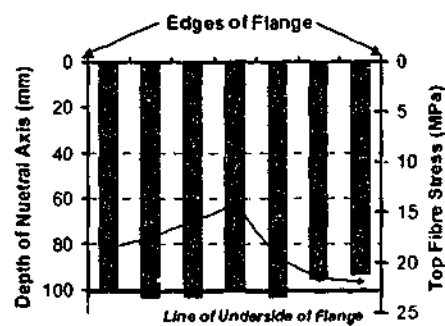


(i) Section A at 180kN

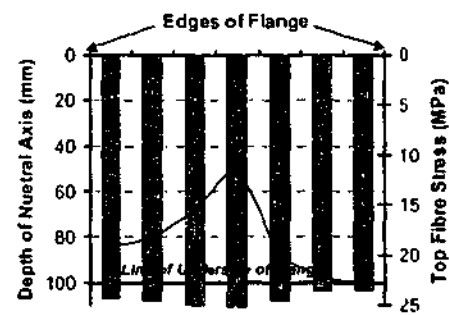


(j) Section A at 200kN

Figure C. 3-1 Continued



(k) Section A at 220kN



(l) Section A at 237.8kN

Figure C. 3-1 Continued

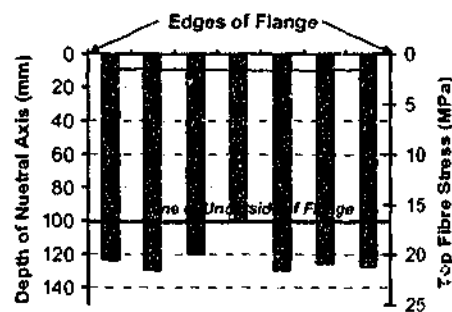
C.3.2 Section B

From the start of the test, and until a level of applied load of 78kN (corresponding to the formation of the first diagonal web crack), the position of the neutral axis remained constant at the centre of the width of the web of the specimen. This is illustrated by Figure C. 3-2 (a)-(c). Throughout this range of applied load, the depth of the neutral axis in the flanges decreased at a uniform rate. The depth of the axis at the centre of the width of the web was the minimum value throughout this duration of loading.

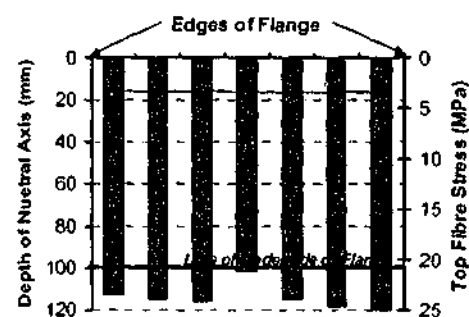
At a level of applied load of 78kN (corresponding to the formation of the first of the diagonal web cracks), the neutral axis suddenly shifted to a location within the depth of the flange. Between this load level and that of 86kN, the neutral axis throughout the entire width of the specimen shifted closer to the top surface of the specimen. Beyond this level of applied load of 86kN (the load corresponding to the appearance of the second diagonal web crack), the neutral axis moved at a very slow rate toward the top of the specimen, remaining almost constant in depth at the centre of the web. This trend ceased at a level of applied load of $P=120\text{kN}$, and is illustrated in Figure C. 3-2 (e) – (f). Between this level of load and that of $P=212\text{kN}$, the neutral axis position at the centre of the web moved very slowly away from the top surface of the flange, remaining almost constant in position, whilst the location of the axis in the flange moved deeper into the flange at a much faster rate. This can be seen in part (g)-(j) in the figure below.

Beyond this level of load (and following the formation of the critical diagonal web crack), the strain profiles showed compression throughout the width of the flanges. This is reflected in Figure C. 3-2 (k)-(l) with exceptionally low values of neutral axis depth calculated at most locations in the flanges. These figures also show a movement away of the neutral axis at the centre of the width of the web away from the top surface of the specimen. It is noted that the neutral axis at section B moved out of the flange at a level of load of approximately 180kN.

The distribution of stress again remained constant throughout the width of the specimen at the early stages of loading. At a level of applied load of 120kN, the magnitude of the stress at the centre of the web decreased relative to that in the flanges. The stress was minimum at the centre of the width of the web was displayed by the specimen between levels of applied load of 120-180kN, as can be seen in Figure C. 3-2 (f) – (i). As the neutral axis began to move out of the flange overhangs (beginning at a level of applied load of 173kN), the distribution of stress across the width of the flange favoured the left side flange overhang, and the maximum compressive stress was at the centre of width of the web. This remained until the appearance of the critical diagonal web crack at a level of applied load of 212kN, at which load the distribution of stress that favoured the right side flange overhang, and a minimum magnitude at the centre of width of the web prevailed.

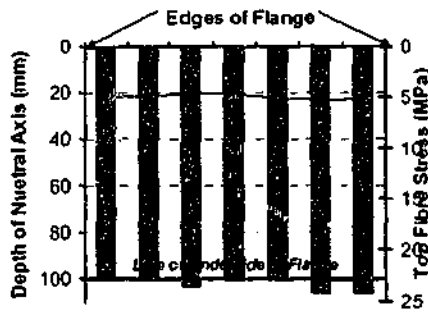


(a) Section B at 20kN

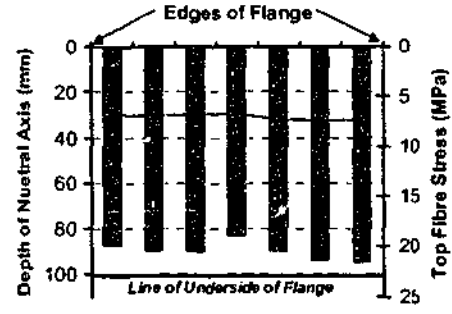


(b) Section B at 40kN

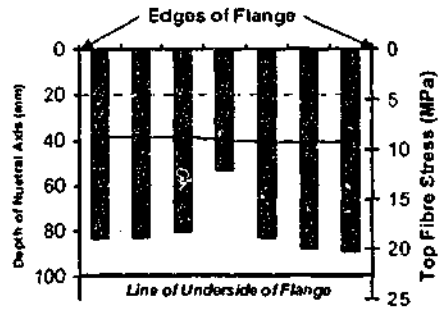
Figure C. 3-2 Distributions of neutral axis on section A of specimen B17 at 20kN intervals



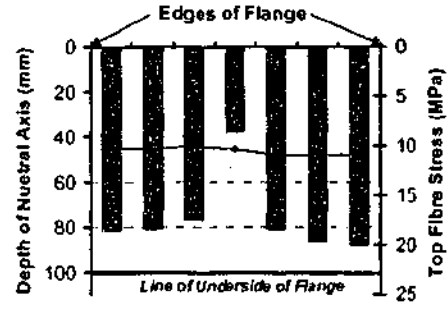
(c) Section B at 60kN



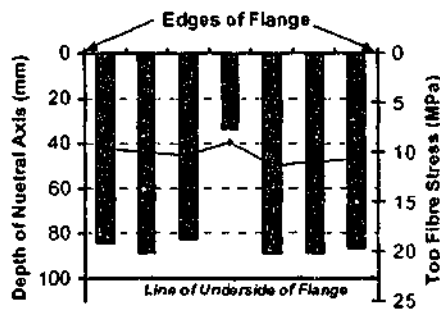
(d) Section B at 80kN



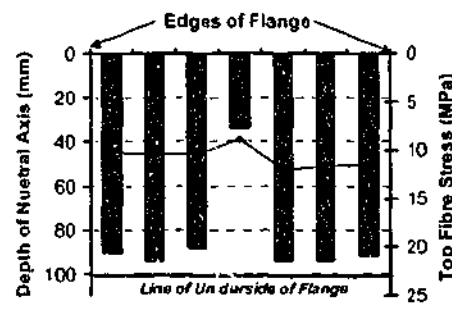
(e) Section B at 100kN



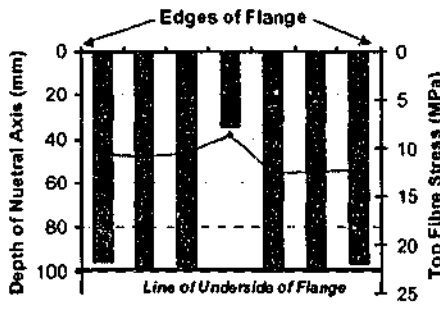
(f) Section B at 120kN



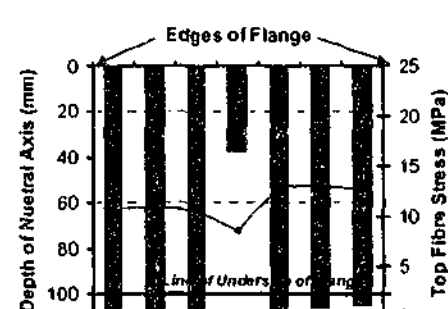
(g) Section B at 140kN



(h) Section B at 160kN

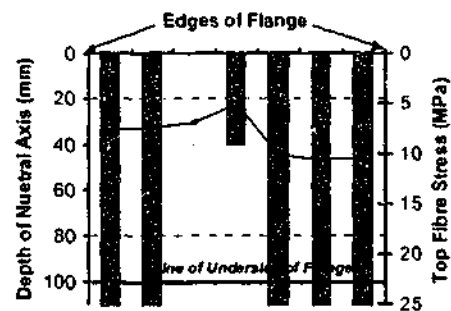


(i) Section B at 180kN

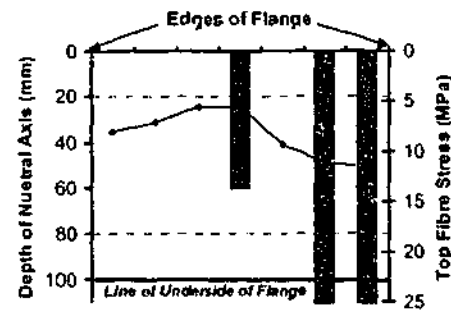


(j) Section B at 200kN

Figure C. 3-2 Continued



(k) Section B at 220kN



(l) Section B at 237.8kN

Figure C. 3-2 Continued

C.4 The Relationship of the Failure Mechanism and the Longitudinal Strains

The formation of the failure mechanism of this specimen forced redistributions of strain within the flange during the application of the controlled displacement.

The formation of two diagonal web cracks at levels of load of 78kN and 86kN produced a difference in neutral axis position in the flange overhangs relative to that in the web. At both sections, the position of the neutral axis at the centre of the width of the web was closer to the top surface of the specimen after the formation of these cracks. Each of these sections also produced a compressive stress distribution on the top surface of the flange that had a minimum stress at the centre of the width of the web. Coupling these two facts together suggests a greater magnitude of compression force in the flanges than in the web. Therefore, the formation of the mechanism throughout the application of the controlled displacement forces a redistribution of compressive forces away from the web toward the flange overhangs.

The level of applied load of 120kN marked the beginning of a redistribution of compression strain throughout the flange. The tensile strains on the underside of the flange began to decrease in magnitude, and the compression strains on the top surface of the flange also decreased to maintain equilibrium throughout this redistribution. This redistribution was prevalent between an applied load of 120-140kN. Beyond this level of load, the gradient of increase in strain on both surfaces increased at a slower rate than prior to the redistribution.

This redistribution marks the initiation of a strain profile within the compression region of the specimen that appears to be consistent with a shear compression failure.

The tensile strains on the underside of the flange became compressive at section B at a level of load of approximately 180kN. This was only the case at locations within the flange. The position of the neutral axis in the web region at this level of load was still about 35mm from the top surface of the flange. The propagation of compression forces from the applied load to the support was therefore heavily reliant on the flange overhangs at section B.

The formation of the critical diagonal web crack at a level of applied load of 212kN marked a significant redistribution of strain throughout the width and depth of the flange. Strains in both flange overhangs were significantly higher than those in the web at section B, while the strains at section A shifted closer to zero, becoming compressive strains throughout the width of the specimen. Both sections were in compression throughout the entire depth of the flange, and the compressive strain was at a minimum at the centre of the web.

All of the above are critical redistributions in the consideration of the variation of flange effectiveness throughout the loading of the specimen. The definitions given in Chapter 7 are summarised again below. Given the above discussion, these can now be related to the effect that the formation of the failure mechanism has on the distribution of strain in the flange overhangs of specimen B17.

- *Stage I* : Load Range 78-86kN, the formation of two diagonal web cracks.
- *Stage II* : Load Range 120-140kN, the redistribution within the flange associated with the reversal of strain on the underside of the flange. This is also the initiation of the strain profile associated with the shear compression mechanism.
- *Stage III* : Load Level of 180kN, corresponding to the movement of the neutral axis out of the flanges at section B.
- *Stage IV* : Load level 212kN, the level of load at which the critical diagonal web crack formed.

Appendix D RESULTS OF CHECKS ON THE CALCULATION OF THE INDIVIDUAL BLOCK SHEARS

D.1 Introduction

The calculation of the shear forces in Chapter 7 throughout the width and the depth of the flange required the calculation of shear forces in each block. The required distributions could be obtained from these values.

To check that the results of the calculations were correct, the summation of moments required to calculate the shear force acting on an individual flange point in Equation 3.3.1 in Chapter 3 was taken about a second point to determine if the normal forces that were calculated produced a consistent estimate of the shear force by following the procedure in this chapter. This appendix summarises these results.

D.1.1 *The Methodology*

The second point about which moments were taken to check the value of the shear acting on the flange block was point O shown in Figure D. 1-1. To be consistent with the notation used in this figure, the following notation is used in the presentation of the results below.

1. 'V from ΣM_o ' is used to denote that sectional shear acting on a flange block as calculated from summation of moments about point 'O' in Figure D. 1-1.

2. 'V from ΣM_x ' is used to denote that sectional shear acting on a flange block as calculated from summation of moments about point 'X' in Figure D. 1-1.

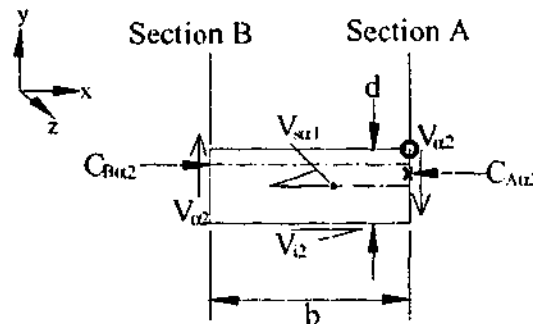
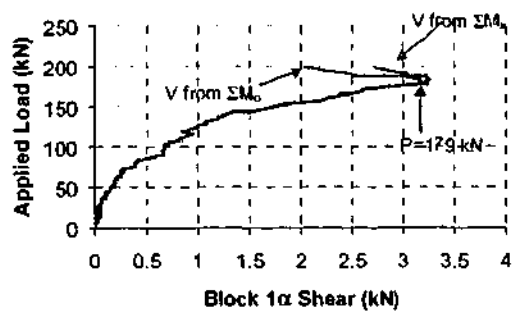


Figure D. 1-1 Elevation of flange block showing the points considered in moment equilibrium for the calculation of the sectional shear on the flange block'

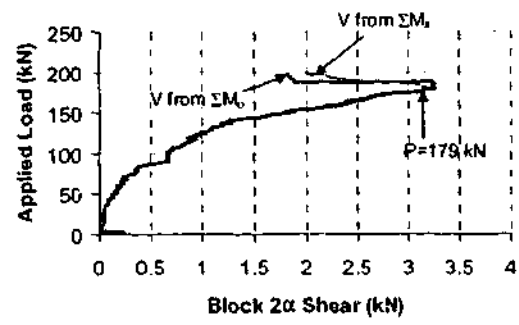
D.2 Results for Specimen B16

The comparison of the shear calculated from summation about points O and X for specimen B16 at each flange block throughout the loading range are shown below in Figure D. 2-1. The range of applied load of 200 kN was the cut off load for consideration of these results as this corresponded to the load at which gauges began to fail as a result of high tensile strains from cracking.

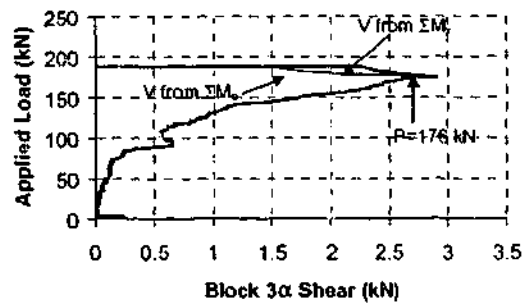
These results show that the check of equilibrium was satisfied for most of the loading range. However, at the final stage of load, these checks were not satisfied, and the results of the shear as calculated from summation about the two points diverge at most locations. Part (d) and (i) of this figure (corresponding to the flange blocks in layer α and β at row 5) show the lowest level of applied load at which divergence begins. This is at a level of applied load of 175kN. The results for the calculation of shear in each flange block are not considered above this level of applied load.



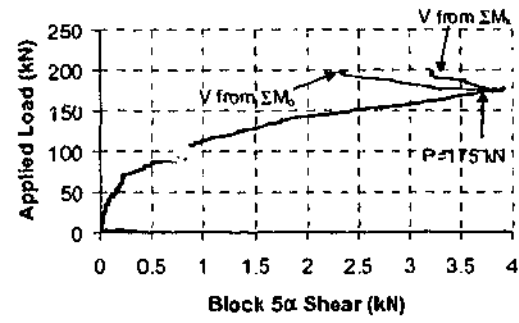
(a) Flange Block 1 α



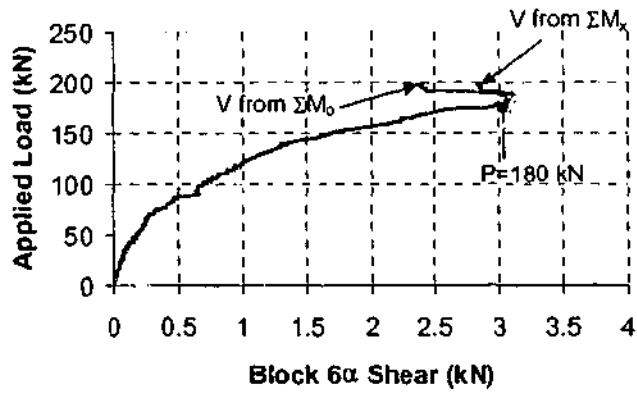
(b) Flange Block 2 α



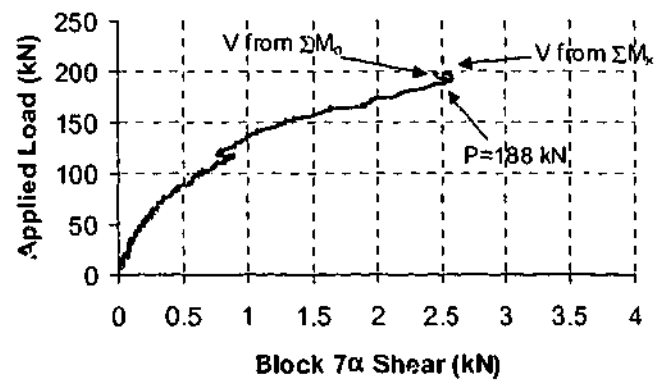
(c) Flange Block 3 α



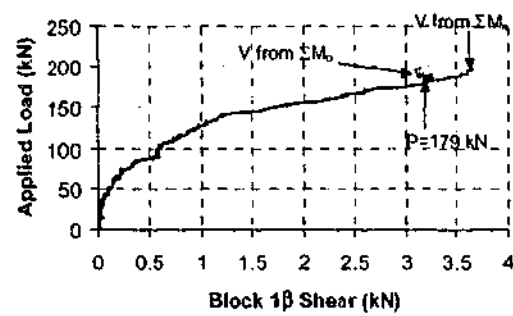
(d) Flange Block 5 α



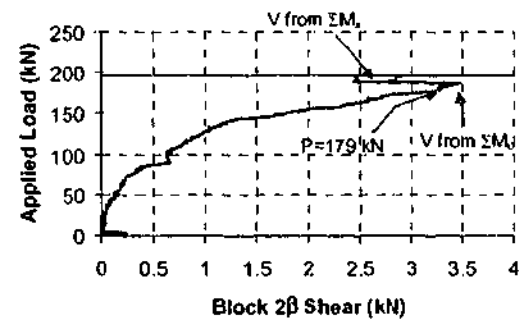
(e) Flange Block 6 α



(f) Flange Block 7 α

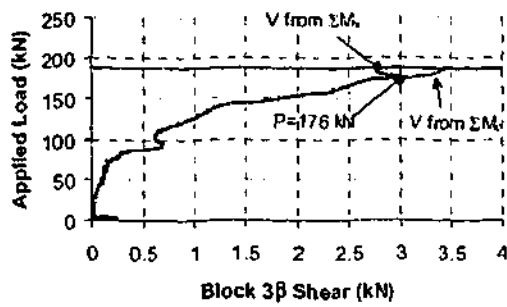


(g) Flange Block 1 β

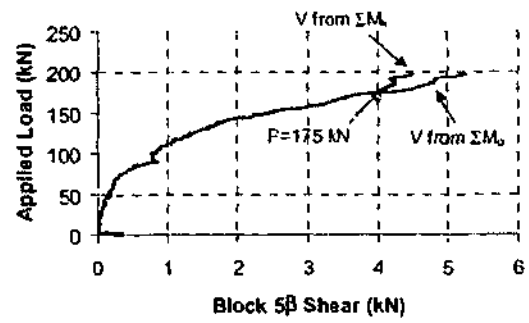


(h) Flange Block 2 β

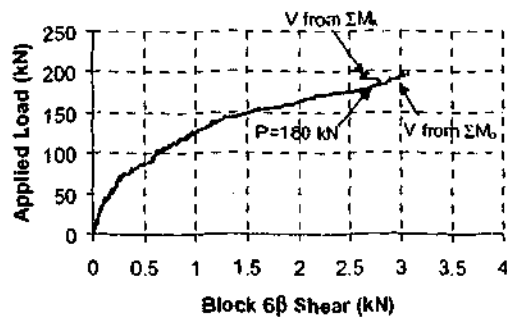
Figure D. 2-1 Results of equilibrium check for specimen B16



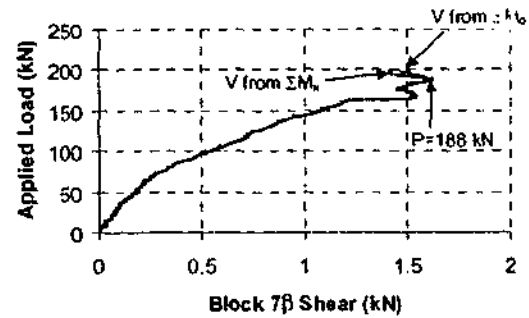
(i) Flange Block 3β



(j) Flange Block 5β



(i) Flange Block 6β

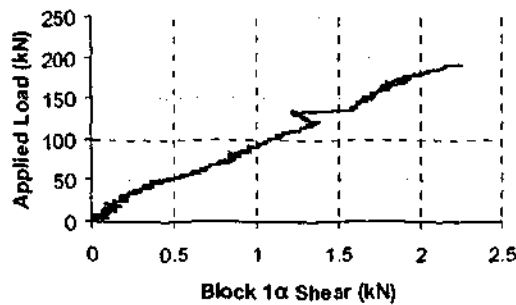


(j) Flange Block 7β

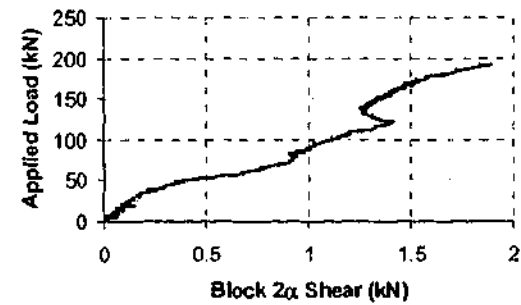
Figure D. 2-1 Continued

D.3 Results for specimen B17

Figure D. 3-1 shows the results of the checks of equilibrium that were applied to specimen B17. The results show no variation between the results that were calculated from summation of moments about the two points (O and X) throughout the entire loading range on this specimen. The results of the calculation of the shears on each individual flange block are therefore considered throughout the entire range of load on this specimen.

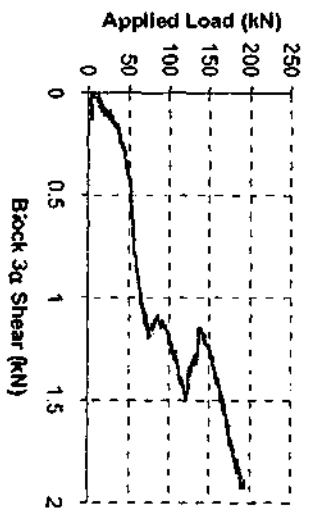


(a) Flange Block 1α

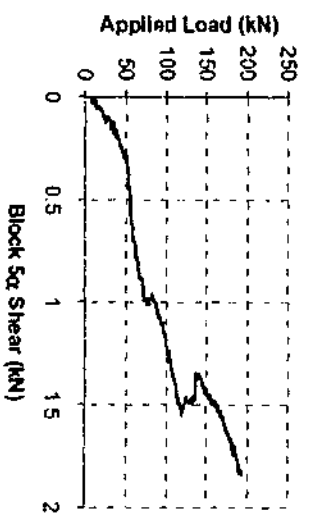


(b) Flange Block 2α

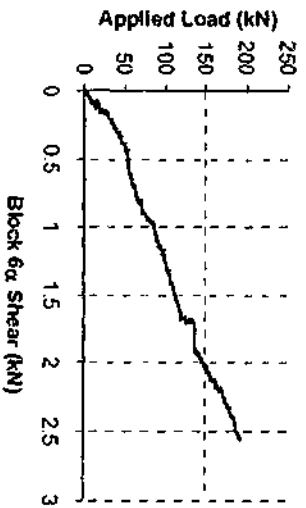
Figure D. 3-1 Results of equilibrium check for specimen B16



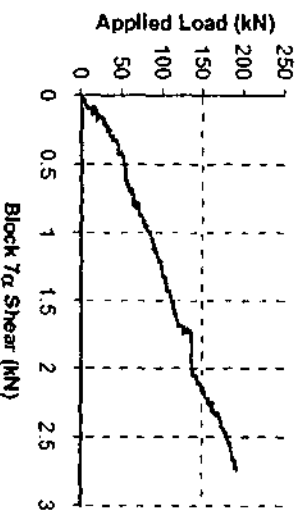
(c) Flange Block 3a



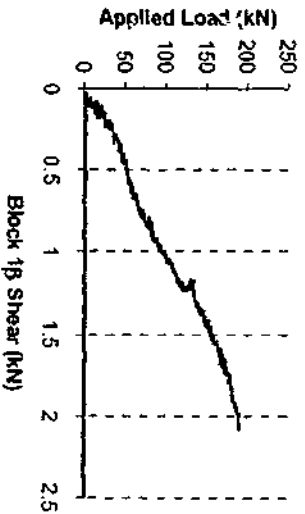
(d) Flange Block 5a



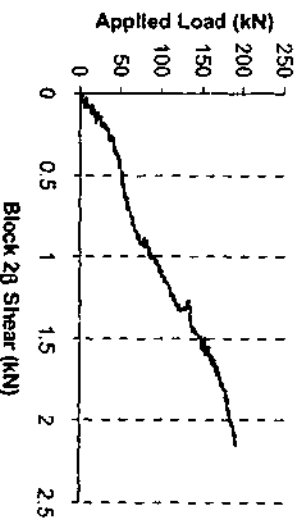
(e) Flange Block 6a



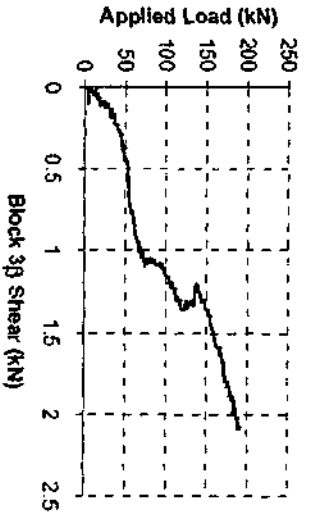
(f) Flange Block 7a



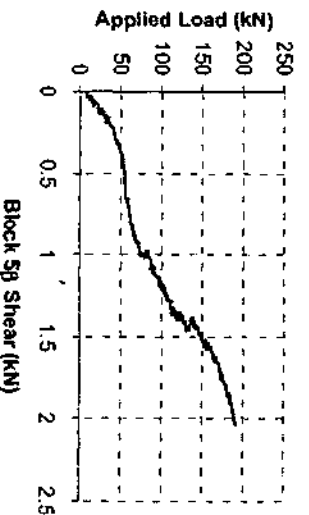
(g) Flange Block 1b



(h) Flange Block 2g

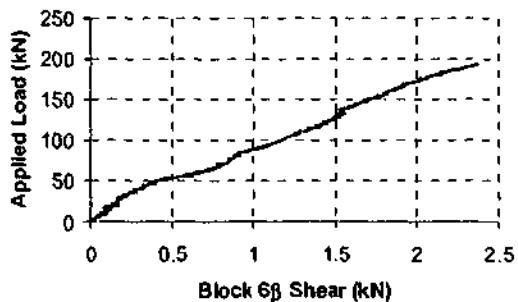


(i) Flange Block 3b

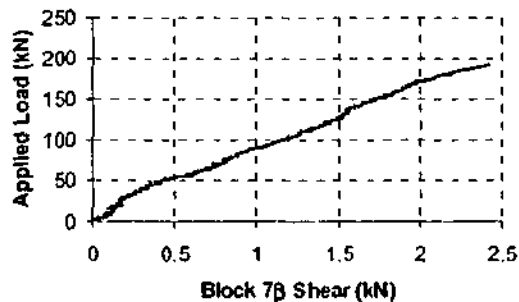


(j) Flange Block 5b

Figure D. 3-1 Continued



(i) Flange Block 6 β



(j) Flange Block 7 β

Figure D. 3-1 Continued

D.4 Concluding Remark

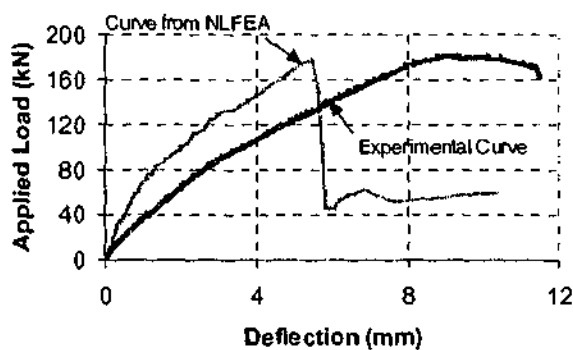
It is noted here that the level of calculation at which the equilibrium checks ceased to be satisfied on specimen B16 corresponded to the formation of strains on the top surface of the flange that were in the vicinity of the cracking strain of concrete. Although specimen B17 displayed a reversal of strain that corresponded to the formation of this component of the shear failure mechanism, this level of strain was not apparent in this specimen.

Appendix E LOAD VS. DEFLECTION PREDICTIONS FROM NLFEA

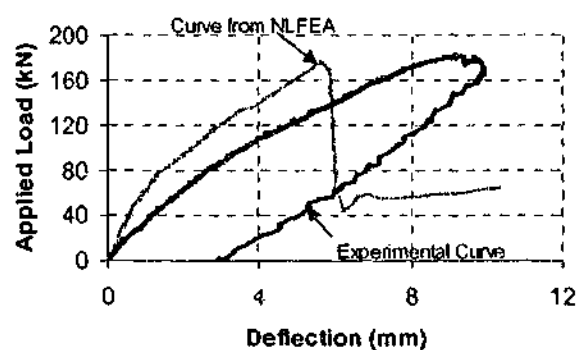
E.1 Introduction

The aim of this appendix is to give the reader a complete comparison of the load-deflection behaviour of each specimen in stage one experimental work with the predicted behaviour as calculated using the NLFEA solution scheme. To give a full demonstration of the NLFEA results, predictions of the load-deflection response for each series will also be presented. No discussion is provided in this appendix as the relevant discussion has been presented in Chapter 8.

E.2 Comparison of NLFEA Load-Deflection Response With the Experimental Response

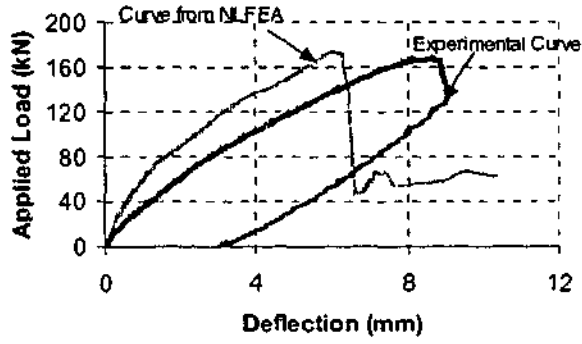


(a) Specimen B1

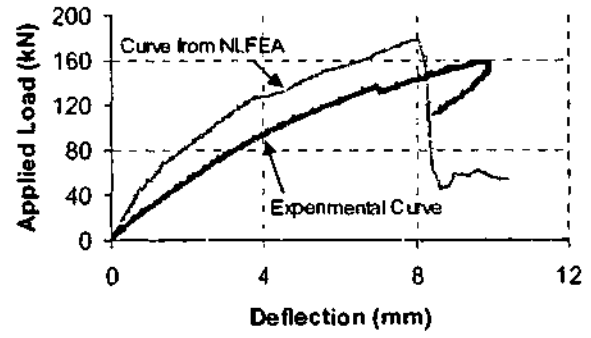


(b) Specimen B2

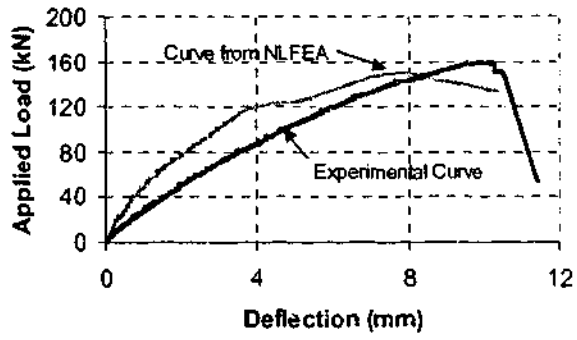
Figure E. 2-1 Comparison of predicted load deflection curves from NLFEA with experimental work



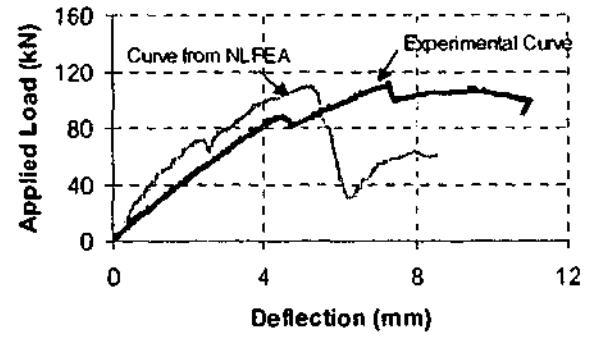
(c) Specimen B3



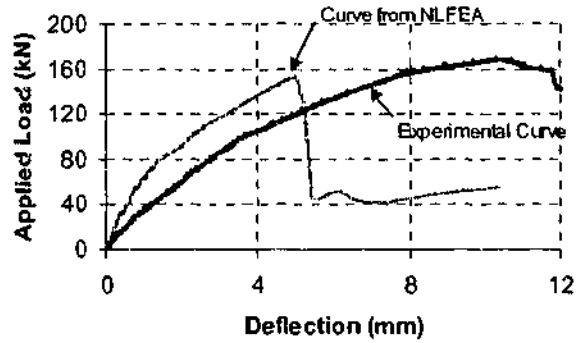
(d) Specimen B4



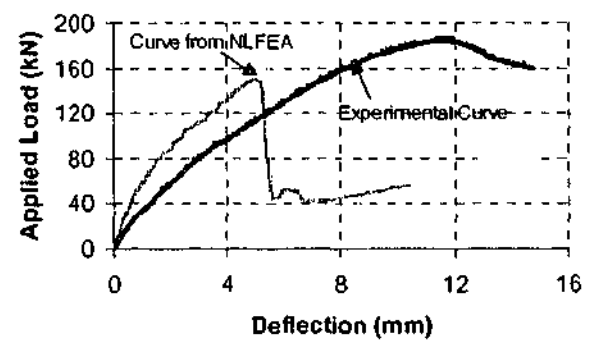
(e) Specimen B5



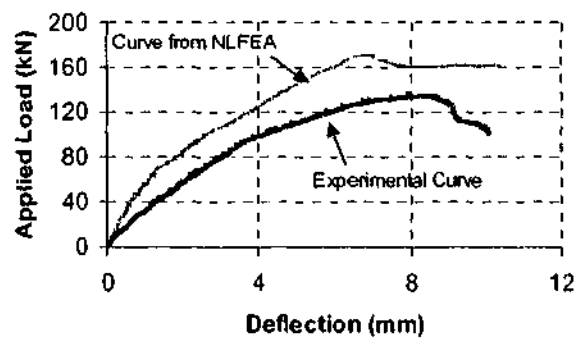
(f) Specimen B6



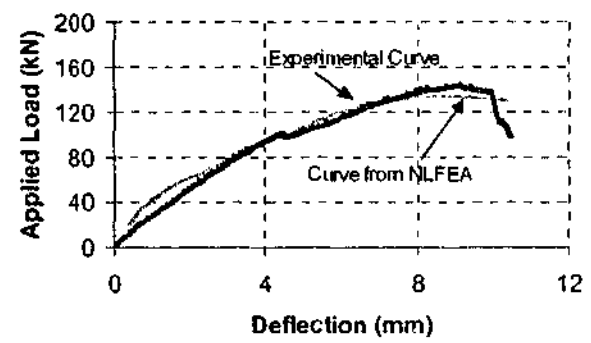
(g) Specimen B7



(h) Specimen B8

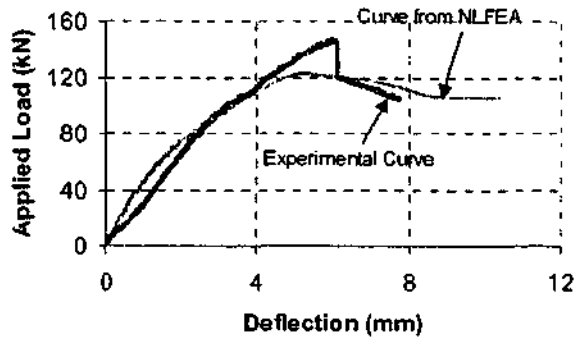


(i) Specimen B9

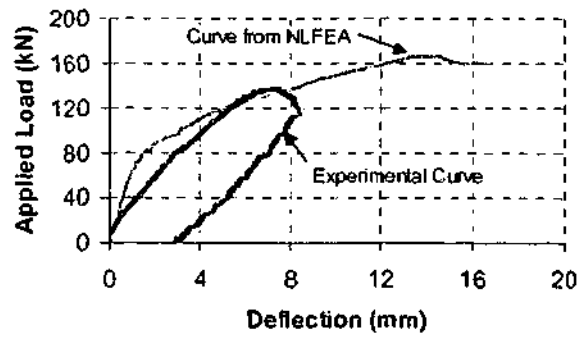


(j) Specimen B10

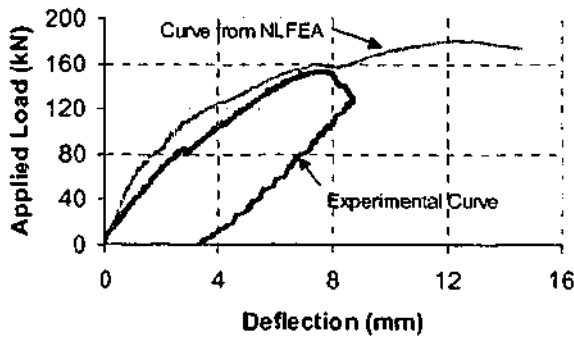
Figure E. 2-1 Continued



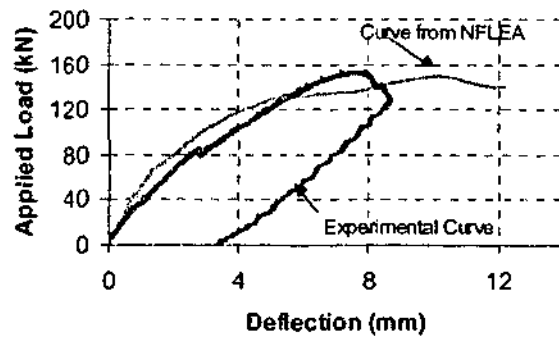
(k) Specimen B11



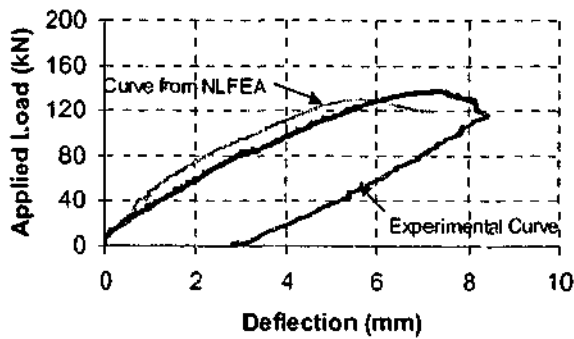
(l) Specimen B12



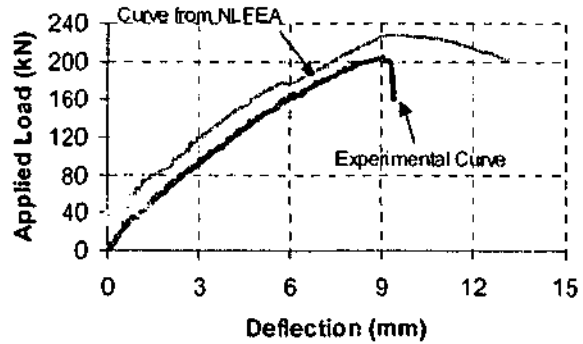
(m) Specimen B13



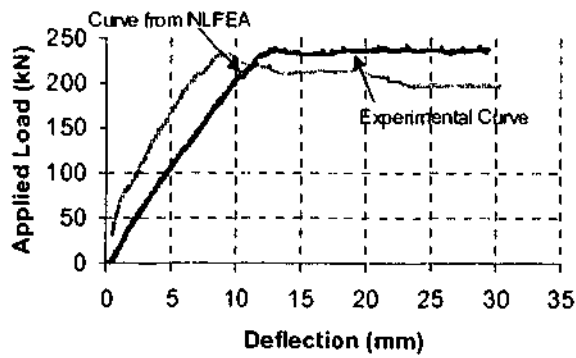
(n) Specimen B14



(o) Specimen B15



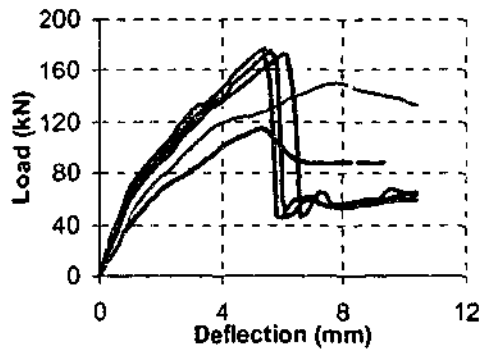
(p) Specimen B16



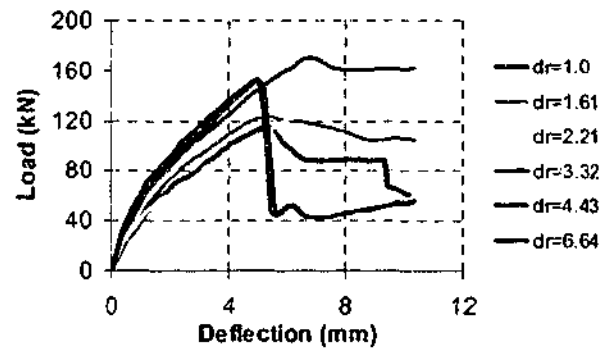
(q) Specimen B17

Figure E. 2-1 Continued

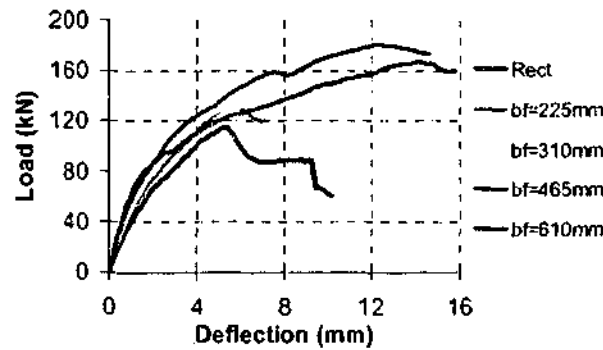
E.3 Comparison of Predicted Load-Deflection Curves Within Each Series



(a) Series 1 ($dr=0.33$)



(b) Series 2 ($dr=0.25$)



(c) Series 3 ($dr=0.16$)

Figure E. 3-1 Comparison of predicted load-deflection curves within each series of specimen

Appendix F EXAMPLE CALCULATION OF THE FLANGE CONTRIBUTION

F.1 Introduction

This appendix presents an example of the procedure to calculate the flange contribution as outlined in Chapter 3 and implemented in Chapter 7. The values of interpolated strain for specimen B16 at a level of applied load of 100kN are operated on with the procedure outlined in Chapter 3 to calculate the flange contribution at this level of applied load. The interpolated value is used in this discussion in an effort to minimise the volume of calculations presented. It is noted however that these values are found by firstly linearly interpolating the measured strain values to determine the strains at the centre of depth of the flange (that is the strains at the bottom of the layer α flange block throughout the width of the flange). Once these values were obtained, they were used with the measured values on the top and underside of the flange to determine the values of the strain at the centre of width of each flange block on the top surface, the underside of the flange, and at the bottom of the layer α blocks. Note that the preceding calculations do not include values for strain, stress, force etc. for row 4 as this is the web of the specimen. None of the quantities calculated in this row are used in the calculations of the flange contribution.

Illustration of the calculation procedure requires the notations outlines in Chapter 3 for the sections, rows and layers used throughout the procedure. The necessary notation for the purpose of this appendix is outlined below in Figure F. 1-1 - Figure F. 1-2.

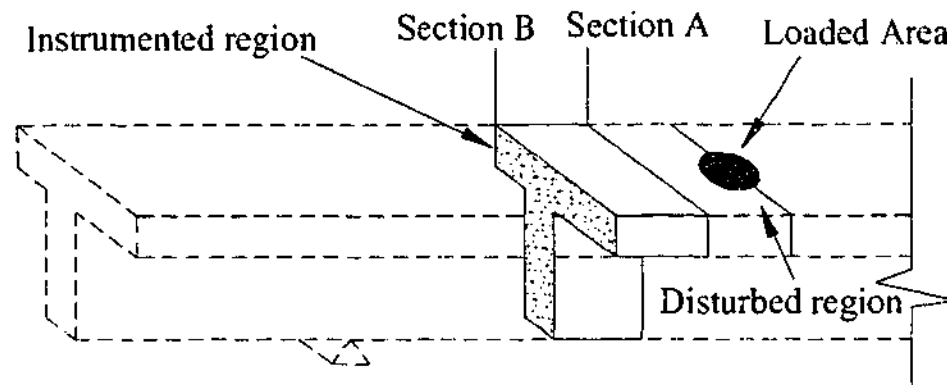


Figure F. 1-1 Identification of Section A and Section B

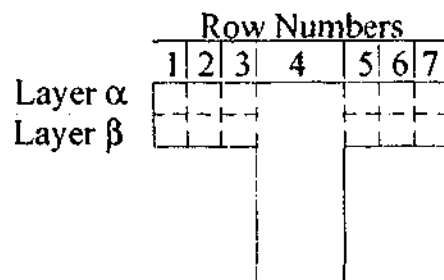


Figure F. 1-2 Notation Used for Location of Flange Blocks

F.2 Calculation Procedure

Figure F. 2-1 shows the value of the interpolated strains calculated for specimen B16 at a level of applied load of 100kN. A positive strain in this figure is a compression strain. This figure also shows a series of dashed lines that are the boundaries to each of the flange blocks. Each flange block has the following geometry.

Flange block width, $b_{fb} = 54.2\text{mm}$

Flange block depth, $d_{fb} = 37.5\text{mm}$

The material properties obtained for this experiment were

$f'_c = 50\text{MPa}$ ($E_c = 41,000\text{ MPa}$ (calculated using CEB-FIP model code 1990))

$f_{y,v} = 300\text{MPa}$

$$f_{y,l} = 350\text{MPa}$$

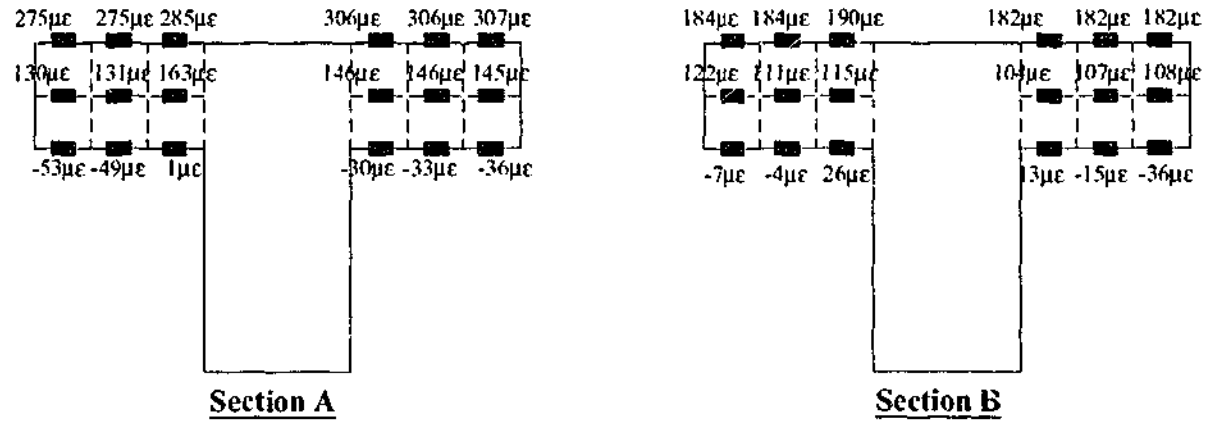


Figure F. 2-1 Interpolated strains for specimen B16 at applied load of 100kN

CALCULATION OF STRESS FROM STRAIN

Using the MCFT relations

$$f_{c2} = f_p \left[2 \left(\frac{\epsilon_2}{\epsilon_o} \right) - \left(\frac{\epsilon_2}{\epsilon_o} \right)^2 \right],$$

$$f_p = \frac{f'_c}{\beta}; \quad \beta_d = \frac{1}{1 + C_s C_d} \leq 1.0; \quad C_d = 0.35(-\epsilon_{c1} / \epsilon_{c2} - 0.28)^{0.8}$$

and

$$f_{c1} = \begin{cases} E_c \epsilon_1 & \epsilon_1 \leq \epsilon_{cr} \\ \frac{f_{cr}}{1 + \sqrt{200\epsilon_1}} & \epsilon_1 > \epsilon_{cr} \end{cases}$$

From the CEB-FIP Model Code (1990), the tensile strength of concrete in uniaxial tension is $f_{cr} = 4.6\text{MPa}$, using the Youngs Modulus of $E_c = 39000\text{MPa}$, the cracking strain is calculated as:

$$\epsilon_{cr} = 4.6/41000 = 112\mu\epsilon$$

At row 1 on section A:

The top layer stress is $50(2(275/2000) - (275/2000)^2) = 12.8$ MPa (Compressive)

Centre of depth stress is $50(2(130.4/2000) - (130.4/2000)^2) = 6.3$ MPa (Compressive)

Stress on underside of slab is $41000 \times 51.6 = 2.35$ MPa (Tensile)

The strains in Figure F. 2-1 are all less than this, so in this example, only the linear elastic part of the tensile response of concrete needs to be considered. The following values of stress are obtained at each flange block:

Table F. 2-1 Stresses at the centre of width of each flange block (on the top and bottom of each flange block)

Row Number	Section A Stresses (MPa)				Section B Stresses (MPa)			
	Layer α		Layer β		Layer α		Layer β	
	Top	Bottom	Top	Bottom	Top	Bottom	Top	Bottom
1	12.8	6.3	6.3	-2.4	8.8	5.9	5.9	-0.4
2	12.8	6.3	6.3	-2.1	8.8	5.4	5.4	-0.3
3	13.3	7.8	7.8	0.1	9.1	5.6	5.6	1.3
5	14.2	7.1	7.1	-1.4	8.7	5.1	5.1	0.7
6	14.1	7.0	7.0	-1.4	8.7	5.2	5.2	-0.3
7	14.2	7.0	7.0	-1.4	8.7	5.3	5.3	-1.5

Note: Compressive stresses are positive.

LOCATION OF NEUTRAL AXIS IN EACH ROW

Calculate the location of the neutral axis by assuming that a linear strain gradient exists over the depth of the flange of the specimen, using the strain at the top of the flange and the strain on the underside of the flange.

$$d_n = \frac{\epsilon_{top}}{\epsilon_{top} - \epsilon_{bot}}$$

where ϵ_{top} is the strain on the top surface of the flange block, ϵ_{bottom} is the strain on the underside of the flange, and d_f is the depth of the flange (=75mm). The expression above calculates the depth of the neutral axis from the top surface of the flange.

In row i

$$d_n = 275 / ((275 - (-53.6)) / 75) = 62.8 \text{ mm}$$

Applying this approach to all other rows at the two sections of flange results in the following:

Table F. 2-2 Location of the neutral axis in each flange block

Row Number	Section A Neutral Axis Depth (mm)	Section B Neutral Axis Depth (mm)
1	62.8	72.8
2	63.6	72.8
3	75.4	84.9
5	68.3	80.1
6	67.7	70.0
7	67.1	65.5

CALCULATE THE FORCE IN EACH FLANGE BLOCK

The tension and compression forces are calculated in each flange block. This calculation assumes a linear stress distribution throughout the depth of the flange in each flange block as shown in Figure F. 2-2. In this figure, σ_{top} is the stress at the top of the flange block, σ_{bottom} is the stress at the bottom of the flange block. Using the values of stress in Table F. 2-1, the locations of the neutral axes in each layer in Table F. 2-2, and the dimensions of each flange block, the following forces are obtained in each flange block:

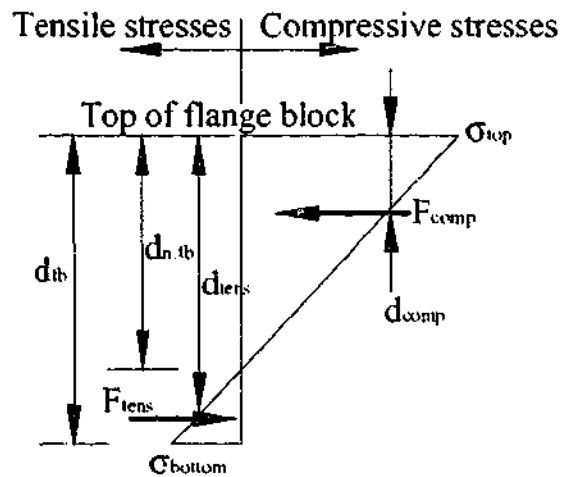


Figure F. 2-2 Linear Stress Distribution Throughout the Depth of a Flange Block

For this distribution of stress, the longitudinal forces are calculated as:

$$F_{comp} = d_{fb} b_{fb} \left(\frac{\sigma_{top}}{2} \right)$$

$$F_{tens} = (d_{fb} - d_{n.fb}) b_{fb} \left(\frac{\sigma_{bottom}}{2} \right)$$

where $d_{n.fb}$ is the distance from the top of the flange block to the neutral axis. The distribution of stress is not always as above, and some modifications need to be made to this formulation to calculate the longitudinal forces.

For flange block 1α

$$F_{comp} = 37.5 * 54.2 * (4.5 + (12.80 - 4.5) / 2) = 19.4 \text{ kN}$$

$$F_{tens} = (75 - 62.76) * 54.2 * (0 / 2) = 0 \text{ kN}$$

The latter is logical as the neutral axis lies outside of the flange, hence there will be no tensile force acting throughout the depth of the flange.

Using the values of stress in Table F. 2-1, the locations of the neutral axes in each layer in Table F. 2-2, and the dimensions of each flange block, the following forces are obtained in for the remainder of the flange blocks.

Table F. 2-3 Forces in Each Flange Block

Row Number	Section A Flange Block Forces (kN)				Section B Flange Block Forces (kN)			
	Layer α		Layer β		Layer α		Layer β	
	Comp.	Tens.	Comp.	Tens.	Comp.	Tens.	Comp.	Tens.
1	19.4	0.0	4.5	0.8	14.9	0.0	5.7	0.0
2	19.4	0.0	4.7	0.7	14.4	0.0	5.2	0.0
3	21.4	0.0	8.0	0.0	14.9	0.0	7.0	0.0
5	21.6	0.0	6.1	0.3	14.0	0.0	5.8	0.0
6	21.5	0.0	6.0	0.3	14.1	0.0	4.6	0.1
7	21.5	0.0	5.8	0.3	14.2	0.0	3.0	0.4

Comp. Denotes the magnitude of the compressive forces in the layer
Tens. Denotes the magnitude of the tension forces in the layer

CALCULATE THE LEVER ARMS OF THE FORCES IN EACH FLANGE BLOCK

To perform the summation of moments required to calculate the shear force acting on a block, the lever arm of each longitudinal force is located. For the stress distribution shown above, the lever arms of the forces measured from the top of the flange block are calculated using:

$$d_{comp} = \frac{1}{3}d_{n,fb}$$

$$d_{tens} = d_{n,fb} + \frac{2}{3}(d_{fb} - d_{n,fb})$$

where d_{comp} and d_{tens} are the lever arms of the compression and tension forces, respectively, measured from the top of the flange block as defined above in Figure F. 2-2.

Table F. 2-4 Lever arms of longitudinal forces in flange blocks

Row Number	Section A Lever Arms (mm)				Section B Lever Arms (mm)			
	Layer α		Layer β		Layer α		Layer β	
	d_{comp}	d_{tens}	d_{comp}	d_{tens}	d_{comp}	d_{tens}	d_{comp}	d_{tens}
1	16.6	0.0	8.8	33.8	17.5	0.0	11.8	36.8
2	16.6	0.0	9.1	34.1	17.3	0.0	11.8	36.8
3	17.1	0.0	12.6	0.0	17.3	0.0	14.8	0.0
5	16.7	0.0	10.7	35.7	17.1	0.0	13.9	0.0
6	16.7	0.0	10.4	35.4	17.2	0.0	10.8	35.8
7	16.6	0.0	10.2	35.2	17.2	0.0	9.3	34.3

CALCULATE THE FORCE IN THE LONGITUDINAL REINFORCING BARS

The reinforcing was located at the centre of the flange in the specimens. Assuming perfect bond between the steel and the concrete, the strain in the reinforcing is equal to the interpolated strain shown above in Figure F. 2-1.

The maximum of the strains above ($\epsilon=163.2\mu\epsilon$) results in a maximum value of compressive force equal to

$$F_{rein\alpha} = A\epsilon E = \frac{\pi}{4} (6.5)^2 (163.2 \times 10^{-6}) \times \frac{200,000}{1000} = 1.1 kN$$

In this case, this is very small and will have an insignificant affect on the outcome of the shear force, and is therefore not considered in the ensuing calculations. This quantity is not ignored in the calculations in the main text.

CALCULATE THE SHEAR LAG

Equation 3.3.7 in Chapter 3 infers that given the full depth flange block shown below in Figure F. 2-3, the shear lag is given by the equation

$$\Delta C + \Delta V_s = 0$$

where ΔC is the difference in the compression forces acting on each layer (it was found in general that the net longitudinal force acting on a row of the flange was compressive), and ΔV_s is the difference in shear lag forces acting on the faces of the flange block. The shear lag forces are those calculated throughout the full depth of the flange.

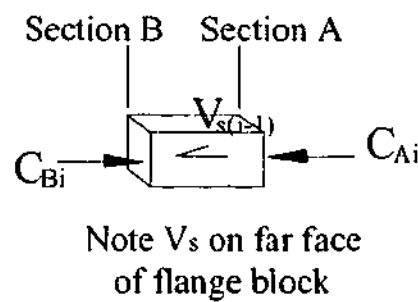


Figure F. 2-3 Full Depth Flange Block Showing Longitudinal Forces Acting

As stated in Section 3.3.1.5, the shear lag forces are assumed to be distributed equally throughout the two layers in the flange, so the flange block shear lag force is half of the above.

Referring to the values in Table F. 2-3, the shear lag force on row 1 is calculated as follows:

$$\text{Row 1: } C_A = 19.4 + 4.5 - 0.8 = 23.2 \text{ kN}$$

$$C_B = 14.9 + 5.7 - 0.0 = 20.6 \text{ kN}$$

$$\Delta C = 23.2 - 20.6 = 2.6 \text{ kN}$$

$$V_{s(i-1)} = 0 \text{ kN (as this is the free surface on the edge of the flange)}$$

Therefore,

$$V_{si} = -2.6 \text{ kN}$$

Note that the negative sign indicates that the shear lag force is acting in a direction opposing the longitudinal force on Section A.

Therefore the shear lag on the two layers throughout the depth at row 1 is as follows

$$V_{s\alpha 1} = V_{s\beta 1} = 2.6/2 = 1.3 \text{ kN}$$

Applying this to each row throughout the width of the flange yields the following magnitudes of shear lag throughout the depth of the flange.

Table F. 2-5 Shear lag on flange blocks

Row Number	Shear Lag (kN) (Calculated throughout the depth of the flange)	Shear Lag Acting on Each Layer Throughout the Depth of the Flange (kN)
1	2.6	1.3
2	6.6	3.3
3	14.3	7.15
5	12.8	6.4
6	15.0	7.5
7	10.2	5.1

Note that a positive shear lag is assumed to oppose a compressive force on Section A.

CALCULATE THE INTERFACE SHEAR ACTING BETWEEN LAYERS THROUGHOUT THE DEPTH OF THE FLANGE

Using Equation 3.3.8, the interface shear on any flange block in layer α is calculated as follows:

$$V_{i1} = -C_{B\alpha 2} + C_{A\alpha 2} + V_{s\alpha 1} - V_{s\alpha 2}$$

Considering the longitudinal forces and the shear lag acting on flange block 1α shown below in Figure F. 2-4.

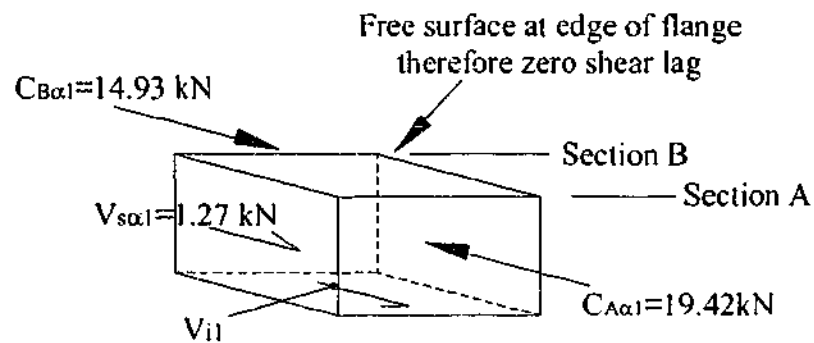


Figure F. 2-4 Longitudinal Forces and Shear Lag Forces Acting on Flange Block 1α

A positive interface shear is assumed to act in the direction opposing a compression force on Section A. Application of the above equilibrium equation yields:

$$V_{i1} = 3.2 \text{ kN}$$

Note that the interface shear acting on flange block 1β will be equal and opposite to this value, therefore only requiring consideration of the flange blocks in layer α flange blocks to calculate interface shear. Repeated application of this procedure results in the following values of the interface shear for the remainder of the flange blocks in the flange.

Table F. 2-6 Shear lag on flange blocks

Row Number	Interface Shear (V_i (kN))
1	3.2
2	3.1
3	2.8
5	3.8
6	3.1
7	2.3

CALCULATE THE SECTIONAL SHEAR ON EACH FLANGE BLOCK

Using Equation 3.3.2, the sectional shear force on a flange block in any row j , in layer α (shown in Figure F. 1-2) is calculated using the following:

$$V_{\alpha j} = \frac{-(0.5d_{fb} - L_{CA\alpha j})V_{S\alpha j-1} + (0.5d_{fb} - L_{CA\alpha j})V_{S\alpha j} - (L_{CB\alpha j} - L_{CA\alpha j})C_{B\alpha j} + (d_{fb} - L_{CA\alpha j})V_{ij}}{b}$$

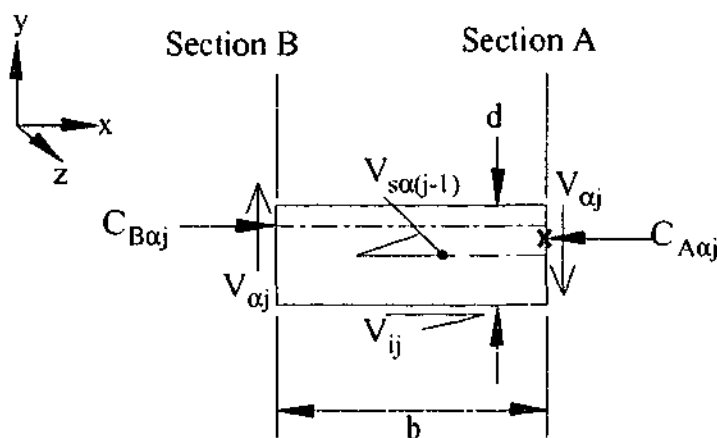


Figure F. 2-5 Forces Acting on an Flange Block in Row j Layer α

It is noted that in Figure F. 2-5, the shear lag force $V_{S\alpha j}$ is acting on the surface on the back of the block which is not shown.

The following values have been obtained throughout the calculation procedure thus far for layer 1 α .

$$C_{A\alpha 1} = 19.4\text{kN}$$

$$C_{B\alpha 1} = 14.9\text{kN}$$

$$L_{CA\alpha 1} = 16.6\text{mm}$$

$$L_{CB\alpha 1} = 17.5\text{mm}$$

$$V_{S\alpha 1} = 1.4\text{kN}$$

$$V_{ij} = 3.1\text{kN}$$

Substituting these values into the above equation yields:

$$V_{\alpha 1} = 0.7 \text{ kN}$$

Repeating this procedure for all other flange blocks yields the following:

Table F. 2-7 Shear lag on flange blocks

Row Number(j)	Layer α Shear ($V_{\alpha j}$ (kN))	Layer β Shear ($V_{\beta j}$ (kN))
1	0.7	0.6
2	0.6	0.6
3	0.5	0.6
5	0.8	0.8
6	0.7	0.6
7	0.6	0.2

CALCULATE THE FLANGE CONTRIBUTION

The sum of the individual flange block shears above yields the total magnitude of shear force in the flange at this level of applied load:

$$\text{Sum of flange block shears} = 7.6 \text{ kN}$$

The specimen is loaded and supported as shown in Figure F. 2-6.

Therefore, for an applied load of 100kN, the shear at this section is:

$$V = (2.2/3) \times 100 = 73.3 \text{ kN}$$

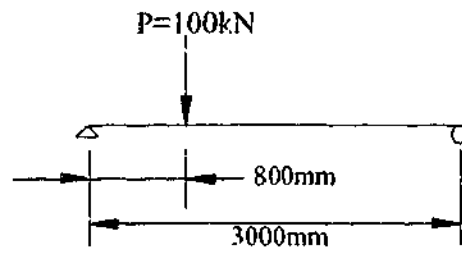


Figure F. 2-6 Schematic of Loading Applied to Specimen

Flange contribution = $7.6/73.3 \times 100$

Flange contribution = 10.4%

Appendix G PUBLICATIONS ARISING FROM THIS RESEARCH

- Al-Mahaidi, R. S., Taplin, G., Giaccio, C. and Bouilly, G. (2000), "Strength and load distribution analysis of a T-beam bridge deck", *Austrroads 4th Bridge Engineering Conference*, Adelaide, 261-264.
- Giaccio, C., Al-Mahaidi, R. S. and Taplin, G. (2000a), "Flange effectiveness in the shear strength of RC T-beams", *APSEC 2000*, K.L., 462-472.
- Giaccio, C., Sonnenberg, A. M. C., Taplin, G., Al-Mahaidi, R. S. and Guifre, A. (2000b), "Theoretical and proposed experimental investigation into the ultimate strength of RC T-beam bridges", *Austrroads 4th Bridge Engineering Conference*, Adelaide, 15-30
- Giaccio, C., Al-Mahaidi, R. S. and Taplin, G. (2002), "Experimental measurement of sectional forces in reinforced concrete slabs", *ACMSM 17*, Gold Coast, 175-180.
- Giaccio, C., Al-Mahaidi, R. S. and Taplin, G. (2002), "Experimental study on the effect of flange geometry on the shear strength of point loaded RC T-beams", *Canadian Journal of Civil Engineering*, in *Canadian Journal of Civil Engineering*, **29** (6), pp. 911-918.
- Giaccio, C., Al-Mahaidi, R. S. and Taplin, G. (2003a), " Flange Contribution to the resistance of shear of RC T-Beams ", Under preparation.
- Giaccio, C., Al-Mahaidi, R. S. and Taplin, G. (2003b), "Redistribution of flange strains and the formation of the shear mechanism in RC T-beams", Under preparation.
- Giaccio, C., Al-Mahaidi, R. S. and Taplin, G. (2003c), " Shear strength of RC T-beam bridge decks: Are we designing for the right thing?", Accepted for publication in APSEC 2003 proceedings.
- Giaccio, C., Al-Mahaidi, R. S. and Taplin, G. (2003d), " NLFEA of RC T-beams using solid elements ", Accepted for publication in APSEC 2003 proceedings.
- Giaccio, C., Al-Mahaidi, R. S. and Taplin, G. (2003e), " The Effect of the flange on the shear strength of RC T-beams ", *Concrete in the 3rd Millenium Conference* 17-19 July 2003 Brisbane, 1157-1166.